

Multifunctional Catalysts used in the Thermo-Catalytic Cracking of Hydrocarbon
Feedstocks for the Production of Light Olefins

Nabil Al-Yassir

A Thesis
In
The Department
Of
Chemistry and Biochemistry

Presented in Partial Fulfillment of the Requirements
for the Degree of Doctor of Philosophy at
Concordia University
Montreal, Quebec, Canada

December 2007

© Nabil Al-Yassir, 2007



Library and
Archives Canada

Bibliothèque et
Archives Canada

Published Heritage
Branch

Direction du
Patrimoine de l'édition

395 Wellington Street
Ottawa ON K1A 0N4
Canada

395, rue Wellington
Ottawa ON K1A 0N4
Canada

Your file *Votre référence*

ISBN: 978-0-494-34790-4

Our file *Notre référence*

ISBN: 978-0-494-34790-4

NOTICE:

The author has granted a non-exclusive license allowing Library and Archives Canada to reproduce, publish, archive, preserve, conserve, communicate to the public by telecommunication or on the Internet, loan, distribute and sell theses worldwide, for commercial or non-commercial purposes, in microform, paper, electronic and/or any other formats.

The author retains copyright ownership and moral rights in this thesis. Neither the thesis nor substantial extracts from it may be printed or otherwise reproduced without the author's permission.

AVIS:

L'auteur a accordé une licence non exclusive permettant à la Bibliothèque et Archives Canada de reproduire, publier, archiver, sauvegarder, conserver, transmettre au public par télécommunication ou par l'Internet, prêter, distribuer et vendre des thèses partout dans le monde, à des fins commerciales ou autres, sur support microforme, papier, électronique et/ou autres formats.

L'auteur conserve la propriété du droit d'auteur et des droits moraux qui protègent cette thèse. Ni la thèse ni des extraits substantiels de celle-ci ne doivent être imprimés ou autrement reproduits sans son autorisation.

In compliance with the Canadian Privacy Act some supporting forms may have been removed from this thesis.

Conformément à la loi canadienne sur la protection de la vie privée, quelques formulaires secondaires ont été enlevés de cette thèse.

While these forms may be included in the document page count, their removal does not represent any loss of content from the thesis.

Bien que ces formulaires aient inclus dans la pagination, il n'y aura aucun contenu manquant.


Canada

ABSTRACT

Multifunctional Catalysts used in the Thermo-Catalytic Cracking of hydrocarbon Feedstocks for the Production of Light Olefins

Nabil Al-Yassir
Concordia University, 2007

Light olefins such as ethylene and propylene, are considered the backbone of the petrochemical industry. They are the precursors of numerous plastic materials, synthetic fibers and rubbers. Commercially proven light olefin production technologies such as Steam Cracking (SC), Fluid Catalytic Cracking (FCC), and Deep Catalytic Cracking (DCC) are believed to have reached their full potential and cannot accommodate current demands of the petrochemical industry. The market demand for ethylene and propylene is projected to be about 140 and 90 million tons by year 2010, respectively. These current technologies cannot respond sufficiently to the rapidly growing demand for propylene, since propylene is only produced as a co-product of ethylene production. In addition, the high-energy consumption and the high GHG emissions are major setbacks for SC, which is regarded as the main light olefin technology. Thus, it is imperative that a new alternative should be developed in order to improve the production of light olefins. Thermo-Catalytic Cracking (TCC) has been recognized as a promising alternative route for light olefins production. Although, this process is still in the development stage, preliminary results show that the TCC offers several major advantages when compared to conventional SC: higher combined yields of light olefins, and significant energy savings.

In this dissertation, the TCC activities, kinetic study, and structural-textural-surface properties of different catalyst formulations, which have been investigated

thoroughly for their potential use in the TCC process, will be discussed. We report on our efforts to date to develop a suitable and an efficient catalyst that is characterized by high activity, high selectivity to light olefins, and high stability. A particular formulation studied was the hybrid catalyst configuration in which two components, microporous (zeolite) and mesoporous co-catalyst (supported metal oxide (i.e. $\text{MoO}_3\text{-CeO}_2$), were firmly bound to each other within a clay binder, such that a “pore continuum” effect was developed. Another version was the mesoporous supported bi-oxide catalyst, which is based on $\text{MoO}_3\text{-CeO}_2$ supported on high surface area-metal oxide. Explicitly, it was found that supported bi-oxide catalysts are quite active, stable and selective to light olefins in the Thermo-Catalytic Cracking of n-hexane, which was used as a model molecule for petroleum light naphtha. Furthermore, it was observed that the physico-chemical properties and subsequently the catalytic performance of these catalysts were influenced by many factors. Ytria stabilized alumina aerogel, which was prepared via sol-gel synthesis using super critical drying techniques, was considerably more effective as a catalyst support. Our results showed unambiguously that yttria stabilized alumina aerogel did not only possess a high surface area, but also was thermally and hydrothermally stable. In addition, it demonstrated a high ability of inducing homogenous distributions of impregnated metal oxides at high calcination temperature. The latter has resulted in significant improvements in the dispersion degree of Mo, Ce and MoCe species, and the retardation of sintering and sublimation of Mo species. More significantly, it was found that the on-stream-long term stability and the selectivity to light olefins over aromatics were increased upon the addition of CeO_2 into the supported mono-oxide MoO_3 catalyst.

PROFESSIONAL ACKNOWLEDGMENTS

Hidden between lines and figures of this thesis is a story. It is a story of adventure, sacrifice, love, gratitude, friendship, and most importantly, maturation. It's a classic tale of the birth of one person's awareness.

First and foremost, I would like to express my extreme gratitude to my supervisor Prof. Raymond Le Van Mao for giving me the opportunity to work in his lab over the past 5 years. I would like to thank you for introducing me to the field of catalysis, petroleum chemistry and zeolite, which I firmly believe taught me more about chemistry and chemical engineering than I would have imagined possible. I have learned immensely throughout the course of this degree from your comments, feedback and steady guidance. Without your valuable insight and input, as well as your extensive expertise this work would not have been possible or might not have ever come to fruition. I am thankful for the intellectual freedom you granted and the latitude to take this research in whatever direction I saw fit. I am also grateful for sending me to innumerable international and national conferences, which undoubtedly help me become a well-rounded scientist. I cannot adequately express how thankful I am.

I cannot fail to mention my thesis committee members, Prof. Georges Y. M. Dènès, Prof. Marcus F. Lawrence, and Prof. Peter H. Bird. I wish to express my thanks and appreciations for their helpful suggestions, encouragement and support throughout the course of this degree. Special thanks to Prof. Georges Y. M. Dènès for his useful suggestions and fruitful discussions concerning the solid-state chemistry aspects of this thesis. I would like to thank Prof. John A. Capobianco and Prof. Louis A. Cuccia for their

support and advice. I would also like to thank prof. Mamoun Medraj for accepting to be the external examiner to the department.

I would like to express my sincere appreciation to Prof. Harold H. Kung (Northwestern University/ Department of Chemical and Biological Engineering) for accepting to be my external examiner and taking the time to go through this thesis. It is an honor to have you as external examiner. Your extraordinarily creative and original contributions to the field of catalysis and reaction engineering have left a great impact on our understanding of reaction mechanisms of zeolite in the petroleum catalytic cracking. I have personally benefited a great deal from some of your well-cited work about surface acidity and transition metals.

I would like to sincerely thank the current and past Industrial Catalysis Group; Dr. Ngoc Thanh Vu, Lin Lu, Qun Zhao, Dr. AbdulHafeez Muntaser, and Hai Tao Yan. Thank you for your support, helpful advice, and putting up with my many moods (mainly bad ones). I would like to also thank the undergraduate students who worked with me; David Nguyen, Francine Heng, Angelique Fortier, and Samira Ansary.

From the bottom of my heart, I would like to sincerely and wholeheartedly thank my colleagues and best friends; Dr. Fiorenzo Vetrone, and Dr. John Christopher Boyer. We started out as work colleagues and somehow became close friends. I am grateful for your endless support, and useful advice. Over the course of my degree, you have made the department environment not only entertaining, but also intellectually stimulating as well. I always had a tremendous respect for your creativity, work originality, and work ethics. This opportunity has undoubtedly resulted in making me a well-rounded scientist and open-minded person. Special thanks to Dr. Fiorenzo Vetrone. I have learned a lot

from you, and my words cannot express my sincere gratitude. I thank you personally for the many heated political debates, which I have to admit changed the way I look at things in life. I would sincerely like to thank my friend Alwin Thurainayagam and Jamil Hantash for their valuable friendship and personal support. You were truly good friends with all meanings and like brothers to me. I would also like to thank Dr. Sean Hughes, Rafik Naccache, Francesca Mangiarini, and Dr. Venkataramanan Mahalingam for their companionship as well as many interesting days and nights.

This work was financially supported by grants from the Natural Sciences and Engineering Research Council (NSERC) of Canada, and Valeo Management. I would like to acknowledge Concordia University for partial personal funding during my Ph.D. studies (Concordia University Graduate Fellowship, Garnet Strong Scholarship, Campaign for Concordia Graduate Awards, and France and Andre Desmarais Graduate Fellowships).

PERSONAL ACKNOWLEDGMENTS

Needless to say, this entire Ph.D. dissertation would be at most a dream were it not for my loving family. I do not know how to start this, but I do know that no matter how much I say, or how long it will take me to finish it, my words will not be enough and definitely will run out before I adequately express my deep gratitude and appreciation to my whole family. They have supported me in many, many ways and this Ph.D. is as much as yours as it is mine. To my beloved parents: my father Othman H. Al-Yassir, and my mother Nadia H. Fathallah (Al-Yassir). Your countless emotional, moral and of course financial support, endless love, and unconditional sacrifice are the reasons why I made it to this point in my life. Your encouragement meant the world to me. You have waited so long for this moment to come true; I am glad that your waiting has finally been rewarded. I cannot fail to mention my older sister Soha Al-Shaali and her husband Salem Al-Shaali for their love, understanding and support. You have always been an important source of encouragement and support, and I was very fortunate to have both of you in my life. I would like also to truthfully thank my younger sister Nesreen Al-Yassir for her never-ending support and love. I must also mention and how can I forget my four beautiful nieces and nephews; Mariam Salem Al-Shaali, Shouq Salem Al-Shaali, Rashed Salem Al-Shaali and Mohamed Salem Al-Shaali. Their presence gave my life a beautiful taste and wonderful happiness. I cannot imagine my life without them. They were one of the best things I have in this difficult life.

*Whatever I have accomplished pales in comparison to
having you all in my life*

This Ph.D. Dissertation is dedicated;

To my beloved mother Nadia and father Othman

To my sister Soha and her husband Salem Al-Shaali

To my sister Nesreen

*To my beautiful nieces, Mariam & shoug Al-Shaali
and nephews, Rashed & Mohamed Al-Shaali*

*"Those truly fear Allah among His Servants who have knowledge: for Allah is
Exalted in Might Oft-Forgiving"*

(The Angels Originator: Holy Qur'an)

TABLE OF CONTENTS

LIST OF FIGURES	XVII
LIST OF SCHEMES.....	XXII
LIST OF TABLES.....	XXIII
CONTRIBUTIONS OF AUTHORS	XXVI
CHAPTER I.....	1
GENERAL INTRODUCTION	1
1.1. PREAMBLE	2
1.2. Crude Oil.....	3
1.2.1. The Origin of Crude Oil.....	3
1.2.2. The Chemical Composition of Crude Oil	4
1.2.3. Processing of Crude Oil	4
1.3. Catalytic and non-Catalytic Petroleum Processes.....	8
1.3.1. Thermal (steam) Cracking (SC).....	8
1.3.2. Catalytic Cracking	10
1.3.2.1. Catalytic Cracking Reaction Mechanism.....	11
1.4. Light Olefins	16
1.4.1. Overview of the Industrial Significance of Light Olefins	16
1.4.2. Main Industrial Technologies for Light Olefin Production	18
1.4.3. Roadblocks in the Light Olefins Industry	19
1.4.4. Paving the Way	20
1.4.5. Thermo-Catalytic Cracking (TCC) - Groundbreaking Olefin Technology	22
1.5. OUTLINE	24
1.6. REFERENCES	31
Chapter II.....	34
Experimental Evidence for the pore Continuum in Hybrid Catalysts used in the Selective Deep Catalytic Cracking of n-Hexane and petroleum Naphthas.....	34

ABSTRACT.....	35
2.1. INTRODUCTION	36
2.2. EXPERIMENTAL.....	37
2.2.1. Preparation of the Hybrid Catalysts.....	37
2.2.2. Catalyst Characterization.....	39
2.2.3. Experimental set-up for catalytic testing	39
2.3. RESULTS AND DISCUSSION.....	40
2.3.1. Isotherms of adsorption and desorption of nitrogen	40
2.3.2. Catalytic performance.....	44
2.4. CONCLUSION.....	49
2.5. ACKNOWLEDGEMENTS.....	50
2.6. AUTHOR'S NOTES AND SIGNIFICANCE OF PAPER TO THESIS.....	50
2.7. REFERENCES	51
Chapter III	53
Physico-chemical properties of mixed molybdenum and cerium oxides supported on silica-alumina and their use as catalysts in the Thermo-Catalytic Cracking (TCC) of n-hexane.....	53
ABSTRACT.....	54
3.1. INTRODUCTION	55
3.2. EXPERIMENTAL.....	57
3.2.1. Catalyst Preparation.....	57
3.2.2. Catalyst Characterization.....	59
3.2.3. Experimental set-up for catalytic testing	60
3.3. RESULTS AND DISCUSSION.....	61
3.3.1. Mono-component MoO ₃ /SiAl and CeO ₂ /SiAl catalysts.....	61
3.3.2. Bi-component co-impregnated MoO ₃ -CeO ₂ /SiAl catalysts	69
3.4. CONCLUSION.....	76

3.5. ACKNOWLEDGEMENTS	77
3.6. AUTHOR'S NOTES AND SIGNIFICANCE OF PAPER TO THESIS.....	77
3.7. REFERENCES	78
 Chapter IV.....	 82
Thermal Stability of Alumina Aerogel doped with Yttrium Oxide, used as a Catalyst Support for the Thermo-Catalytic Cracking (TCC) Process; An Investigation of its Textural and Structural Properties	82
ABSTRACT.....	83
4.1. INTRODUCTION	84
4.2. EXPERIMENTAL.....	87
4.2.1. Preparation of Catalyst Supports	87
4.2.2. Catalyst Supports Characterization.....	87
 4.3. RESULTS AND DISCUSSION	 89
4.4. CONCLUSION.....	104
4.5. ACKNOWLEDGEMENTS.....	104
4.6. AUTHOR'S NOTES AND SIGNIFICANCE OF PAPER TO THESIS.....	104
4.7. REFERENCES	105
 Chapter V.....	 109
Evaluating and Understanding the Hydrothermal Stability of Alumina Aerogel doped with Yttrium Oxide, used as a Catalyst Support for the Thermo-Catalytic Cracking (TCC) Process	109
ABSTRACT.....	110
5.1. INTRODUCTION	111
5.2. EXPERIMENTAL.....	114
5.2.1. Materials	114
5.2.2. Characterization	115
5.2.3. Hydrothermal stability tests	117

5.3. RESULTS AND DISCUSSION	117
5.3.1 Short review of pertaining information to the thermal and hydrothermal stability of alumina.....	117
5.3.2. Hydrothermal Stability of yttria doped alumina Aerogel	120
5.3.3. Thermal and Hydrothermal Stability of yttria impregnated alumina.....	133
5.3.4. Comparison between yttria doped alumina aerogel and yttria impregnated alumina (conventional alumina and alumina aerogel).....	143
5.4. CONCLUSION.....	146
5.5. ACKNOWLEDGEMENTS.....	147
5.6. AUTHOR'S NOTES AND SIGNIFICANCE OF PAPER To THESIS	147
5.7. REFERENCES	148
Chapter VI.....	152
Catalysts for the Thermo-Catalytic Cracking (TCC) Process: Interactions between the yttria in yttria doped alumina aerogel and the mono-oxide MoO ₃ , CeO ₂ , and bi-oxide MoO ₃ -CeO ₂ species.....	152
ABSTRACT.....	153
6.1. INTRODUCTION	154
6.2. EXPERIMENTAL.....	156
6.2.1. Catalyst Preparation.....	156
6.2.1.1. Catalyst support	156
6.2.1.2. Supported mono- and bi-oxide based catalysts.....	156
6.2.2. Catalyst Characterization.....	157
6.3. RESULTS AND DISCUSSION.....	159
6.3.1. Supported mono-oxide MoO ₃	159
6.3.1.1. Textural properties	159
6.3.1.2. Surface configuration of Mo oxide species	160
6.3.1.3. Retarding effect of doped yttria on the sublimation of MoO ₃	167
6.3.1.4. More on the effect of doped yttria on the MoO ₃ dispersion	172
6.3.2. Supported mono-oxide CeO ₂	175
6.3.2.1. Textural Properties.....	175
6.3.2.2. Surface configuration of Ce oxide species.....	176
6.3.2.3. More about CeO ₂ dispersion	180
6.3. Supported bi-oxide MoO ₃ -CeO ₂	185
6.3.3.1. Textural properties	185

6.3.3.2. Surface configuration of bi-oxide Mo-Ce species	186
6.3.3.3. Thermal Analysis Results	190
6.3.3.4. More on the dispersion of supported bi-oxide MoO ₃ -CeO ₂ catalysts.....	192
6.4. CONCLUSION.....	193
6.5. ACKNOWLEDGEMENTS	194
6.6. AUTHOR'S NOTES AND SIGNIFICANCE OF PAPER TO THESIS.....	195
6.7. REFERENCES	195
Chapter VII	200
Supported MoO ₃ -CeO ₂ catalysts used in the Thermo-Catalytic Cracking (TCC) Process for the Production of Light Olefins. Effects of Surface Acidity and other Physico-Chemical Properties on performance and kinetic behavior.....	200
ABSTRACT.....	201
7.1. INTRODUCTION	203
7.1.1. Production of Light Olefins	203
7.1.2. Thermal cracking and catalytic cracking	204
7.1.3. Objectives of the present study	206
7.2. EXPERIMENTAL	207
7.2.1. Catalyst Preparation	207
7.2.2. Catalyst Characterization	207
7.2.3. Thermo-Catalytic Cracking Activities	209
7.2.4. Kinetic study of steam cracking and TCC reactions.....	210
7.2.4.1. Thermal (steam) cracking (SC).....	210
7.2.4.2. Thermo-Catalytic Cracking (TCC).....	211
7.3. RESULTS AND DISCUSSION	212
7.3.1. Detailed acidity investigation	212
7.3.2. Thermo-Catalytic Cracking (TCC) activities of supported mono- and bi-oxide based catalysts.....	229
7.3.3. Kinetic study	241
7.4. CONCLUSION.....	244

7.5. ACKNOWLEDGEMENTS	245
7.6. AUTHOR’S NOTES AND SIGNIFICANCE OF PAPER TO THESIS.....	245
7.7. REFERENCES	245
CHAPTER VIII	250
CONCLUSIONS, ONGOING and FUTURE WORK, AND SIGNIFICANCE	250
8.1. GENERAL CONCLUSION	251
8.2. ONGOING and FUTURE WORK	257
8.2.1. Short Term Objectives	257
8.2.2. Long Term Objectives	259
8.2.2.1. Hydrogen Spillover (HSO) Phenomenon	260
8.2.2.2. Pore Continuum Configuration.....	262
8.2.2.3. Evaluation of the existence of hydrogen spillover phenomenon (HSO) with Ni-cocatalyst // zeolite pore continuum configuration in the TCC process	263
8.2.2.4. Identification of the beneficial role of HSO on the TCC catalyst.....	265
8.2.2.4.1. The TCC activities and stabilities of model molecules	265
8.2.2.4.2. Analysis of Carbonaceous deposits (coke)	266
8.3. THE SIGNIFICANCE OF THIS THESIS	267
8.3.1 Thermal-Catalytic Cracking process.....	267
8.3.2. Research and development in the field of catalysis	267
8.3.3. The Canadian petroleum industry and the environment	268
8.4. REFERENCES	269

- Fig.3.4:** Raman spectra of (a) unsupported MoO₃-CeO₂ catalysts with different [Ce]/[Mo] molar ratio, A) 0.13, B) 0.30, C) 0.41, D) 0.59 and E) 0.88, and (b) silica-alumina supported bi-component MoO₃-CeO₂ catalysts prepared by co-impregnation and with different [Ce]/[Mo] molar ratio, A) 0.13, B) 0.30, C) 0.41, D) 0.59 and E) 0.88 72
- Fig.3.5:** X-ray diffraction patterns of silica-alumina supported bi-component catalysts ([Ce]/[Mo] = 0.41), with different preparation methods, A) co-impregnation (MoCe/SiAl), B) Sequential Impregnation (Mo → Ce/SiAl), and C) Reverse Sequential Impregnation (Ce → Mo/SiAl), (*) Reflections due MoO₃, (#) Reflections due to Al₂(MoO₄)₃ and (^) Reflections due to CeO₂ crystallites..... 75
- Fig.3.6:** Raman spectra of silica-alumina supported bi-component catalysts ([Ce]/[Mo] = 0.41), with different preparation methods, A) co-impregnation (MoCe/SiAl), B) Sequential Impregnation (Mo → Ce/SiAl), and C) Reverse Sequential Impregnation (Ce → Mo/SiAl) 75
- Fig.4.1:** X-ray diffraction patterns of samples calcined at 750 °C for 3 h. (A) conventional Al₂O₃, (B) undoped alumina aerogel, (C) 2.5 Y₂O₃-Al₂O₃, (D) 5.0 Y₂O₃-Al₂O₃ (E) 10.0 Y₂O₃-Al₂O₃, and (F) 20.0 Y₂O₃-Al₂O₃. * γ-Al₂O₃..... 91
- Fig.4.2:** X-ray diffraction patterns of samples calcined at 1000 °C for 3 h. (A) conventional Al₂O₃, (B) undoped alumina aerogel, (C) 2.5 Y₂O₃-Al₂O₃, (D) 5.0 Y₂O₃-Al₂O₃ (E) 10.0 Y₂O₃-Al₂O₃, and (F) 20.0 Y₂O₃-Al₂O₃. (*) γ-Al₂O₃, (+) θ-Al₂O₃, and (-) α-Al₂O₃..... 91
- Fig.4.3:** X-ray diffraction patterns of samples calcined at 1100 °C for 3 h. (A) conventional Al₂O₃, (B) undoped alumina aerogel, (C) 2.5 Y₂O₃-Al₂O₃, (D) 5.0 Y₂O₃-Al₂O₃ (E) 10.0 Y₂O₃-Al₂O₃, and (F) 20.0 Y₂O₃-Al₂O₃. (+) θ Al₂O₃, (-) α-Al₂O₃, and (^) YAlO₃..... 92
- Fig.4.4:** X-ray diffraction patterns of samples calcined at 1200 °C for 3 h. (A) conventional Al₂O₃, (B) undoped alumina aerogel, (C) 2.5 Y₂O₃-Al₂O₃, (D) 5.0 Y₂O₃-Al₂O₃ (E) 10.0 Y₂O₃-Al₂O₃, and (F) 20.0 Y₂O₃-Al₂O₃. (-) α-Al₂O₃, and (^) YAlO₃ 92
- Fig.4.5:** TEM micrographs and electron diffraction patterns (represented by *) of samples calcined at 750 °C for 3 h. (A) conventional Al₂O₃, (B) undoped alumina aerogel, (C) 10 Y₂O₃-Al₂O₃, (D) and (E) are 10.0 Y₂O₃-Al₂O₃, calcined at 1000 °C and 1100 °C, respectively 95
- Fig.4.6:** Loss of surface area of samples calcined at 750 °C and 1000 °C for 50 h. (a) conventional alumina, (b) undoped alumina aerogel, (c) 2.5 wt.% Y₂O₃-Al₂O₃, (d) 10.0 wt.% Y₂O₃-Al₂O₃ and (e) 20.0 wt.% Y₂O₃-Al₂O₃ 97

Fig.4.7: ^{27}Al MAS NMR of samples calcined at 750 °C for 3 h. (A) conventional Al_2O_3 , (B) undoped alumina aerogel, (C) 2.5 $\text{Y}_2\text{O}_3\text{-Al}_2\text{O}_3$, (D) 5.0 $\text{Y}_2\text{O}_3\text{-Al}_2\text{O}_3$ (E) 10.0 $\text{Y}_2\text{O}_3\text{-Al}_2\text{O}_3$, and (F) 20.0 $\text{Y}_2\text{O}_3\text{-Al}_2\text{O}_3$. (G) and (H) are 10.0 $\text{Y}_2\text{O}_3\text{-Al}_2\text{O}_3$, calcined at 1000 °C and 1100 °C, respectively 103

Fig.5.1A-B: Loss of total pore volume of various samples as a function of different exposure time to steam at (A) 750 °C and (B) 1000 °C 121

Fig.5.2: (a) XRD patterns of conv.alumina extrudates after exposure to steam at high temperature; A and B are sample powder [15] and extrudate, respectively. C-F are sample extrudates exposed to steam for 1, 5, 10 and 24 h, respectively. (b) represents the undoped alumina aerogel extrudate. (c) represents the 10.0 wt.% yttria doped alumina aerogel extrudate. (*) $\gamma\text{-Al}_2\text{O}_3$, (+) $\theta\text{-Al}_2\text{O}_3$, (-) $\alpha\text{-Al}_2\text{O}_3$, and (#) Bentonite 122

Fig.5.3: FTIR spectra of adsorbed pyridine on; a) conv.alumina, b) undoped alumina aerogel, c-e) yttria doped alumina aerogel with 5.0, 10.0 and 20.0 wt.% yttria, respectively, and f-g) 10.0 wt.% yttria impregnated alumina and alumina aerogel, respectively. (* Lewis sites)..... 128

Fig.5.4: ^1H MAS NMR of samples calcined at 750 °C for 3 h. (A) conv.alumina, (B) undoped alumina aerogel, (C) 10.0 $\text{Y}_2\text{O}_3\text{-Al}_2\text{O}_3$, and (D) 20.0 $\text{Y}_2\text{O}_3\text{-Al}_2\text{O}_3$ 131

Fig.5.5: XRD patterns of calcined samples at different temperature; A- Conv.alumina, B- 5.0 $\text{Y}_2\text{O}_3/\text{Al}_2\text{O}_3$, C- 10.0 $\text{Y}_2\text{O}_3/\text{Al}_2\text{O}_3$, and D- 20.0 $\text{Y}_2\text{O}_3/\text{Al}_2\text{O}_3$. (*) $\gamma\text{-Al}_2\text{O}_3$, (+) $\theta\text{-Al}_2\text{O}_3$, (-) $\alpha\text{-Al}_2\text{O}_3$ (^) YAlO_3 , and (<) Y_2O_3 136

Fig.5.6: XRD patterns of calcined samples at at different temperature; A- alumina aerogel, B- 5.0 $\text{Y}_2\text{O}_3/\text{aerogel}$, C- 10.0 $\text{Y}_2\text{O}_3/\text{aerogel}$, and D- 20.0 $\text{Y}_2\text{O}_3/\text{aerogel}$. (Note: for symbols refer to Fig. 5.5)..... 138

Fig.5.7: Loss of BET specific surface area (S_{BET}) as a function of different calcination temperature at different duration, of yttria impregnated conv.alumina (A) and alumina aerogel (B) with various yttria loadings, respectively 141

Fig.5.8: Loss of BET specific surface area (S_{BET}) as a function of different exposure time to steam at different temperature, of 10.0 wt.% yttria impregnated conventional alumina (A) and alumina aerogel (B), respectively 142

Fig. 5.9: ^{27}Al MAS NMR of samples calcined at 750 °C for 6 h. (A) conv.alumina [15], (B) alumina aerogel [15], (C) and (D) 10.0 and 20.0 wt.% yttria doped alumina aerogel, respectively [15], (E) and (F) 10.0 and 20.0 wt.% yttria impregnated conv.alumina, respectively, and (G) and (H) 10.0 and 20.0 wt.% yttria impregnated alumina aerogel, respectively (* spinning side bands (SSB)) 146

Fig.6.1 (a-c): X-ray diffraction patterns of supported mono-oxide MoO ₃ catalysts, with different MoO ₃ loadings (wt.%), (A) 0.0, (B) 2.0, (C) 5.0, (D) 8.0, (E) 12.0, (F) 15.0, and (G) 20.0. (^) Reflections due to γ -Al ₂ O ₃ (JCDPS No. 29-0063), and (>)Y ₂ (MoO ₄) ₃ (JCPDS No.28-1451)	162
Fig.6.2 (a-c): Laser Raman spectra of mono-oxide MoO ₃ catalysts, with different MoO ₃ loadings (wt.%), (A) 2.0, (B) 5.0, (C) 8.0, (D) 12.0, (E) 15.0, and (F) 20.0	166
Fig.6.3: DTA/TGA curves of A) unsupported MoO ₃ , B) and C) unsupported bi-oxide MoO ₃ -CeO ₂ with [Ce]/[Mo] of 0.13 and 0.44, respectively. (-----) DTA and (_____) TGA	167
Fig.6.4 (A-C): TGA curves of calcined supported mono- and bi-oxide catalysts; a) support, b) and c) mono-oxide MoO ₃ with 12.0 and 20.0 wt.% MoO ₃ loadings, respectively, and d) and e) bi-oxide MoO ₃ -CeO ₂ with [Ce]/[Mo] of 0.13 and 0.44, respectively	169
Fig.6.5: Zeta potential curves of dispersed particles versus pH of aqueous solutions for pure Y ₂ O ₃ (+), conv.alumina (■), alumina aerogel (●), 2.5 wt.% (▲), 10.0 wt.% (▼) and 20.0 wt.% (◆) yttria doped alumina aerogel (Y ₂ O ₃ -Al ₂ O ₃)	175
Fig.6.6 (a-c): X-ray diffraction patterns of supported mono-oxide CeO ₂ catalysts, with different CeO ₂ loadings (wt.%), (A) 2.0, (B) 4.0, (C) 6.0, (D) 8.0, (E) 10.0 and (F) 15.0. (^) Reflections due to γ -Al ₂ O ₃ , and (<) CeO ₂ (JCPDS No.34-0394)	177
Fig.6.7: A) X-ray diffraction patterns of 15.0 wt.% CeO ₂ catalysts loaded onto different supports (re-plot of Fig.6 (a-c). B) Unit cell parameters (nm) of unsubstituted CeO ₂ or substituted CeO ₂ solid solution (Ce _{1-x} Y _x O _{2-x/2}) as a function of various catalyst supports; (■) conv.alumina, (●) alumina aerogel, (▲) 2.5 wt.%, (▼) 10.0 wt.% and (◆) 20.0 wt.% yttria doped alumina aerogel.....	183
Fig.6.8 (a-d): X-ray diffraction patterns of supported bi-oxide MoO ₃ -CeO ₂ catalysts, with different [Ce]/[Mo] molar ratio; (A) 0.13, (B) 0.44, and (C) 0.88. (^) Reflections due to γ -Al ₂ O ₃ , (<) CeO ₂ , (*) MoO ₃ (JCPDS No. 35-0609).....	187
Fig.6.9 (a-d): laser Raman spectra of supported bi-oxide MoO ₃ -CeO ₂ catalysts with different [Ce]/[Mo] molar ratio; (A) 0.13, (B) 0.44, and (C) 0.88.....	188
Fig.7.1: Variation of the 1444 cm ⁻¹ Lewis sites band area as a function of different catalyst support with various ceria loadings	216
Fig.7.2: FTIR spectra of supported mono-oxide MoO ₃ with various MoO ₃ loadings (wt.%); A) 0.0, B) 4.0, C) 8.0, D) 12.0, and E) 20.0 after pyridine adsorption at 100 °C for two different catalyst support (a) conv.alumina, (b) undoped alumina aerogel, and (c) 10.0 wt.% yttria doped alumina aerogel. (d) represents Brönsted/Lewis sites ratio verses	

different MoO₃ loadings on different supports; (■) conv.alumina, (◆) undoped aerogel, (▲) and (▼) are 10.0 and 20.0 yttria doped alumina aerogel 217

Fig.7.3: Variation of (a) the 1540 cm⁻¹ Brönsted sites band area and (b) the 1444 cm⁻¹ Lewis sites band area of Mo supported catalysts as a function of pyridine desorption temperature 223

Fig.7.4: FTIR spectra of supported bi-oxide MoO₃-CeO₂ with different [Ce]/[Mo] ratios; A) 0.13, B) 0.44, and C) 0.88, after pyridine adsorption at 100 °C for two different catalyst support (a) conv.alumina and (b) 10.0 wt.% yttria doped alumina aerogel. (c) represents Brönsted/Lewis sites ratio vs. various [Ce]/[Mo] ratios on different supports; (■) conv.alumina, (◆) undoped aerogel, (▲) and (▼) are 10.0 and 20.0 yttria doped alumina aerogel 226

Fig.7.5: FTIR spectra of yttria doped alumina aerogel supported (a) 12.0 wt.% MoO₃, and (b) 0.44 MoO₃-CeO₂, after pyridine adsorption at 100 °C and outgassing at different temperature; (A) 100, (B) 200, (C) 300, (D) 400, and (E) 500 °C. (c) represents the Brönsted (B) and Lewis (L) acid sites band area of supported MoO₃ and MoO₃-CeO₂ ((■) and (▼) are L and B of supported MoO₃, respectively). ((◆) and (▲) are L and B of supported MoO₃-CeO₂, respectively) 228

Fig.7.6: TCC activities of mono-oxide CeO₂ with various ceria loadings supported on A) conv.alumina, B) undoped alumina aerogel, C) 10.0 yttria doped alumina aerogel. (▼) total conversion (C_t); (◆) selectivity to light olefins; (▲) selectivity to BTX. 231

Fig.7.7: Pore size distribution curves (dv/d log D) of MoO₃ (●), CeO₂ (▲) and MoO₃-CeO₂ (*) catalysts supported on (a) conv.alumina (■) and (b) 10.0 wt.% Y₂O₃-Al₂O₃ (■). The contents of MoO₃ and CeO₂ were 12.0 wt.% and 2.0 wt.%, respectively for mono-oxide catalyst, and [Ce]/[Mo] ratio = 0.13 for bi-oxide catalyst 235

Fig.7.8: Amount (a) and combustion temperature (b) of carbonaceous deposits (coke) on different supported catalyst system. The number between parenthesis represents the [Ce]/[Mo] ratio 240

Fig.7.9: Total conversion (C_t in Mole fraction) versus residence time (t_r in s) in the steam cracking of n-hexane; A,A' = 913.15 K, B,B' = 933.15 K, C,C' = 953.15 K, D,D' = 973.15 K, E, E' = 993.15 K 241

Fig.7.10: Total conversion (C_t in Mole fraction) versus contact time (t in s) in the TCC of n-hexane; A,A' = 913.15 K, B,B' = 933.15 K, C,C' = 953.15 K, D,D' = 973.15 K, E, E' = 993.15 K, (a) 12.0 wt.% MoO₃/ 10.0 wt.% yttria doped alumina aerogel, and (b) 12.0 wt.% MoO₃-6.0 wt.% CeO₂/ 10.0 wt.% yttria doped alumina aerogel 242

LIST OF SCHEMES

Scheme 1.1: Steam cracking. Reaction mechanism.....	10
Scheme 1.2: Individual steps of catalytic cracking reactions.....	11
Scheme 1.3: The main important current sources of light olefins	18
Scheme 1.4: Schematic representation of TCC multi-zone reactor configuration.....	23
Scheme 7.1: Tetrahedral and octahedral surface molybdate species on the surface of yttria doped alumina aerogel [50].....	221
Scheme 7.2: Reaction pathway of the dehydrocyclization reaction of paraffin molecule (olefins are formed by β -scission cracking of starting carbenium ion, R = -H or -CH ₃) [5]	237
Scheme 8.1: schematic representation of spillover phenomenon; from an active metal adsorbing surface onto a catalyst support, and then onto another surface that is in contact with the support.....	261
Scheme 8.2: schematic representation of hydrogenation of chemisorbed pyridine to piperidine on Ni promoted supported bi-oxide hybrid catalysts, after exposure to H ₂ (the effect of HSO phenomenon)	264

LIST OF TABLES

Table 1.1: The boiling points and carbon chain length for various crude oil fractions [1]	7
Table 2.1: Volume of nitrogen adsorbed and desorbed, a comparison between hybrid catalyst and its corresponding mechanical solid mixture	44
Table 2.2: Conversion of n-hexane obtained with the Hybrid catalyst and its corresponding solid mixtures (of different extrudate diameters).....	45
Table 2.3: Product selectivities for hybrid catalyst and the corresponding mechanical solid mixtures of extrudates of different diameters (Catalyst composition is 46 wt.% H-silicalite and 56 wt.% cocat 1)	46
Table 2.4: Catalytic activity of the extrudates of bentonite (Bent) and of some parent solids used as supports or active components.....	48
Table 2.5: Catalytic activity of the cocatalysts with different supports and their corresponding hybrid catalysts (44 wt.% HZ. Cocat 1 = MoO ₃ -CeO ₂ /SiAl; Cocat 2 = MoO ₃ -CeO ₂ /SiO ₂).....	49
Table 3.1: Textural properties of the support, bulk and silica-alumina supported MoO ₃ catalysts; all samples were activated at 650°C in air for 3h.....	63
Table 3.2: Textural properties of bulk and supported silica-alumina supported CeO ₂ catalysts; all samples were activated at 650°C in air for 3h.....	66
Table 3.3: Catalytic activity of mono-component silica-alumina supported MoO ₃ with various MoO ₃ loadings in the TCC of n-hexane ^a	67
Table 3.4: Acid site density of silica-alumina supported mono-component and bi-component catalysts; all catalysts were activated at 650°C in air for 3h prior to surface acidity analysis.....	68
Table 3.5: Catalytic activity of mono-component silica-alumina supported CeO ₂ with various CeO ₂ loadings in the TCC of n-hexane ^a	69
Table 3.6: Catalytic activity of t bi-component silica-alumina supported mixed MoO ₃ -CeO ₂ prepared by co-impregnation with various [Ce]/[Mo] Molar ratios, in the TCC of n-hexane ^a	70
Table 3.7: Catalytic activity of bi-component silica-alumina supported mixed MoO ₃ -CeO ₂ based catalysts ([Ce]/[Mo] = 0.41) prepared by two-step impregnation method (sequential and reverse sequential impregnation) in the TCC of n-hexane ^a	73

Table 4.1: X-ray diffraction pattern results of the conventional alumina, undoped and yttria doped alumina aerogel with various yttria loadings ^(a)	90
Table 4.2: Changes in the BET specific surface area of conventional alumina, undoped and yttria doped alumina aerogel as a function of calcination temperature for 3 h.....	96
Table 5.1: Changes in the BET specific surface area (S_{BET}) of different catalyst supports (in extrudate form) as a function of exposure time to steam, at $T = 750\text{ }^{\circ}\text{C}$, and H_2O flow rate = 1.1 ml/h^a	120
Table 5.2: Changes in the BET specific surface area (S_{BET}) of different catalyst supports (in extrudate form) as a function of exposure time to steam, at $T = 1000\text{ }^{\circ}\text{C}$, and H_2O flow rate = 1.1 ml/h^a	123
Table 5.3: Approximate quantity of -OH groups lost, and distribution of (subsequently formed) Lewis sites upon calcinations in dry air	127
Table 5.4: X-ray diffraction pattern results of the conventional alumina, undoped alumina aerogel and yttria doped alumina with various yttria loadings ^a	134
Table 5.5: Changes in the specific surface area (S_{BET}) and total pore volume of yttria-impregnated alumina (i.e. conv.alumina and alumina aerogel) as a function of calcination temperature for 6 h.....	139
Table 6.1: Textural properties of mono-oxide MoO_3 catalysts supported on different support.....	160
Table 6.2: TGA of the region between 750 to 1100 $^{\circ}\text{C}$ of supported mono-oxide and bi-oxide catalysts	168
Table 6.3: Textural properties of mono-oxide CeO_2 catalysts supported on different support.....	176
Table 6.4: The crystallite size (nm) of substituted CeO_2 solid solution in the supported mono-oxide CeO_2 , and CeO_2 crystallites in the bi-oxide $\text{MoO}_3\text{-CeO}_2$	178
Table 6.5: Textural properties of bi-oxide $\text{MoO}_3\text{-CeO}_2$ catalysts supported on different support; all samples were activated at $750\text{ }^{\circ}\text{C}$ in air for 3 h.....	185
Table 7.1: Total acid sites density (mmol g^{-1}) by $\text{NH}_3\text{-TPD}$ of supported mono-oxide and bi-oxide based catalysts	214
Table 7.2: Thermo-Catalytic Cracking (TCC) of n-hexane over different alumina oxide based catalysts ^a	230

Table 7.3: Thermo-Catalytic Cracking (TCC) of n-hexane over supported mono-oxide MoO ₃ based Catalysts ^a	233
Table 7.4: Thermo-Catalytic Cracking (TCC) of n-hexane over supported bi-oxide MoO ₃ -CeO ₂ based Catalysts	239
Table 7.5: The activation energy (E _a) and the pre-exponential factor (A) in the steam cracking and Thermo-Catalytic Cracking (TCC) of n-hexane	241
Table 8.1: TCC activities of heavy feedstocks using the hybrid catalyst containing the co-catalyst ^a	259
Table 8.2: Typical analysis of different petroleum feedstocks	260
Table 8.3: Performance of the hybrid catalyst containing HZSM-5 (Si/Al = 25) as the microporous zeolite component, and Ni-cocatalyst as the mesoporous component ^a	263
Table 8.4: The chemical structure and boiling point range of different class of PNA hydrocarbons	266

CONTRIBUTIONS OF AUTHORS

The following summarizes the contributions of each the authors cited in this dissertation.

CHAPTER II: “Experimental evidence for the Pore Continuum in Hybrid Catalysts used in the Selective Deep Catalytic Cracking (SDCC) of n-Hexane and Petroleum Naphthas”

R. Le Van Mao: project supervisor and manuscript preparation

N. Al-Yassir: experimental work

D. T. T. Nguyen: aided in experimental work

CHAPTER III: “Physico-chemical properties of mixed molybdenum and cerium oxides supported on silica-alumina and their use as catalysts in the Thermo-Catalytic Cracking (TCC) of n-hexane”

N. Al-Yassir: experimental work and manuscript preparation

R. Le Van Mao: project supervisor

CHAPTER IV: “Thermal Stability of Alumina Aerogel doped with Yttrium Oxide, used as a Catalyst Support for the Thermo-Catalytic Cracking (TCC) Process; An Investigation of its Textural and Structural Properties”

N. Al-Yassir: experimental work and manuscript preparation

R. Le Van Mao: project supervisor

CHAPTER V: “Evaluating and Understanding the Hydrothermal Stability of Alumina Aerogel Doped with Yttrium oxide, used as a Catalyst Support for the Thermo-Catalytic Cracking (TCC) Process”

N. Al-Yassir: experimental work and manuscript preparation

R. Le Van Mao: project supervisor

CHAPTER VI: “Catalysts for the Thermo-Catalytic Cracking (TCC) Process: Interactions between the yttria in yttria doped alumina aerogel and the mono-oxide MoO_3 , CeO_2 , and bi-oxide $\text{MoO}_3\text{-CeO}_2$ species

N. Al-Yassir: experimental work and manuscript preparation

R. Le Van Mao: project supervisor

CHAPTER VII: “ Thermo-Catalytic Cracking Performance and kinetic Study of n-Hexane over Ytria doped Alumina Aerogel Supported bi-oxide $\text{MoO}_3\text{-CeO}_2$ used in the Thermo-Catalytic Cracking (TCC) Process for the Production of Light Olefins: Relation to Surface Acidity and other Physico-Chemical Properties”

N. Al-Yassir: experimental work and manuscript preparation

R. Le Van Mao: project supervisor

CHAPTER I

GENERAL INTRODUCTION

1.1. PREAMBLE

Light olefins and diolefins such as ethylene, propylene, butenes and butadienes are considered the backbone of the petrochemical industry. They are the precursors of numerous plastic materials, synthetic fibers and rubbers. The most prevalent technologies for producing these precursors are Steam Cracking (SC) and recently Fluid Catalytic Cracking (FCC) using ZSM-5 zeolite containing catalysts. Also significant, but far less dominant are Deep Catalytic Cracking, Catalytic Dehydrogenation, Methanol to Olefins, and Olefin Metathesis. Many other technologies have been studied and developed, but none have yet reached commercial implementation: examples are Catalytic Cracking and Oxidative Dehydrogenation. The market demand for ethylene and propylene in the year 2000 was 89 and 51 million metric tons (Mt), respectively. It is expected that the demand for ethylene and propylene by the year 2010 will increase to about 140 and 90 million Mt, respectively. However, with the current olefin technologies, it is becoming increasingly difficult and costly to satisfy the market demands and meet the stringent environmental regulations. Propylene is produced as a by-product of both SC and FCC, thus the strongly increasing propylene demand cannot be satisfied by the current technologies. In addition, the increasingly stringent environmental regulations requiring lower level of green house gas emissions, and the high energy consumptions are imposing a great deal of pressure on the olefin industry. The key olefin technologies are believed to have reached their full potential and cannot accommodate current demands of the petrochemical industry, let alone those of the future. Thus, it is imperative that we develop a new alternative to improve the production of light olefins.

Thermo-Catalytic Cracking (TCC) has been recognized as a promising alternative route for light olefins production and has been extensively studied since 1998. Although, this process is still in the development stage, preliminary results show that the TCC offers several major advantages when compared to conventional SC: higher combined yields of ethylene and propylene, lower emission of green house gases, significant energy savings, and capability of reducing the commercially low-valued heavy products (i.e. polynuclear aromatics). The TCC process, which can selectively produce light olefins, combines the effects of thermal and catalytic cracking reactions. Several catalyst formulations have been investigated such as hybrid catalyst configuration in which two components, microporous (zeolite type) and mesoporous co-catalyst (supported metal oxide), were firmly bound to each other within a clay binder, such that a “pore continuum” effect was developed. Another version of the catalyst is the mesoporous supported metal oxide catalyst, which is based on molybdenum-cerium oxides supported on high surface area and thermally-hydrothermally stable irreducible metal oxide.

Further improvements to the TCC are challenging and can be achieved by properly balancing various aspects of the catalyst configuration and the reaction parameters. However, the catalyst configuration remains the key factor that needs to be carefully and thoroughly investigated. A deeper understanding of the origin of the synergy between the different components within the catalyst structure, the influence of the physical and chemical factors, and the role of thermal cracking are necessary to provide significant improvements to the TCC.

1.2. Crude Oil

1.2.1. The Origin of Crude Oil

Crude oil is commonly referred to as petroleum, which is derived from the Latin *petra*-rock and *oleum*-oil. It is also sometimes informally called black gold. It can be defined as a naturally occurring brown to black flammable liquid that consist of a mixture of hydrocarbons that exists in liquid phase in natural oil underground reservoirs and remains liquid at atmospheric pressure after passing through surface separating facilities. It is generally accepted that crude oils are derived from marine animals and plants debris subjected to high temperature and pressure [1]. Scientists believed that the bodies of dead prehistoric sea animals and plants became trapped and covered by layers of sediments. Clearly, this process happened before they had time to decay in the air. After millions of years (approximately 300 million years), presence of anaerobic bacterial, heat and pressure changed or transformed them into crude oil and natural gas [2]. It is also agreed that the transformation may have been catalyzed by rock constituents.

1.2.2. The Chemical Composition of Crude Oil

Crude oil is a very complex mixture that consists of the following compounds; hydrocarbon compounds (mainly made of carbon and hydrogen), non-hydrocarbon compounds (Sulfur, nitrogen and oxygen compounds), and organometallic compounds and inorganic salts (Na, Mg, Ca, Ni and V). On average, crude oils are made of the following elements or compounds: carbon 84 %, hydrogen 14 %, sulphur 1-7 %, nitrogen < 1.0 %, Oxygen < 1.0 %, Metals < 1.0 % and salts < 1.0 % [1].

1.2.3. Processing of Crude Oil

As previously mentioned that the crude oils are a complex mixture of different types of hydrocarbons. These hydrocarbons must be separated in order to make crude oils more usable. The process is known as petroleum refining. In petroleum refining, crude

oils will undergo several processes including **Physical Separation** and **Chemical Conversions**. Fig.1.1 shows a schematic representation of petroleum refining process.

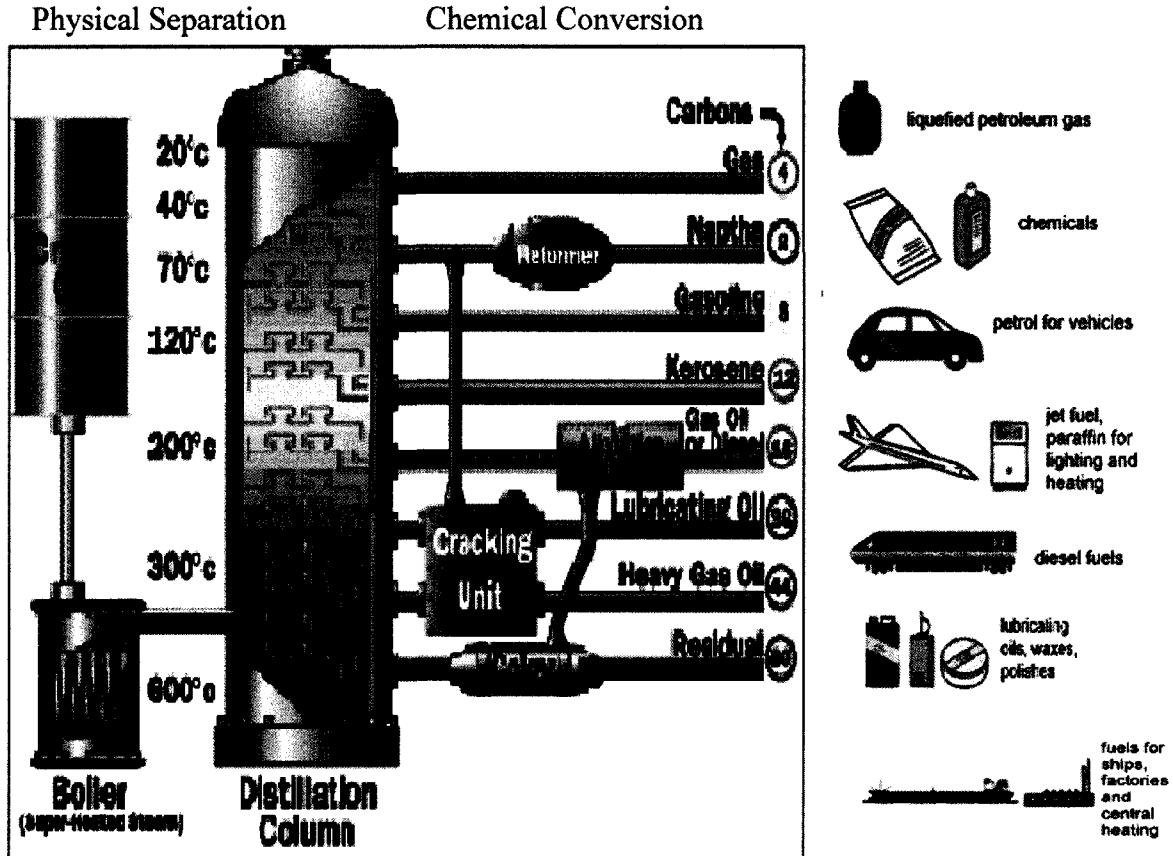


Fig.1.1: Schematic representation of Petroleum Refining [3]

Physical separation by Fractional Distillation

This separation technique is based on the fact that crude oil is a complex mixture of different hydrocarbon classes that have different boiling points. Basically, crude oil will be heated at $T = 600^{\circ}\text{C}$ and then the vapours will enter the distillation column. The column is hot at the bottom and cold at the top, so the vapour cools as they rise. Vapours condense onto a fractionation trays (30-50 trays) when they reach the part of the column,

which is cooler than their boiling point. The bubble caps help to slow down the vapours as they rise through the column. This separation, which is performed under atmospheric pressure, is called Atmospheric Fractional Distillation. However, heavier petroleum feedstocks are separated by Vacuum Fractional Distillation, which is performed under vacuum in the presence of superheated steam. The key point is to lower the pressure, so the boiling points will be lowered as well. This would mean that the heavy feedstocks can be further separated without heating them and risking breaking them apart. The typical feedstock would be heavy residue from the distillation column and the product obtained will be vacuum gas oil, lubricating oil and asphalt. Table 1.1 shows the approximate boiling points and carbon chain length for various crude oil fractions.

Table 1.1: The boiling points and carbon chain length for various crude oil fractions
[1]

Petroleum Products	Crude Oil Fractions	Carbon Chain Length	Boiling Range (°C)	Uses
Hydrocarbon Gases	Liquefied Petroleum gases			Cooking and industrial gas, Ammonia, Alcohol, Motor fuel oil (LPG), Paint, Resins
	Chemical Industry Feedstocks	1-4	<5	Rubber products
	Carbon Black			Printing inks and rubber industry
Light Distillates	Light Naphtha	5-9	35-90	Olefins, solvents and chemical industry solvents
	Intermediate Naphtha	5-10	20-200	Aviation and motor gasoline
	Heavy Naphtha	10-16	80-200	Kerosene (i.e. commercial and military jet fuels, and tractor fuels)
	Gas oil	14-20	260-340	Diesel, Heating, and cracking stock
Heavy Distillates	Technical oils			Textile oils, and white oil-food industry
	Lubricating oils	20-70	330-upward	Motor and engine oils, Lubricating grease
	Paraffin Wax			Rubber industry, Food and paper industry, Candle and matches
	Petrolatum			Petroleum jelly, cosmetics and cable coatings
Residue	Residual Fuel oil	>70	Non-distillable	Boiler and process fuel oils (i.e. factories, central heating) as well as
	Asphalts			Paving asphalts, roofing materials, insulating and foundation protections, and waterproof paper products
Refinery by-Products	Coke			Electrodes and fuels
	Sulphonate			Emulsifiers
	H ₂ SO ₄			Synthetic fertilizer and chemicals
	Sulphur			Chemicals
	Hydrogen			Hydrocarbon reformation

Chemical Conversions

This is the next step that occurs in petroleum refining after the atmospheric or vacuum fractional distillation. Clearly, in the chemical conversion there will be a change in the chemical composition, unlike the physical separation. Chemical conversions in petroleum refining are generally used to;

1. Reduce the harmful impurities in petroleum fractions and residues to control pollution and to avoid poisoning the processing catalysts. For instance, demetallization (removal of metals such as Ni or V), desulfurization (removal of sulphur), and denitrogenation (removal of nitrogen).
2. Upgrade lower-value materials into more valuable products. For instance Steam Cracking and Fluid Catalytic Cracking are used to convert the gas oils into petrochemicals and transportation fuels.
3. Improve the characteristics of fuels. Catalytic reforming and isomerization to convert lower-octane naphtha fractions into higher-octane products.

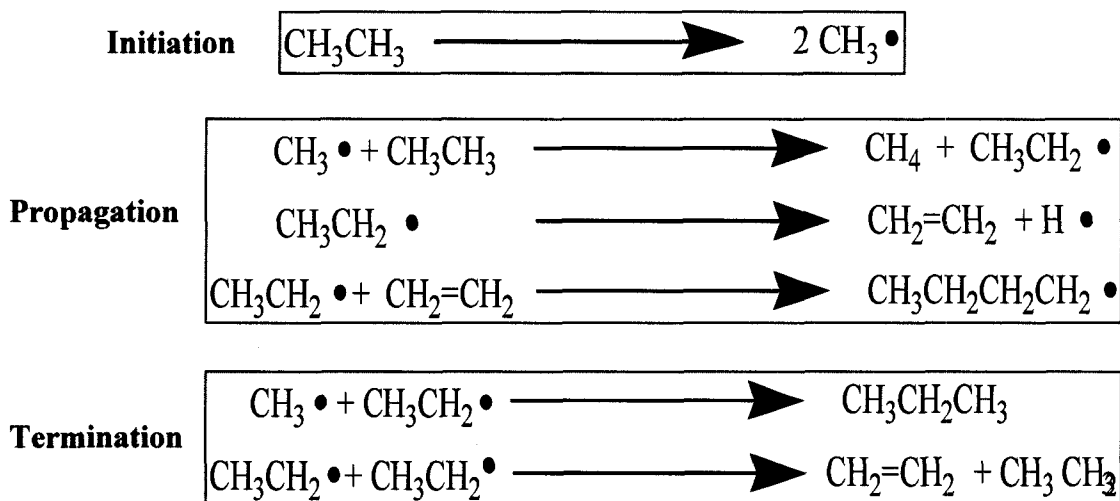
1.3. Catalytic and non-Catalytic Petroleum Processes

Certainly, there are numerous catalytic (i.e. reforming, alkylation, catalytic cracking, etc.) and non-catalytic (steam, thermal, coking, viscosity-breaking, etc...) petroleum chemical conversion processes. However, for the sake of this thesis and its main objective (i.e. production of light olefins) we will limit our discussion to the most important processes; steam cracking (non-catalytic), and catalytic cracking.

1.3.1. Thermal (steam) Cracking (SC)

This process is regarded as a non-catalytic thermal cracking process. It is the most prevalent technology for the production of light olefins, with a worldwide production of

more than 150 million MT of ethylene and propylene annually [4]. It is performed in the presence of steam at high temperature. The main reasons for using steam is to lower the hydrocarbon partial pressure, and to help partially remove the coke formed during the pyrolysis of hydrocarbons ($C + H_2O \rightarrow CO + H_2$) [5]. The feedstocks for SC units ranges from light paraffinic hydrocarbons (i.e. ethane and propane, obtained mainly from various natural gas sources) to various petroleum fractions and residue (i.e. naphtha or gas oil) [5]. SC produces primarily ethylene and propylene, secondarily, depending on the type of feedstock, a C_4 fraction rich in butadiene and a C_5^+ fraction with a high content of aromatics, and finally hydrogen. The SC reaction is highly endothermic, with reaction temperature ranges from 700 to 900°C, and higher according to the type of feedstocks treated, while the residence time ranges from a few seconds to a fraction of a second [5]. The yields of SC products can be increased by increasing the reaction cracking severity (i.e. increasing the reaction temperature and reducing the residence time). However these severe conditions are constrained by several factors such as the metallurgy of the cracking tubes and rapid coking tendency in the cracking coils. In addition, this will also raise the issue of energy cost and environmental concern. The reaction mechanism, which proceeds through the formation of free radicals, is a chain reaction that entails initiation (formation of radical), propagation, and termination (annihilation of free radicals). Scheme 1.1 shows the reaction mechanism of steam cracking, illustrated with ethane [5];



Scheme 1.1: Steam cracking. Reaction mechanism

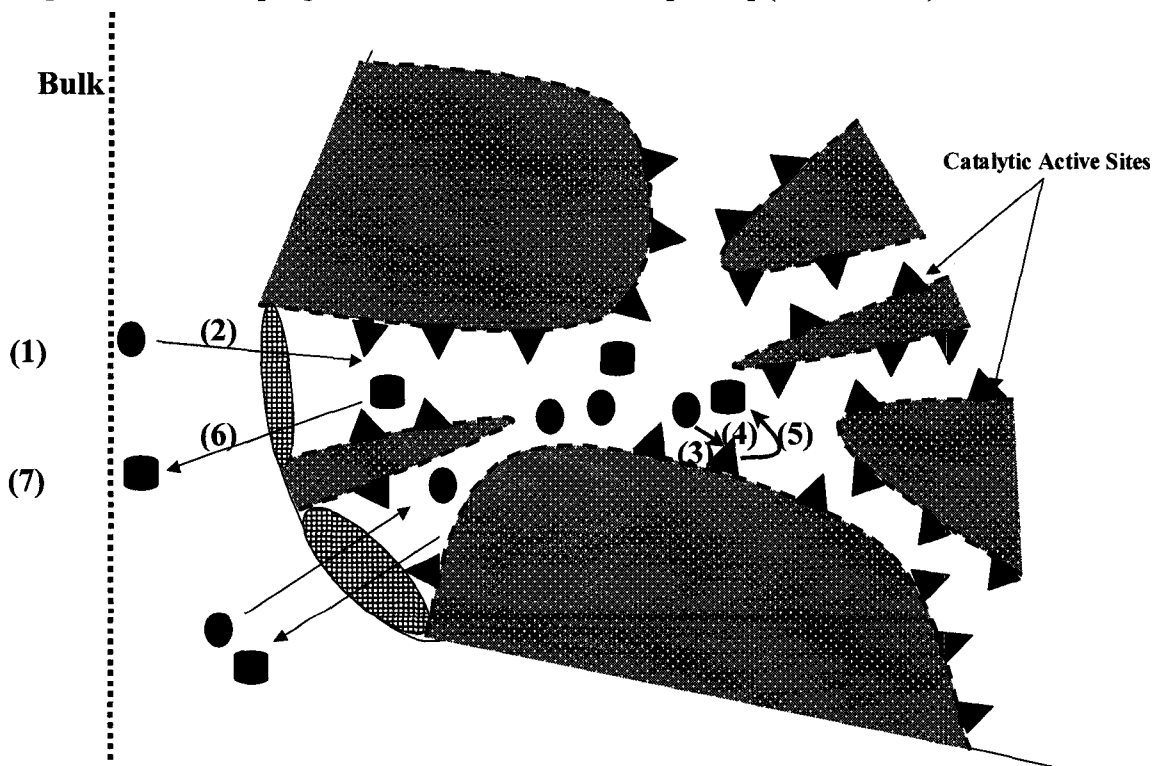
1.3.2. Catalytic Cracking

Catalytic cracking operates at moderate temperature in the presence of a catalyst. It is a remarkably versatile and flexible process, with principal aim to crack lower-value stocks and produce higher-value light and middle distillates. It also produces light hydrocarbon gases, which are important feedstocks for petrochemicals [1]. Catalytic cracking utilizes a wide range of solid catalysts, but mainly zeolite. The Y zeolite is the main zeolitic component in cracking catalysts. it can be incorporated in industrial catalysts in various form; REHY (partially rare earth-exchanged HY), REY (rare earth-exchanged Y), HUSY (H form of ultra stable Y zeolite) and REHUSY (rare earth-exchanged H form USY) [6]. Fluid Catalytic Cracking (FCC) is the most common example of catalytic cracking. Other catalytic cracking processes include the hydrocracking and Deep Catalytic Cracking (DCC) [1,4,6]. FCC can be considered as the main process for large-scale gasoline production with high octane number even 60 years after its introduction [7]. In addition to transportation fuels, light olefins are produced

only as secondary products. The reaction is endothermic, with temperatures ranging from 450 to 560 °C. An interesting feature of this process is the use of fluidized bed technology in order to provide an instantaneous regeneration of zeolite, which normally undergoes a significant deactivation. This deactivation results from the formation of carbonaceous deposits (coke) that are formed during the hydrocarbon reactions.

1.3.2.1. Catalytic Cracking Reaction Mechanism

Catalytic cracking is a heterogeneously acid catalyzed reaction, which is composed of purely chemical reactions. In order for catalytic cracking reactions to take place, the reactants should be transported to the catalyst surface. Thus, apart from the actual chemical reaction (via carbocations (carbenium or carbonium) [6,8-10]), diffusion (configurational, Knudsen, or molecular), adsorption, and desorption are of great importance for the progress of the overall reaction [11,12] (scheme 1.2.).



Scheme 1.2: Individual steps of catalytic cracking reactions

They are; 1) external diffusion of reactants from the bulk phase to catalyst surface, 2) internal diffusion of the reactants into the pores, 3) adsorption of the reactants on the active sites, 4) chemical reactions on these active sites, 5) desorption of the products from the active sites, 6) internal counter-diffusion of the products from the pores, and 7) external-counter-diffusion of the products from the catalyst surface into the bulk phase.

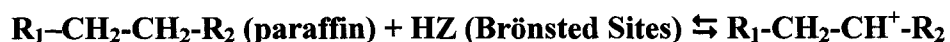
Step 4 represents the key step in catalytic cracking. Cracking of hydrocarbons over acidic catalysts (i.e. zeolites, amorphous silica-alumina, metal oxide, etc..) is generally accepted to take place by a chain carbocation-type reaction mechanism, which involves C-C bond rupture. From the point of view of the mechanism, the acid sites (i.e. Brönsted and Lewis) are believed to be the catalytic active sites. The chain catalytic reaction proceeds through three steps, the initiation (formation of carbocation), propagation, and termination (desorption of product and restoration of active sites).

Initiation step involves the formation of carbenium and/or carbonium-like intermediates, through the interaction of adsorbed hydrocarbon with the active sites. However, there is still some controversy involving the initiation step and the nature of the acid sites. Several possibilities have been suggested and are widely accepted in the literature.

1- Tung et al [13] and others [14,15] have suggested that a carbenium ion can be formed via the abstraction of a hydride by a Lewis sites.



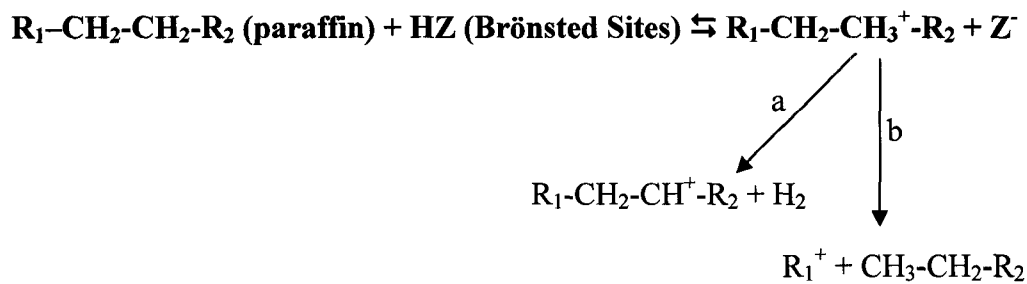
2- Greensfelder et al [16] and others [17-20] have suggested that carbenium ions can be formed, as well, via abstraction of a hydride ion by a strong Brönsted sites.



3- It has been also suggested that the initial carbenium ion can be formed via the protonation of olefinic species, which are present in the feed as either impurities or formed by thermal cracking (thermal cracking should be kinetically favoured, $T = 500$ °C). [9,21].



4- It was also suggested that the paraffin cracking could start from a carbonium ion transition state. This was proposed by Haag and Dessau [22] in 1984, and since then gained a lot of recognition in the literature [10]. They proposed that a C-C bond could be protonated by Brönsted acid sites forming a pentacoordinated carbonium ion. The carbonium ion can then split to produce a smaller paraffin and a carbenium ion. As an alternate path, the carbonium ions may convert into a carbenium ion by the loss of a hydrogen molecule.



Subsequently, the following could happen to the carbenium ions formed.

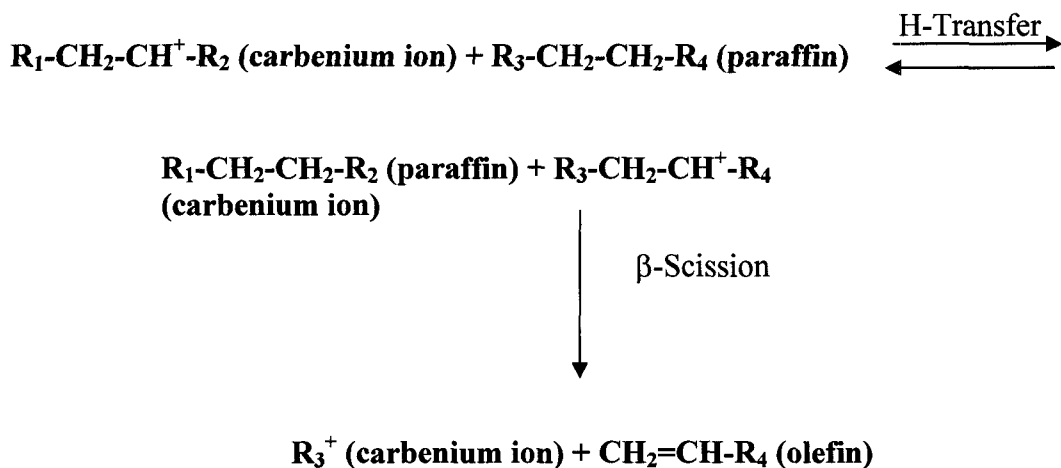
a) The carbenium ions formed by any of the above mentioned mechanisms may desorb as an olefins and restore the active Brönsted sites [8]. If the source of the carbenium ion is the pentacoordinate carbonium ion, then this is the Haag-Dessau cracking mechanism, also known as the protolytic cracking, monomolecular cracking and carbonium ion

cracking mechanisms. This reaction is highly favoured at high temperature, low conversion and low hydrocarbon partial pressure and by zeolites with high constraint indexes (i.e. ZSM-5) [10, 23 and reference therein].

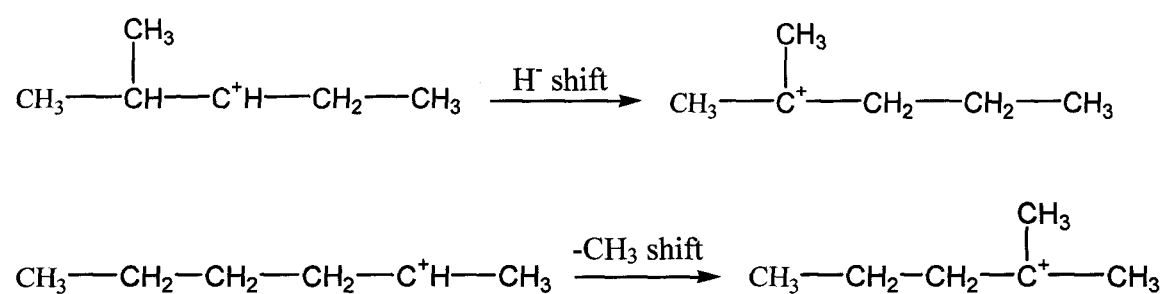
b) It is possible that the carbenium ion undergoes a β -scission cracking (C-C bond cleavage in the β -position to the atom carrying the positive charge), leading to the formation of a smaller olefin and a smaller carbenium ion [23].

c) It is possible that this carbenium ion, which is still adsorbed on the active sites, may initiate several types of reactions such as hydrogen transfer (HT), isomerization, aromatization, cyclization, polymerization, etc [9 and reference therein].

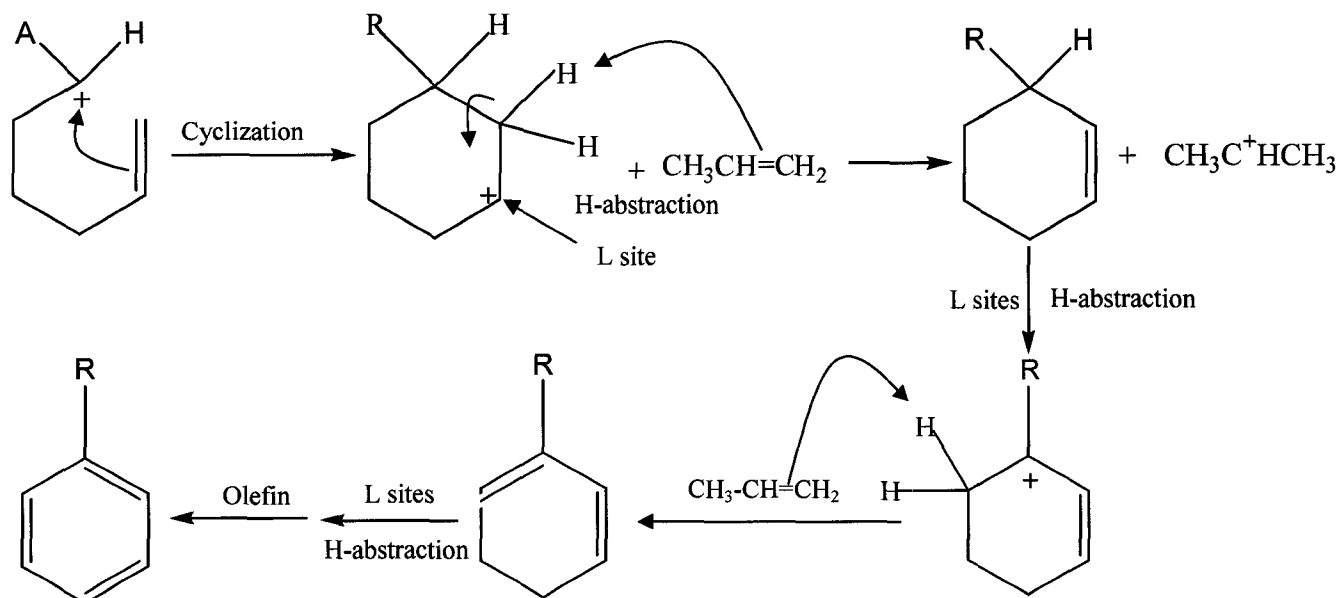
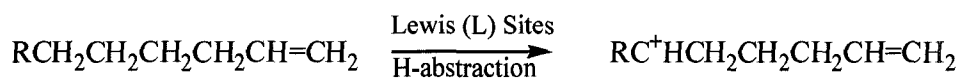
i) The adsorbed carbenium ion may interact with a neutral paraffin molecule via hydride transfer, leading to the formation of a new carbenium ion, which in turn undergoes a β -scission cracking. This is called a bimolecular reaction, and it is highly favourable at low temperature, high hydrocarbon partial pressure, and by zeolite with low constraint indexes and high acid density (i.e. HY).



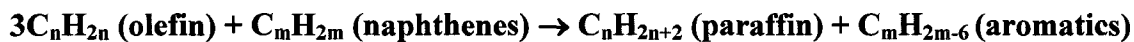
ii) The adsorbed carbenium ion may isomerise via hydride (H⁻) shift (charge isomerization) or methyl (-CH₃) shift (skeletal isomerization) into more stable carbenium ions (i.e. 3⁰ (tertiary) > 2⁰ > 1⁰ (primary)). The reaction mechanism of the skeletal isomerization is widely accepted to involve the intermediate formation of protonated cyclopropyl ions (PCP) [8 and reference therein]. The isomerized carbenium ion may desorb as branched olefin and restore the active sites.



iii) The adsorbed carbenium ion may undergo an aromatisation reaction. This can occur via the dehydrocyclization reaction of paraffin, as long as the formed olefinic species has a configuration that is conducive to cyclization [1].



Another alternative path to aromatization is the hydrogen transfer reaction [23,24]. The adsorbed carbenium ion on the active site may interact with a saturated molecule in the gas phase (i.e. naphthalene), thereby extracting a hydride from it and escaping in the gas phase.



1.4. Light Olefins

1.4.1. Overview of the Industrial Significance of Light Olefins

The importance of light olefins industry stems from the great demands for polyolefins mainly polyethylene and polypropylene. Fig.1.2 represents the main end uses of ethylene [24] and propylene (1970 and 2004) [25]. The share of polyolefins of the total

polymer market increased from 30 % to 60 % since 1970 [26]. The best forecast suggests that this demand will continue to grow, due to the constant growing demands from developing countries such as China and India, and the fact that there are only few materials that can match the versatility and economy of these polyolefins [26 and references therein].

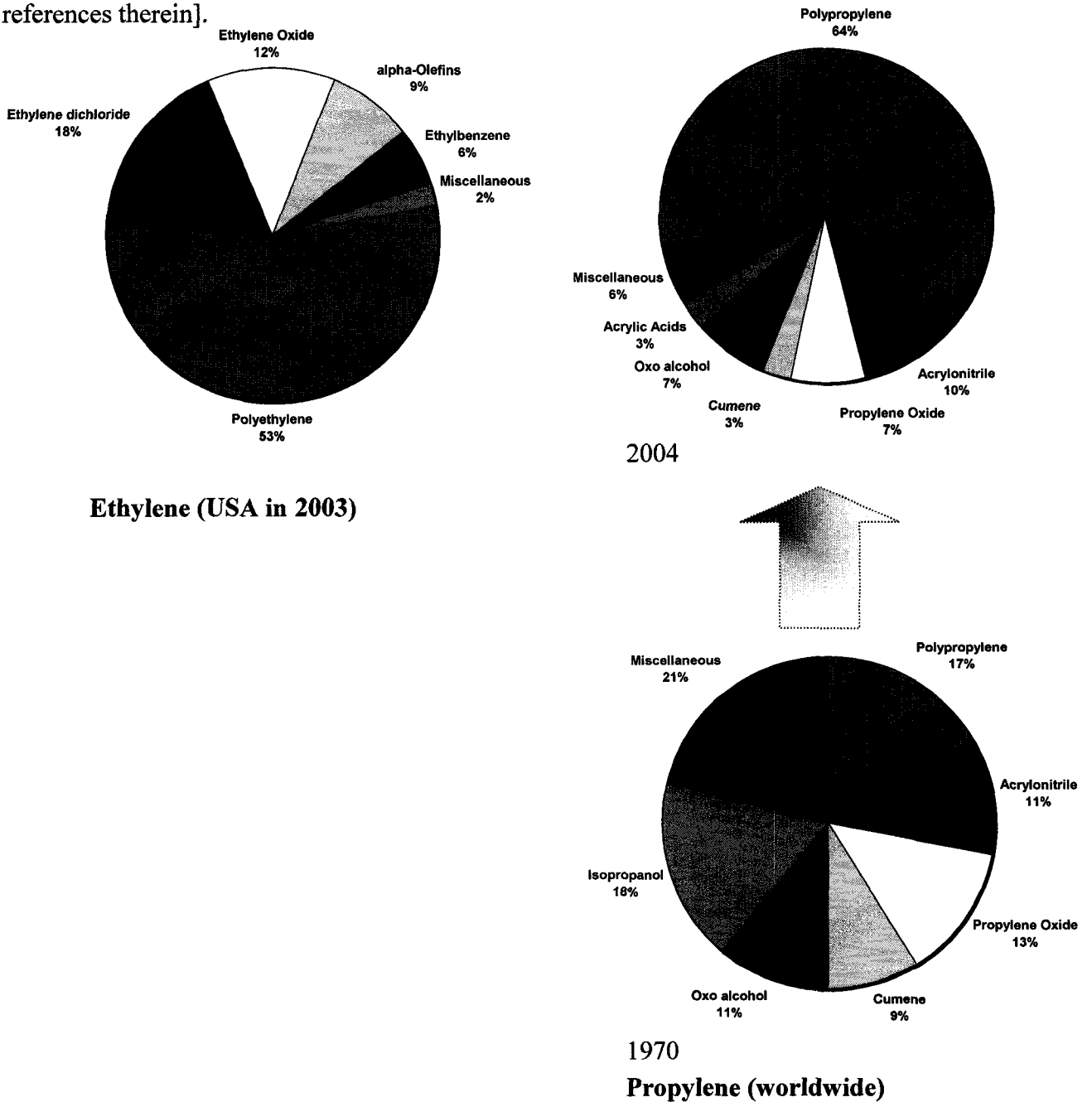
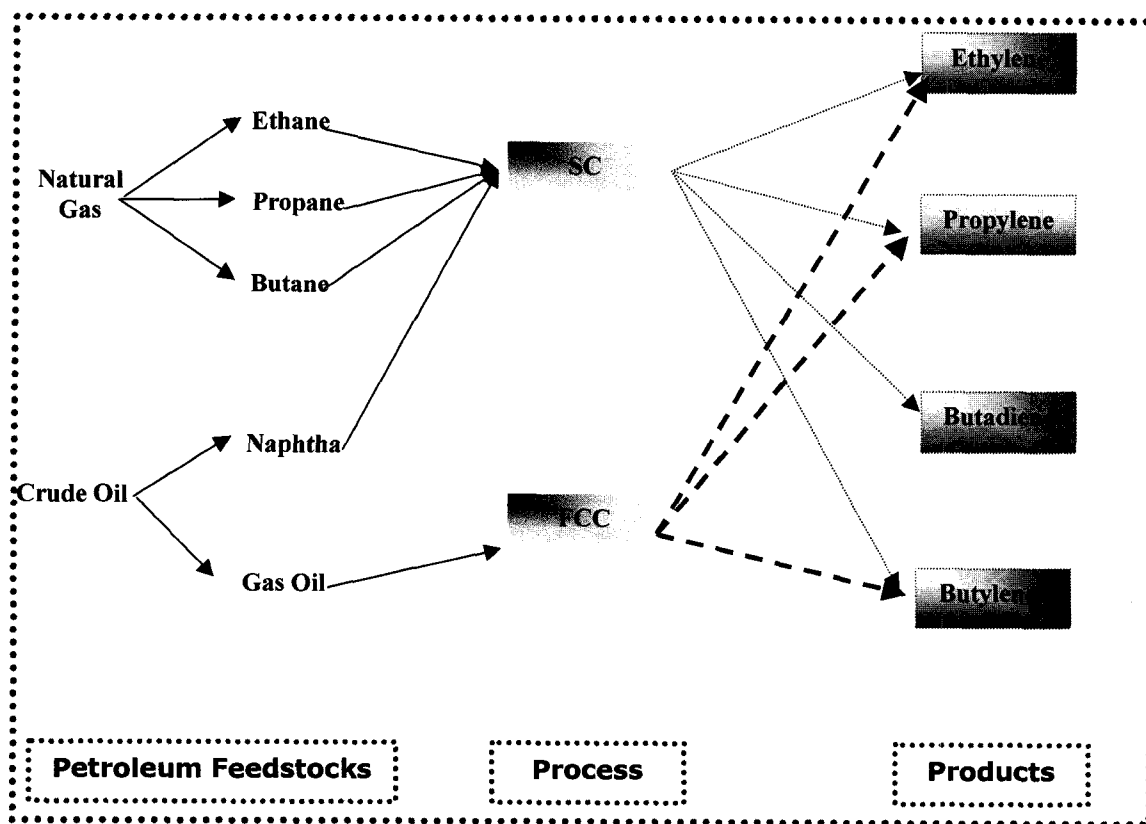


Fig.1.2: The main end uses of ethylene and propylene [25,27]

1.4.2. Main Industrial Technologies for Light Olefin Production

At the outset, light olefins were produced industrially by several chemical processes other than the pyrolysis of petroleum fractions. For instance, ethylene was produced by the dehydration of ethyl alcohol or by partial hydrogenation of acetylene [5]. However, as the demand for light olefins grew producers tuned into petroleum feedstocks as a vital source for light olefins. As previously mentioned, steam cracking and Fluid Catalytic Cracking are among the most important processes that exploit natural gas and petroleum fractions (i.e. light gases, naphtha, gas oil) for the production of light olefins. These processes are fully developed and commercialized. Below is an overview of the most important processes as presented in scheme 1.3.



Scheme 1.3: The main important current sources of light olefins

1.4.3. Roadblocks in the Light Olefins Industry

One of the main significant obstacles facing the light olefin industry is the rapid growth in the demand for propylene. Fig. 1.3 [25] shows the high propylene demands in the world since 1990s where Asia (i.e. China and India) is going to be the dominant region with respect to propylene demand in the near future. Propylene is viewed by many as a by-product or at best co-product of ethylene production in SC. About 68 % of world propylene is produced as a co-product to ethylene by the SC and about 29 %, is produced as a co-product to gasoline in the FCC of gas oils. The remaining 3 % is produced via other processes [28]. The yields of propylene capable of being produced via SC process are always going to be fixed with some limited flexibility [25]. Therefore, as the propylene growth rate increases, this will cause a great deal of pressure on conventional olefin technologies (i.e. particularly SC).

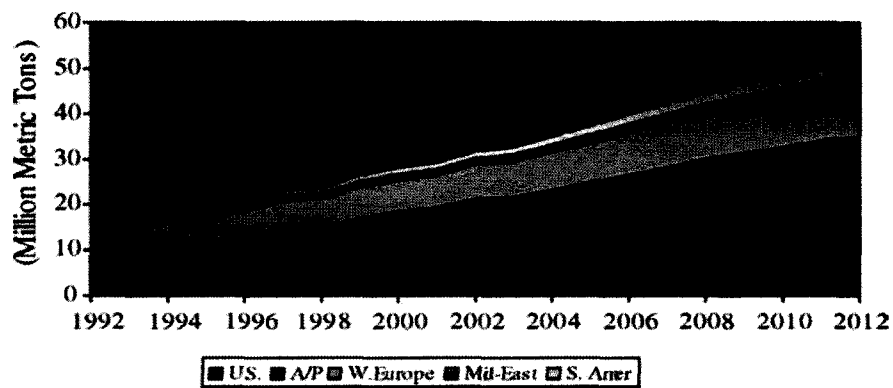


Fig.1.3: Regional propylene demands [25]

Another significant obstacle is the energy consumption. The current SC process uses as much as 40 % of the energy consumed by the entire petrochemical industry [29], due to high operating temperature (i.e. $T = 780-1000^{\circ}\text{C}$). Furthermore, the new stringent environmental regulations requiring low emissions of green house gases (GHG) such as

CH₄ and CO₂ produced during the run-regeneration cycle continue to put a strain on conventional technologies. The total GHG emissions in Canada for 2003 were estimated to be 740 Mt CO₂ eq (megatonnes of CO₂ equivalent). CO₂ emissions contributed the largest share of 2003 emissions at 79 %, while CH₄ accounted for 13 % [30]. The petroleum industry as a whole contributed about 19 % of Canada's GHG emissions.

1.4.4. Paving the Way

The imminent difficulties facing the light olefins industry have inspired researchers around the world to improve the existing conventional technologies or develop innovative technologies. For instance,

I) Steam Cracking: This process is fully developed and appears to have reached its full potentials in which improvements in yield and product selectivity are becoming quite difficult. Most of the improvements were only limited to furnace and pyrolysis tube designs. In one report [31] it was shown that the formation of carbonaceous deposits was lowered using silicon carbide as the construction material for the cracking furnace. However, these improvements will only be addressing the environmental concerns and to some extent the high operating costs, leaving out the problems with propylene production.

II) Fluid Catalytic Cracking: Although, this process is one of the core processes of petroleum refining, its capability to meet today's light olefin and especially propylene market demands are quite difficult. Several approaches have been taken in order to improve the yield of propylene from FCC units. In one approach, a new specialized catalyst additive (i.e. modified ZSM-5) was added along with the conventional FCC catalysts [24]. The incorporation of ZSM-5 has significantly increased the ratio of

protolytic (monomolecular) cracking to β -scission (bimolecular) cracking. Thus, the hydrogen transfer reaction and coke formation decreased, while the yield of light olefins (propylene) increased. However this increase in the propylene yield came at the price of decreased gasoline production and was not enough to satisfy the propylene demands. In another approach, researchers at the Research Institute of Petroleum Processing and Sinopec International in China developed a new catalytic cracking process called Deep Catalytic Cracking (DCC) for the production of propylene and amylenes (i.e. currently there are several commercial plants running in both China and Thailand with a capacity of 1.5 million Mt) [4,24]. This process operates with the same principles as FCC. The reactor and regenerator are similar to FCC. However, innovation in both catalyst development and severity of conditions enables DCC to produce more olefins than FCC. The operating conditions are more severe than those in conventional FCC but less severe than in steam cracking. Although, this process shows a significant improvement in olefin production [24], the type of catalyst (i.e. ZSM-5) and the severity of the operating conditions (i.e. high temperature) raise an important issue. Zeolites such as ZSM-5 are quite active with a very high initial conversion, however they undergo a very rapid catalytic deactivation. This fast deactivation can be eliminated by using the fluidized bed technology, however degradation of the ZSM-5 structure is expected to occur over several run-regeneration cycles, which will significantly hinder its long-term stability.

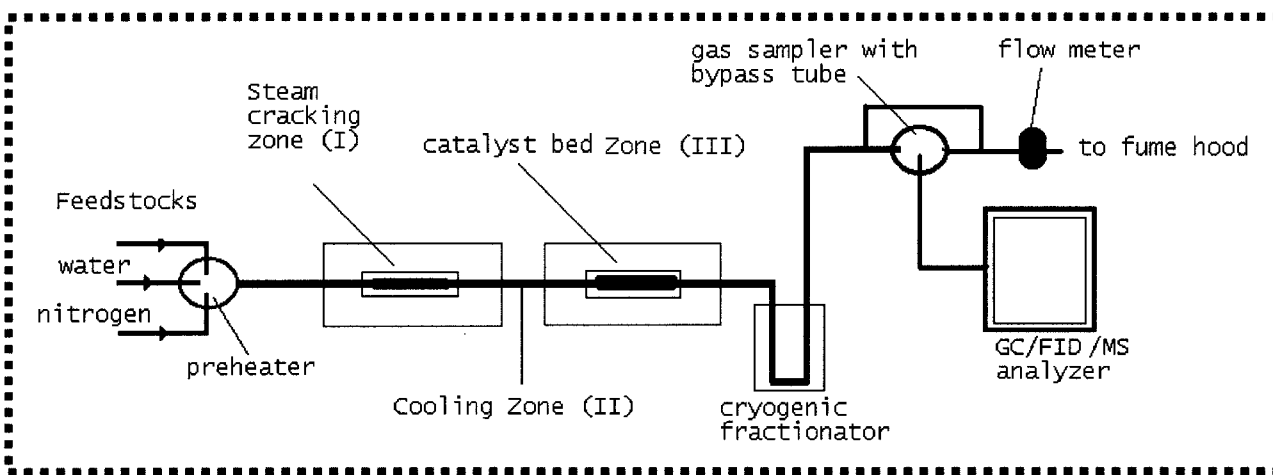
III) Other Significant Approaches: There have been several additional investigated approaches to maximize propylene yields with lower energy and resource savings. Catalytic Cracking was recently investigated in Japan by AIST (Advanced Industrial Science and Technology). This catalytic cracking process uses La-modified ZSM-5 as

catalyst. It was reported [29] that cracking light naphtha at 650°C resulted in an overall combined yield of ethylene and propylene of about 60 wt.% with significant savings in production costs. Another approach was Oxidative Dehydrogenation to overcome the thermodynamic limitations of the conventional Catalytic Dehydrogenation. In this approach, propylene is obtained by oxidative dehydrogenation of propane in the presence of oxygen or air at very low temperature (about 350°C) using supported transition metal oxides as catalyst [32]. Olefin Metathesis was also developed to provide an opportunity to achieve olefins interchangeably [33]. In this process propylene can be obtained by combining ethylene and butylenes from a naphtha SC unit.

1.4.5. Thermo-Catalytic Cracking (TCC) - Groundbreaking Olefin Technology

The beginning of Thermo-Catalytic Cracking processes dates to almost twenty years ago. In 1988 a process aimed at upgrading the products of propane steam cracking was successfully developed [24]. It was based on the integration of a small catalytic reactor containing modified ZSM-5 at the outlet of a propane steam cracking unit. The results showed an increase in the ethylene, butene and aromatic yields. Ten years later, a process analogous to the one developed in 1988 was introduced [35,36]. This process was called Selective Deep Catalytic Cracking (later on upgraded to Thermo-Catalytic Cracking) of petroleum feedstocks for the production of light olefins. The TCC process combines two distinctive cracking processes; steam and catalytic cracking. Several catalyst configurations have been tested since then, and include: modified ZSM-5 [35,36], silicalite [37,38], and hybrid catalysts containing microporous zeolitic components and mesoporous supported chromium or molybdenum co-catalyst [36-38], as well as purely mesoporous supported mixed oxides [38-45].

There are two process versions of the TCC: one-zone and multi-zone reactors. In a one-zone reactor version, the catalysts have to work under steam atmosphere and at a quite high temperature. The other version is the multi-zone reactor configuration, which consists of a precatalytic zone (quartz beads) and a catalyst bed (catalyst extrudates) (scheme 1.4).



Scheme 1.4: Schematic representation of TCC multi-zone reactor configuration

1.5. OUTLINE

This section outlines the format of this manuscript-based thesis.

Chapter I

This chapter provided a general introduction to light olefins and the most important catalytic and non-catalytic reaction mechanisms in petroleum conversion, as well as any necessary background information that is required to read this thesis. In particular, we presented an overview of the industrial significance of light olefin and their commercially proven production technologies. In addition, we have discussed in detail the challenges facing the light olefins production technologies, and what has been done so far to tackle these challenges. The important features of the Thermo-Catalytic Cracking (TCC) process were also presented.

Chapter II

This chapter presents the synthesis, textural properties, and the Thermo-Catalytic Cracking (formerly known as Selective Deep Catalytic Cracking (SDCC)) activities of the hybrid catalyst configuration. This configuration consists of two components bound firmly to each other within a clay binder; microporous (zeolite type) and mesoporous cocatalyst (supported metal oxide). The microporous zeolite component was an acidified silica-rich ZSM-5 (H-silicalite), and the mesoporous was an amorphous silica-alumina doped with molybdenum and cerium oxides. When compared to a mechanical mixture of extrudates made of H-silicalite and silica-alumina based cocatalyst, respectively, the hybrid catalyst gives faster adsorption of nitrogen and desorption of preadsorbed nitrogen. On the other hand, a much higher conversion of n-hexane (cracking) was obtained with the hybrid catalyst while the product selectivities are almost the same for

all the cases. Such behaviour is ascribed to the kinetic effect of the “pore continuum” being formed in the hybrid catalyst pore system, which has as a consequence to speeding up the diffusion of reactant molecules and that of reaction products into, and out of, zeolite micropores.

Chapter III

This chapter presents the synthesis, textural-structural-surface properties, and the Thermo-Catalytic Cracking activities of another catalyst configuration. It is the silica-alumina supported mono- and bi-oxide $\text{MoO}_3\text{-CeO}_2$ based catalysts. The influence of metal loadings, preparation method (i.e. co-impregnation versus sequential and reverse sequential impregnation), calcinations temperature, and the nature of catalyst support were examined. The textural-structural-surface properties were examined via different characterization techniques such as BET surface area, X-ray diffraction, and Laser Raman spectroscopy. The catalytic performance was evaluated in the TCC of n-hexane, which was used as a model molecule for petroleum naphtha. The loadings and the chemical states of metal oxides incorporated separately had significant effects on the catalytic activities of the resulting mono-oxide MoO_3 or CeO_2 catalysts. Addition of cerium to molybdenum had a favourable effect on the production of light olefins in the TCC of n-hexane up to a certain level of cerium loading. The catalytic performance of the bi-oxide catalysts also depended significantly on the incorporation methods. It was found that the co-impregnation of MoO_3 and CeO_2 , which led to the highest production of light olefins, was more effective than the sequential or reverse sequential impregnation. However, the most prominent observations were the fast segregation of active and promoter species (i.e. formation of large bulk crystallites), and the subsequent negative

impact on the catalytic performance (i.e. lower conversion, high selectivity to aromatics and thus low catalytic on-stream-long term stability). These results were a clear representation of the strong influence of the catalyst support on the physic-chemical-catalytic properties.

Chapter IV

Ideally, an appropriate support should be able to improve the dispersion of active and promoter species, promote effective metal-support interactions, and retain the unique properties of the impregnated metals (i.e. surface acid-base, redox properties, etc.). In addition, the support should possess high surface area and mechanical strength as well as be thermally and hydrothermally stable. In our previous work (N. Al-Yassir and R. Le Van Mao, *Appl. Catal.* **305** (2006) 130, (Chapter III)), we have found that the physico-chemical properties and subsequently the catalytic activities of the bi-oxide $\text{MoO}_3\text{-CeO}_2$ configuration were significantly reduced upon using the amorphous silica-alumina ($\text{SiO}_2 = 86.0$ wt.%, and $\text{Al}_2\text{O}_3 = 14.0$ wt.%) as a support. This was mainly attributed to the weak ability of silica-alumina to promote a high surface dispersion of impregnated metals, due to the low concentration of surface hydroxyl groups and low isoelectric point (IEP). Therefore, our attention was diverted into another catalyst support. Conventional transition alumina, which is by far the most widely used catalyst support in petroleum, chemical and pollution control processes, was considered as an interesting support for the TCC mesoporous mixed oxide catalyst. However, its poor thermal stability hindered its effectiveness as a catalyst support for the TCC process. In order to overcome this significant setback, alumina aerogel doped with yttrium oxide was prepared via sol-gel synthesis route using the supercritical drying technique. We have addressed the influence

of the chemical (sol-gel) and physical (drying) processing technique on the pore structure and on crystalline structure transformation in alumina. In addition, we have proposed a new explanation that accounts for the delay in the alumina rate of sintering and phase transitions. The results were presented in comparison with conventional alumina, which was obtained by the thermal dehydration of boehmite.

Chapter V

The hydrothermal stability is another important characteristic of catalyst support. Steam is co-fed in the TCC process along with hydrocarbons in order to lower the partial pressure of hydrocarbons (i.e. minimize the condensation-side reaction rate), and partially removed carbonaceous (coke) deposit). However, steam could have a negative impact on the catalyst, particularly the alumina-based support. This is attributed to the fact that surface area loss, and phase transition of alumina, are greatly facilitated by the presence of steam. We have shown in our previous work (N. Al-Yassir and R. Le Van Mao, *Appl. Catal.* **317** (2007) 275, (Chapter IV)) that yttria doped alumina aerogel prepared via sol-gel method using the supercritical drying technique is quite thermally stable. The current work presents results concerning the hydrothermal stability of yttria doped alumina aerogel, The influence of atmospheric steam at 750 and 1000 °C on the rate of sintering of yttria doped alumina aerogel with various yttria contents was investigated. Several techniques were used to characterize the solid samples such as BET N₂ adsorption measurements, X-ray diffraction, thermogravimetric analysis, FTIR of adsorbed pyridine, and ¹H and ²⁷Al MAS NMR. It was found that the hydrothermal stability of yttria doped alumina aerogel was greatly improved compared to alumina aerogel and conventional alumina. These significant improvements were attributed to the combined effect of the

sol-gel method and the presence of yttrium ions. Ytria doped alumina aerogel with various yttria loadings - when compared to undoped alumina aerogel - exhibited lower concentrations of surface -OH groups, higher amounts of bridged -OH groups and lower degrees of crystallinity with smaller particle sizes. This chapter also reports the thermal and hydrothermal stability of yttria impregnated alumina (conventional and aerogel). Comparison between yttria impregnated alumina and yttria doped alumina revealed that incorporating yttria directly into the alumina aerogel structure is more effective than impregnating it onto the surface.

Chapter VI

It is well known that the physico-chemical, and consequently the catalytic properties of supported metal oxides catalysts, are influenced by many factors, however the nature of the catalyst support is one of the most important. Its role on the catalytic performance of supported catalysts depends greatly on the degree of interactions between the support and incorporated metals. In this chapter, we report another interesting property of yttria doped alumina aerogel besides its high thermal and hydrothermal stability (N. Al-Yassir and R. Le Van Mao, *Appl. Catal.* **317** (2007) 275, (Chapter IV), N. Al-Yassir and R. Le Van Mao, *Canadian Journal of Chemistry* (2007) in press, (Chapter V)). It was found that yttria doped alumina aerogels with various yttria loadings (2.0-20.0 wt.%) were highly effective in homogenously dispersing the active species, thus minimizing the formation of bulk crystallites. The supported catalysts were characterized by N₂ adsorption, X-ray diffraction, laser Raman, and thermogravimetric analysis. In addition, ¹H MAS NMR and iso-electric point techniques were used exclusively to characterize the various catalyst supports. It was explicitly found that yttria doped

alumina aerogel is far more capable of homogeneously dispersing the active molybdenum species and significantly retarding their sintering at quite high calcination temperature than conventional alumina and alumina aerogel. This can be attributed to the incorporation of yttria into alumina aerogel network, which led to a change in the support surface charge (IEP) and subsequently the stability of surface molybdate species. The dispersion degree of ceria (substituted ceria) on supported mono-oxide CeO_2 was improved as well, upon using yttria doped alumina aerogel. In the bi-oxide $\text{MoO}_3\text{-CeO}_2$, characterization results have indicated the presence of surface interaction between Mo and Ce, probably through the formation of surface “Mo-O-Ce” type phase between the dispersed ceria and the molybdate monolayer.

Chapter VII

This chapter represents the most important part of the thesis, since it correlates the Thermo-Catalytic Cracking activities and kinetic study of the supported mono- and bi-oxide $\text{MoO}_3\text{-CeO}_2$, with the previously investigated physico-chemical properties (Chapter IV, V, and VI). The Thermo-Catalytic Cracking Performance and kinetic study of n-hexane over supported mono- and bi-oxide $\text{MoO}_3\text{-CeO}_2$ has been investigated in order to determine the catalytic roles of surface acidity and other physico-chemical properties. It was found that the surface acidity was significantly influenced by the nature of the catalyst support, and the nature and loading of metal oxides. Supported mono-oxide CeO_2 catalysts displayed only Lewis type-sites, whereas the surface acidity of supported mono-oxide MoO_3 catalysts was characterized by the presence of Brönsted and largely Lewis sites. The Brönsted sites of yttria doped alumina aerogel supported Mo catalysts were found to exist in lower concentration and were less acidic, when compared to those

supported on conventional alumina or undoped alumina aerogel. Addition of CeO₂ to the supported MoO₃ catalysts led to a decrease in the density of Brönsted acid sites most likely due to neutralization effects, whereas Lewis acid sites appeared to be only slightly altered. The Thermo-Catalytic Cracking activities suggested that supported mono-oxide MoO₃ and bi-oxide MoO₃-CeO₂ catalysts are more catalytically active than supported CeO₂. It was noted that the total conversion, which increased as the MoO₃ loadings increased up to 12.0 wt.%, was mainly attributed to the presence of Brönsted acid sites. The selectivity for aromatics also increased at the expense of light olefins. The extent of that increase was much higher upon using yttria doped alumina aerogel instead of undoped alumina aerogel as a support. Addition of CeO₂ to the yttria doped alumina aerogel supported MoO₃ resulted in the decrease of the total conversion and the selectivity to aromatics. This was mainly related to the decrease in the total acid density, thus reducing the extent of hydrogen transfer and aromatization reactions.

Chapter VIII

Brief conclusions of the work presented in this thesis are given as well some suggestions for short- and long-term future work. In addition, the current and anticipated significance of this thesis are presented.

At the end of each chapter, linking texts will be provided summarizing the key points required for proceeding onto the next chapters

1.6. REFERENCES

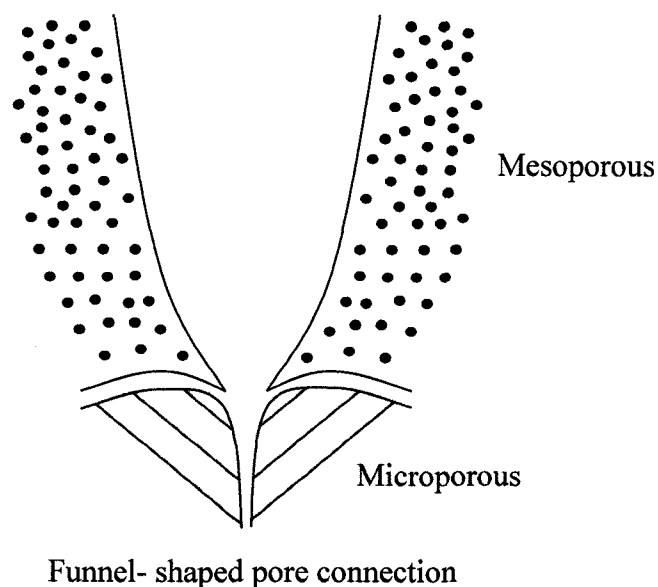
- [1] S. Matar, L.F. Hatch, in; Chemistry of Petrochemical Processes, 2nd edition, Gulf Professional Publishing, 2001.pp. 1-28.
- [2] <http://www.osti.gov/bridge/servlets/pur/10169154-cT5xip/10169154.PDF> (petroleum study). And <http://www.sjgs.com/oil.html>
- [3] <http://science.howstuffworks.com/oil-refining2.htm>
- [4] D.A. Hunt, in: Handbook of Petroleum Refining Processes, 2nd ed., ed. R.A. Meyers, McGraw Hill, Boston, (1997).
- [5] A. Chauvel and G. Lefebvre, in; Petrochemical Processes, Vol.1 (Edition Technip, Paris, 1989), pp. 118-194, and 169-227.
- [6] P. Leprince, in; Conversion Processes, (Editions Technip, Paris, 1998.), pp. 169-223.
- [7] D. Decroocq, in: Catalytic Cracking Of Heavy Petroleum Reactions, Technip, Paris, (1984), pp.73-114.
- [8] A. Corma, A. Martinez in: M. Guisnet, J-P. Gilson (Eds) Zeolites for Cleaner Technologies, Vol.3, Imperial College Press, (2002), pp. 29-55.
- [9] S. Raseev, in: Thermal and Catalytic Processes in Petroleum Refining, Marcel Dekker, Inc. New York, (2003), pp. 275-421.
- [10] S. Kotel, H. Knözinger, B. C. Gates, *Micropor. Mesopor. Mater.* **35** (2000) 11.
- [11] J. Hagen in: Industrial Catalysis, A Practical Approach, 1st ed., Wiley-VCH Verlag GmbH, Weinheim, Germany, (1999), pp. 83-98.
- [12] B.C. Gates, in: Catalytic Chemistry, John Wiley & Sons, Inc., New York, (1992), pp. 268- 275.
- [13] S. E. Tung, E. McIninch, *J. Catal.* **10** (1968) 166.

- [14] D. M. Nace, *Ind. Eng. Chem. Prod. Res. Dev.* **8** (1969) 31.
- [15] A. Borodzinski, A. Corma, B. W. Wojciechowski., *Canad. J. Chem. Eng.* **58** (1980) 219.
- [16] B. S. Greensfelder, H. H. Voge, G. M. Good, *Ind. Eng. Chem.* **49** (1957) 742.
- [17] P. B. Janardhan, R. Rajeswari, *Ind. Eng. Chem. Prod. Res. Dev.* **16** (1977) 1.
- [18] J. Planelles, F. Sanchez-Martin, F. Tomas, A. Corma, *J. Mol. Catal.* **32** (1985) 365.
- [19] J. abbot, I. D. Head, *J. Catal.* **125** (1990) 187.
- [20] M. L. Poustma, in *Zeolite Chemistry and Catalysis* Ed. J. A. Rabo, (ACS Monograph, Washington DC, 1976, 117), 505.
- [21] B. S. Greensfelder, H. H. Voge, G. M. Good, *Ind. Eng. Chem.* **41** (1949) 2573.
- [22] W. O. Haag, R. M. Dessau, Proc. 8th Int. Congr. Catal.(Berlin, 1984, Vol. II) 305.
- [23] J. Scherzer, *Catal. Rev.-Sci. Eng.* **31** (1989) 215.
- [24] X. Zhao, R.H. Harding, *Ind. Eng. Chem. Res.* **38** (1999) 3854.
- [25] J.S. Plotkin, *Catal.Today.* **106** (2005) 10.
- [26] J.R. Severn, J.C. Chadwick, R. Duchateau, and N. Friederichs, *Chem.Rev.* **105** (2005) 4073.
- [27] The Innovation Group (TIG), <http://www.the-innovation-group.com/contact.htm>.
- [28] A.M., Aitani, *Oil ,Gas (Hamburg) Germany* **30** (2004) 36
- [29] Y.Yoshimura, N. Kijima, T. Hayakawa, K. Murata, K. Suzuki, et al., *Catalysis Surveys From Japan*, **4** (2000) 157.
- [30] Canada. Environmental Canada. Canada's Greenhouse Gas Inventory report (Overview 1990-2003). October 2005, <http://www.ec.gc.ca>.
- [31] J. Alagy, C. Busson, P. Chaverot, Institut Francais du Petrole, Fr., FR 2584733

- (1987)
- [32] A. Corma, J.M. LopezNieto, N. Paredes, A. Dejoz, and I. Vazquez, *Stud. Surf., Sci. Catal.* **82** (1994) 113
- [33] J. Handzlik, J. Stoch, J. Ogonowski, M. Mikolajczyk, *J. Mol. Catal. A: Chem.* **157** (2000) 237.
- [34] R. Le Van Mao, Concordia University, US Patent 4, 732, 881 (1988).
- [35] R. Le Van Mao, S. Melancon, C. Gauthier-Campbell, P. Kletnieks, *Catal. Lett.* **73** (2001) 181.
- [36] S. Melancon, R. Le Van Mao, P. Kletnieks, D. Ohayon, S. Intem, M.A. Saberi, D. McCann, *Catal. Lett.* **80** (2002) 103
- [37] R. Le Van Mao, N. Al-Yassir and D. T.T. Nguyen., *Micropor. Mesopor. Mater.* **85** (2005) 176.
- [38] N. Al-Yassir, R. Le Van Mao, and F. Heng, *Catal. Lett.* **100** (2005) 1.
- [39] R. Le Van Mao, N-T. Vu, N. Al-Yassir, N. Francois and J. Monnier, *Top. Catal.* **37** (2006) 107.
- [40] N. Al-Yassir, R. Le Van Mao, *Appl. Catal. A: Gen.* **305** (2006) 130.
- [41] R. Le Van Mao, N.T. Vu, N. Al-Yassir, N. Francois, J. Monnier, *Top. Catal.* **37** (2006) 107.
- [42] N. Al-Yassir, R. Le Van Mao, *Appl. Catal. A: Gen.* **317** (2007) 275.
- [43] N. Al-Yassir, R. Le Van Mao, *Appl. Catal. A: Gen.* **332** (2007) 273.
- [44] N. Al-Yassir, R. Le Van Mao, *Can. J. Chem.* (in press, Ms. No. CJC 07316).
- [45] R. Le Van Mao, N.T. Vu, N. Al-Yassir, H.T.Yan, *Ind. Eng. Chem. Res.* (Submitted, Ms. No. tie071629).

Chapter II

Experimental Evidence for the pore Continuum in Hybrid Catalysts used in the Selective Deep Catalytic Cracking of n-Hexane and petroleum Naphthas



Graphical Abstract: Concept of pore continuum in hybrid catalysts

Published as:

R. Le Van Mao, N. AL-Yassir, D. T. T. Nguyen,

Microporous, Mesoporous Materials, **85** (2005) 176-182.

ABSTRACT

The hybrid catalyst investigated in this work comprises an acidified silica-rich ZSM-5 zeolite, the microporous H-silicalite, and a mesoporous cocatalyst, being an amorphous silica-alumina doped with molybdenum and cerium oxides. When compared to a mechanical mixture of extrudates made of H-silicalite and silica-alumina based cocatalyst, respectively, the hybrid catalyst gives faster adsorption of nitrogen and desorption of preadsorbed nitrogen. On the other hand, a much higher conversion of n-hexane (cracking) was obtained with the hybrid catalyst while the product selectivities are almost the same for all the cases. Such behavior is ascribed to the kinetic effect of the pore continuum being formed in the hybrid catalyst pore system, which has a consequence to speed up the diffusion of reactant molecules into and the reaction products out of the zeolite micropores. By changing the support for the cocatalyst, which is now a mesoporous silica, we observe the same pore continuum effect, i.e. the resulting hybrid catalyst shows a very significant activity enhancement.

2.1. INTRODUCTION

Polyfunctional catalysts capable of catalyzing multistep reactions are today subjects of numerous investigations. Microporous materials such as zeolites are catalysts or catalyst supports of choice for many reactions. Despite many advantages associated with such materials (large surface areas, molecular sieving effect, shape-selectivity), the limited size of their pores normally disfavors their use in reactions involving bulky molecules. In a “configurational” diffusive regime, a small change in the molecular structure of the reactant may have great influence on the diffusion within the zeolite pore system. The quasi-matching between the diffusing molecule and the size of the zeolite pore may result in fast diffusion rates (floating molecules). However, for any molecule which diffuses in or out of a zeolite pore, an external “energy barrier” due to a sudden change in the diffusion regime during the inward diffusion (of reactant molecules) or a sudden change in the surface curvature during the outward diffusion of products [1], has to be considered. It is quite important to mention that the “energy barrier” term is used only to simplify the existence of the natural barrier associated with the pore mouth structure of microporous zeolite materials. In order to decrease the negative effect of such an energy barrier and thus ease the inward or outward diffusion, mesoporous cocatalyst particles are firmly bound to the (microporous) zeolite particles, so that the zeolite micropores are now directly connected to the cocatalyst mesopores thus forming funnel-shaped pore connections. This is the concept of the pore continuum [2], which has found applications in several reactions, which make use of zeolites (aromatization [2,3], selective deep catalytic cracking [2,4]). The pore continuum concept received a strong support from a theoretical investigation of El-Nafaty and Mann [5] who concluded

“geometrically interspersed network” exhibited the fastest kinetics due to the direct micro-macro pore links.

Hybrid catalysts, which are prepared according to the pore continuum concept by pressing two catalytic components (microporous zeolite + mesoporous cocatalyst) within a rigid binder matrix, can profit from the fast diffusion of reacting species between the two surfaces, which may contain different active sites [4]. The microporous material used in this work is an acidified silica-rich ZSM-5 zeolite, H-silicalite, together with a cocatalyst – a mesoporous silica-alumina doped with molybdenum and cerium oxides.

In the following, the results of the nitrogen sorption isotherms will be jointly used with the data of the catalytic conversion of n-hexane (used as model molecule for the selective deep catalytic cracking or SDCC of naphthas) to evidence the effect of pore continuum in the hybrid catalyst. Some data for DTA-TGA (differential thermal / thermogravimetric analyses) will also be utilized to help imagine the geometric dispersion of the particles of the various components in the hybrid catalyst.

2.2. EXPERIMENTAL

2.2.1. Preparation of the Hybrid Catalysts

H-silicalite (HZ)

The H-silicalite was prepared by mixing 1.0 g of HISIV 3000 (Molsive adsorbent, a silica-rich ZSM-5 zeolite, from UOP) with 5 ml of NH₄Cl (10 wt % aqueous solution). The resulting mixture was stirred for 12 hours at room temperature and allowed to settle down for one hour. The mixture was then filtered and the resulting powder was mixed again with the NH₄Cl solution, and stirred for other 10 hours at room temperature. The solid obtained by filtration (without washing), was left at room temperature for 30 min,

dried overnight at 120 °C and then activated at 550 °C for 3 hours. The H-silicalite obtained, which is herein referred to as HZ, had the following physicochemical properties: Si/Al = 218, total surface area = 369 m²/g and microporosity = 136 m²/g.

Molybdenum and cerium-based cocatalyst (Cocat)

A solution of 8.5 g of ammonium molybdate hexahydrate (Aldrich) in 50.0 ml of distilled water was mixed with a solution of 2.7 g of cerium (III) nitrate in 40.0 ml of distilled water. The resulting solution was homogeneously impregnated onto 50.0 g of silica-alumina (Aldrich, catalyst support grade 135, SiO₂ = 85.6 wt.%; Al₂O₃ = 14.4 wt.%, surface area = 443 m²/g). The solid was first left at room temperature for 30 min, then dried overnight at 120 °C and finally activated at 550 °C for 3 hours. The resulting material, referred to as Cocat 1, had the following physicochemical properties: SiO₂ = 73.7 wt.%, Al₂O₃ = 12.5 wt.%, MoO₃ = 11.9 wt.%, CeO₂ = 1.9 wt.%, total surface area = 335 m²/g, micropore surface area = 0 m²/g. In other preparations, the silica-alumina support was replaced by silica gel (J.T. Baker, surface area = 280 m²/g, entirely mesoporous) and the resulting material was referred as Cocat 2, i.e. MoO₃-CeO₂/SiO₂.

Hybrid catalysts

A series of hybrid catalysts was prepared by admixing the Cocat 1 with the H-Silicalite powder materials in well-defined proportions, so that the final catalysts had the following formula: Cocat 1 (100 -X)// (X) HZ, X being the weight percent of H-Silicalite in the solid mixtures. The extrudates of these hybrid catalysts were obtained by extrusion with 20 wt.% of bentonite clay (Spectrum products). These hybrid catalysts were dried overnight at 120 °C and finally activated at 650 °C for 3 hours. They are referred to as

Cocat 1/(X) HZ. Another catalyst was obtained by extrusion with bentonite using the Cocat 2 and HZ: this hybrid catalyst is herein referred to as Cocat 2/(44) HZ.

Mechanical mixtures

The mechanical (solid) mixtures were obtained by mechanically mixing individual microporous (HZ) and mesoporous (Cocat) extrudates (20 wt.% of bentonite) of different diameters together. Initially, the HZ and Cocat extrudates (all calcined at 650 °C for 3 hours) were mildly crushed and then sieved through different sieves of different mesh sizes corresponding to following apertures: 2.0 mm, 1.7 mm, 1.4 mm and 0.85 mm.

2.2.2. Catalyst Characterization

2.2.2.1. The acidified silicalite (HZ, powder) and the Cocat (powder) were analyzed by atomic spectroscopy for their chemical composition. The cerium concentration in the Cocat was determined by gravimetry.

2.2.2.2. The BET total and micropore surface areas were determined by nitrogen adsorption / desorption, using a Micromeritics ASAP 2000 apparatus.

2.2.2.3. Thermal gravimetric and differential thermal analyses were carried out using a PL Thermal Science Model STA 1500 apparatus (combined TGA/DTA system, average sample size = 13-18 mg; heating rate = 10.0 °C/min) in air atmosphere (flow rate = 20 ml/min).

2.2.3. Experimental set-up for catalytic testing

Experiments were performed using a Lindberg one zone tubular furnace. The reactor vessel consisted of a quartz tube 55 cm in length and 1.5 cm in diameter.

Testing procedures and data reporting

n-Hexane was used as model molecules for the conversion of petroleum naphthas. Liquids, n-hexane and water were injected into a vaporizer using two infusion pumps. In the vaporizer, nitrogen used as a carrier gas was mixed with n-hexane vapors and steam. The gaseous stream was then sent into the tubular reactor. The testing conditions were as follows: weight of catalyst = 2.2 g, weight hourly space velocity (WHSV) = grams of reactant, i.e., n-hexane injected per hour per gram of catalyst = 1.52 h⁻¹, water/hydrocarbon molar ratio = ca. 0.5 (0.11 g/g), reaction temperature = 640°C, nitrogen flow rate = 3.0 ml/min, duration of the run = 5h. Gaseous and liquids were collected separately using a system of condensers. The gas-phase components were analyzed using a Hewlett-Packard 5890 FID gas chromatograph equipped with a 30-m-long GS-alumina micropacked column (J&W Scientific), while the liquid phase analysis was carried out using a Hewlett-Packard 8790 FID gas chromatograph.

The total n-paraffin conversion (mol% or wt.%) is expressed as follows:

$$C_t = \frac{\text{moles of converted n-paraffin}}{\text{moles of n-paraffin fed}} \times 100$$

The selectivity (to product i) is expressed as follows:

$$S_i = \frac{\text{number of carbon atoms of product i}}{\text{number of carbon atoms of converted products}} \times 100$$

2.3. RESULTS AND DISCUSSION

2.3.1. Isotherms of adsorption and desorption of nitrogen

Fig.2.1 and 2.2 show the isotherms of nitrogen adsorption and desorption for the H-silicalite and the cocatalyst, respectively. The shapes of these isotherms (and the resulting hysteresis loops) are characteristic of a “predominantly” microporous material [7,8] and a mesoporous one [8], respectively. Fig.2.3 reports the desorption pore volume plot (desorbed volume versus pore diameter = pore size distribution) of the H-silicalite.

Besides the desorption region of micropores, one can see a peak at circa 3.5 nm: this can be ascribed to the desorbed volume corresponding to the (larger) pore mouths of the H-silicalite. On the other hand, the desorption pore volume plot of the cocatalyst exhibited a broad peak of pores of 7.0 nm diameter (Fig.2.4). No micropores were detected.

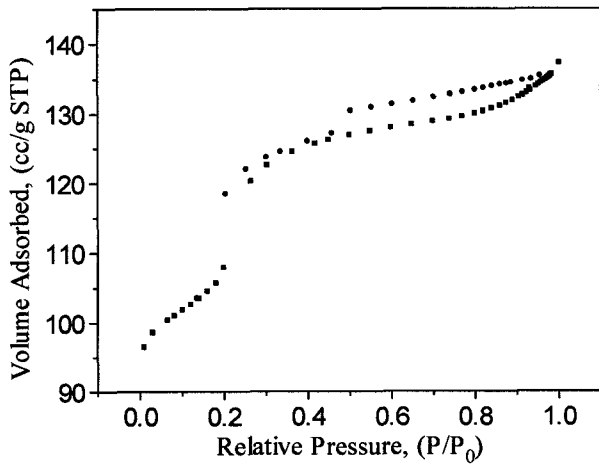


Fig.2.1: Nitrogen Isotherm plot of the H-Silicalite (▲ Adsorption ● Desorption)

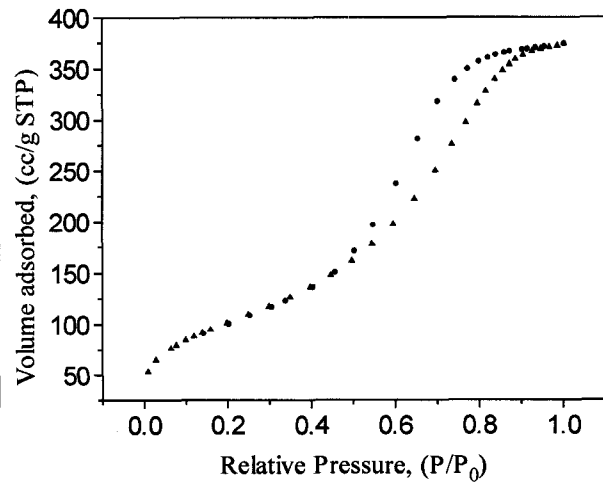


Fig.2.2: Nitrogen Isotherm plot of the cocatalyst 1 (▲ Adsorption ● Desorption)

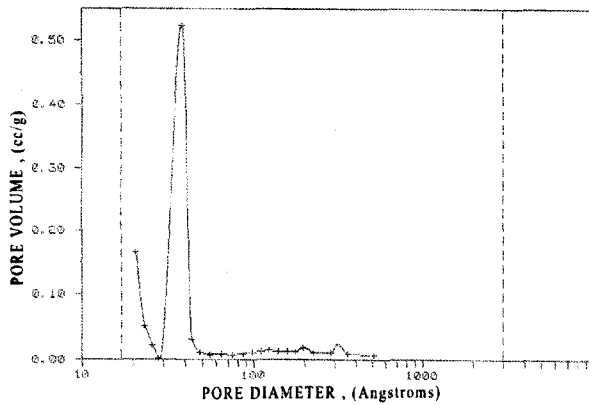


Fig.2.3: Variation of nitrogen desorbed volume verses pore diameter (H-Silicalite)

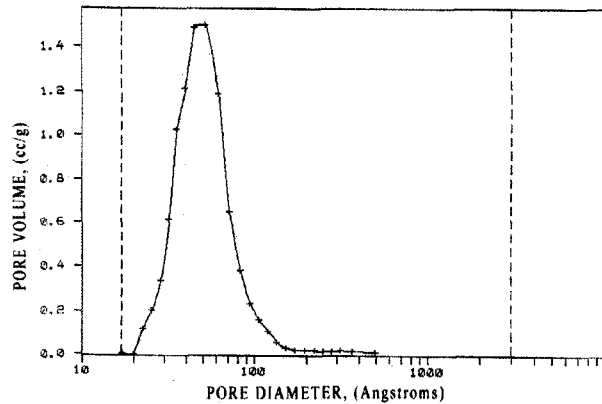


Fig.2.4: Variation of nitrogen desorbed volume verses pore diameter (cocatalyst 1)

Fig.2.5 shows the nitrogen adsorption and desorption isotherms obtained with a mechanical mixture of the H-silicalite extrudates (44 wt.%) and the cocatalyst ones (56 wt.%), both extrudates having the same diameter (2.00 mm). These isotherms, which were the sums of the sorption isotherms of two separate components, respectively, had obviously intermediary shapes. Fig.2.5 also shows the nitrogen adsorption and desorption isotherms of the hybrid Catalyst (extrudate form) that comprised the same proportions of H-silicalite (44 wt.%) and cocatalyst (56 wt.%). With respect to the mechanical mixture, the shape of the hysteresis loop was significantly different, suggesting a quite different sorption behavior.

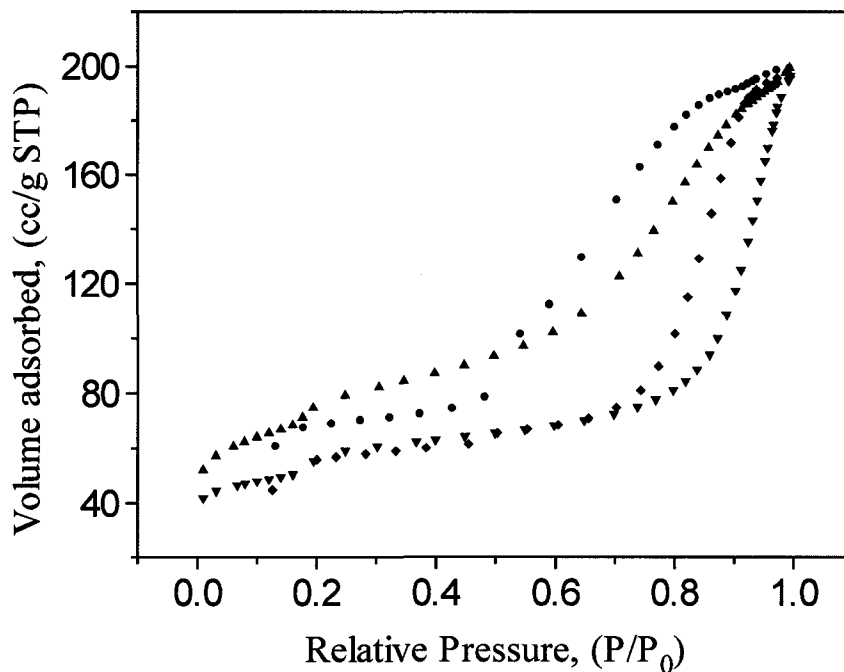


Fig.2.5: Nitrogen Isotherm plot of A- Hybrid Catalyst and B- Mechanical Mixture (▲ Adsorption and ● Desorption curves of Hybrid catalyst; ▼ Adsorption and ◆ Desorption curves of Mechanical solid mixture)

In fact, a close look reveals that in the adsorption phase, the values of adsorbed nitrogen obtained with the hybrid catalyst in the quasi entire range of relative pressure of nitrogen (> 0.0 to < 1.0), were significantly higher than those of the mechanical mixture whereas the total volume of nitrogen adsorbed (relative pressure = 1.0) was almost the same for both samples, i.e. 190 ml/g (Fig.2.5 and Table 2.1). In particular, the volumes of nitrogen adsorbed between the 0.4 and 0.7 values of the relative pressure, were 11.5 ml/g and 34 ml/g for the mechanical mixture and the hybrid catalyst, respectively. On the other hand, the desorption isotherm of the hybrid catalyst also indicated a more important desorption of adsorbed nitrogen: in fact, between the 0.7 and 0.4 values of the relative pressure, almost 80 ml of nitrogen were desorbed by 1g of the hybrid catalyst (Fig.2.5 and Table 2.1) while within the same relative pressure range, only 11.5 ml of nitrogen were desorbed by 1 g of the mechanical mixture (Fig.2.5 and Table 2.1). Since the driving force for diffusion (increase or decrease of relative pressure of nitrogen) was the same for both samples, the much higher volumes of adsorbed nitrogen and of desorbed nitrogen observed with the hybrid catalyst – when compared to the corresponding mechanical mixture, suggested that in both phases of adsorption and desorption, the hybrid catalyst gave higher rates of adsorption or desorption, i.e. in final consideration, faster (inward or outward) diffusion of nitrogen molecules or higher values of diffusivity [9]. In addition, the comparison between the desorption pore volume plots obtained with the hybrid catalyst extrudates (Fig.2.6) and the mechanical mixture (Fig.2.7) shows two completely different desorption behaviors.

Table 2.1: Volume of nitrogen adsorbed and desorbed, a comparison between hybrid catalyst and its corresponding mechanical solid mixture

Catalyst	Phase	Relative Pressure, P/P_0	Volume Adsorbed, (cc/g STP)	ΔV (cc/g STP)	Approximate $\Delta V/\Delta(P/P_0)$,
Hybrid Catalyst	Adsorption	0.4	86	34	113
		0.7	120		
	Desorption	0.7	150	80	267
Mechanical Mixture	Adsorption	0.4	62.5	11.5	38
		0.7	75.0		
	Desorption	0.7	75.0	11.5	38
		0.4	62.5		

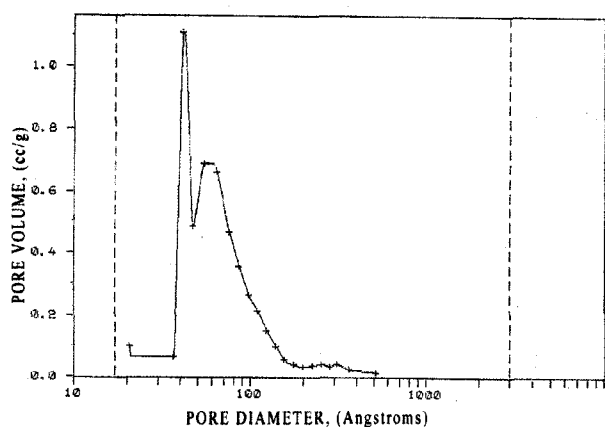


Fig.2.6: Variation of nitrogen desorbed volume verses pore diameter (Hybrid catalyst)

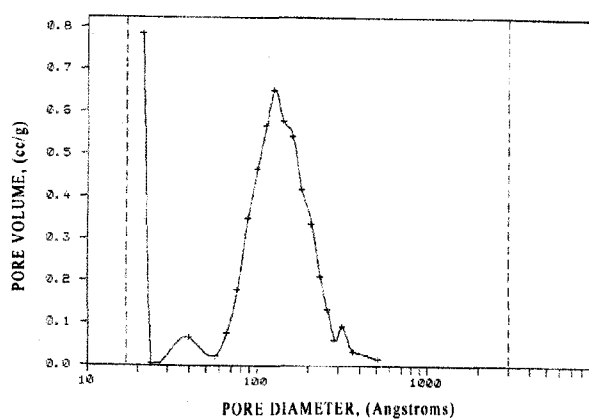


Fig.2.7: Variation of nitrogen desorbed volume verses pore diameter (Mechanical mixture)

2.3.2. Catalytic performance

The maximum value of n-hexane conversion was obtained with a hybrid catalyst comprising 44 wt.% of H-silicalite and 56 wt.% of cocatalyst 1 (Table 2.2). This surprising result had already been reported in our previous works, which involved not only n-hexane but also petroleum naphthas as feeds [4,10]. By using mechanical mixtures, which contained the same proportions of the two catalytic components, we obtained the same trends, i.e. a maximum conversion at 44 wt.% of extrudates of H-

silicalite and 56 wt.% of extrudates of cocatalyst 1 (Table 2.2). However, mechanical mixtures experienced extremely modest increases of n-hexane conversion.

Table 2.2: Conversion of n-hexane obtained with the Hybrid catalyst and its corresponding solid mixtures (of different extrudate diameters)

Catalyst Composition	100 wt% HZ	90 wt% HZ & 10 wt% Cocat 1	44 wt% HZ & 56 wt% Cocat 1	25 wt% HZ & 75 wt% Cocat 1	10 wt% HZ & 90 wt% Cocat 1
Hybrid Catalyst (Ex.Diameter: 2.0 mm)*	32.6	43.0	56.9	48.2	41.4
Mechanical Mixture (Ex.Diameter: 2.0 mm)*	32.6	31.0	37.2	31.2	29.9
Mechanical Mixture (Ex.Diameter: 1.7 mm)*	31.2	30.5	34.8	29.9	27.2
Mechanical Mixture (Ex.Diameter: 1.4 mm)*	32.8	30.9	34.4	32.4	29.9
Mechanical Mixture (Ex.Diameter: 0.85 mm)*	32.3	32.6	36.1	31.6	28.0

* Ex = Extrudate

Table 2.3 reports almost same product selectivities for the hybrid catalyst and the corresponding mechanical mixtures of extrudates of different diameter. This suggests that the enhanced conversion was closely related to some kinetic phenomena occurring within the hybrid catalyst framework, i.e. this was not due to some (surface) structural change of the two catalytic components. It is worth noting that some small changes in the product selectivities for aromatics (small increase, mostly for the product benzene) and methane (small decrease) were observed with the best hybrid catalyst configuration – when compared to other hybrid configurations. This could be ascribed to the formation of bifunctional catalytic sites in the contact region between the “large” pore mouths of the

H-silicalite and the mesopores of the cocatalyst. Cerium cations (known to have strong redox properties as well as hydrogen exchange capability) contained in the cocatalyst might be ion-exchanged with some protons of the H-silicalite, which were located in the pore mouths. This bore some similarity with the aromatization of light paraffins [3]. In fact, on these bifunctional sites, some propylene molecules might undergo dehydrocyclization to benzene, preventing the formation of methane through the well-known (secondary) cracking reaction: propylene \rightarrow ethylene + methane.

Table 2.3: Product selectivities for hybrid catalyst and the corresponding mechanical solid mixtures of extrudates of different diameters (Catalyst composition is 46 wt.% H-silicalite and 56 wt.% cocat 1)

Catalyst Composition S _i (wt.%)	Hybrid Catalyst (HZ// Cocat 1)	Mechanical Mixture (Ex.D.: 2.0 mm)	Mechanical Mixture (Ex.D.: 1.7 mm)	Mechanical Mixture (Ex.D.: 1.4 mm)	Mechanical Mixture (Ex.D.: 0.85 mm)
Olefins (C ₂ ⁻ - C ₃ ⁻)	59.3	62.4	60.9	61.2	64.2
Olefins (C ₂ ⁻ - C ₄ ⁻)	73.2	76.7	75.0	75.6	77.9
Methane	5.6	8.0	9.1	9.0	9.1
C ₁ -C ₄ Paraffin	20.1	17.6	18.4	19.2	18.5
BTX Aromatics	5.3	3.6	4.5	2.6	2.0

Therefore, the more rapid adsorption of reactant molecules and desorption of the product molecules from the hybrid catalyst might be the origin of its higher performance in the conversion of n-hexane since this would more rapidly free the active sites of the zeolite structure for further adsorption and conversion of reacting species. Such interpretation is perfectly in line with the concept of pore continuum [2]: essentially, a product molecule which diffuses in or out of a micropore (of the zeolite) does not have to overcome an important “energy barrier” if the mouth of the zeolite micropore is in close contact with that of the cocatalyst mesopore. In addition, an optimal composition (of microporous and mesoporous materials) is needed for a maximum activity because the

particles of the two types have to be distributed in some optimal way one around another [5]. Also, the binder (here, bentonite) plays some important role in promoting such catalytic activity enhancement because a tight contact between the particle surfaces (good pore connections) is absolutely necessary. On the other hand, the much lower coke build-up in the hybrid catalyst (Fig.2.8, 2.2 ± 1.80 wt.%) when compared to the corresponding mechanical mixture (Fig.2.9, 9.3 ± 1.30 wt.%), suggests that the optimal distribution of particles within hybrid extrudates – as mentioned earlier – might consist of large cocatalyst aggregates surrounded by (tiny) submicron-sized particles as observed by scanning electron microscopy in many hybrid catalysts [2,3]. In fact, coke precursors, which diffuse through the zeolite particles, usually undergo cracking, thus preventing the accumulation of coke in the hybrid catalyst network.

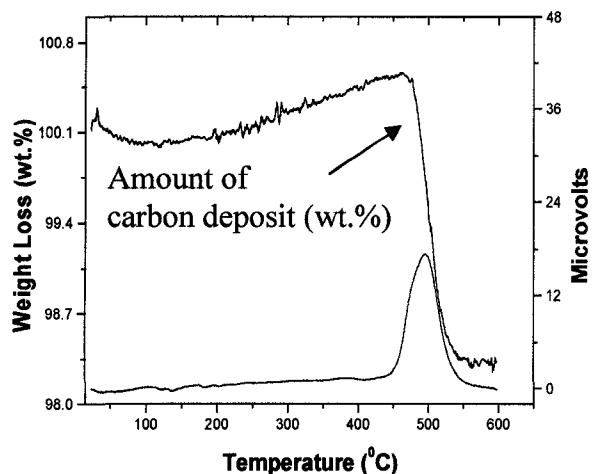


Fig.2.8: DTA/TGA curves for the combustion of Coke deposited into the Hybrid catalyst

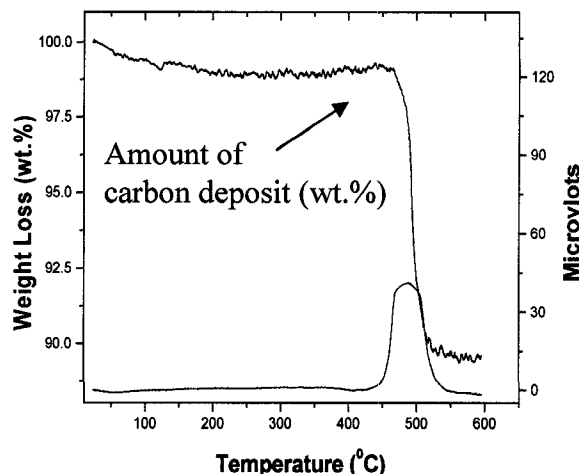


Fig.2.9: DTA/TGA curves for the combustion of Coke deposited into the Mechanical solid mixture

To ensure that bentonite used as binder did not have any significant effect on the catalytically active components during the final thermal treatment of the hybrid catalysts, i.e. there was no solid-state Al transfer from the bentonite to the silicalite which might enhance the surface acidity, a series of tests was carried out with several “catalysts” (all activated at 650 °C for 3 hours) and the catalytic results obtained are reported in Table 2.4. Thus, the activity and product selectivities of extrudates made of bentonite (Bent) were not significantly different from those of the untreated silicalite (Z /bent), meaning that there was no Al exchange between the binder and the silicalite particles. Table 4 also shows the higher activity of the (extrudates of) treated silicalite (HZ), which was due to its (low) acid site density corresponding to the low Al content and its additional acidity created by intentionally leaving chlorine from the NH₄Cl treatment (no washing after the ion- exchange) [11]. In Table 2.4, is also reported the catalytic activity of the (extrudates of) silica-alumina (SiAl) whose surface acidity was quite significant, but slightly lower than the HZ sample [11]. However, the combination of HZ and SiAl, two solids having quite comparable surface acidities, provided a hybrid catalyst (HZ//SiAl) whose extrudates exhibited much higher catalytic activity (Table 2.4, last column).

Table 2.4: Catalytic activity of the extrudates of bentonite (Bent) and of some parent solids used as supports or active components

Catalyst Composition	Bent	Z/bent	HZ	Silica- alumina	(56) SiAl// (44) HZ
Conversion (wt.%)	23.5	22.2	32.6	29.3	40.9
Product Selectivity (wt.%)					
Olefins (C ₂ = - C ₃ =)	67.4	66.2	63.0	67.5	58.8
Olefins (C ₂ = - C ₄ =)	80.8	80.3	79.6	82.2	76.2
Methane	7.2	7.1	5.9	6.4	4.3
C ₁ -C ₄ Paraffin	14.2	13.8	16.5	14.4	20.1
BTX Aromatics	0.2	0.7	0.2	0.2	1.1

Finally, changing the support of the cocatalyst – from silica-alumina (Cocat 1) to less acidic silica (Cocat 2) – slightly decreased the conversion. However, like in the case of the hybrid catalyst Cocat 1/(44)HZ, the Cocat 2/(44) HZ sample gave a conversion significantly higher than those of the monocomponent constituting catalysts, HZ (Table 2.4) and Cocat 2 (Table 2.5). These results provided new and convincing evidence for a pore continuum effect within the hybrid catalyst network.

Table 2.5: Catalytic activity of the cocatalysts with different supports and their corresponding hybrid catalysts (44 wt.% HZ. Cocat 1 = MoO₃-CeO₂/SiAl; Cocat 2 = MoO₃-CeO₂/SiO₂)

Catalyst Composition	Cocat 1	Cocat 2	Cocat 1// (44) HZ	Cocat 2// (44) HZ
Conversion (wt.%)	30.8	28.6	56.9	47.5
Product Selectivity (wt.%)				
Olefins (C ₂ – C ₃)	61.1	66.0	59.3	64.8
Olefins (C ₂ – C ₄)	75.1	81.1	73.2	80.2
Methane	10.4	7.0	5.6	6.3
C ₁ -C ₄ Paraffin	18.0	14.0	20.1	15.1
BTX Aromatics	2.1	0.4	5.3	1.0

2.4. CONCLUSION

The inward and outward diffusion rates of nitrogen observed with the hybrid catalyst extrudates were higher than those of a mechanical mixture of extrudates, both solids containing the same proportions of microporous zeolite and mesoporous cocatalyst. On the other hand, the same hybrid catalyst showed a much higher conversion of n-hexane than its counterpart (the mechanical mixture), while the product selectivities were almost the same. Both phenomena were interpreted as direct results of the formation of a pore continuum within the hybrid catalyst pore network.

2.5. ACKNOWLEDGEMENTS

Financial support from NSERC (Natural Science and Engineering Research Council of Canada) and Valeo Management are acknowledged.

2.6. AUTHOR'S NOTES AND SIGNIFICANCE OF PAPER TO THESIS

This work presents a continuation toward further understanding the pore continuum concept that exists between microporous and mesoporous materials. Our group was the first to report and examine this newly developed concept [2]. In this study, we have found that the hybrid catalyst, which is comprised of microporous H-silicalite and a mesoporous amorphous silica-alumina supported molybdenum and cerium oxides gives, for instance, faster adsorption of nitrogen and desorption of preadsorbed nitrogen when compared to the corresponding mechanical mixture. Such behavior was ascribed to the kinetic effect of the pore continuum being formed in the hybrid catalyst pore system, which has the consequence of speeding up the diffusion of reactant molecules and that of reaction products from the zeolite micropores. It is worth mentioning that the existence of pore continuum concept was supported by several studies concerning the hierarchial meso-micro porous structure [13-15].

Although, the fast deactivation rate and diffusion limitations in the zeolite system were reduced upon using the pore continuum configuration, they remain an obstacle that significantly hinders the effectiveness of zeolite. Therefore, we have decided to shift our attention to the mesoporous supported metal oxide catalyst, which was used in the hybrid catalyst as the mesoporous component. In the next chapters (III-VII), we will describe thoroughly our examination of this mesoporous configuration. It is worth mentioning that the pore continuum concept is revisited once again in the last chapter (Future work). Our

preliminary results showed that the zeolite deactivation rate could be significantly improved in the pore continuum configuration upon the addition of the right mesoporous cocatalyst.

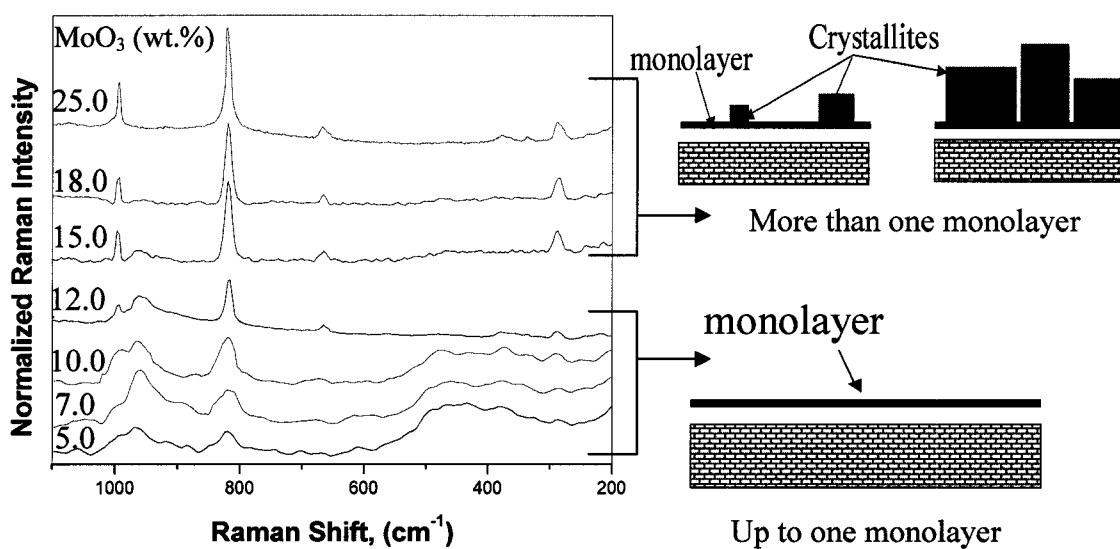
2.7. REFERENCES

- [1] E.G. Derouane, J.M. Andre and A. A. Lucas, *J. Catal.* **110** (1988) 58.
- [2] R. Le Van Mao, *Micropor. Mesopor. Mater.* **28** (1999) 9.
- [3] R. Le Van Mao, J. Yao, L.A. Dufresne, R. Carli, *Catal. Today* **31** (1996) 247.
- [4] S. Melancon, R. Le Van Mao, P. Kletnieks, D. Ohayon, S. Intem, M.A. Saberi and D. McCann, *Catal. Lett.* **80** (3-4) (2002) 103.
- [5] U.A. El-Nafaty and R. Mann, *Chem. Eng. Science*, **54** (1999) 3475.
- [6] R. Le Van Mao, S. Melancon, C. Gauthier-Campbell and P. Kletnieks, *Catal. Lett.* **73** (2-4) (2001) 181.
- [7] S.V. Webb and W.C. Conner, in *Characterization of Porous Solids II*, F. Rodriguez-Reinoso, J. Rouquerol, K.S.W. Sing and K.K. Unger (Ed.), Elsevier Sc. Publ. B.V. (Amsterdam), 991, 31.
- [8] E. Robens and K.F. Krebs, in *Characterization of Porous Solids II*, F. Rodriguez-Reinoso, J. Rouquerol, K.S.W. Sing and K.K. Unger (Ed.), Elsevier Sc. Publ. B.V. (Amsterdam), 1991, 133.
- [9] D.M. Ruthven, in *Fundamentals of adsorption*, Proc. Second Eng. Foundation Conf., Athanasios I. Liapis (Ed.), publ. Eng. Foundation (New York), 1987, p. 29.
- [10] R. Le Van Mao, N. Al-Yassir, D. T.T. Nguyen and J. Monnier, 18th Canadian Symposium on Catalysis, Montreal (Canada), May 16-19, 2004.
- [11] N. Al-Yassir, R. Le Van Mao and F. Heng, *Catal. Lett.*, **100** (2005) 1.

- [12] Q. Tan, X. Bao, T. Song, Y. Fan, G. Shi, B. Shen, C. Liu, X. Gao, *J. Catal.* **251** (2007) 69.
- [13] Y. Ding, J. Liang, Y. Fan, Y. Wang, X. Bao, *Catal. Today*, **125** (2007) 178.
- [14] V. M. Akhmedov, S. H. Al-Khowaiter, *Cat. Rev. - Sci. Eng.*, **49** (2007) 33.

Chapter III

Physico-chemical properties of mixed molybdenum and cerium oxides supported on silica-alumina and their use as catalysts in the Thermo-Catalytic Cracking (TCC) of n-hexane



Graphical Abstract: Raman spectra of silica-alumina supported mono-oxide MoO₃ as a function of Mo loadings, and schematic representation of monolayer coverage

Published as:

N. Al-Yassir and R. Le Van Mao,

Applied Catalysis A: General **305** (2006) 130-139.

ABSTRACT

Mixed oxides, $\text{MoO}_3\text{-CeO}_2$, were being used as catalysts for the cracking (TCC) of liquid hydrocarbon feedstocks. The dispersion and interactions of MoO_3 , CeO_2 , and mixtures thereof impregnated into the silica-alumina surface were investigated using several techniques, which included X-ray diffraction (XRD) and laser Raman spectroscopy (LRS). The loadings and the chemical states of metal oxides incorporated separately had significant effects on the catalytic activities of the resulting mono-component catalysts. Addition of cerium to molybdenum had a favorable effect on the production of light olefins in the TCC of n-hexane up to a certain level of cerium loading. In fact, high loadings of molybdenum and/or cerium favored the formation of aromatics, instead. The catalytic performance of the bi-component catalysts also depended significantly on the incorporation methods. It was found that the co-impregnation of MoO_3 and CeO_2 , which led to the highest production of light olefins, corresponded to the formation of (surface) cerium molybdate to the highest extent. On the other hand, the catalysts prepared by the two-step impregnation methods (sequential and reverse sequential impregnation) showed much lower catalytic performance due to low Mo-Ce interactions as suggested by an important segregation of the active phases, mostly MoO_3 . The sequence of catalytic performance (to the desired products, i.e. light olefins) fully coincided with that of the dispersion of molybdate species on the support surface.

3.1. INTRODUCTION

Light olefins and diolefins such as ethylene, propylene, butenes and butadienes are precursors of numerous plastic materials, synthetic fibers and synthetic rubbers. These precursors are mainly produced by several conventional petroleum processes that include Steam Cracking (SC), Fluid Catalytic Cracking (FCC) and Deep Catalytic Cracking (DCC) [1-2]. However, these conventional processes suffer from several major drawbacks such as severe environmental problems, high energy cost and/or lack of catalyst long-term stability. Recently, a new emerging process known as Thermo- Catalytic Cracking (TCC) has been developed, aiming at achieving higher combined yield of ethylene and propylene, but at lower energy consumption and lower greenhouse gases emission as well [3-11]. TCC is a combination of (mild) thermal cracking and catalytic cracking, the latter making use of unique hybrid or novel mesoporous mixed oxide catalysts. In the hybrid catalyst configuration, two components, microporous (zeolite type) and mesoporous (cocatalyst), were firmly bound to each other within a clay binder, such that a “pore continuum” effect was developed, allowing the rapid diffusion of reacting species from micropores to the mesopores or vice-versa [8-11]. Another version developed was the novel mesoporous mixed oxide catalyst, which is based on supported mixed molybdenum-cerium oxides [5,6,10].

In general, both molybdenum oxide and cerium oxide based catalysts have attracted the attention of many researchers, because of their numerous applications in various fields. For instance, molybdenum oxide based catalysts have been widely used in many important catalytic reactions [12], which include olefin metathesis [13], oxidation and ammoxidation reactions [14,15], as well as hydrotreating [16]. Furthermore, cerium oxide forms an integral part of three-way catalysts (TWC) for automotive exhaust treatment [17] and

serves as a promoter for the fluid catalytic cracking (FCC) catalysts [18]. The success of cerium oxide relies on its unique features that include its ability to release and store oxygen (high oxygen mobility) couples with the ability to shift easily between the reduced and oxidized states ($\text{Ce}^{3+} \rightleftharpoons \text{Ce}^{4+} + e^-$) (unique redox properties) [19,20].

Nevertheless, to our knowledge, no work has been reported yet in the literature on silica-alumina supported bicomponent $\text{MoO}_3\text{-CeO}_2$ system. Therefore, an attempt was made in this present study to shed some light into the properties of this catalyst system. In the previous publication [10], we have laid the general features of the effect of doping cerium oxide into the supported molybdenum oxide catalyst. Cerium oxide, incorporated as a dopant, has a main catalytic effect of increasing the selectivity to light olefins and diolefins while the production of BTX aromatics significantly decreases. In the present study, we were attempting to provide some basic insights into the physico-chemical properties and structure of silica-alumina supported mono-component MoO_3 , CeO_2 and bi-component $\text{MoO}_3\text{-CeO}_2$ catalysts, and the effect of catalyst preparation. Therefore, a systematic study was undertaken on the characterization of silica-alumina supported mono-component MoO_3 , CeO_2 and bi-component $\text{MoO}_3\text{-CeO}_2$ catalysts by various techniques such as Brunauer-Emmett-Teller (BET) surface area and pore volume, X-ray diffraction (XRD), Laser Raman spectroscopy (LRS, a powerful tool to investigate supported metal oxides) and ammonia temperature-programmed desorption (surface acidity). The catalytic properties were evaluated during the TCC of n-hexane used herein as a model molecule for petroleum naphthas, and the results were discussed in relation with the structural properties.

3.2. EXPERIMENTAL

3.2.1. Catalyst Preparation

Catalyst support

Commercial amorphous silica-alumina (SiAl) (Aldrich, catalyst support grade 135, SiO₂ = 86 wt.%; Al₂O₃ = 14 wt.%) was used as a support. Prior to impregnation it was calcined at 650 °C for 3h. This treatment results in silica-alumina with a surface area of 421 m²/g and a pore volume of 0.680 cm³/g, as measured with the BET technique.

Mono-component silica-alumina supported catalysts

MoO₃/silica-alumina catalysts (MoO₃/SiAl)

A series of MoO₃/silica-alumina catalysts with MoO₃ loadings in the range of 1.0-33.0 wt.% MoO₃ were prepared by impregnation method. The required amount of ammonium heptamolybdate (AHM) (NH₄)₆Mo₇O₂₄·4H₂O salt (Aldrich) was dissolved in distilled water and then added to silica-alumina. The impregnation solutions were at pH 5.3-5.5. After impregnation, samples were first left at 60 °C for 3 h for slow evaporation of water, dried overnight at 120°C and finally activated in air at 650 °C for 3 h. MoO₃/SiAl with different MoO₃ loadings are noted as xMoO₃/SiAl, where x is the MoO₃ content in wt.%. Pure MoO₃ was obtained by calcining ammonium heptamolybdate in air at 650 °C for 3h.

CeO₂/silica-alumina catalysts (CeO₂/SiAl)

A series of CeO₂/silica-alumina with CeO₂ loadings in the range of 1.0-15.0 wt.% CeO₂ were prepared by impregnation method. The required amount of cerium (III) nitrate Ce(NO₃)₃·6H₂O salt (Aldrich) was dissolved in distilled water and then added to silica-alumina support. The impregnation solutions were dependant on the amount of cerium (III) nitrate and ranges from pH 3.5-1.5 with respect to CeO₂ loadings, 1.0-15.0 wt.%. Similar procedures as MoO₃/SiAl

catalysts were used. CeO₂/SiAl with different CeO₂ loadings are noted as yCeO₂/SiAl, where y is the CeO₂ content in wt.%. Pure powder CeO₂ was obtained by calcining cerium (III) nitrate in air at 650°C for 3h.

Unsupported Mixed MoO₃-CeO₂ catalysts (MoO₃-CeO₂)

A series of unsupported MoO₃-CeO₂ catalysts with different [Ce]/[Mo] molar ratios in the range of 0.13-0.88 were prepared by co-precipitation method. Aqueous solutions of AHM and cerium (III) nitrate were mixed together for ca. 10 min. and then the resulting precipitate was filtered. The precipitates were dried overnight at 120 °C and then activated in air at 650 °C for 3 h. The amount of AHM was kept constant, while the amount of cerium (III) nitrate was varied in order to obtain different [Ce]/[Mo] molar ratios.

Bi-component silica-alumina supported Mixed MoO₃-CeO₂(MoO₃-CeO₂/SiAl)

co-Impregnation method (CoI):

A series of MoO₃-CeO₂/SiAl catalysts with different [Ce]/[Mo] molar ratios were prepared by co-impregnation method. In the range of [Ce]/[Mo] ratios from 0.13-0.88, MoO₃ loadings were kept always constant at ca. 11.6 wt.%, while the CeO₂ loadings were varied from ca. 1.75 wt.% - 12.0 wt.% (i.e. CeO₂ in wt.% was 1.75, 4.0, 6.0, 8.0 and 12.0 for samples with [Ce]/[Mo] = 0.13, 0.30, 0.41, 0.59 and 0.88, respectively). Aqueous solutions of AHM salt and Cerium (III) nitrate salts were mixed together for ca. 10 min. and then were impregnated on silica-alumina. The impregnation solutions were dependant on the [Ce]/[Mo] ratios and ranges from pH 4.2-1.6 with respect to [Ce]/[Mo] molar ratios, 0.13-0.88. After impregnation, samples were first left at 60 °C for 3 h for slow evaporation of water, dried overnight at 120 °C and finally activated in air at 650°C for 3 h (catalysts prepared by co-impregnation are designated by MoCe/SiAl).

Sequential impregnation (SeI) and Reverse sequential impregnation (RSI) methods:

Samples with the following [Ce]/[Mo] molar ratio = 0.41 (the MoO₃ and CeO₂ contents were 11.6 wt.% and 5.6 wt.%, respectively) were prepared by both sequential and reverse sequential impregnation. In sequential impregnation, an aqueous solution of AHM salt (pH 5.3-5.5) was impregnated first into the silica-alumina followed by drying and calcinations. Then, an aqueous solution of cerium (III) nitrate salt (pH 3.5) was later impregnated into the calcined mixture (catalysts prepared by sequential impregnation are designated by Mo→Ce/SiAl). In reverse sequential impregnation method; similar procedures and conditions were used except that the order of impregnated species was reversed (catalysts prepared by reverse sequential impregnation are designated by Ce→Mo/SiAl).

Catalyst extrudates

The extrudates of all prepared catalysts were obtained by extrusion with bentonite clay (Aldrich), (Spectrum products, 20.0 wt.% of the previous solid mixtures). These catalysts were dried overnight at 120°C and then activated in air at 650 °C for 3 h.

3.2.2. Catalyst Characterization

3.2.2.1. The surface areas of the catalysts were determined by the BET method using nitrogen physisorption at 77 K. The measurements were carried out using Micromeritics ASAP 2000 apparatus. Samples were degassed for 4h at 220 °C before N₂ physisorption.

3.2.2.2. X-ray Powder diffraction (XRD) was carried out on a Philips diffractometer equipped with a PW 1050/25 focusing goniometer, which has been automated with the VisX122D system from Diffraction Technologies. The Ni filtered K α radiation of Cu was used ($\lambda_{K\alpha 1} = 1.54051\text{\AA}$) and diffractometer was operated at 40kV and 20mA. The powder patterns were recorded in the step scanning mode from 10-60°(2 θ) at a detector angular speed of 0.3 °/min

with a step size of 0.05° . The XRD phases present in the samples were identified with the help of the JCPDS (Joint Committee on Powder Diffraction Standards) powder data files [21].

3.2.2.3. Raman spectra were collected with a Nexus FT-Raman spectrometer. The spectra were recorded at room temperature using the 1064 nm line of Nd-YAG laser for excitation. The laser was operated at 0.7 watt and data were recorded using the OMNIC software. The wavenumber obtained from spectra are accurate to within 2 cm^{-1} .

3.2.2.4. Ammonia adsorption and temperature-programmed desorption (TPD) technique was used for the study of the surface acidity. To prevent physisorption phenomena, ammonia was adsorbed at $100\text{ }^\circ\text{C}$. The measurement of acid site density was carried out by heating the ammonia treated catalyst at a constant flow rate of nitrogen (ultra high pure) from $100\text{ }^\circ\text{C}$ (temperature of ammonia adsorption) to $650\text{ }^\circ\text{C}$. Using a $0.02\text{ N CH}_3\text{COOH}$ solution that was then back-titrated with 0.01 N NaOH solution in accordance with the method reported in [22].

3.2.3. Experimental set-up for catalytic testing

Experiments were performed using a Lindberg one zone tubular furnace. The reactor vessel consisted of a quartz tube 55 cm in length and 1.5 cm in diameter.

Testing procedures and data reporting

For the conversion of petroleum naphthas, n-hexane was used as a model. Liquids, n-hexane and water, were injected into a vaporizer using two infusion pumps. In the vaporizer, nitrogen used as a carrier gas was mixed with n-hexane vapors and steam. The gaseous stream was then sent into the tubular reactor. The testing conditions were as follows: weight of catalyst = 2.2 g , weight hourly space velocity (WHSV) = grams of reactant, i.e., n-hexane injected per hour per gram of catalyst = 1.52 h^{-1} , water/hydrocarbon molar ratio = ca. 0.5 (0.11 g/g), reaction temperature = 680°C , nitrogen flow rate = 3.0 ml/min , duration of the run = 5 h .

Gases and liquids were collected separately using a system of condensers. The gas-phase components were analyzed using a Hewlett-Packard 5890 FID gas chromatograph equipped with a 30-m-long GS-alumina micropacked column (J&W Scientific), while the liquid phase analysis was carried out using a Hewlett-Packard 8790 FID gas chromatograph equipped with a 50-m-long PONA capillary column. The catalytic activities results were reproducible within ± 1.75 wt.%.

The total n-paraffin conversion (mol% or wt.%) is expressed as follows:

$$C_t = \frac{\text{moles of converted n-paraffin} \times 100}{\text{moles of n-paraffin fed}}$$

The selectivity (to product i) is expressed as follows:

$$S_i = \frac{\text{number of carbon atoms of product i}}{\text{number of carbon atoms of converted products}} \times 100$$

3.3. RESULTS AND DISCUSSION

3.3.1. Mono-component MoO₃/SiAl and CeO₂/SiAl catalysts

Mo oxides as metal oxides of Group 6 have several oxidation states, which may affect their catalytic activity, mostly when they are supported on “irreducible” oxides such as silica or silica-alumina. In its most stable oxidation state (+6), MoO₃ also exhibits acidity of some strength and of both natures (Brönsted and Lewis) [23]. Surface structure of a supported metal oxide catalyst is of key importance for its catalytic properties. Several other physico-chemical parameters are also important such as surface area and porosity [24], degree of dispersion, number of coverage layers, possibility of interaction with the support, surface restructuring during the reaction at high temperature or high pressure, as well as amounts and methods of incorporation of active species [25]. Knowing the total BET surface area and the theoretical surface coverage of a molecule of MoO₃ [26,27], the surface density of Mo, as well as the

corresponding surface coverage as a fraction of a monolayer was calculated (Table 3.1). However, the reality is much more complicated than this ideal situation since: a) the support is always heterogeneous so that it can host extraneous species only in certain locations. As a result, the surface saturation – in monolayer configuration - is reached in much smaller fraction [28,29]; b) the adsorption of the metal oxide onto the support surface is never homogeneous and may be in monomeric or polymeric form in relation to the isoelectric point of the support, IEPS [30 and refs. therein]; c) the density and type of surface hydroxyl (-OH) groups on the support surface may have a great influence on the dispersion of the incorporated species [31,32]; d) surface restructuration may occur during the catalyst preparation or testing. Therefore, the experimentally determined actual monolayer loading on different supports are always less than the theoretical estimation. In our present study, the experimentally determined MoO₃ monolayer on silica-alumina support corresponded to about 31 % of the theoretical monolayer estimation (case of MoO₃ loading with 12.0 wt.%) as shown in Table 3.1. In our case, the increasing loading of MoO₃ significantly and gradually diminished the surface area and the pore volume of the final catalysts. This was due to the progressive occlusion of the pores of the support by MoO₃ crystallites whose size increased with increasing loadings. These crystallites were visible by the XRD only when the loading was higher than 12 wt. %, probably because below that value, the crystal size was smaller than 5.0 nm (Fig.3.1a).

Table 3.1: Textural properties of the support, bulk and silica-alumina supported MoO₃ catalysts; all samples were activated at 650°C in air for 3h

Catalyst	MoO ₃ (wt.%)	S _{BET} (m ² /g)	Pore Volume (cm ³ /g)	Average surface coverage *	
				Mo surface density (Mo atoms/nm ²)	As a fraction of monolayer (θ)
Mo (1.0)/SiAl	1.0	384	0.615	0.11	0.02
Mo (2.0)/SiAl	2.0	389	0.626	0.22	0.04
Mo (5.0)/SiAl	5.0	359	0.573	0.60	0.12
Mo (10.0)/SiAl	10.0	347	0.562	1.21	0.24
Mo (12.0)/SiAl	12.0	328	0.541	1.53	0.31
Mo (15.0)/SiAl	15.0	270	0.491	2.32	0.47
Mo (18.0)/SiAl	18.0	240	0.471	3.14	0.63
Mo (25.0)/SiAl	25.0	131	0.372	7.98	1.60
Mo (33.0)/SiAl	33.0	64.5	0.281	21.4	4.28
Silica-alumina	0.0	421	0.680	-----	
MoO ₃ [♦]	100	2.5	0.004	-----	

* Assumption: θ MoO₃ = 0.2 nm²

♦ MoO₃ obtained by calcining ammonium molybdate tetrahydrate in air at 650 °C for 3h

Figure 3.1a clearly shows that MoO₃ on silica-alumina support forms an X-ray amorphous monolayer on the silica-alumina at Mo loading up to 1.53 atoms/nm² (equivalent to 12.0 wt.% MoO₃). However, at higher loadings, new XRD peaks appeared and are ascribed to bulk MoO₃ crystallites. These reflections (shown with (*)) are ascribed to bulk MoO₃, with the orthorhombic crystal structure (JCPDS No. 35-0609) [33]. Furthermore, it is noteworthy to mention that at very high loadings (higher than 12.0 wt.% MoO₃), XRD revealed in addition to MoO₃ crystallites the presence of a new phase (Figure 3.1a), which may be attributed to the formation of Al₂(MoO₄)₃ (JCPDS No. 23-0764) by solid-state reaction between bulk MoO₃ and the alumina containing support.

These results were further supported by laser Raman spectroscopy, which provided more structural details due to its high sensitivity, particularly toward the presence of microcrystallites (< 40Å) and XRD amorphous particles [34]. For instance, the more sensitive

laser FT-Raman spectroscopy showed the presence of much smaller sized crystallites, i.e. when the loading of MoO₃ was only 5.0 wt. % (Figure 3.1b), as evident from the presence of Raman bands (ca. 285, 375, 475 and 966 cm⁻¹) that are characteristics of surface octahedral polymolybdate species (Mo₇O₂₄⁶⁻, Mo₈O₂₄⁴⁺) [35-37]. Additionally, Raman bands that are unambiguously attributed to bulk MoO₃ crystallites (285, 667, 819 and 995 cm⁻¹) [38] were also observed in samples with MoO₃ loading of 10.0 wt.% and higher. It is noteworthy to mention that XRD did not detect the presence of MoO₃ crystallites in samples with 10-12.0 wt.% MoO₃, while Raman spectroscopy clearly did. These small crystallites resulted from an easy conversion of surface polymolybdate species upon calcinations at elevated temperature. This was attributed to the weak molybdate interaction with the silica-alumina support, which has a low surface concentration of hydroxyl groups (-OH), and molybdate anions [31-32,39].

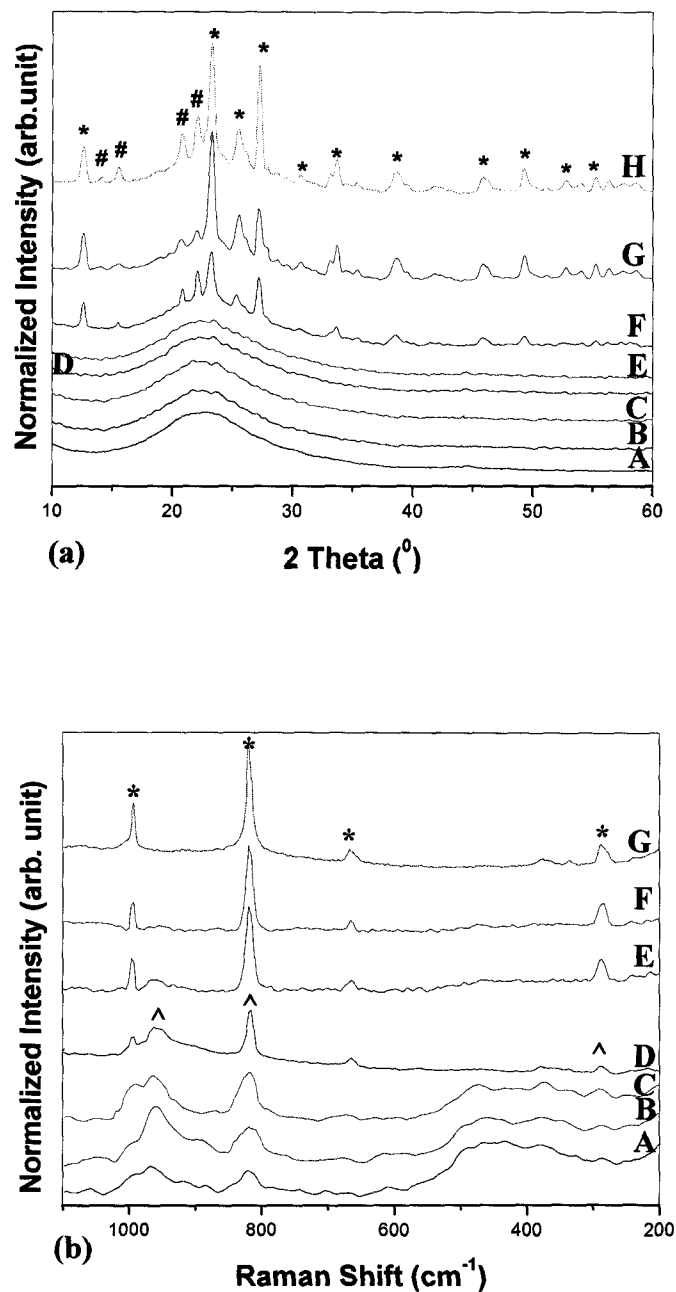


Fig.3.1: (a) X-ray diffraction patterns of silica-alumina (SA) supported MoO₃ catalysts with different MoO₃ loading, A) 0.0 wt.%, B) 5.0 wt.%, C) 7.00 wt.%, D) 10.0 wt.%, E) 12.0 wt.%, F) 15.0 wt.%, G) 18.0 wt.% and H) 25.0 wt.%. (*) Reflections due to bulk MoO₃ phase, (#) reflections due to Al₂(MoO₄)₃. (b) Raman spectra of SA supported MoO₃ as a function of MoO₃ loading; A) 5.0 wt.%, B) 7.0 wt.%, C) 10.0 wt.%, D) 12.0 wt.%, E) 15.0 wt.%, F) 18.0 wt.% and G) 25.0 wt.% (^) dispersed molybdate species and (*) MoO₃ crystallites.

On the other hand, the same phenomena of surface area and pore volume decreasing with increasing CeO₂ loading were observed (Table 3.2). However, the variations of these

physical properties were much less drastic than that involving MoO₃, suggesting that CeO₂ crystallites were relatively smaller.

Table 3.2: Textural properties of bulk and supported silica-alumina supported CeO₂ catalysts; all samples were activated at 650°C in air for 3h

Catalyst	CeO ₂ (wt.%)	S _{BET} (m ² /g)	Pore Volume (cm ³ /g)
Ce (1.0)/SiAl	1.0	365	0.594
Ce (2.0)/SiAl	2.0	358	0.589
Ce (3.0)/SiAl	3.0	361	0.593
Ce (6.0)/SiAl	6.0	342	0.540
Ce (8.0)/SiAl	8.0	316	0.488
Ce (12.0)/SiAl	12.0	322	0.508
Ce (15.0)/SiAl	15.0	295	0.468
CeO ₂ [♦]	100	48.3	0.156

♦ CeO₂ obtained by calcining cerium (III) nitrate tetrahydrate in air at 650 °C for 3h

Fortunately, these crystallites could be seen through XRD, already at quite low loading, i.e. 3 wt. %, as evident from Fig.3.2, which shows the presence of diffraction peaks that are ascribed to bulk CeO₂ crystallites (shown with (^) (JCPDS No. 34-0394)) [40]. In addition, there was no interaction between the incorporated Ce species and the SiAl support [41,42]. Krause et al [41] have reported that cerium silicate was formed only if Ce/SiO₂ was reduced by hydrogen at 800 °C in the presence of Rh. Similarly, Shyu et al [42] have reported that the formation of CeO₂ monolayers on Al₂O₃ was ascribed to the accommodation of cerium ions in the surface vacancies inherent in the defective spinel structure assumed by the support, leading to the formation of species easily reducible at 600 °C to small crystallite of cerium aluminate, which could not be detected by XRD. The low affinity or interaction among CeO₂ and SiO₂ or Al₂O₃ might be due to the high redox ability of CeO₂ [43].

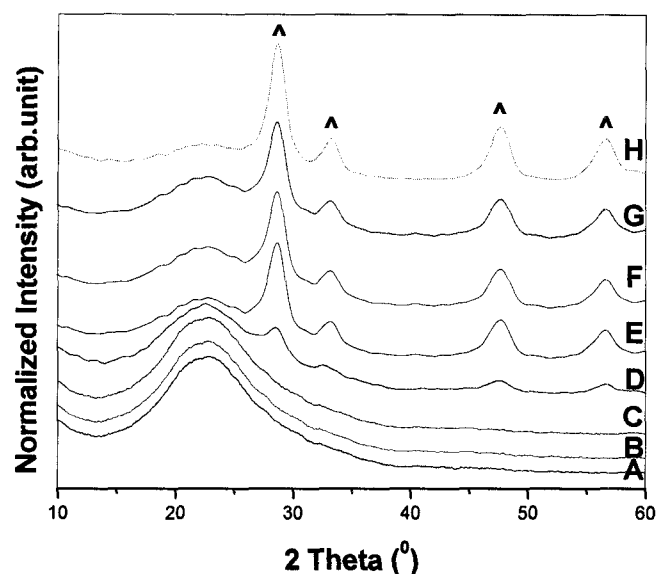


Fig.3.2: X-ray diffraction patterns of silica-alumina supported CeO₂ catalysts with different CeO₂ loading, A) 1.0 wt.%, B) 2.0 wt.%, C) 3.0 wt.%, D) 6.0 wt.%, E) 8.0 wt.%, F) 12.0 wt.% and G) 15.0 wt.% (^) Reflections due to bulk CeO₂ phase

Table 3.3 reports the catalytic performances of the MoO₃/SiAl catalysts. Since these catalysts were tested in conditions where thermal cracking was also present, silica-alumina (support) based extrudates were used as a reference catalyst tested in the same reaction conditions as the mono-component or bi-component catalysts.

Table 3.3: Catalytic activity of mono-component silica-alumina supported MoO₃ with various MoO₃ loadings in the TCC of n-hexane ^a

Catalyst	Silica-alumina	Mono-component MoO ₃ (x)/silica-alumina				
	(x): MoO ₃ Loading (wt%)	0.00	2.0	7.0	12.0	18.0
Conversion, C ₁ (wt%)	50.4	52.1	55.2	56.8	57.8	60.4
Product Selectivity, S ₁ (wt%)						
C ₁ -C ₄ alkane	12.9	14.6	14.5	15.1	15.1	15.6
C ₅ ⁺ naphthenes	3.10	3.36	4.64	5.29	5.46	5.93
C ₂ ⁻ -C ₄ ⁻ olefins and diolefins	82.2	79.3	77.5	75.5	73.3	71.2
BTX aromatics	1.87	2.74	3.29	4.10	6.14	7.35

^a(C₁-C₄): Methane, Ethane, Propane, Butane, (C₂⁻-C₄⁻): Ethylene, Propylene, Butenes, Butadiene; (BTX): Benzene + Toluene +Xylene

Thus, increasing the loading of MoO₃ resulted in higher conversion of n-hexane, as also suggested by the higher surface acidity of MoO₃ (Table 3.4). It is worth noting that the generation of Brønsted acid sites following the incorporation of molybdenum oxide on the silica-alumina surface as reported elsewhere [10] results from the interactions between molybdate anionic species and different types of hydroxyl groups present on the support surface [23,44-45]. A careful assessment of Table 3.3 reveals that product selectivity toward BTX (Benzene-Toluene-Xylene) formation increased with samples up to 12.0 wt.% MoO₃ loading. However, at very high loadings where large crystallites of MoO₃ and Al₂(MoO₄)₃ appeared on the surface as suggested by both XRD and LRS, the selectivity to BTX aromatics and their precursors (C₅⁺ naphthenes) increased drastically, at the expense of light olefins and diolefins. This behaviour has been attributed in the past to the aromatization character of MoO₃, mainly the dehydrocyclization reactions of paraffins [46].

Table 3.4: Acid site density of silica-alumina supported mono-component and bi-component catalysts; all catalysts were activated at 650°C in air for 3h prior to surface acidity analysis

Catalyst	Acid Sites Density	
	mmol/g	μmol/m ²
Silica-alumina (SA)	0.538	1.28
MoO ₃ (12.0) /silica-alumina	0.784	2.39
CeO ₂ (6.0) /silica-alumina	0.494	1.45
MoO ₃ -CeO ₂ /silica-alumina [Ce]/[Mo] = 0.41	0.672	2.21

The catalytic performances of the CeO₂/SiAl are reported in Table 3.5. In general, since CeO₂ had mild basic properties [47], its effect was to gradually decrease the conversion with increasing loadings as shown in Table 3.5. The acid character of silica-alumina was not greatly affected upon the incorporation of cerium as revealed by surface acidity measurements reported in Table 3.4. This had been also observed by several researchers [48]: "... basic sites

were newly regenerated on the catalyst surfaces by the rare earth loading although the acid character of the catalyst was mostly not affected by the modification...”. The inhibition of olefin adsorption by loaded rare earth metal oxides was assumed to be the major cause of low aromatics formation. This is only the case with the highly dispersed ceria species. Similar effect produced by the newly incorporated “sorption” sites, which were capable of removing the carbenium ions, thus shortening their residence time on the acid sites, was also observed with Zn species in the isomerization of n-heptane [49]. However, when the CeO₂ was higher than 12.0 wt. %, the H-transfer capacity of this rare-earth metal oxide [50] finally changed the trend of the product formation, now towards higher production of aromatics.

Table 3.5: Catalytic activity of mono-component silica-alumina supported CeO₂ with various CeO₂ loadings in the TCC of n-hexane ^a

Catalyst (y): CeO ₂ , (wt%)	Mono-component CeO ₂ (y)/Silica-alumina						
	1.00	2.00	3.00	5.00	8.00	12.00	15.00
<i>Conversion, C_i (wt%)</i>	50.5	49.3	48.6	46.3	46.0	45.3	44.1
<i>Product Selectivity, S_i (wt%)</i>							
C ₁ -C ₄ alkane	12.6	12.5	12.80	14.5	14.0	14.3	14.5
C ₅ ⁺ naphthenes	3.73	3.43	3.62	3.61	4.17	4.76	5.33
C ₂ ⁻ -C ₄ ⁻ olefins and diolefins	81.0	81.7	79.6	76.4	76.1	75.1	73.8
BTX aromatics	2.62	2.39	4.02	5.42	5.74	5.87	6.41

^a For symbols see table 3.3

3.3.2. Bi-component co-impregnated MoO₃-CeO₂/SiAl catalysts

Up to [Ce]/[Mo] molar ratio of 0.41 in the co-impregnated catalysts, the product selectivity to BTX aromatics and their precursors (C₅⁺ naphthalenes) slightly decreased, while the selectivity to light olefins and diolefins significantly increased (Table 3.6). However, due to the increasing presence of the basic Ce containing species, the conversion gradually decreased. The maximum performance for light olefins was observed with the [Ce]/[Mo] molar ratio of 0.41. However, at much higher ratio, the opposite variation trend was observed instead, i.e. more aromatics and less olefins were formed. Therefore, within well-defined and quite broad

range of [Ce]/[Mo] molar ratio, the production of olefins was favoured at the expense of aromatics and their precursors.

Table 3.6: Catalytic activity of t bi-component silica-alumina supported mixed MoO₃-CeO₂ prepared by co-impregnation with various [Ce]/[Mo] Molar ratios, in the TCC of n-hexane ^a

Catalyst [Ce]/[Mo] Molar Ratio	Bi-component Mixed MoO ₃ -CeO ₂ /silica-alumina				
	0.13	0.30	0.41	0.59	0.88
(CeO ₂) ^b wt.%	(1.75)	(4.0)	(5.6)	(8.0)	(12.0)
Conversion, C _i (wt%)	62.5	58.3	57.7	54.8	53.3
Product Selectivity, S _i (wt%)					
C ₁ -C ₄ alkane	16.1	15.4	12.9	12.9	14.9
C ₅ ⁺ naphthenes	7.11	6.61	5.89	6.90	6.30
C ₂ ⁼ -C ₄ ⁼ olefins and diolefins	71.6	73.1	78.1	75.5	72.5
BTX aromatics	5.23	4.90	3.15	4.72	6.30

^a For symbols see table 3.3, ^b MoO₃ content was constant at 11.6 wt.% in all samples.

Analyzing the structure of surface species of supported bi-component MoO₃- CeO₂ catalysts is quite significant in order to explain the outstanding behaviour of these catalysts in the TCC of n-hexane, when compared to supported mono-component catalysts. However, it is essential to analyze the structure of the possible species that may be formed upon the simultaneous mixing Mo and Ce precursors without the presence of the support in order to use it as a guide for the analysis of the surface structural data of silica-alumina supported mixed MoO₃-CeO₂ catalysts. On the other hand, the phase distributions of unsupported and supported mixed oxide systems, are not necessarily similar since phase distribution may change as a result of the interactions with the support materials. Therefore, this approach should be only used with extreme caution especially in the case of supported materials. XRD patterns (Fig.3.3a) and laser Raman (Fig.3.4a) of unsupported bi-component MoO₃-CeO₂ catalysts prepared by co-precipitation, clearly confirmed the presence of cerium molybdenum having the structure of Ce₂Mo₄O₁₅, as identified in refs [51,52]. Fig.3.3a showed the reflections that are

characteristics of $Ce_2Mo_4O_{15}$ (shown with (+) (JCPDS No.30-0304)). While, Raman spectra (Figure 2.3b) showed the presence of strong bands at (ca. 949 and 936), and weak bands at (ca. 978, 917, 889, 781 and 365 cm^{-1}). These bands are believed to be that of cerium molybdenum compound [52,53]. It is also noteworthy to mention that the structural analysis (both XRD and LRS) of unsupported bi-component catalysts revealed the presence of MoO_3 phase along with cerium molybdenum phase. Moreover, the XRD patterns (Fig.3.3b) of silica-alumina supported MoO_3 - CeO_2 catalysts showed the presence of two main phases, the amorphous phase, characterized by the amorphous hump, due to the amorphous silica-alumina support and crystalline phases, MoO_3 and CeO_2 . In addition, the XRD patterns suggested that cerium molybdate compound is highly dispersed on the support surface since no diffraction peaks can be ascribed to cerium molybdate compound.

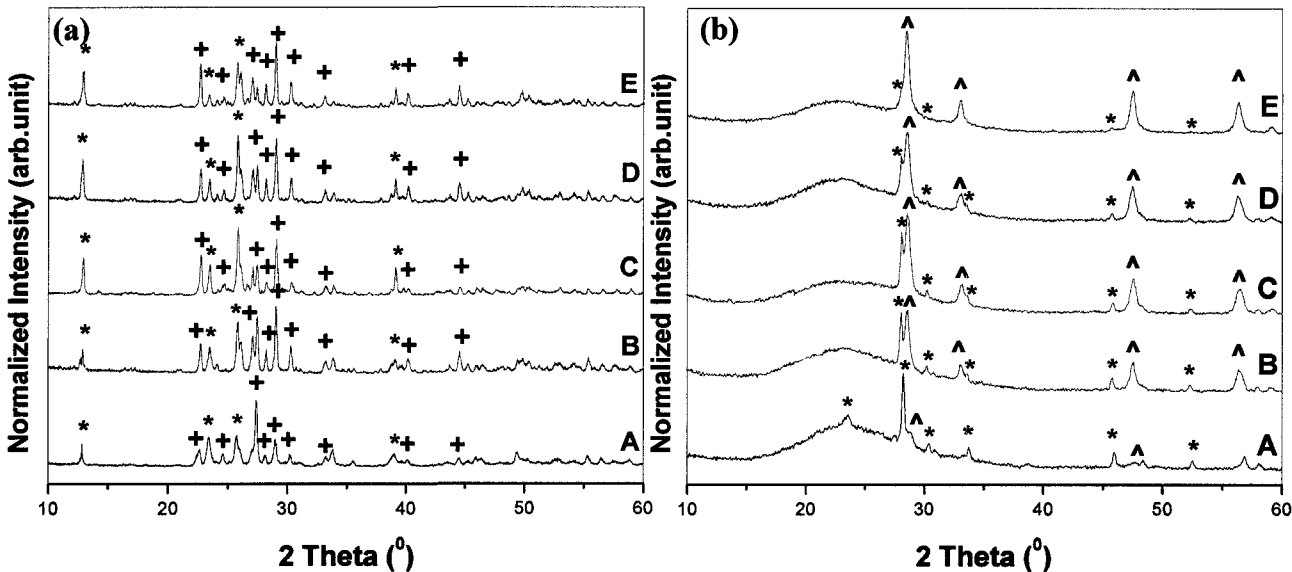


Fig.3.3: X-ray diffraction patterns of (a) unsupported MoO_3 - CeO_2 catalysts prepared by coprecipitation, with different [Ce]/[Mo] molar ratio, A) 0.13, B) 0.30, C) 0.41, D) 0.59 and E) 0.88, (+) Reflections due to Mo-Ce phase ($Ce_2Mo_4O_{15}$), and (*) Reflections due to MoO_3 crystallites, and (b) silica-alumina supported bi-component MoO_3 - CeO_2 catalysts prepared by co-impregnation, with different [Ce]/[Mo] molar ratio, A) 0.13, B) 0.30, C) 0.41, D) 0.59 and E) 0.88

These results were further supported by laser FT-Raman spectroscopy (Fig.3.4). Fig.3.4 clearly showed the presence of several Raman bands at (ca. 320, 380, 466, 825, 910, 955 and 995 cm^{-1}). Raman band observed at 466 cm^{-1} is assigned to bulk CeO_2 crystallites [53], while the simultaneous presence of Raman bands near 825 and 995 cm^{-1} are clearly indicative of bulk MoO_3 crystallites [38]. Furthermore, Raman bands observed at 320, 380, 910 and 955 cm^{-1} are most probably due to the vibration of cerium molybdate in which molybdenum atom is in an octahedral position (most probable structure is $\text{Ce}_2\text{Mo}_4\text{O}_{15}$ (Fig.3.4a)).

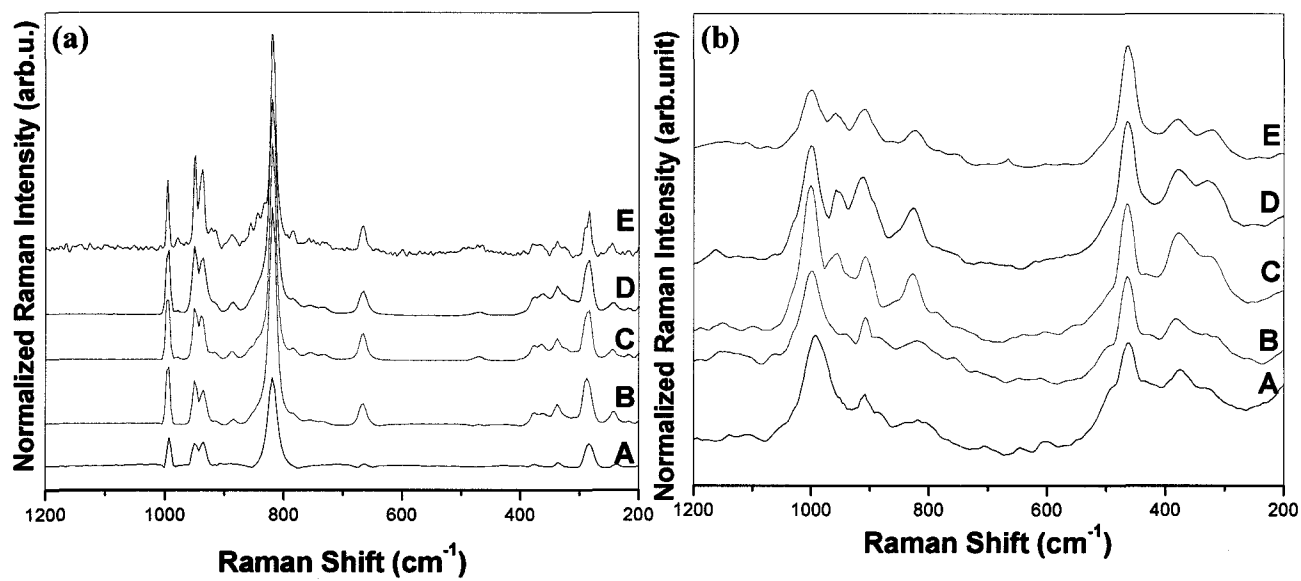


Fig.3.4: Raman spectra of (a) unsupported $\text{MoO}_3\text{-CeO}_2$ catalysts with different $[\text{Ce}]/[\text{Mo}]$ molar ratio, A) 0.13, B) 0.30, C) 0.41, D) 0.59 and E) 0.88, and (b) silica-alumina supported bi-component $\text{MoO}_3\text{-CeO}_2$ catalysts prepared by co-impregnation and with different $[\text{Ce}]/[\text{Mo}]$ molar ratio, A) 0.13, B) 0.30, C) 0.41, D) 0.59 and E) 0.88

To elucidate this further, we compare the Raman spectrum of unpromoted samples (i.e. silica-alumina supported MoO_3 with no cerium, MoO_3 loading of 12.0 wt.%), (Fig.3.1b) to that of promoted sample (i.e. silica-alumina supported $\text{MoO}_3\text{-CeO}_2$, $[\text{Ce}]/[\text{Mo}] = 0.41$), (Fig.3.4b). Raman bands at 320, 380 and 910 cm^{-1} were not observed in the Raman spectrum of

unpromoted sample while it was clearly observed in the Raman spectrum of promoted samples. In addition to that, Raman spectrum of unpromoted sample shows the presence of ill-defined broad Raman band centered at ca. 966 cm^{-1} , however this band became more resolved and shifted to 955 cm^{-1} in the promoted sample. Therefore, the only possible assignment for these bands is that they are due to the vibration of cerium molybdate species. Table 3.7 reports the catalytic performance of the bi-component catalysts (i.e. catalysts with $[\text{Ce}/[\text{Mo}] = 0.41)$ obtained by two-step impregnation of MoO_3 and CeO_2 into the silica-alumina support. None of these catalysts showed product selectivities to light olefins as high and those to aromatics as low, as the corresponding co-impregnated samples (Tables 3.6 and 3.7). In addition, when CeO_2 was incorporated first and the quite massive loading of MoO_3 was done after, the resulting catalysts were not as selective to light olefins as the samples resulting from the sequential impregnation. Thus, the following sequence of decreasing catalytic performance (i.e. desired production of light olefins and undesired formation of aromatics) was obtained:

(most active) $\text{CeMo}/\text{SiAl} > \text{Mo} \rightarrow \text{Ce}/\text{SiAl} > \text{Ce} \rightarrow \text{Mo}/\text{SiAl}$ **(least active)**

Table 3.7: Catalytic activity of bi-component silica-alumina supported mixed MoO_3 - CeO_2 based catalysts ($[\text{Ce}]/[\text{Mo}] = 0.41$) prepared by two-step impregnation method (sequential and reverse sequential impregnation) in the TCC of n-hexane ^a

Catalyst Preparation Method	Mo → Ce/SiAl	Ce → Mo/SiAl
	Sequential Impregnation (Mo → Ce)	Reverse Sequential Impregnation (Ce → Mo)
$[\text{Ce}]/[\text{Mo}] = 0.41$ ($\text{CeO}_2 = 5.6 \text{ wt. \%}$) ^b		
Conversion, C_1 (wt.%)	59.4	55.5
Product Selectivity, S_i (wt.%)		
C_1 - C_4 alkane	14.1	15.5
C_5^+ naphthenes	8.30	7.94
C_2^- - C_4^- olefins and diolefins	71.7	69.3
BTX aromatics	5.90	7.30

^a For symbols see table 2.3, ^b MoO_3 content was constant at ca. 11.6 wt.% in all samples

Fig.3.5 and 3.6 show the XRD patterns and Raman spectra of silica-alumina supported bi-component prepared by two-step impregnation, respectively. It is clearly shown that the population of bulk MoO_3 crystallites over the dispersed molybdate species appear to increase drastically with catalysts prepared by two-step impregnation. Catalysts prepared by sequential impregnation in which Mo was incorporated first followed by subsequent addition of Ce precursors into the support indicated that the molybdate dispersion was drastically reduced. XRD patterns (Fig.3.5) revealed the presence of more reflections that are ascribed to MoO_3 and $\text{Al}_2(\text{MoO}_4)_3$ crystallites, while Raman spectra (Fig.3.6) showed the presence of clear Raman bands that are unambiguously assigned to MoO_3 crystallites. On the contrary, when Ce was incorporated prior to Mo, Ce deposited on the support as segregated CeO_2 . This strongly implies that the silica-alumina did not undergo any modifications that might play a role in influencing the subsequent addition of Mo. In fact, when Mo was incorporated later on, it was poorly dispersed on the support, as clearly demonstrated by the presence of more intense MoO_3 crystallite peaks, which indicate the presence of more ordered MoO_3 crystallites as shown in the XRD patterns and Raman spectra of catalysts obtained by reverse sequential impregnation (Fig.3.5 and 3.6, respectively).

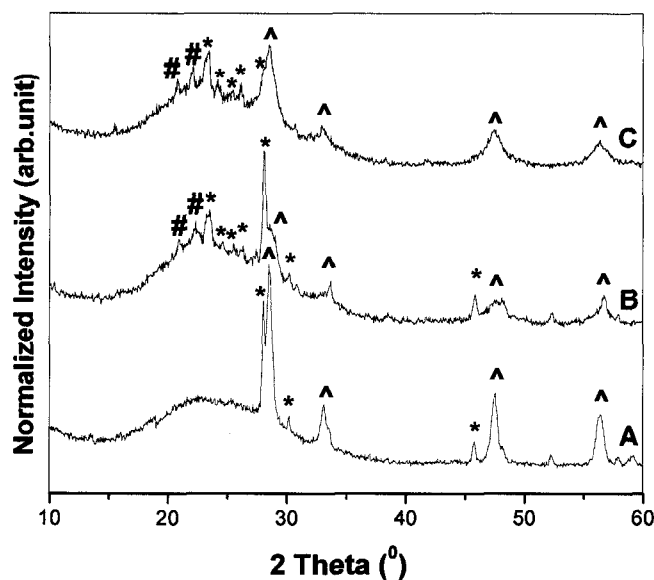


Fig.3.5: X-ray diffraction patterns of silica-alumina supported bi-component catalysts ($[\text{Ce}]/[\text{Mo}] = 0.41$), with different preparation methods, A) co-impregnation (MoCe/SiAl), B) Sequential Impregnation (Mo \rightarrow Ce/SiAl), and C) Reverse Sequential Impregnation (Ce \rightarrow Mo/SiAl), (*) Reflections due MoO_3 , (#) Reflections due to $\text{Al}_2(\text{MoO}_4)_3$ and (^) Reflections due to CeO_2 crystallites

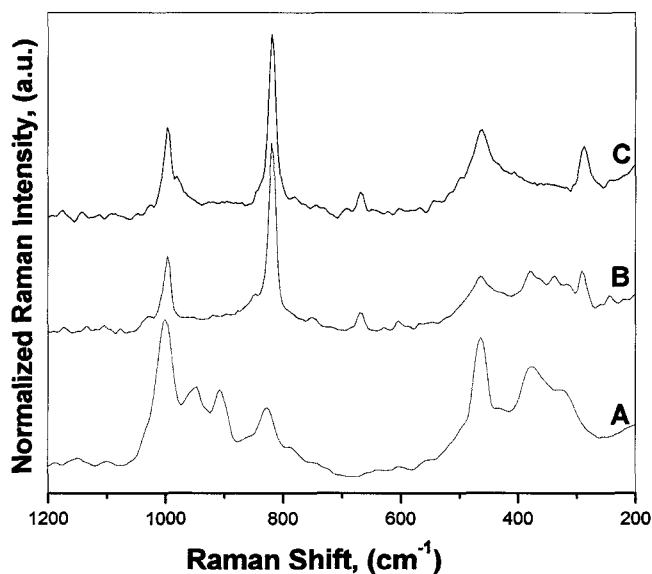


Fig.3.6: Raman spectra of silica-alumina supported bi-component catalysts ($[\text{Ce}]/[\text{Mo}] = 0.41$), with different preparation methods, A) co-impregnation (MoCe/SiAl), B) Sequential Impregnation (Mo \rightarrow Ce/SiAl), and C) Reverse Sequential Impregnation (Ce \rightarrow Mo/SiAl)

Based on the catalytic activity and surface structural analysis of bi-component MoO₃- CeO₂ catalysts prepared by different methods, the following points can be deduced:

- a) The sequential loadings of metal oxides exceeding the monolayer coverage had the tendency to hinder the catalytic effect of the first metal oxide on the resulting bi-component catalysts.
- b) The formation of the probably labile cerium molybdate compound (in the co-impregnated and to a lesser extent, in the sequentially loaded Mo → Ce) resulted in the coupling of a Mo active site with a Ce one. This interpretation coincided with the XRD and LRS observations which led to the following sequence of decreasing dispersion of surface molybdate species (or increasing segregation of MoO₃ as large crystallites):

(most dispersed) CeMo/SiAl > Mo → Ce/SiAl > Ce → Mo/SiAl **(least dispersed)**

- c) Finally, as evidenced by the difference in behaviour between these bi-component catalysts and the similarity of the previously shown sequences of dispersion of molybdate species and catalytic performance, in the co-impregnated catalysts whose loadings were reasonably low (ex: [Ce]/[Mo] molar ratio of 0.41), the coupled active sites were predominantly located at the most external surface of the catalyst particles (i.e. on top of the bulk MoO₃ layers), so that they were fully accessible to reactant molecules.

3.4. CONCLUSION

The loadings and the chemical states of metal oxides incorporated separately had significant effects on the catalytic activities of the resulting mono-component catalysts. Addition of cerium to molybdenum had a favourable effect on the production of light olefins in the TCC of n-hexane up to a certain level of cerium loading. In fact, high loadings of

molybdenum and/or cerium favoured the formation of aromatics, instead. The catalytic performance of the bi-component catalysts also depended significantly on the incorporation methods. It was found that the co-impregnation of MoO_3 and CeO_2 , which led to the highest production of light olefins, corresponded to the formation of (surface) cerium molybdate to the highest extent, i.e. to the ideal coupling of active sites. On the other hand, the catalysts prepared by the two-step impregnation methods (sequential and reverse sequential impregnation) showed much lower catalytic performance due to low Mo-Ce interactions as suggested by an important segregation of the active phases, mostly MoO_3 .

3.5. ACKNOWLEDGEMENTS

Financial support from NSERC (Natural Science and Engineering Research Council of Canada) and Valeo Management are acknowledged.

3.6. AUTHOR'S NOTES AND SIGNIFICANCE OF PAPER TO THESIS

This work on the synthesis, characterization and catalytic activities was the first article to be published in the literature on amorphous silica-alumina supported MoO_3 - CeO_2 . This study has shown that supported bi-oxide are catalytically active and selective to light olefins under the Thermo-Catalytic Cracking conditions. Our studies have also determined that metal loadings, calcination temperature, preparation methods, and more importantly nature of the support, play significant roles in influencing the physico-chemical properties and subsequently catalytic activities.

The following chapters present a continuation toward understanding and further developing the supported bi-oxide configuration. It was clear that the nature of the support plays the most significant role in influencing catalytic activities. Amorphous silica-alumina failed to maintain a high dispersion of impregnated Mo and Ce species, and thus resulted in

low catalytic activities. In the next chapter, we will be exploring another potential support for the TCC catalysts, which is transition alumina. Although, transition alumina is widely used in many industrial applications, it is only limited to low temperature reactions (< 600 °C). This is due to its poor thermal and hydrothermal stability, as well as low ability to disperse metal particles at high calcination temperature. Therefore, in the next upcoming chapters (IV-VII) these drawbacks will be addressed thoroughly.

3.7. REFERENCES

- [1] A. Chauvel, G. Lefebvre, in: *Petrochemical Processes*, Vol. 1 ,Technip, Paris, (1989), pp. 117-165.
- [2] D.A. Hunt, in: *Handbook of Petroleum Refining Processes*, 2nd ed., ed. R.A. Meyers, McGraw Hill, Boston, (1997) pp. 3.101-3.112.
- [3] R. Le Van Mao, Concordia University, US Patent 4, 732, 881 (1988).
- [4] R. Le Van Mao, S. Melancon, C. Gauthier-Campbell, P. Kletnieks, *Catal. Lett.* **73** (2001) 181.
- [5] R. Le Van Mao, and N. Al-Yassir, 18th *North American Catalysis Society Meeting*, Cancun, Mexico, (June 1-6, 2003), p. 367.
- [6] R. Le Van Mao, N.T. Vu, N. Al-Yassir and J. Monnier, *Novel Processes for Refining. Syn Fuels and Petrochemicals Congress, at AChemAMERICA*, Mexico City, Mexico (April 12-15, 2005).
- [7] R. Le Van Mao, N-T. Vu, N. Al-Yassir, N. Francois, J. Monnier, *Top. Catal.* **37** (2006) 107.
- [8] R. Le Van Mao, *Micropor. Mesopor. Mater.* **28** (1999) 9.
- [9] S. Melancon, R. Le Van Mao, P. Kletnieks, D. Ohayon, S. Intem, M.A. Saberi, D.

- McCann, *Catal. Lett.* **80** (2002) 103.
- [10] N. Al-Yassir, R. Le Van Mao, and F. Heng, *Catal. Lett.* **100** (2005) 1
- [11] R. Le Van Mao, N. Al-Yassir and D. Nguyen, *Micropor. Mesopor. Mater.* **85** (2005) 176.
- [12] J. Haber, “*The role of Molybdenum in Catalysis*”, Climax Molybdenum Co., Ann Arbor, MI, 1981.
- [13] J. Handzlik, J. Stoch, J. Ogonowski, M. Mikolajczyk, *J. Mol. Catal. A: Chem.* **157** (2000) 237.
- [14] C. Louis, J.M. Tatibouet, and M. Che, *J. Catal.* **109** (1988) 354.
- [15] M. de Boer, A.J. van Dillen, D.C. Koningsberger, J.W. Geus, M.A. Vuurman, I.E. Wachs, *Catal. Lett.* **11** (1991) 227.
- [16] C. Song and X. Ma, *Appl. Catal. B: Environ.* **41** (2003) 207.
- [17] A. Trovarelli, *Catal. Rev.-Sci. Eng.* **38** (1996) 439.
- [18] J. Scherzer, *Catal. Rev.-Sci. Eng.* **31** (1989) 215.
- [19] P. Fornasiero, R. Di Monte, G. Ranga Rao, J. Kaspar, S. Meriani, A. Trovarelli, M. Graziani, *J. Catal.* **151** (1995) 168.
- [20] A. Trovarelli, C. de Leitenburg, G. Dolcetti, *CHEMTECH* **27** (1997) 32
- [21] JCPDS, X-ray Powder Data File, International Center for Diffraction Data, Pennsylvania, 1989.
- [22] S. Xiao, R. Le Van Mao, G. Denes, *J. Mater. Chem.* **5** (1995) 1251
- [23] H.H. Kung, in *Transition metal oxides, Stud. In Surf. Science and Catalysis*, Elsevier, Amsterdam (1989) p 83.
- [24] K.R. Reddy, T. Bhaskar, K. V.R. Chary, *Langmuir* **19** (2003) 10795.

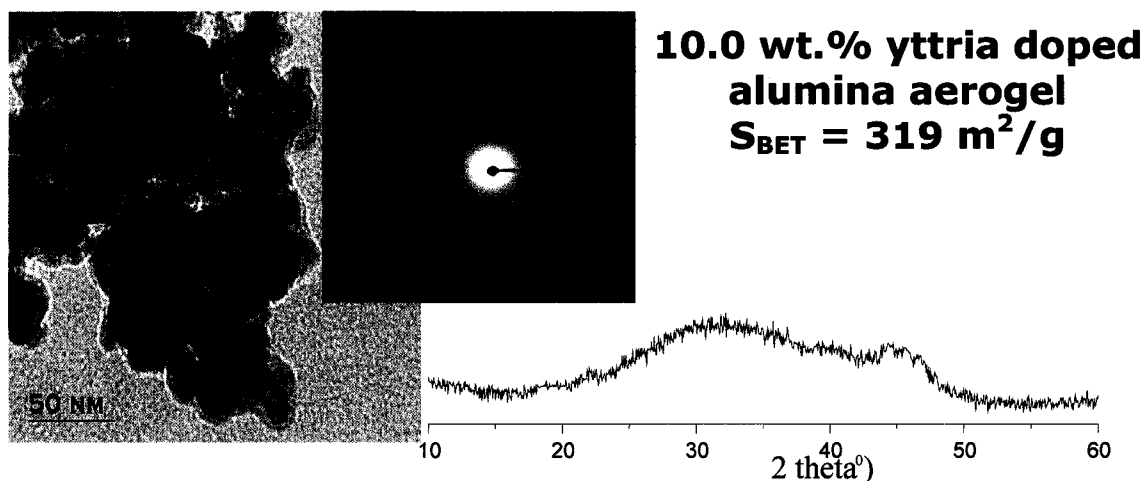
- [25] M.S.Rana, S.K.Maity, J.Ancheyta, G.M. Dhar, T.S.R. Prasada Rao, *Appl. Catal. A: Gen.* **268** (2004) 89.
- [26] Y. Xie, Y. Yang, *Adv. Catal.* **37** (1990) 1.
- [27] J. Sonnemans, and P. Mars, *J. Catal.* **31** (1973) 209.
- [28] Y. Liu, Y. Xie, G. Xie, Y. Tang, *Cuihua Xuebao* **6** (1985) 101.
- [29] H. Hu, I.E.Israel and S.R.Bare, *J.Phys.Chem.* **99** (1995) 1089.
- [30] J. Leyrer, B. Vielhaber, M.I. Zaki, Z. Shuxian, J. Weitkamp and H. Knozinger, *Mater. Chem. and Physics*, **13** (1985) 301.
- [31] C.V. Caceres, J.L.G. Fierro, J. Lazaro, A. Lopez Agudo, and J. Soria, *J. Catal.* **122** (1990) 113.
- [32] F.D. Hardcastle and I.E. Waschs, *J.Mol.Catal.* **46** (1988) 173.
- [33] S.Gong, H. Chen, W. Li, B. Li, *Catal. Commu.* **5** (2004) 621.
- [34] M.A.Banares, and I.E. Wachs, *J.Raman Spectrosc.* **33** (2002) 359.
- [35] G.Mestl, T.K.K.Srinivasan, *Catal.Rev. - Sci.Eng.* **40** (1998) 451.
- [36] A.N.Desikan, L.Huang, and S.T.Oyama, *J.Phys.Chem.* **95** (1991) 10050.
- [37] P. Dufresne, E. Payen, J.P. Grimblot, and J.P. Bonnelle, *J.Phys.Chem.* **85** (1981) 2344.
- [38] I.E.Wachs, *Catal.Today*, **27** (1996) 437.
- [39] L. Qu, W. Zhang, P.J. Kooyman and R. Prins, *J. Catal.* **215** (2003) 7.
- [40] M.M. Mohamed, *Appl. Catal. A: Gen.* **267** (2004) 135.
- [41] K.R. Krause, P. Schabes-Retchkiman and L.D. Schmidt, *J. Catal.* **134** (1992) 204.
- [42] J.Z. Shyu, W.H. Weber, H.S. Gandhi, *J.Phys.Chem.* **92** (1988) 4964.
- [43] T. Yamamoto, T. Matsuyama, T. Tanaka, T. Funabiki, and S. Yoshida, *Phys. Chem.*

Chem. Phys., **1** (1999) 2841.

- [44] S. Rajagopal, J.A. Marzari, and R. Miranda, *J. Catal.* **151** (1995) 192.
- [45] L. Wang, L. Tao, M. Xie, G. Xu, J. Huang and Y. Xu, *Catal. Lett.* **21** (1993) 35.
- [46] F. Solymosi and R. Barthos, *Catal. Lett.* **101** (2005) 235.
- [47] C. Morterra and G. Magnacca, *J.Chem.Soc., Faraday Trans.*, **92** (1996) 5111.
- [48] K. Wakui, K.I. Satoh, G. Sawada, K. Shiozawa, K.I. Matano, K. Suzuki, T. Hayakawa, K. Murata, Y. Yoshimura and F. Mizukami, in *Porous Materials in Environmentally Friendly Processes*, Ed. I. Kiricsi, G.Pal-Borbely, J.B. Nagy and H.G. Karge, *Studies in Surface Science and Catalysis*, Vol. 125, Elsevier Sc. (Amsterdam), (1999), 449.
- [49] M.A. Saberi, R. Le Van Mao, M. Martin and A.W.H. Mak, *Appl. Catal. A: Gen.* **214** (2001) 229.
- [50] X. Zhao, R.H. Harding, *Ind. Eng. Chem. Res.* **38** (1999) 3854.
- [51] J.C.J. Bart, N. Giordano, *J. Less Common Met.* **46** (1976) 17.
- [52] T.L. Barr, C.G. Fries, F. Cariati, J.C.J. Bart, N. Giordano, *J.Chem.Soc. Dalton Trans*, **9** (1983) 1825.
- [53] X.M. Lin, L.P.Li, G.S. Li, W.H. Su, *Mater.Chem.Phys.* **69** (2001) 236.

Chapter IV

Thermal Stability of Alumina Aerogel doped with Yttrium Oxide, used as a Catalyst Support for the Thermo-Catalytic Cracking (TCC) Process; An Investigation of its Textural and Structural Properties



Graphical Abstract: X-ray diffraction, TEM micrographs and electron diffraction pattern of 10.0 wt.% yttria doped alumina aerogel calcined at 750 °C for 3h

Published as:

N. Al-Yassir and R. Le Van Mao,

Applied Catalysis A: General **317** (2007) 275-283.

ABSTRACT

Undoped and yttria doped alumina aerogel are prepared by the (solution) sol-gel method using a supercritical drying technique. The doping concentrations are in the range of 2.5-20.0 wt.% Y_2O_3 , using yttrium (III) nitrate as a precursor. The effect of yttria doping on the structural and textural properties of alumina aerogel is investigated by BET surface area measurement, X-ray diffraction (XRD), TEM and ^{27}Al MAS NMR. This method of preparation of alumina aerogel provides the most important increase in surface area at 750 °C and up to 1000 °C, when compared to conventional alumina that is obtained via thermal dehydration of boehmite. These results show that the much smaller size of crystallites of alumina aerogel is quite efficient of retarding the sintering occurring at these high temperatures. Further improvements in thermal stability are obtained by incorporation of yttrium species during the aerogel preparation. The stabilizing effect goes through a maximum with a yttrium content of ca. 10 wt. %. The presence of yttrium significantly delays the lattice rearrangement into new phases, as normally experienced by the conventional alumina when the temperature increases. These yttrium species induce the formation of distorted tetrahedral Al sites. Such a binding effect of Y to Al is clearly detected by ^{27}Al MAS NMR at 750 °C already. However, at 1200 °C, even the doped aerogel cannot withstand the combined effect of sintering and α -phase transformation, so that extremely low surface areas corresponding to those of alumina α -phase and segregated Y- Al_2O_3 are obtained.

4.1. INTRODUCTION

Thermo-Catalytic Cracking (TCC) of petroleum feedstocks is a new emerging process for the production of light olefins (i.e. ethylene and propylene, with the yield of the latter intermediate being much higher than that obtained by the steam cracking [1-6]. This process was developed in response to the rapidly growing worldwide demand for propylene [7] and to the increasingly stringent environmental regulations that require low greenhouse gas emissions (i.e. CO₂). The market demand for propylene worldwide in the year 2000 was 51 million metric ton (mt), and it is expected that demand to grow up to 90 mt with an annual growth rate of about 4.5-5.5 % [8]. However, the current conventional technologies (i.e. SC and Fluid Catalytic Cracking (FCC)) cannot respond adequately to such rapid increase, since propylene is only produced as a co-product in these processes. The TCC process has been considered more advantageous than SC since it produces higher combined yields of ethylene and propylene with a propylene/ethylene product ratio close to 1.0, requires lower energy costs and is a more environmentally friendly process. This process, which uses supported mixed oxides containing catalysts, operates at relatively high temperature (i.e. 720 °C). Therefore, evaluating the thermal stability of the catalyst support is of paramount importance for the overall TCC catalytic activities.

Supported metal oxide catalysts are extensively used in the petroleum, chemical, and pollution control industries [9]. Their physicochemical and catalytic properties are highly influenced by several factors such as the amounts and nature of metal oxides, the preparation methods, the pH of impregnating solution, and the drying and calcination temperature [10]. However, the type of support used plays a vital role in influencing the structure and subsequently the catalytic performance of supported metal oxides [10,11]. Therefore, the

search for an appropriate support is considered as a crucial step. Ideally, an appropriate support should be able to improve the dispersion of active components, promote effective metal-support interactions, and retain the unique properties of the impregnated metals (i.e. surface acid-base, redox properties, etc). In addition, the support should possess high surface area, mechanical strength as well as be thermally and hydrothermally stable [12]. Transition γ -alumina, silica, amorphous silica-alumina, TiO_2 and ZrO_2 are some examples of catalyst supports used in the chemical industry and petrochemical industry. TiO_2 and ZrO_2 are quite unsuitable for industrial applications that require high temperature and high surface area, due to their low thermal stability, quite small surface area and high price [13]. Silica and amorphous silica-alumina as catalyst supports are quite attractive due to their high surface area. However, they do not have the ability to promote a high surface dispersion of impregnated metals, due to the low concentration of surface hydroxyl groups and low isoelectric point (IEP) [14]. This was in complete agreement with our earlier investigation of the performance of catalysts based on supported $\text{MoO}_3\text{-CeO}_2$ [6]. In fact, it was found that silica-alumina used as support showed weak metal-support interactions that might lead to the segregation of the active MoO_3 phase.

Conventional transition γ -alumina, which is obtained mainly via thermal dehydration of boehmite at 400-450°C [15], is by far the most widely used catalyst support [16]. This alumina shows various properties such as moderate surface area, good mechanical strength and limited concentration of defects in its crystalline structure [16]. However, the thermal and hydrothermal stability [16-18] remain the most significant drawbacks of γ -alumina in high temperature reactions requiring the presence of steam. At elevated temperature γ -alumina loses its surface area causing the sintering of surface active phases, which will consequently

degenerate the catalytic activity. It is believed that the loss of surface area of γ -alumina at high temperature is caused by the combination of two phenomena: sintering and phase transformation [19]. Sintering which is a process involving the decrease of surface energy of alumina particles, starts at as low as 600 °C, followed by structural transformations (sequence of phase transformations according to the γ -(δ)- θ - α sequence) (the existence of (δ) phase depends on the starting precursor and decomposition temperature) ending with the α -phase that occurs at temperatures above 1000 °C [13,16-19]. Many cations [13,16-22] such as La^{3+} , Ce^{4+} , Ba^{2+} , and Zr^{4+} incorporated by different methods have demonstrated a great influence in delaying or retarding the sintering and α -phase transformation of γ -alumina. On the other hand, alumina obtained via the solution-sol-gel method using a supercritical drying technique provides improved and controllable morphological and chemical properties (i.e. high porosity with large surface area, uniform particle size, etc) when compared to conventional γ -alumina [23-26]. These properties have shown further improvements upon the addition of dopants such as lanthanides [27,28] and other oxides [29-31] (i.e. SiO_2 , TiO_2 and ZrO_2).

In the present investigation, we have evaluated the suitability of using yttria doped alumina aerogel as a potential catalyst support for the TCC process. Y_2O_3 is considered as an interesting dopant, particularly for its application in high temperature ceramics. The effect of Y_2O_3 doping on the thermal stability of alumina aerogel has been investigated before [32,33], however to our knowledge there is no detailed investigation of the effect of yttria doping on the properties of alumina aerogel, and a wide range of yttria concentrations in the preparation, as well as, the utilization of various spectroscopic techniques of characterization. Therefore, the main objectives of the present study were to give a detailed investigation of the structural and textural properties of alumina aerogel and the effect of yttria doping on these properties at high

temperatures. To accomplish these goals, a systematic study was undertaken on the characterization of catalyst supports by various techniques such as BET surface area, XRD, TEM and ^{27}Al MAS NMR.

4.2. EXPERIMENTAL

4.2.1. Preparation of Catalyst Supports

The yttria doped alumina aerogel was prepared by a technique similar to that previously reported [32,33]. The precursors used were aluminum tri-sec-butoxide (Strem chemicals, 98 %) and yttrium (III) nitrate hexahydrate (Strem chemicals, 99.9 %), the latter replacing the more expensive yttrium acetylacetonate used in refs [32,33]. They were dissolved in 2-butanol (Aldrich), and methanol (Aldrich), respectively. Yttrium concentration was varied in order to have 2.5, 5.0, 10.0 and 20.0 wt.% of Y_2O_3 . Y_2O_3 - Al_2O_3 with different Y_2O_3 contents is noted as $x\text{Y}_2\text{O}_3$ - Al_2O_3 , where x is the Y_2O_3 content in wt %. The preparation procedures for undoped alumina aerogel were similar to that of yttria doped alumina aerogel, except no dopant was used. Conventional alumina, used for comparison purpose, was available commercially from Strem Chemicals and noted in this text as conventional Al_2O_3 . Before characterization, the various samples were calcined in air at 750, 1000, 1100 and 1200 °C for 3 h, unless specified otherwise.

4.2.2. Catalyst Supports Characterization

4.2.2.1. The specific surface areas and pore size distributions of the samples were determined by the BET method using nitrogen physisorption at 77 K. The measurements were carried out using Micromeritics ASAP 2000 apparatus. Samples were outgassed in vacuum for 4h at 220°C before N_2 physisorption. Specific surface areas were calculated according to Brunauer-Emmett-Teller (BET) method and the pore size distributions were obtained according to

Barret-Joyner-Halenda (BJH) method from the adsorption data. BET specific surface area results are within accuracy of $\pm 5.5 \text{ m}^2/\text{g}$.

4.2.2.2. X-ray Powder diffraction (XRD) was carried out on a Philips diffractometer equipped with a PW 1050/25 focusing goniometer, which had been automated with the VisX122D system from diffraction technologies. The Ni filtered $K\alpha$ radiation of Cu was used ($\lambda_{K\alpha 1} = 1.54051 \text{ \AA}$) and diffractometer was operated at 40kV and 20mA. The powder patterns were recorded in the step scanning mode from 10-60°(2 θ) at a detector angular speed of 0.3 °/min with a step size of 0.05° in order to reduce the background noise. The XRD phases present in the samples were identified with the help of the JCPDS (Joint Committee on Powder Diffraction Standards) powder data files [34].

4.2.2.3. Transmission Electron Microscopy (TEM) images and Electron Diffraction patterns were recorded using a JEOL JEM-2000 FX microscope operating at 80 KV equipped with a charged-coupled device (CCD)-camera (Gatan). Samples were mounted on a microgrid formvar/carbon supported on a 300 mesh copper grid (3mm in diameter) film by placing a few droplets of a suspension of the ground sample in ethanol (0.1 wt.% solution) on the grid, followed by drying under ambient conditions.

4.2.2.4. ^{27}Al Magic Angle Spinning Nuclear Magnetic Resonance (MAS NMR) measurements were carried out in a Bruker NMR spectrometer model DSX-300 (magnetic field 7.04 T). ^{27}Al MAS NMR spectra were obtained at the frequency of 78.23 MHz with a 20° pulse length of 2 μs and 1 s delay between pulses and a spectral range of 40-75 kHz. The samples were spun at 14 KHz in N_2 using 4 mm ZrO_2 rotors, and typically 540 FIDs were collected for each sample. The chemical shifts were measured relative to external $\text{Al}(\text{OH})_6^{3+}$ standard with an accuracy of ± 0.5 ppm. Prior to measurement, the samples were dehydrated by evacuation to a pressure

below 5 μm Hg in a Micromeritics ASAP-2000 instrument (BET apparatus) at 200 °C overnight. The samples were then transferred in a helium atmosphere to a moisture-free N_2 atmosphere glove box and packed in sealed tubes. Then, they were transferred from sealed tubes and packed into ZrO_2 rotors.

4.3. RESULTS AND DISCUSSION

The main results of our investigations on the properties of the alumina materials using X-ray diffraction, TEM and BET surface area measurement techniques are given in the following. XRD (Figures 4.1-4.4 and Table 4.1) clearly showed that the conventional alumina underwent phase transformation, when heated at high temperatures, in accordance with the following sequence: $\gamma \rightarrow \theta \rightarrow \alpha$. This was in complete agreement with previous investigations [18,21,35]. In fact, conventional alumina upon calcination at 750 °C showed the presence of γ -phase which was transformed to both θ - and α -phase at 1000 °C. Calcination at 1200 °C resulted in the formation of the α -phase solely, suggesting that α -phase (corundum), being the most thermodynamically stable phase, readily occurred at 1000 °C and reached completion at 1200 °C [21,35]. Undoped alumina aerogel showed only the γ -phase at 750°C (Table 4.1). Broad diffraction peaks of this crystalline phase (Figure 4.1) indicated that the undoped alumina aerogel was not well crystallized. However, at 1000 °C undoped alumina aerogel showed the presence of γ - and traces of θ -phase, without any signs of α -phase (Fig.4.2). Further calcination to 1100 °C resulted in the transformation of γ -phase into θ -phase with some traces of α -phase, the latter became the dominant phase at 1200 °C (Fig.4.3).

Table 4.1: X-ray diffraction pattern results of the conventional alumina, undoped and yttria doped alumina aerogel with various yttria loadings ^(a)

Sample	Calcination condition			
	750 °C for 3 h.	1000 °C for 3 h.	1100 °C for 3 h.	1200 °C for 3 h.
Conventional alumina (0.76) ^(b) (0.253) ^(c)	γ -Al ₂ O ₃	θ -, and α -Al ₂ O ₃	α -Al ₂ O ₃ + traces of θ -phase	α -Al ₂ O ₃
Undoped alumina aerogel (0.34) ^(b) (1.150) ^(c)	γ -Al ₂ O ₃	γ -Al ₂ O ₃ + traces of θ -phase	θ -Al ₂ O ₃ + traces of α -phase	α -Al ₂ O ₃
2.5 wt.% Y ₂ O ₃ -Al ₂ O ₃ (0.35) ^(b) (0.790) ^(c)	Amorphous + traces of γ -phase	γ -Al ₂ O ₃	YAlO ₃ + traces of θ -Al ₂ O ₃	YAlO ₃ + α -Al ₂ O ₃
5.0 wt.% Y ₂ O ₃ -Al ₂ O ₃ (0.33) ^(b) (0.975) ^(c)	Amorphous + traces of γ -phase	γ -Al ₂ O ₃	YAlO ₃ + traces of θ -Al ₂ O ₃	YAlO ₃ + α -Al ₂ O ₃
10 wt.% Y ₂ O ₃ -Al ₂ O ₃ (0.34) ^(b) (0.906) ^(c)	Amorphous	γ -Al ₂ O ₃	YAlO ₃ + traces of θ -Al ₂ O ₃	YAlO ₃ + α -Al ₂ O ₃
20 wt.% Y ₂ O ₃ -Al ₂ O ₃ (0.36) ^(b) (0.617) ^(c)	Amorphous	Amorphous + traces of γ -Al ₂ O ₃	YAlO ₃ + traces of θ -Al ₂ O ₃	YAlO ₃ + α -Al ₂ O ₃

^(a) γ -Al₂O₃ (JCPDS No. 10-425), θ -Al₂O₃ (JCPDS No. 35-0121), α -Al₂O₃ (JCPDS No. 10-173), YAlO₃ (JCPDS No. 16-219 or 38-222). ^(b) Density in g/cm³. ^(c) Pore volume in cm³/g

Yttria doped alumina aerogel with different yttria loadings (2.5-20.0 wt.%), when calcined at 750 °C, showed the presence of amorphous structure for all samples with some traces of γ -Al₂O₃ in samples with lower loadings (2.5-5.0 wt.% Y₂O₃, Table 4.1). In fact, as the yttria loading increased up to 20.0 wt.%, the hump that was characteristic of an amorphous structure increased in intensity (Fig.4.1). However, samples of yttria doped alumina aerogel with yttria loading in the range of 2.5-10.0 wt.%, when calcined at 1000 °C, showed the presence of only γ -Al₂O₃. At that temperature, the sample containing 20.0 wt. % yttria, still showed the amorphous alumina which coexisted with γ -Al₂O₃. There was no diffraction peak that could be attributed to either θ - or α -phase, thus indicating clearly an improved thermal stability (Fig.4.2). Further calcination at 1100 °C resulted in the appearance of θ -phase and that

of yttria-alumina phase (YAlO_3) as evidenced by the presence of its characteristic diffraction peaks (Fig.4.3). Figure 4.3 also showed that as the yttria loading increased, the diffraction peaks of YAlO_3 crystalline phase became sharper indicating that the gels were well crystallized in this phase. It was quite clear that at 1100 °C, although yttrium ions delayed the formation of $\alpha\text{-Al}_2\text{O}_3$, they did cause the formation of some Y-alumina phase. Finally, when yttria doped alumina aerogel samples were calcined at 1200 °C, both $\alpha\text{-Al}_2\text{O}_3$ and YAlO_3 were readily detected. Comparison between the XRD patterns of yttria doped alumina aerogel at 1100 °C (Fig.4.3) and 1200 °C (Fig.4.4), showed that the θ -phase that was observed at 1100 °C, was completely transformed into α -phase at 1200 °C. Moreover, the YAlO_3 was better crystallized at 1200 °C, as evidenced by the sharpness of XRD peaks.

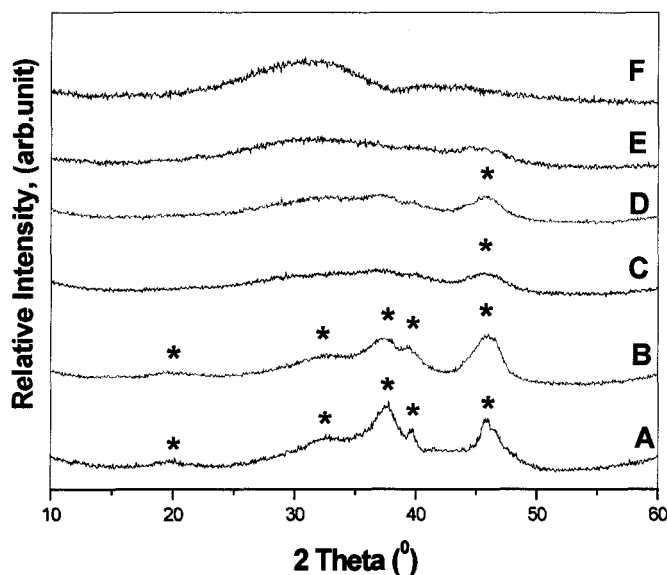


Fig.4.1: X-ray diffraction patterns of samples calcined at 750 °C for 3 h. (A) conventional Al_2O_3 , (B) undoped alumina aerogel, (C) 2.5 $\text{Y}_2\text{O}_3\text{-Al}_2\text{O}_3$, (D) 5.0 $\text{Y}_2\text{O}_3\text{-Al}_2\text{O}_3$ (E) 10.0 $\text{Y}_2\text{O}_3\text{-Al}_2\text{O}_3$, and (F) 20.0 $\text{Y}_2\text{O}_3\text{-Al}_2\text{O}_3$. (*) $\gamma\text{-Al}_2\text{O}_3$. * $\gamma\text{-Al}_2\text{O}_3$

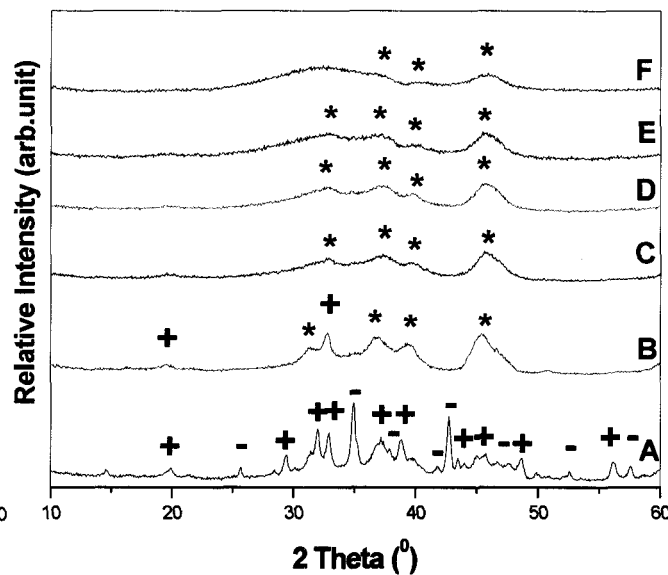


Fig.4.2: X-ray diffraction patterns of samples calcined at 1000 °C for 3 h. (A) conventional Al_2O_3 , (B) undoped alumina aerogel, (C) 2.5 $\text{Y}_2\text{O}_3\text{-Al}_2\text{O}_3$, (D) 5.0 $\text{Y}_2\text{O}_3\text{-Al}_2\text{O}_3$ (E) 10.0 $\text{Y}_2\text{O}_3\text{-Al}_2\text{O}_3$, and (F) 20.0 $\text{Y}_2\text{O}_3\text{-Al}_2\text{O}_3$. (*) $\gamma\text{-Al}_2\text{O}_3$, (+) $\theta\text{-Al}_2\text{O}_3$, and (-) $\alpha\text{-Al}_2\text{O}_3$

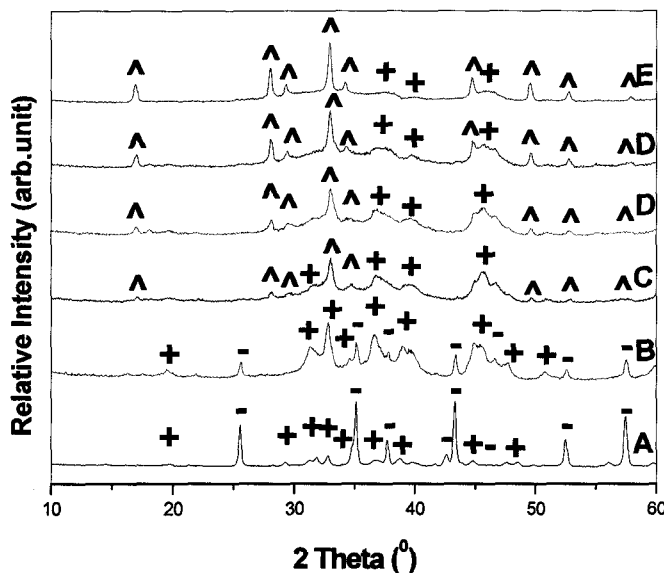


Fig.4.3: X-ray diffraction patterns of samples calcined at 1100 °C for 3 h. (A) conventional Al_2O_3 , (B) undoped alumina aerogel, (C) 2.5 $\text{Y}_2\text{O}_3\text{-Al}_2\text{O}_3$, (D) 5.0 $\text{Y}_2\text{O}_3\text{-Al}_2\text{O}_3$ (E) 10.0 $\text{Y}_2\text{O}_3\text{-Al}_2\text{O}_3$, and (F) 20.0 $\text{Y}_2\text{O}_3\text{-Al}_2\text{O}_3$. (+) $\theta\text{-Al}_2\text{O}_3$, (-) $\alpha\text{-Al}_2\text{O}_3$, and (^) YAlO_3

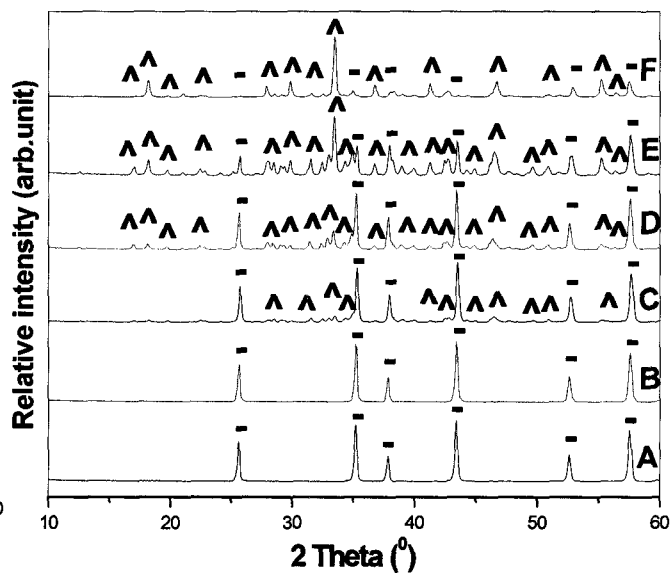


Fig.4.4: X-ray diffraction patterns of samples calcined at 1200 °C for 3 h. (A) conventional Al_2O_3 , (B) undoped alumina aerogel, (C) 2.5 $\text{Y}_2\text{O}_3\text{-Al}_2\text{O}_3$, (D) 5.0 $\text{Y}_2\text{O}_3\text{-Al}_2\text{O}_3$ (E) 10.0 $\text{Y}_2\text{O}_3\text{-Al}_2\text{O}_3$, and (F) 20.0 $\text{Y}_2\text{O}_3\text{-Al}_2\text{O}_3$. (-) $\alpha\text{-Al}_2\text{O}_3$, and (^) YAlO_3

TEM images and electron diffraction patterns of conventional alumina, undoped and yttria doped alumina aerogel (10.0 wt.% Y_2O_3) calcined at 750 °C for 3 h. are shown in Fig.4.5 (A-C) and (A* -C*), respectively. The TEM images of conventional alumina and alumina aerogel revealed important differences between them in terms of morphology and crystallinity. In fact, the TEM micrograph of conventional alumina (Fig.4.5A), compared to that of the undoped alumina aerogel (Fig.4.5B), showed the presence of large alumina sheets, which appeared to be well structurally organized and crystallized. Moreover, the electron diffraction pattern of conventional alumina (Fig.4.5A*) indicated the presence of diffuse rings with noticeable diffraction patterns, while the diffraction pattern observed for undoped alumina aerogel (Fig.4.5B*) was much weaker suggesting a lower degree of crystallinity. On the other hand, the TEM micrograph of alumina aerogel doped with 10.0 wt.% yttria exhibited an amorphous structure (Fig.4.5C) and its electron diffraction pattern (Fig.4.5C*) showed only diffuse rings with no clear diffraction pattern (i.e. another indication for amorphous material). Further, the TEM image and electron diffraction pattern of yttria doped alumina aerogel with 10.0 wt.% Y_2O_3 , this time calcined at 1000 °C for 3 h (Fig.4.5D and Fig.4.5D*, respectively), revealed that there was a change in the morphology and crystallinity when compared to the ones calcined at 750 °C (Fig.4.5C and Fig.4.5C*), presumably due to the formation of lowcrystallinity γ -phase as indicated by XRD results (Fig.4.2E and Table 4.1). In fact, the electron diffraction pattern of this material (Fig.4.5D*) showed the presence of diffuse rings with very weak diffraction pattern, clearly supporting that the γ -phase formed had a low degree of crystallinity. When calcined at 1100 °C for 3 h, the same sample showed, however, the presence of well-defined crystalline phases (Fig.4.5E and Fig.4.5E*). The

crystalline material exhibited diffraction patterns, which might be attributed to crystalline YAlO_3 and $\theta\text{-Al}_2\text{O}_3$ phase, as also indicated by previous XRD data (Fig.4.3E and Table 4.1).

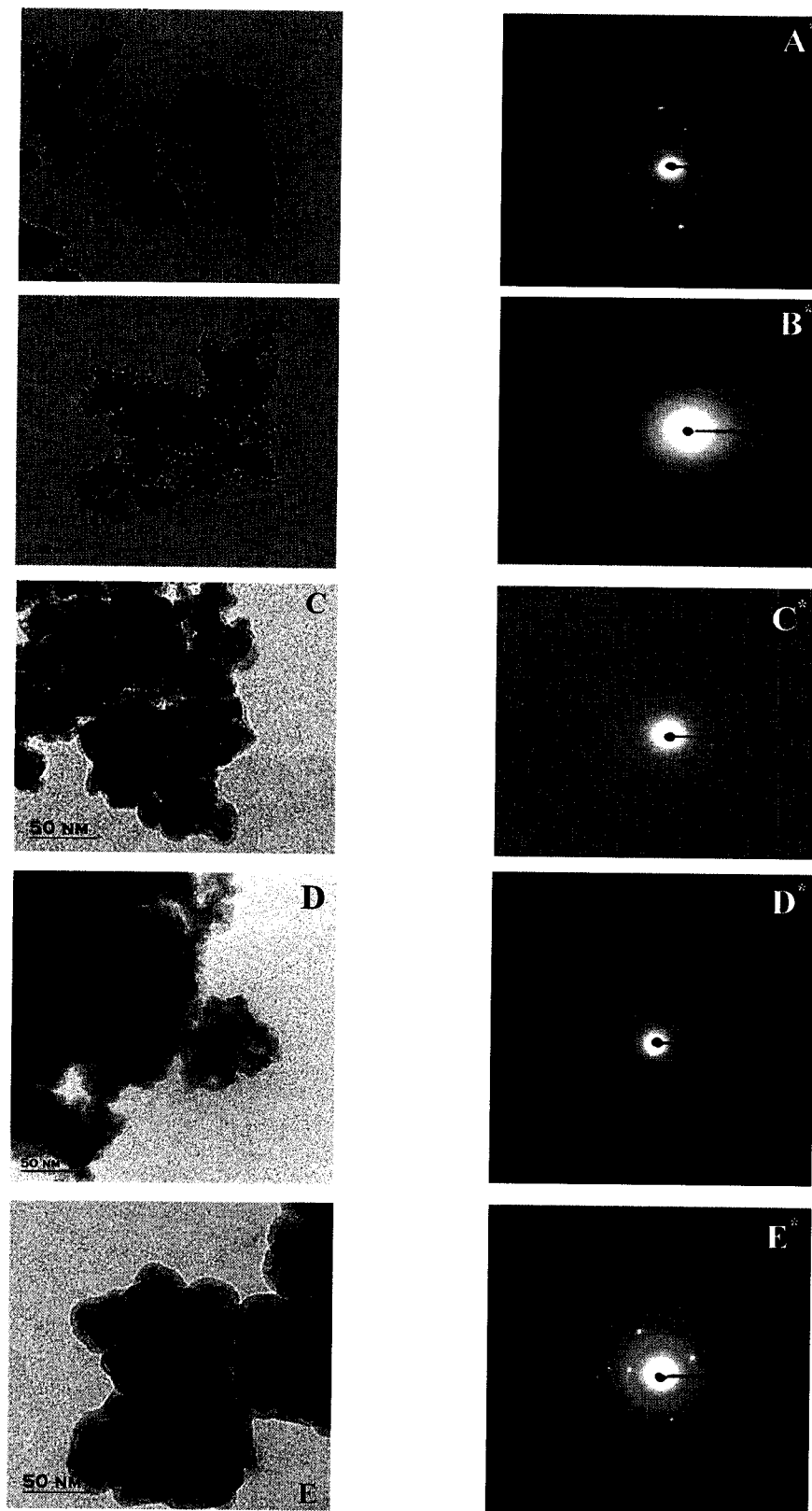


Fig.4.5: TEM micrographs and electron diffraction patterns (represented by (*)) of samples calcined at 750 °C for 3 h. (A) conventional Al_2O_3 , (B) undoped alumina aerogel, (C) 10 Y_2O_3 - Al_2O_3 , (D) and (E) are 10.0 Y_2O_3 - Al_2O_3 , calcined at 1000 °C and 1100 °C, respectively

Changes in the BET specific surface area of conventional alumina, undoped and yttria doped alumina aerogel samples calcined at different temperature for 3h are shown in Table 4.2 Up to 1100 °C, undoped and yttria doped alumina aerogels all exhibited much higher specific surface area when compared to conventional alumina. However, the most important effect leading to surface area “conservation” was due to the sol-gel technique, which provided values of surface area, up to 1100 °C, more than double than those of conventional alumina. Table 4.2 also showed that the incorporation of yttria to alumina aerogel during its preparation has caused a positive change in the specific surface area depending on the yttria loading. In fact, doped alumina aerogel with yttria loading between 5.0-10.0 wt.% exhibited the maximum specific surface area. This value decreased with higher loading (i.e. 20 wt.% Y₂O₃). It is noteworthy that this was observed irrespective of calcination temperature.

Table 4.2: Changes in the BET specific surface area of conventional alumina, undoped and yttria doped alumina aerogel as a function of calcination temperature for 3 h

Sample	BET Specific Surface Area, m ² /g			
	750°C (Δ) ^(a)	1000°C (Δ) ^(a)	1100°C (Δ) ^(a)	1200°C
Conventional Al ₂ O ₃	116 (0)	51 (0)	20 (0)	7
Undoped alumina aerogel	277 (139)	100 (96)	62 (210)	11
2.5 wt.% Y ₂ O ₃ -Al ₂ O ₃	300 (159)	123 (141)	51 (155)	9
5.0 wt.% Y ₂ O ₃ -Al ₂ O ₃	331 (185)	145 (184)	79 (295)	10
10.0 wt.% Y ₂ O ₃ -Al ₂ O ₃	319 (175)	136 (167)	73 (265)	11
20.0 wt.% Y ₂ O ₃ -Al ₂ O ₃	254 (119)	86 (67)	35 (75)	9

^(a) % Increase in specific surface area when compared to conventional alumina

Fig.4.6 that reported the loss of specific surface area after 50 h of calcination at various temperatures, clearly showed the higher thermal stability of yttria doped alumina aerogel compared to convention alumina. For instance, yttria doped alumina aerogel with

10.0 wt.% Y_2O_3 that was calcined at 1000 °C for 50 h only suffered a loss of ca.19 % of its surface area (initial value obtained with 3h calcination), while conventional alumina lost ca. 69 % of its surface area (comparison done with an already much lower initial value). These results could be interpreted as more evidence for the improved thermal stability of yttria doped alumina aerogel when compared to conventional alumina. It is worth mentioning that no changes with respect to the structure were detected as a result of long calcinations time. This was clearly confirmed by the XRD.

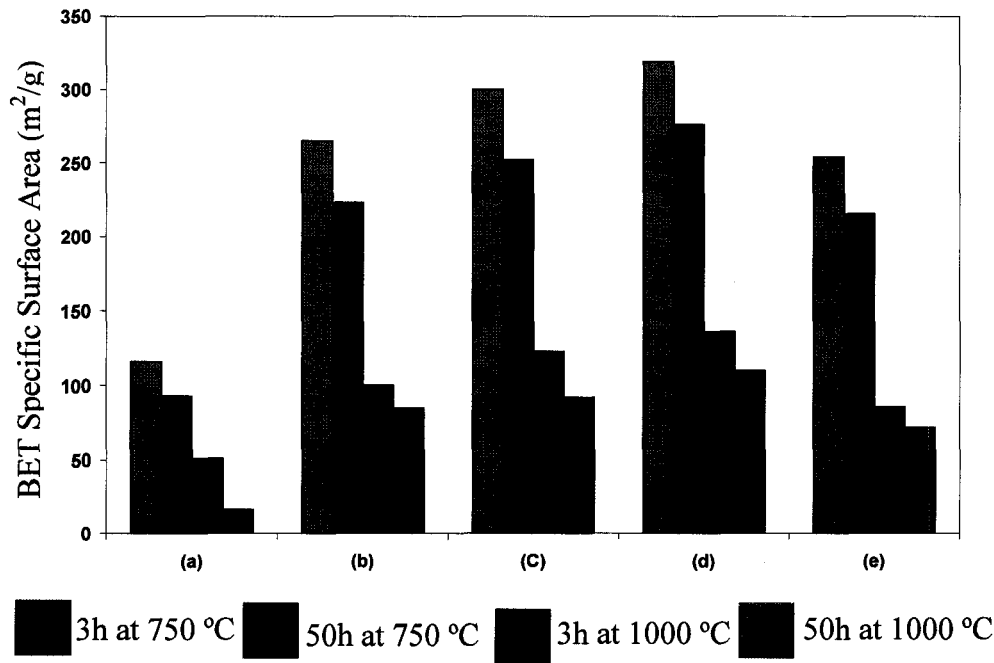


Fig.4.6: Loss of surface area of samples calcined at 750 °C and 1000 °C for 50 h. (a) conventional alumina, (b) undoped alumina aerogel, (c) 2.5 wt.% $Y_2O_3-Al_2O_3$, (d) 10.0 wt.% $Y_2O_3-Al_2O_3$ and (e) 20.0 wt.% $Y_2O_3-Al_2O_3$

As reported in the introduction section, the mechanism by which alumina loses its surface area (i.e. sintering or textural transformation, followed by structural transformation) has been extensively studied and is quite well understood [12,17,35,36],

although some controversial opinions about the relative importance of these transformations still exist [19,20]. First of all, it has been proposed that the thermal stability of alumina depends greatly on the contacts between alumina particles, and the surface defects (i.e. cationic and anionic vacancies, the latter are also created by elimination of -OH groups). Therefore, the key for significantly decreasing the rate of sintering is to minimize the contact between alumina particles and neutralize or reduce the effect of surface defects [37]. In the present study, the most important improvements in the thermal stability, when compared to conventional alumina, is observed with the (undoped) alumina aerogel at 750 °C and 1000 °C. This is believed to be due to the effect of the sol-gel synthesis method using the supercritical drying technique, which results in the formation of microcrystalline alumina whose very tiny particles are hardly detectable by XRD diffraction and TEM techniques. Thus, the lower the particle radius, the larger the surface area and the slower the sintering process at elevated temperatures. Solution sol-gel syntheses have shown several advantages over other preparation methods (i.e. hydrolysis, precipitation...etc) mainly due to their versatility that allows better control of textural, composition, homogeneity and structural properties [38]. The observed high porosity (i.e. low density, Table 4.1) and consequently high specific surface area of alumina aerogel samples (Table 4.2) can be attributed to the supercritical (or hypercritical) drying of liquids contained in the gel. This specific type of drying resulted in the preservation of the textural properties of wet gels, since the interfacial tension associated with the liquid-vapour meniscus was not allowed to form in the capillaries (pores) [23-25,32]. Yttria doped alumina aerogel displayed further improvement in the thermal stability compared to undoped alumina aerogel (and thus, conventional alumina).

However, as mentioned previously, the influence of yttria was only observed up to 1000 °C, since at a higher calcination temperature while yttrium ions could delay the formation of α -Al₂O₃, they also caused the nucleation of Y-alumina phase (YAlO₃) and subsequently, the segregation of this species from the bulk. Finally, at 1200 °C, all samples exhibited the α -Al₂O₃ phase (and YAlO₃ for all yttrium doped materials) (Table 4.1) with very low surface areas (Table 4.2).

It has been reported in the literature [13,17,18,21,22,27-31] that dopants or additives such as alkaline earth or rare earth metals play a significant role in increasing the thermal stability of alumina structure, however there is still a debate about the exact stabilization mechanism. Oudet et al [18] and Beguin et al [22] attributed the stabilizing effect of lanthanum on alumina to the formation of surface lanthanum aluminate. Kumar et al [31] and Kobayashi et al [28] explained the mechanism for stability enhancement of lanthanum as follows: “rare-earth cations enter the interstitial positions of transition alumina lattice and decrease the oxygen vacancies formed in the neck regions which are the nucleation sites of α -Al₂O₃”. Other authors [19,20] preferred the use of terminology such as “dispersion of rare-earth ions”. However, insertion of dopants as interstitial cations might be quite difficult in the case of alumina since the Al³⁺ ionic radius is small ($r_{\text{Al}^{3+}} = 0.051 \text{ nm}$) [36]. In the present investigation, the positive effect of yttria on the thermal stability of alumina aerogel samples is reasonably assumed to be due to the formation of yttrium aluminate species. Their presence was only confirmed by ²⁷Al MAS NMR, since XRD patterns showed that no crystalline phases other than alumina can be detected in yttria doped alumina aerogel up to 1000 °C. The reason for that could be due to the limitation of XRD technique (i.e. the Y-alumina crystallites are below the threshold

of detection by XRD). The ^{27}Al MAS NMR of conventional alumina, undoped and yttria doped alumina aerogel calcined at 750 °C are shown in Fig.4.7 A-F. Careful examination of these figures revealed that all samples clearly showed two peaks, one centered at ca. 3.0-7.0 ppm and another one at ca. 57-65 ppm. These peaks are assigned unambiguously to octahedral and tetrahedral coordinated aluminium, respectively [39,40]. Furthermore, another peak around ca. 33.0 ppm was solely observed in yttria doped alumina aerogel, whose intensity increased as the yttria loading increased. Therefore, we believe that the peak observed around ca. 33 ppm is closely associated with the presence of yttria. This peak could be assigned to (surface and lattice) distorted tetrahedral aluminium (Al_{tetra}) bonded to yttrium through a bridge of oxygen (distorted $\text{Al}_{\text{tetra}}\text{-O-Y}$ bond). It is worth mentioning that the ^{27}Al MAS NMR peak observed in the region of 20-40 ppm in various alumina materials has been assigned to different types of Al^{3+} species and it is obvious from the literature that there is a difference in opinion concerning its assignment. Usually, this peak has been assigned to aluminium surrounded by five oxygen atoms (pentacoordinated aluminium) [41]. Iwamoto et al [42] reported that the peak around 35 ppm could be assigned to surface tetrahedral $\text{Al}_{\text{tetra}}\text{-O-P}$ in molybdenum-phosphorous-alumina catalysts synthesized via sol-gel method. Wang et al [43] in their investigation of alumina structure prepared by sol-gel method have also observed a peak around 33.0 ppm, which they assigned to aluminium ions in octahedral sites with some of the lattice oxygen ions being replaced by hydroxyl groups. In our case, we do not give any preference to the origin (i.e. distorted tetrahedral or octahedral) or the location of these distorted Al bound to Y (i.e. located on the particle surface or in the bulk) for the following reasons: a) to have a retarding action on sintering phenomena of alumina

particles (as in the case of the small sized (undoped) aerogel), Y species should be bound to some surface Al; b) however, during the synthesis, the sec-Al butoxide forms a quite homogeneous gel upon addition of yttrium nitrate, that immediately undergoes hydrolysis when a stoichiometric quantity of water is added. The resulting (very) light aerogel particles do not show any apparent mass “expulsion” of yttrium species to the surface, suggesting that Y species are still “homogeneously” distributed in the alumina particles. ^{27}Al MAS NMR spectrum of yttria doped alumina aerogel sample (with 10.0 wt.% Y_2O_3) calcined at 1000 °C (Fig. 4.7G) also showed the presence of a peak around ca. 33 ppm, however its intensity appeared to be reduced when compared to same sample calcined at 750 °C. Further calcination of the same sample at 1100 °C showed the presence of only two peaks that can be assigned to octahedral and tetrahedral coordinated aluminium, without the sign of any peak in between (Fig.4.7H). This would imply that the Y-alumina phase that was observed in samples calcined at 750 and 1000 °C, had been now displaced from the alumina lattice (and surface) to form the segregated YAlO_3 at 1100 °C. Hence, these Y-alumina species observed at 750 °C and 1000 °C are believed to be the “loosely bound” YAlO_3 . Thus, the enhancement of thermal stability of alumina aerogel upon yttria doping and calcined at up to 1000 °C, can be related to the formation of these Y-alumina species. The presence of these species has led to the reduction of the concentration of alumina surface defects, which are one of the main causes of particle sintering and subsequent phase transformation. They probably help immobilizing the surface alumina ions into a more stable structure (Y-alumina structure). In addition, it is also reasonable to mention that these species must have an influence on the alumina surface –OH groups, since these groups are considered to be also major players in

alumina sintering and phase transformation at high temperature, mostly in the presence of steam (hydrothermal stability [44]).

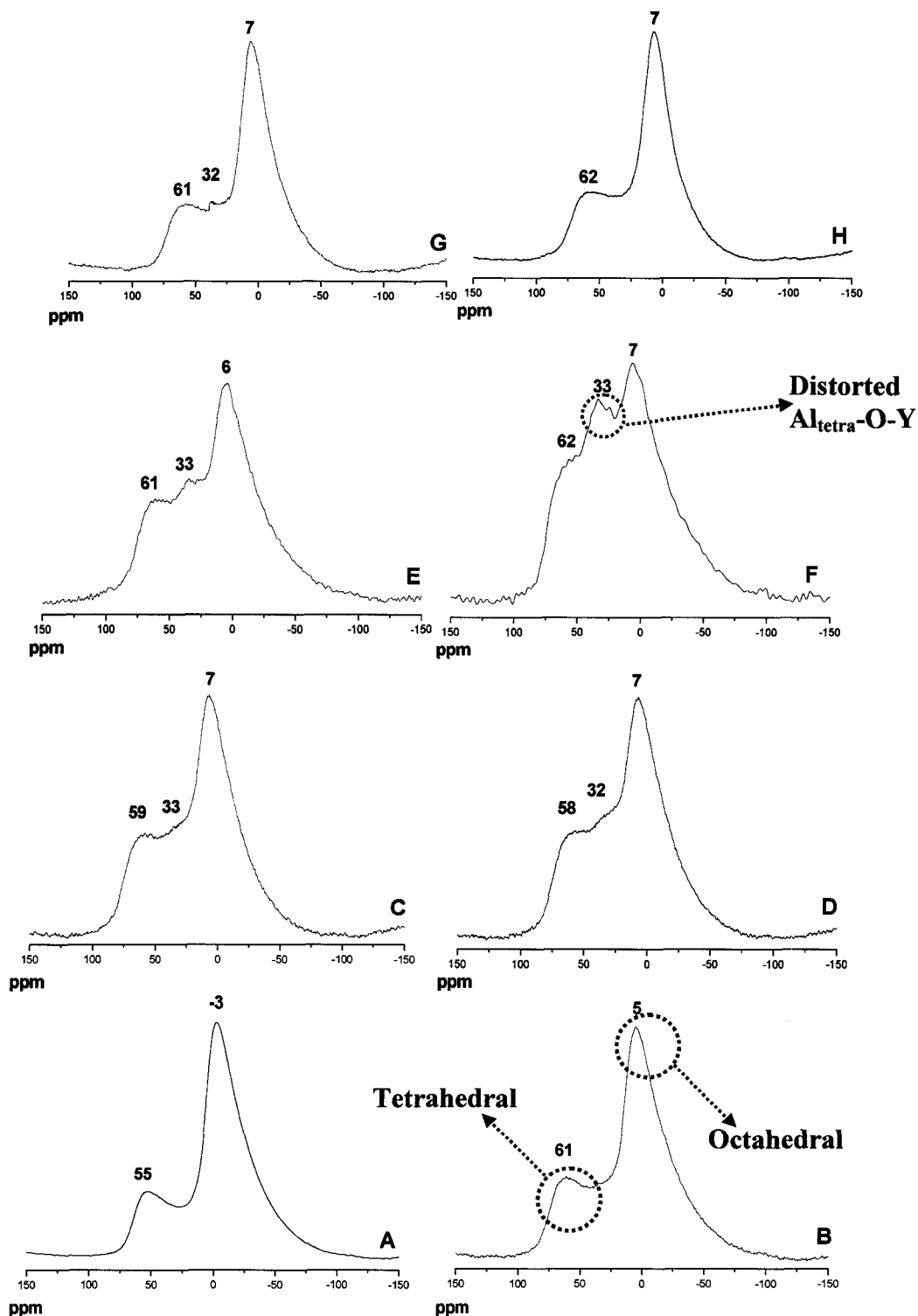


Fig.4.7: ^{27}Al MAS NMR of samples calcined at 750 °C for 3 h. (A) conventional Al_2O_3 , (B) undoped alumina aerogel, (C) 2.5 $\text{Y}_2\text{O}_3\text{-Al}_2\text{O}_3$, (D) 5.0 $\text{Y}_2\text{O}_3\text{-Al}_2\text{O}_3$ (E) 10.0 $\text{Y}_2\text{O}_3\text{-Al}_2\text{O}_3$, and (F) 20.0 $\text{Y}_2\text{O}_3\text{-Al}_2\text{O}_3$. (G) and (H) are 10.0 $\text{Y}_2\text{O}_3\text{-Al}_2\text{O}_3$, calcined at 1000 °C and 1100 °C, respectively

4.4. CONCLUSION

Alumina aerogel prepared by the sol-gel method using a supercritical drying technique showed better thermal stability when compared to conventional alumina obtained by thermal dehydration of boehmite. The improvements in the thermal stability of yttria doped alumina aerogel were attributed to both the sol-gel method (inducing the formation of small sized alumina particles) and the formation of Y-alumina species. These species, which were confirmed by ^{27}Al MAS NMR and XRD, are believed to retard the sintering of alumina particles and delay the α -phase transformation, thus increasing the thermal stability of the material.

4.5. ACKNOWLEDGEMENTS

Financial support from NSERC (Natural Science and Engineering Research Council of Canada) and Valeo Management (Quebec) are acknowledged. The authors also thank Dr. Cedric Malveau (university of Montreal) for technical assistance with ^{27}Al MAS NMR. Also, we thank Jeannie Mui (McGill University) for technical assistance with the TEM measurements.

4.6. AUTHOR'S NOTES AND SIGNIFICANCE OF PAPER TO THESIS

Transition γ -alumina is by far the most widely used catalyst support in petroleum, chemical and pollution control processes. However, the thermal stability remains the most significant drawback of γ -alumina at high temperature reactions (Thermo-Catalytic Cracking (TCC)). This work has addressed this particular setback of alumina. We have examined the influence of the chemical (sol-gel) and physical (drying) processing technique on the pore structure and on crystalline structure transformation in alumina. It

was concluded that yttria doped alumina aerogel is more thermally stable than undoped aerogel and conventional alumina. The higher thermal stability was attributed to the combined effect of sol-gel method and yttria. This work is of great significance to thesis, since it clearly showed that alumina could be stabilized up to 1100 °C by incorporating yttria via sol-gel method. Thus, used effectively as a catalyst support for the TCC process and other high temperature reactions (i.e. Three-Way Catalysts (TWC)).

The following chapter investigates the hydrothermal stability of yttria doped alumina aerogel, which is very critical for the TCC process. Steam is co-fed in the process along with hydrocarbons in order to lower the partial pressure of hydrocarbons and partially removed carbonaceous (coke) deposits. However, steam could have a negative impact on the catalyst, particularly the alumina-based support. This is attributed to the fact that surface area loss and phase transition of alumina are greatly facilitated by the presence of steam. Therefore, it is essential to determine whether yttria doped alumina aerogel is hydrothermally stable or not.

4.7. REFERENCES

- [1] R. Le Van Mao, Concordia University, US Patent 4, 732, 881 (1988).
- [2] R. Le Van Mao, Concordia University, US Patent 7,026,263 B2 (Apr. 11, 2006) and other PCT patent applications (2004-2005).
- [3] R. Le Van Mao, S. Melancon, C. Gauthier-Campbell, P. Kletnieks, *Catal. Lett.* **73** (2001) 181.
- [4] S. Melancon, R. Le Van Mao, P. Kletnieks, D. Ohayon, S. Intem, M.A. Saberi, D. McCann, *Catal. Lett.* **80** (2002) 103.
- [5] R. Le Van Mao, N.T.Vu, N. Al-Yassir, N. Francois, J. Monnier, *Top.Catal.* **37**

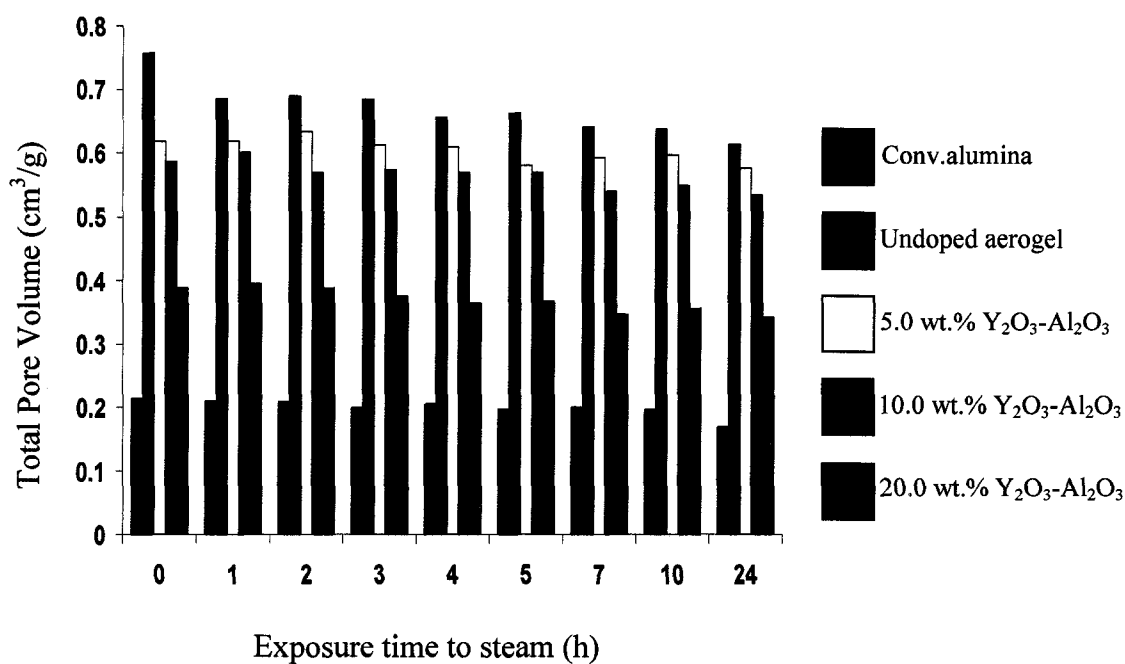
- (2006) 107.
- [6] N. Al-Yassir, and R. Le Van Mao, *Appl. Catal. A: Gen.* **305** (2006) 130.
- [7] J.S. Plotkin, *Catal.Today.* **106** (2005) 10.
- [8] P. Pujado, D. Greer, J. Andersen, T. Foley, V. Bhirud, *pre-print Archive-American Institute of Chemical Engineering*, {Spring National Meeting}, New Orleans, LA, USA. March 11-14 (2002) 2471.
- [9] C.L. Thomas, *Catalytic processes and Proven Catalysts*, Academic Press, New York, 1970.
- [10] R. Prins, V.H.J. Debber, G.A. Somerjai, *Cata. Rev.–Sci. Eng.* **31** (1989) 41.
- [11] M. Che and C.O. Bennett, *Adv. Catal.* **36** (1989) 55.
- [12] M.F.L. Johnson, *J.Catal.* **123** (1990) 245.
- [13] S. Damyanova, L. Petrov, M.A. Centeno, P. Grange, *Appl.Catal. A: Gen.* **224** (2002) 271.
- [14] G. Muralidhar, F.E. Massoth, J. Shabtai, *J.Catal.* **57** (1990) 99.
- [15] K. Wefers, in: L.D. Hart (Ed.), *Alumina Chemicals: Science and Technology Handbook*, The American Ceramic society, Westerville, Ohio, 1990, pp.13
- [16] H. Topsøe, B.S. Clausen, F.E. Massoth, in: J.R. Anderson, M. Boudart (Eds.), *Catalysis Science and Technology*, vol. 11, Springer, New York, 1996.
- [17] H. Schaper, E.B.M. Doesburg, L.L. Van Reijen, *Appl.Catal.* **7** (1983) 211.
- [18] F. Oudet, P. Courtine, A. Vejux, *J. Catal.* **114** (1988) 112.
- [19] X. Chen, Y. Liu, G. Niu, Z. Yang, M. Bian, A. He, *Appl. Catal. A: Gen.* **205** (2001) 159.
- [20] R.A. Shkrabina, N.A. Koryabkina, V.A. Ushakov, M. Lausberg, E.M. Moroz, Z.R.

- Ismagilov, *Kinet. and Catal.* **37** (1996) 109.
- [21] M. Ozawa, M. Kimura, A. Isogai, *J. Less-common metals.* **162** (1990) 297
- [22] B. Beguin, E. Garbowski, M. Primet, *Appl. Catal.* **75** (1991) 119.
- [23] A. Kytokivi, E.-L. Iakomaa, A. Root, H. Osterholm, J.-P. Jacobs, H.H. Brongersma, *Langmuir.* **13** (1997) 2717
- [24] G.M. Pajonk, *Catal.Today.* **35** (1997) 319.
- [25] R.D. Gonzalez, T. Lopez, R. Gomez, *Catal.Today.* **35** (1997) 293.
- [26] E. Ponthieu, E. Payen, J. Grimblot, in: Y.A. Attria (Ed.),
Sol-Gel Processing and Applications, New York, 1994.
- [27] B.E. Yoldas, *Am. Ceram. Soc. Bull.* **54** (1975) 289.
- [28] H. Kobayashi, K. Tadanaga, T. Minami, *J.Mater.Chem.* **8** (1998) 1241.
- [29] A. Vazquez, T. Lopez, R. Gomez, Bokhimi, A. Morales, O. Novaro, *J. Solid State Chem.* **128** (1997) 161.
- [30] A.D. Irwin, J.S. Holmgreen, J. Jonas, *J. Mater. Sci* **23** (1988) 2908
- [31] K.-N. P. Kumar. J. Tranto, J. Kumar, J.E. Engell, *J. Mater. Sci. lett.*, **15** (1996) 266.
- [32] E.Elaloui, R. Begag, B. Pommier, G.M. Pajonk, *Stud. Surf. Sci. Catal.***143** (2002) 331.
- [33] E.Ponthieu, J. Grimblot, E. Elaloui, G. Pajonk. *J. Mater.Chem.* **3** (1993) 287.
- [34] JCPDS, X-ray Powder Data File, International Center for Diffraction Data,
Pennsylvania, 1989.
- [35] P. Burtin, J.P. Brunelle, M. Pijolat, M. Soustelle, *Appl. Catal.* **34** (1987) 239
- [36] H. Aria, M. Machida, *Appl. Catal. A: Gen.* **138** (1996) 161.
- [37] M. Trueba, S. P. Trasatti, *Eur. J. Inorg. Chem.* (2005) 3393.

- [38] M. Campanati, G. Fornasari, A. Vaccari, *Catal. Today* **77** (2003) 299.
- [39] G.A. Pozarnsky, A.V. McCormicks, *J. Non-Cryst. Solid* **190** (1995) 212.
- [40] T.E. Wood, A.R. Siedle, J.R. ill, R.P. Skarjune, C.J. Goodbrake, *J.Mater. Res. Soc. Symp. Proc.* **180** (1997) 97.
- [41] F.R. Chen, J.G. Davis, J.J. Fripiat, *J.Catal.* **133** (1992) 263.
- [42] R. Iwamoto, C. Fernandez, J.P. Amoureux, J. Grimblot, *J. Phys.Chem. B.* **102** (1998) 4342.
- [43] J.A. Wang, X. Bokhimi, A. Morales, O. Novaro, T. Lopez, R. Gomez, *J.Phys.Chem.***13** (1999) 299.
- [44] N. Al-Yassir and R. Le Van Mao, Canadian Journal of Chemistry, in press (Ms. # CJC07316).

Chapter V

Evaluating and Understanding the Hydrothermal Stability of Alumina Aerogel doped with Yttrium Oxide, used as a Catalyst Support for the Thermo-Catalytic Cracking (TCC) Process



Graphical Abstract: Loss of total pore volume of various samples as a function of different exposure time to steam at 750 °C

Published as:

N. Al-Yassir and R. Le Van Mao,

Canadian Journal of Chemistry, in press (Ms. # CJC07316).

ABSTRACT

The current work presents results concerning the hydrothermal stability of yttria doped alumina aerogel, which was prepared by the sol-gel method using a supercritical drying technique. The influence of atmospheric steam at 750 and 1000 °C on the rate of sintering of yttria doped alumina aerogel with various yttria contents was investigated. BET N₂ adsorption measurements, X-ray diffraction, thermogravimetric analysis, FTIR of adsorbed pyridine, and ¹H and ²⁷Al MAS NMR were used for characterization of solid samples. It was found that the hydrothermal stability of yttria doped alumina aerogel was greatly improved compared to alumina aerogel and conventional alumina. This was evident from the decrease in the loss of surface area and pore volume, and the minimization of structural transformations. These significant improvements were attributed to the combined effect of sol-gel method and the presence of yttrium ions. Yttria doped alumina aerogel with various yttria loadings - when compared to undoped alumina aerogel - exhibited lower concentrations of surface -OH groups, higher amounts of bridged -OH groups and lower degrees of crystallinity with smaller particle sizes. It was also observed that the thermal and hydrothermal stabilities of both yttria impregnated alumina aerogel and conventional alumina were improved but to a much lower extent. These improvements were attributed to the presence of yttria, and subsequently the formation of surface yttrium aluminate. This structure was found to be more thermally stable than bare alumina, due to the presence of fewer surface defects and -OH groups. Therefore, it was concluded that in order to observe the most effective role of yttria, it is quite essential to incorporate it into the alumina structure via the sol-gel technique.

5.1. INTRODUCTION

In recent years there has been much interest in the production of light olefins (i.e. ethylene and propylene) from the petroleum feedstocks. The market demand for ethylene and propylene in year 2000 was 89 and 51 million tons, respectively and will increase (projection) by year 2010 to about 140 and 90 million tons, respectively [1]. The increase is driven largely by the escalating demand for the production of polyethylene and polypropylene, which was estimated to be approximately 110 million tons of polyolefins in 2005 (70 million tons of polyethylene and 40 million tons of polypropylene) [2,3]. Several light olefin technologies have been developed and are currently used for the production of ethylene and propylene; including Steam Cracking (SC), conventional Fluid Catalytic Cracking (FCC), ZSM-5 modified FCC, and Deep Catalytic Cracking (DCC) [4-6]. However, these current technologies cannot respond sufficiently to the rapidly growing demand for propylene, which is growing at much faster rate than ethylene, since propylene is only produced as a co-product of ethylene production [2,3]. In addition, the high-energy consumption and the increasingly stringent environmental regulations that require low green house gas emissions are also putting a pressure on the main light olefin technology (SC) [3].

Thermo-Catalytic Cracking (TCC) of petroleum feedstocks for the production of light olefins has been developed in an attempt to overcome some of these challenges [7-15]. This emerging technology is considered more advantageous than others since it produces higher combined yields of ethylene and propylene, it requires lower energy consumption and is more environmentally friendly process. In one of its several versions, the TCC process employs supported metal oxides catalysts (i.e. bi-oxide $\text{MoO}_3\text{-CeO}_2$),

which operates at mild temperature (725-750 °C) and in the presence of steam. Therefore, it is important to evaluate the thermal and hydrothermal stability of the catalyst support, as well as its ability to promote a homogenous dispersion and distribution of active species and promoters at high temperature.

Conventional γ -alumina was found to have poor thermal and hydrothermal stability, and also to show a weak ability to homogeneously disperse active species at high temperature [16-23]. Thus, to overcome these setbacks, alumina doped with Y_2O_3 was prepared via solution-sol-gel using supercritical drying technique [14,15]. The resulting yttria doped alumina aerogel exhibited outstanding physico-chemical properties, when compared to conventional γ -alumina. It displayed high surface area, and enhanced thermal stability [14]. Furthermore, it was characterized by superior ability to homogeneously disperse the active species and the promoters at quite high calcination temperature [15]. The overall improvements were attributed to the sol-gel method, and more significantly to the incorporation of Y_2O_3 into the alumina aerogel structure [14,15]. In addition to these enhanced properties, the hydrothermal stability remains an important property to examine. Steam is co-fed in the TCC process along with hydrocarbons in order to lower the partial pressure of hydrocarbons (i.e. minimize the condensation-side reaction rate), and partially removed carbonaceous (coke) deposit ($C + H_2O \rightarrow CO + H_2$) (4). However, steam could have a negative impact on the catalyst, particularly the alumina-based support. This is attributed to the fact that surface area loss and phase transition of alumina are greatly facilitated by the presence of steam [19-25]. Johnson [19] has investigated the effect of steam on the rate of sintering of alumina and concluded, "The main role of steam is to maintain the surface concentration of hydroxyl

groups leading to an increase in the rate of sintering”. Therefore, in this present work, we attempt to analyze and evaluate in details the hydrothermal stability of yttria doped alumina aerogel under the TCC and harsher conditions. In addition to that objective, we would like to examine another interesting feature. It was noted [14,26,27] that Y_2O_3 played a major role in improving the thermal stability of alumina aerogel. This was observed when yttria precursor was incorporated into the alumina aerogel structure via the sol-gel preparation (one-pot synthesis) [14,26,27]. We would like to investigate whether yttria will exert a similar effect on the thermal and hydrothermal stability if it is added onto the alumina via the impregnation method. It is worth mentioning that the outcome of this work will be of great significance to other industrial applications that require the presence of steam at high temperature such as methane steam reforming for hydrogen production [28].

To the best of our knowledge, no work has been reported yet in the literature on hydrothermal stability of yttria doped alumina aerogel, and only scarce reports [29] available on the role of yttria on the thermal stability of alumina, via impregnation. Therefore, in order to fulfill our objectives, conventional alumina, undoped alumina aerogel, and a series of yttria doped alumina aerogel and yttria impregnated alumina (conventional alumina and alumina aerogel) with variable amounts of Y_2O_3 were prepared. They were thoroughly characterized by diverse techniques such as Brunauer-Emmett-Teller (BET) surface area, X-ray diffraction (XRD), gravimetric thermal analysis (TGA), Fourier transform infrared spectroscopy (FTIR) of adsorbed pyridine, and 1H and ^{27}Al solid-state Nuclear Magnetic Resonance (1H and ^{27}Al MAS NMR).

5.2. EXPERIMENTAL

5.2.1. Materials

Yttria doped alumina aerogel

The yttria doped alumina aerogel was prepared by previously reported synthetic technique [14,26,27], using aluminum tri-sec-butoxide (Strem chemicals, 98 %) and yttrium (III) nitrate hexahydrate (Strem chemicals, 99.9 %) as precursors. The Yttrium concentration was varied in order to have 5.0, 10.0 and 20.0 wt.%. $Y_2O_3-Al_2O_3$ with different Y_2O_3 contents is noted as $xY_2O_3-Al_2O_3$, where x is the Y_2O_3 content in wt.%. The preparation procedures for undoped alumina aerogel noted in this text as alumina aerogel were similar to that of yttria doped alumina aerogel, except no dopant was used.

Yttria impregnated alumina (i.e. conventional alumina and undoped alumina aerogel)

The required amount of yttrium (III) nitrate hexahydrate was dissolved in distilled water and then impregnated onto alumina. After impregnation, samples were first left at 60°C for 10 h for slow evaporation of water, dried overnight at 120 °C and finally calcined in air at either 750, 1000, 1100, or 1200 °C for 6 h. Two different aluminas were used; conventional alumina, and alumina aerogel. The conventional alumina (γ -form, fine powder) was available commercially from (Strem Chemicals) and noted as conv.alumina. Y_2O_3 /alumina with different Y_2O_3 loadings are noted as xY_2O_3 /alumina, where x is the Y_2O_3 content in wt.%. Prior to impregnation, the supports were calcined at 750 °C for 6 h.

Extrudates

The extrudates of all prepared supports were obtained by extrusion with bentonite clay (Aldrich), (Spectrum products, 20.0 wt.%). They were dried overnight at 120 °C and

then calcined in air 750 or 1000 °C for 3 h, depending on the test conditions. These extrudates were prepared and used solely in the hydrothermal stability tests.

5.2.2. Characterization

5.2.2.1. The specific surface areas and pore volume of samples were determined by the BET method using nitrogen physisorption at 77 K. The measurements were carried out using Micromeritics ASAP 2000 apparatus. Samples were outgassed in a vacuum for 3 h at 220 °C before N₂ physisorption. Specific surface areas were calculated by a multipoint point according to Brunauer-Emmett-Teller (BET) method. The S_{BET} surface area results were reproducible within ± 3.0 m²/g. Pore volume results were obtained according to Barret-Joyner-Halenda (BJH) method from the adsorption data, and were reproducible within ± 0.003 cm³/g.

5.2.2.2. X-ray powder diffraction (XRD) was carried out on a Philips diffractometer equipped with a PW 1050/25 focusing goniometer, which has been automated with the VisX122D system from diffraction technologies. The Ni filtered K α radiation of Cu was used ($\lambda_{K\alpha 1} = 1.54051\text{\AA}$) and diffractometer was operated at 40kV and 20mA. The patterns were recorded in the step scanning mode from 5-60°(2 θ) at a detector angular speed of 0.3 °/min with a step size of 0.05°. The XRD phases were identified with the help of the JCPDS (Joint Committee on Powder Diffraction Standards) powder files [30].

5.2.2.3. Thermogravimetric and differential thermal analysis (TGA/DTA) was carried out using the Stanton Redcroft STA 1500 simultaneous thermal analyzer (PL Thermal Sciences). The samples were heated from ambient temperature to 750 ° C under dry air flow (20.0 ml min⁻¹). The sample weights were ca. 10.0 mg, and the heating rate was 10 °

C min⁻¹. The average uncertainty in the TGA results was determined to be ± 0.9 wt.% for the weight loss.

5.2.2.4. Fourier transform infrared spectra of adsorbed pyridine were recorded in order to elucidate the presence of Lewis Acid sites. The transmission spectra were recorded in Nicolet FTIR spectrometer (Magna 500 model) in the region of 1400-1700 cm⁻¹, with resolution of 4 cm⁻¹. The samples in the form of a self-supporting thin wafer were obtained by compressing a uniform layer of powder (sample/KBr mixture = ca. 0.020g). The thin wafer was then placed in a pyrex cell and outgassed under vacuum (10⁻² mbar) at 300 °C for 4 h. Then, pyridine adsorption was carried out at 100 °C for 2 h under vacuum. After the evacuation, at 100 °C for 1 h, the spectra of adsorbed pyridine were recorded at ambient temperature. Pyridine (Aldrich) was stored on activated molecular sieves. The area under each Lewis IR band was calculated using the Omnic software after correcting the baseline.

5.2.2.5. ²⁷Al Magic Angle Spinning Nuclear Magnetic Resonance (MAS NMR) measurements were carried out in a Bruker NMR spectrometer model DSX-300 (magnetic field 7.04 T). ²⁷Al MAS NMR spectra were obtained at frequency of 78.23 MHz with a 20° pulse length of 2 μs and 1 s delay between pulses and a spectral range of 40-75 kHz. The samples were spun at 14 KHz in N₂ using 4 mm ZrO₂ rotors, and typically 540 FID were collected for each sample. The chemical shifts were measured relative to external Al (OH)₂³⁺ standard with an accuracy of ± 0.5 ppm.

5.2.2.6. ¹H MAS NMR measurements were carried out in a Bruker NMR spectrometer model AV-600 (magnetic field 14.1 T). ¹H MAS NMR spectra were obtained at frequency of 600.14 MHz with a 90° pulse length of 1.7 μs and 5 s delay between pulses

and a spectral range of 100 kHz. The samples were spun at 25 KHz in air using 2.5 mm ZrO₂ rotors, and typically 32 FIDs were collected for each sample. The chemical shifts were referenced TMS (0 ppm). Prior to analysis, samples were dehydrated by evacuation to a pressure below 5 μm Hg in a Micromeritics ASAP-2000 instrument (BET apparatus) at 300 °C overnight. The samples were then transferred in helium atmosphere to a moisture-free N₂ atmosphere glove box and packed in sealed tubes. Then, they were transferred from sealed tubes and packed into ZrO₂ rotors.

5.2.3. Hydrothermal stability tests

Hydrothermal stability experiments were performed using a Lindbergh one zone tubular furnace. About 1.0 g of sample extrudate was placed in a quartz tube (55 cm in length and 1.5 cm in diameter). They were heated at 750 and 1000 °C, respectively for n h (n =1-24 h) in the presence of steam (H₂O flow = 1.1 ml/h) at atmospheric pressure.

5.3. RESULTS AND DISCUSSION

5.3.1 Short review of pertaining information to the thermal and hydrothermal stability of alumina

A great number of studies have shown that the thermal and hydrothermal stability of transition alumina, currently used as catalyst supports for many reactions, is influenced by several factors [16-24]. These factors include the presence of intrinsic cationic and anionic vacancies, and more significantly the surface -OH groups. Burtin et al [17] stated that the mechanism by which alumina loses its surface area at high temperature is a direct result of an interaction between the intrinsic cationic vacancies and anionic vacancies. The latter is also formed by the dehydroxylation of surface -OH groups. The outcome of that reaction is the annihilation of these vacancies, and subsequently the destruction of the spinel lattice and structural rearrangement of constituent ions. Johnson [19] suggested

that the surface hydroxyl groups play a major role in alumina stability. In his proposed model, he stated that particle growth (sintering) occurs by successive elimination of water from two -OH groups residing on adjacent particles, close to an area of contact (19-22). These groups interact through lateral hydrogen bonding [19-22,31]. Subsequently, this will generate Al-O-Al bond, which will bring more -OH groups into adjacency (condensation). A diffusive process is expected to follow condensations to form “necks” between particles. Finally, small particles will grow to larger ones accompanied by significant surface area loss [19]. Whatever the case may be, it is quite evident that -OH groups play the foremost role in alumina sintering, and subsequently in the thermal and hydrothermal stability. The presence of steam is expected to significantly (participate in increasing) the rate of sintering [19-25]. This can be attributed to the main function of steam, which is to maintain the concentration of surface -OH groups that are mainly responsible for the nucleation, and particle growth of transition alumina as described above. The ability of steam to rehydroxylate (rehydrate) the surface of alumina is enhanced by the presence of Lewis acid sites (coordinative unsaturated (cus) cations), which are formed as a result of the dehydroxylation (32-34). In the dehydroxylation process, an oxide ion is lost and hence an oxygen vacancy should be created in order to maintain the electrical neutrality of the structure ($2\langle\text{OH}\rangle_{2-}^+ \rightarrow (\text{H}_2\text{O}) + \langle\text{O}^{2-}\rangle_{2-}^0 + \langle\ \rangle_{2-}^{2+}$) [17]. This will give the rise to the coordinative unsaturated sites (Lewis sites). These sites will allow the interaction with water vapor via a two-step mechanism, which can be summarized as follow ($\square\text{M}^{n+1}\text{O}^{2-} + \text{H}_2\text{O} \rightarrow \text{HO}\text{M}^{n+}\text{OH}$) (\square indicates the vacancy or a coordinative unsaturation) [33-35]. It involves a nondissociative adsorption of water vapor on a Lewis acid site that will essentially involve transfer of electron density to a

Lewis acid site (cus Al), followed by dissociative chemisorption of water [33,34]. Therefore, in order to improve the hydrothermal stability, it is essential to have, to some extent, a low concentration of Lewis sites, which are mainly responsible for the rehydroxylation process. This can be achieved by reducing the degree of dehydroxylation process (removal of -OH groups) from the surface. The above can be accomplished by reducing the number of hydroxyl groups that are responsible for the sintering process. It is worth mentioning that such reduction should not substantially diminish the acid-base properties, or more significantly, the ion-exchange properties of alumina. Moreover, the degree of dehydroxylation can be minimized by having higher number of bridging -OH groups (i.e. held by more than one bond) compared to the terminal ones (i.e. held by one bond) [31]. The latter has been shown to be quite susceptible to sintering process [31]. Furthermore, the contact between alumina particles should be minimized, since dehydroxylation is enhanced by close proximity of condensing particles [36]. In addition, the utilization of strong and stable binder (i.e. bentonite) can also play a role in enhancing the hydrothermal stability. It is also vital to mention that the factors that influence the thermal stability should be also taken into consideration in order to improve the hydrothermal stability. This is due to the fact that hydrothermal stability is measured at high temperature. These factors include the presence of surface defects, degree of crystallinity (i.e. amorphous, crystalline, etc.), and the crystallite sizes of crystalline materials (14 and reference therein). The presence of high number of surface defects and larger crystallites have shown to greatly enhance the sintering process [14].

5.3.2. Hydrothermal Stability of yttria doped alumina Aerogel

BET surface area, pore volume and XRD patterns

The changes in BET specific surface area and pore volume of different catalyst supports, which were subjected to steam at 750 °C with different exposure times are shown in Table 5.1 and Figure 5.1A, respectively.

Table 5.1: Changes in the BET specific surface area (S_{BET}) of different catalyst supports (in extrudate form) as a function of exposure time to steam, at $T = 750$ °C, and H_2O flow rate = 1.1 ml/h^a

Duration of exposure to steam (h)	BET Specific Surface Area (m^2/g)								
	0	1	2	3	4	5	7	10	24
Bentonite	14.0	13.0 (0.93)	n.a.	13.0 (0.93)	n.a.	12.0 (0.86)	n.a.	10.0 (0.71)	9.0 (0.64)
Conv.alumina	107	83.0 (0.78) ^b	82.0 (0.77)	79.0 (0.74)	78.0 (0.73)	75.0 (0.70)	74.0 (0.69)	72.0 (0.67)	70.0 (0.65)
Alumina aerogel	203	167 (0.82)	165 (0.82)	165 (0.82)	160 (0.79)	157 (0.77)	154 (0.76)	154 (0.76)	149 (0.73)
5.0 wt.% $\text{Y}_2\text{O}_3\text{-Al}_2\text{O}_3$	198	188 (0.95)	187 (0.95)	184 (0.93)	182 (0.92)	179 (0.91)	177 (0.89)	172 (0.87)	168 (0.85)
10.0 wt.% $\text{Y}_2\text{O}_3\text{-Al}_2\text{O}_3$	188	185 (1.02)	182 (0.97)	176 (0.94)	176 (0.94)	174 (0.93)	170 (0.91)	170 (0.91)	169 (0.90)
20.0 wt.% $\text{Y}_2\text{O}_3\text{-Al}_2\text{O}_3$	143	135 (0.94)	127 (0.89)	126 (0.88)	126 (0.88)	126 (0.88)	124 (0.87)	125 (0.87)	123 (0.86)

^a No significant area loss was observed as a result of calcination in dry air. ^b Number in parenthesis is the ratio of S_{BET} of sample exposed to wet air (in the presence of steam) to S_{BET} in dry air

It can be seen that the rate of hydrothermal sintering of conv.alumina was greatly facilitated in the presence of steam at 750 °C, which has resulted in ca. 22 % and 35 % surface area loss when exposed for 1 h and 24 h, respectively (Table 5.1). Undoped alumina aerogel showed improvement in the hydrothermal stability. The area loss of undoped alumina aerogel was ca. 18 % and 26 %, when exposed to steam for 1 h and 24 h, respectively. On the contrary, the influence of steam becomes significantly less

pronounced in yttria doped alumina aerogel, and in fact it decreases as the amount of yttria increases from 5.0 to 10.0 wt.%. For example, the area loss for 5.0 wt.% yttria doped alumina aerogel was ca. 5 % and 15 %, when exposed to steam for 1 h and 24 h, respectively. Alumina aerogel doped with 10.0 wt.% yttria showed more outstanding improvements in the hydrothermal stability. This was supported by the small loss in the surface area when compared to the other investigated supports (i.e. only ca. 1.6 % and 10 % area loss when subjected to steam for 1 h and 24 h, respectively). Although, alumina aerogel doped with 20.0 wt.% yttria displayed a slightly higher surface area loss than 10.0 wt.% yttria doped alumina aerogel, it is still more hydrothermally stable than conv.alumina and alumina aerogel. In addition, it was found that Bentonite (extrudate) is hydrothermally stable, as suggested by the low reduction of S_{BET} as function of exposure time to atmospheric steam. It is worth mentioning that the changes in the total pore volume also followed the same pattern as the surface area loss (Fig.5.1A).

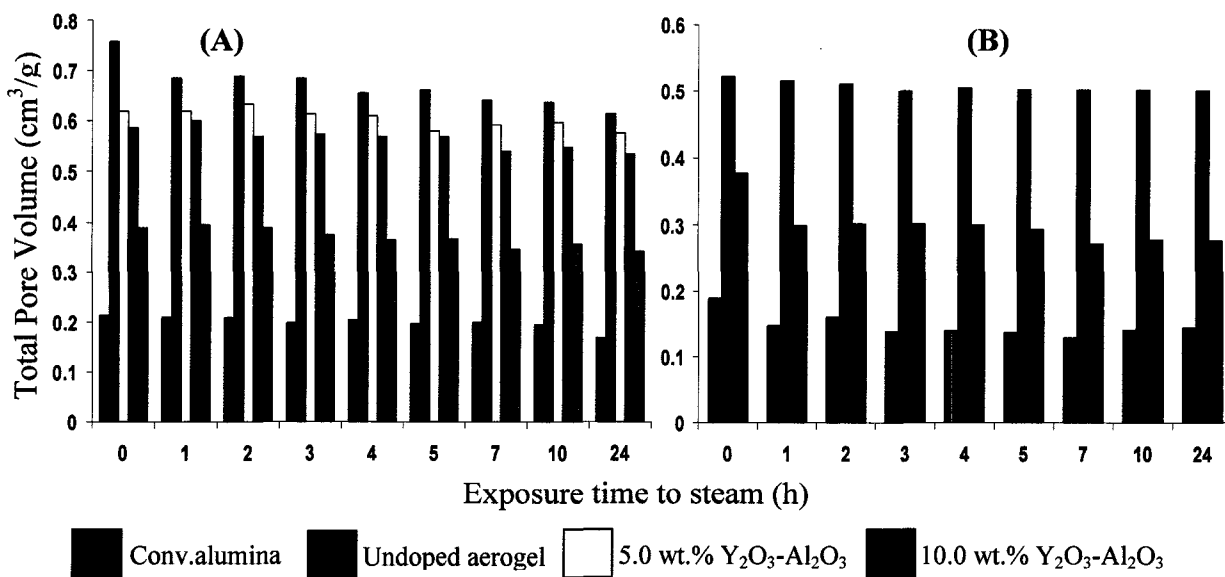


Fig.5.1A-B: Loss of total pore volume of various samples as a function of different exposure time to steam at (A) 750 °C and (B) 1000 °C

Furthermore, the XRD patterns of various investigated supports (extrudates) subjected to steam at 750 °C show that the diffraction peaks appeared to be quite the same when compared to the calcined extrudates (dry air only).

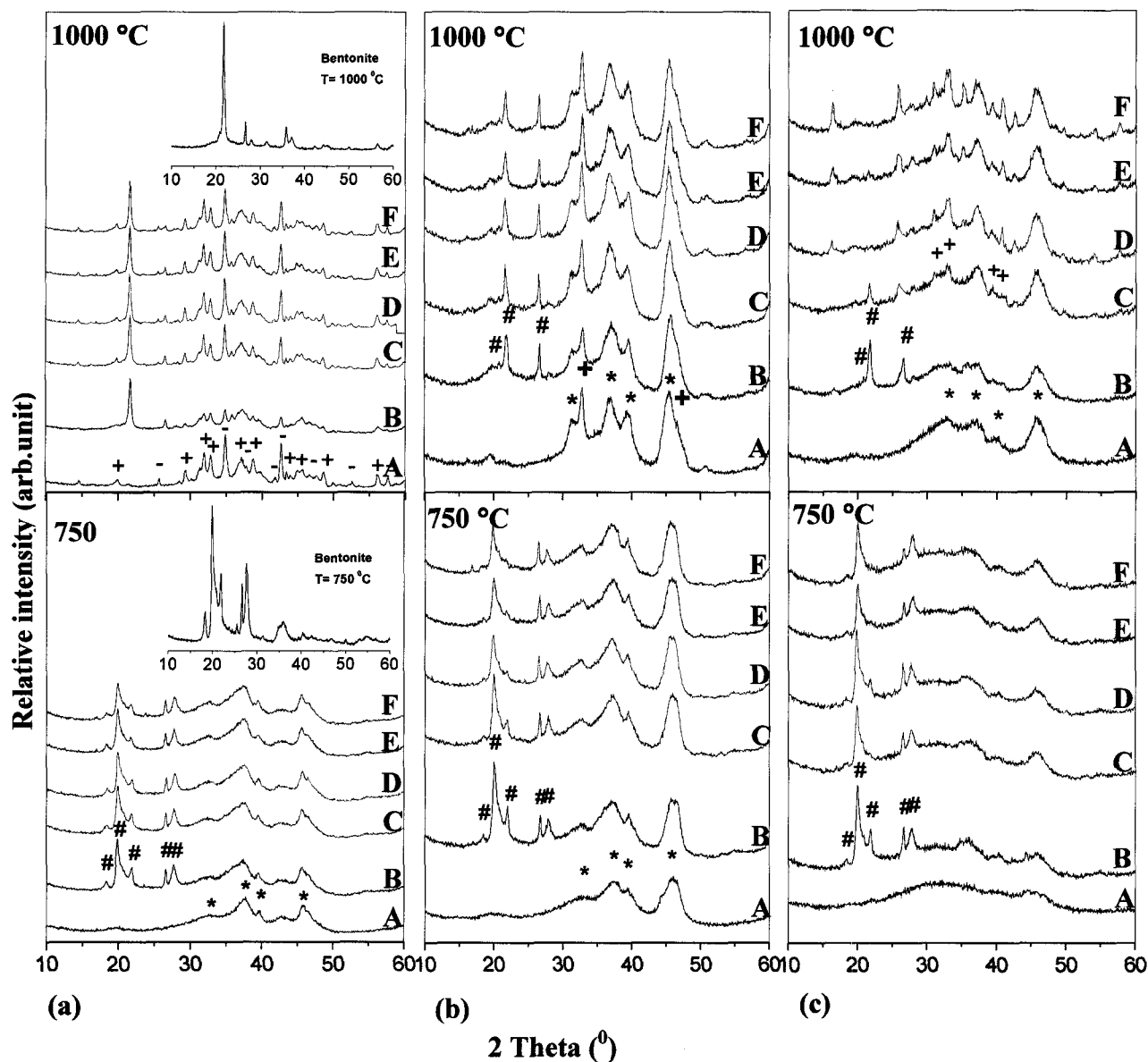


Fig.5.2: (a) XRD patterns of conv.alumina extrudates after exposure to steam at high temperature; A and B are sample powder [15] and extrudate, respectively. C-F are sample extrudates exposed to steam for 1, 5, 10 and 24 h, respectively. (b) represents the undoped alumina aerogel extrudate. (c) represents the 10.0 wt.% yttria doped alumina aerogel extrudate. (*) γ - Al_2O_3 , (+) θ - Al_2O_3 , (-) α - Al_2O_3 , and (#) Bentonite

The comparison between the XRD patterns of 10.0 wt.% yttria doped alumina aerogel extrudates that was subjected to dry air with those of the same treated with wet air, leads to the same conclusion of unchanged structure. These results clearly suggest that the observed loss of surface area was due only to surface and textural transformations (i.e. condensation between hydroxyls on adjacent particles) and did not involve any structural transformation (i.e. formation of new phases such as δ , θ or α).

It is worthwhile noting that the same pattern of improvement in the hydrothermal stability of yttria doped alumina aerogel compared to alumina aerogel and conv.alumina was observed at 1000 °C (Table 5.2 and Fig. 5.1B).

Table 5.2: Changes in the BET specific surface area (S_{BET}) of different catalyst supports (in extrudate form) as a function of exposure time to steam, at $T = 1000$ °C, and H_2O flow rate = 1.1 ml/h ^a

Duration of exposure to steam (h)	BET Specific Surface Area (m^2/g)								
	0	1	2	3	4	5	7	10	24
Conv. alumina	52.0	37.0 (0.71) ^b	37.0 (0.71)	37.0 (0.71)	36.0 (0.70)	34.0 (0.70)	34.0 (0.65)	34.0 (0.65)	32.0 (0.62)
Alumina aerogel	111	86.0 (0.78)	85.0 (0.77)	85.0 (0.77)	85.0 (0.77)	84.0 (0.76)	78.0 (0.70)	76.0 (0.68)	75.0 (0.68)
10.0 wt.% $\text{Y}_2\text{O}_3\text{-Al}_2\text{O}_3$	116	105 (0.91)	105 (0.91)	104 (0.90)	103 (0.89)	103 (0.89)	100 (0.86)	101 (0.87)	100 (0.86)

Note: For symbols, refer to Table 5.1.

For example, the area loss of conv.alumina was ca. 28 % and 37 %, when exposed to steam for 1 h and 24 h, respectively (Table 5.2). Undoped alumina aerogel showed a significant improvement, as evidenced by the lower area loss, which was 22 % and 32 %, when exposed to steam for 1 h and 24 h, respectively. As expected, alumina aerogel doped with 10.0 wt.% yttria displayed much better hydrothermal stability compared to the other supports. The area loss, which was significantly lower than those observed with

other studied supports, was ca. 9 % and 14 %, when exposed to steam for 1 h and 24 h, respectively. Careful assessment of Fig.5.1B, which displays the total pore volume loss of different supports as function of exposure time to steam at 1000 °C, displayed similar conclusion as surface area loss. It was also noted from the XRD patterns of different supports exposed to steam at 1000 °C (Fig.5.2a-c) that steam has provoked structural rearrangements to very small extent. On the other hand, it was quite clear that the structural rearrangements caused by steam were less prominent in yttria doped alumina aerogel samples compared to other studied supports. For instance, the XRD patterns of conv.alumina extrudates that were subjected to steam at 1000 °C showed that the intensity of the reflections that are assigned to α -phase increases when subjected to steam. In addition, the XRD patterns of undoped alumina aerogel extrudates displayed that the intensity of the reflections that are assigned to θ -phase increases when subjected to steam. Although, the reflections that are assigned to the θ -phase start to appear in the 10.0 wt.% yttria doped alumina aerogel extrudates, they were enormously weak and broad when compared to those observed with undoped alumina aerogel extrudates. The broadness of these reflections clearly indicate that the θ -phase is not well crystalline.

Therefore, BET specific surface area, total pore volume, and XRD patterns results have shown that the hydrothermal stability of yttria doped alumina aerogel was greatly improved compared to alumina aerogel and conv.alumina. The results of all investigated supports, which were exposed to steam at either 750 °C or 1000 °C, have unambiguously revealed that the loss of surface area and pore volume, and structural transformation were greatly minimized according to the following order: yttria doped alumina aerogel, followed by undoped alumina aerogel followed by conv.alumina.

Sintering effects of high temperature and steam

It becomes evident that both the sol-gel preparation method and the incorporation of yttrium ions into the alumina aerogel structure play an important role in these improvements. Subsequently, these factors should have a direct effect on the number of Lewis acid sites (the main interaction sites of steam with the alumina surface at high temperature), which are influenced by the surface -OH groups (i.e. concentration and structure). Thus, evaluating the dehydroxylation pattern of surface hydroxyl groups and the Lewis acid sites are of paramount importance in order to elucidate the exact mechanism of hydrothermal stability.

Thermal gravimetric and differential analysis (TGA/DTA) and FTIR of adsorbed pyridine techniques were employed in this investigation to examine the dehydroxylation pattern, and the Lewis sites of different supports, respectively. ^1H MAS NMR measurements were used to investigate the structure of surface -OH groups. It is worth mentioning that the TGA/DTA analysis was performed on samples calcined at 400 °C, in order to be able to observe the dehydroxylation pattern. Whereas, the FTIR of adsorbed pyridine was carried out on samples that were calcined at 750 °C, which is the same temperature used to evaluate the hydrothermal stability. The TGA results obtained with conv.alumina, alumina aerogel, and yttria doped alumina aerogel with different yttria loadings are shown in Table 5.3 (The TGA/DTA graphs are not shown here). The first weight loss in the range 25-250 °C, which was accompanied by an endothermic peak is primarily due to the removal of physisorbed water held on the surface by hydrogen bonding. The weight loss observed above could be also due to the removal of water held in the small pores (Table 5.3). The second weight loss in the range of 300-750 °C (very

broad endothermic peak) corresponded to the loss of water due to dehydroxylation of the surface. Thus, the approximate amounts of surface OH removed upon dehydroxylation by heating between 300–750 °C (N (OH) in moles/g of alumina) were determined by counting 2 moles of OH groups for 1 mole of water evolved. It is quite apparent from data of Table 5.3 that the dehydroxylation pattern was significantly influenced by the structure of the support. Conv.alumina displayed OH loss of about 0.28 (10^{-2} moles/g) while the number for undoped alumina aerogel was much higher (0.98 (10^{-2} moles/g)). However, the OH loss for yttria doped alumina aerogel was continuously decreasing as the amount of yttria doped into alumina aerogel increased (Table 5.3). Therefore, it can be inferred from these results that undoped alumina aerogel had higher concentration of -OH groups, whereas the concentration of these removed groups decreased as the content of yttria doped into alumina aerogel increased. It is worth mentioning that the noted weight loss in the region of 300-750 °C was a continuous mass loss. In addition, the observed weight loss should be entirely due to the dehydroxylation, since the DTA curves did not show any exothermic peaks that can suggest a decomposition process for instance.

Table 5.3: Approximate quantity of -OH groups lost, and distribution of (subsequently formed) Lewis sites upon calcinations in dry air

Sample	Amount of -OH lost		Coordinative unsaturated Lewis Acid Sites (Al_{cus})			
	N (OH) (10^{-2} moles/g) ^b	N (OH) (10^{-2} moles/g) ^c	Estimated area of Lewis Sites observed at 750 °C (Arbitrary unit) ^a			
			[py-L] (1440-1450 cm^{-1})	$VIAl_{cus}$ -py [py-L] _o (1595 cm^{-1})	$IVAl_{cus}$ -O-□- O- $VIAl_{cus}$ -py [py-L] _{o,t} (1610-1620 cm^{-1})	$IVAl_{cus}$ -py [py-L] _t (1625 cm^{-1})
Conv.alumina	0.39	0.28	3.28	0.84	0.25	0.0
Alumina	1.33	0.98	7.31	1.28	0.47	0.0
aerogel						
5.0 wt.% Y_2O_3 - Al_2O_3	1.11	0.85	5.52	1.09	0.32	0.0
10.0 wt.% Y_2O_3 - Al_2O_3	0.92	0.44	4.87	1.17	0.12	0.0
20.0 wt.% Y_2O_3 - Al_2O_3	0.78	0.14	3.45	1.13	0.0	0.0
10.0 wt.% Y_2O_3 / conv.alumina	0.22	0.05	0.55	0.0	0.0	0.0
10.0 wt.% Y_2O_3 / Al_2O_3 aerogel	0.95	0.42	0.78	0.0	0.0	0.0

^a The area under the Lewis IR band was calculated using the Omnic software after correcting the baseline. ^b Amount (or Number (N)) of -OH lost in the region 25-250 °C (physisorbed water). ^c Amount of -OH lost in the region between 300-750 °C

The FTIR of pyridine adsorption technique was also employed in order to reveal the presence of Lewis acid sites. Figure 5.3 shows the presence of several IR bands, which are characteristics of different types of Lewis acid sites [35,37,38]. The observed bands, which are more sensitive to aluminium coordination and structural vacancies were 1595, 1610-1620, and 1625 cm^{-1} (37 and references therein). The band observed at 1595 cm^{-1} is ascribed to Lewis coordinated to $VIAl_{cus}$ ions ([py-L]_o) [37]. The band observed at 1610-1620 cm^{-1} can be ascribed to pyridine Lewis coordinated by an $VIAl$ - Al_{IV} cation pair ([py-L]_{o,t}) [37], or to vacancies shared by two Al^{3+} ions according to Busca's model [35].

The band observed at 1625 cm^{-1} is ascribed to pyridine Lewis coordinated to IVAl_{cus} ions ($[\text{py-L}]_i$) [37]. The band observed at $1440\text{-}1450\text{ cm}^{-1}$ is also ascribed to Lewis sites [38]. Figure 5.3 shows the FTIR spectra of pyridine adsorbed on conv.alumina, alumina aerogel, and yttria doped alumina aerogel with different yttria loadings (all being calcined at $750\text{ }^\circ\text{C}$), and the approximate concentrations of different Lewis acid sites are reported in Table 5.3 (the extinction coefficients of these adsorbed pyridine peaks being assumed to be equal). It is clear from Fig.5.3 and Table 5.3 that alumina aerogel has a higher number of Lewis sites when compared to conv.alumina, as suggested by the higher Lewis site band area. Furthermore, the number of these sites decreases as the amount of yttria doped into alumina aerogel increases, when compared to undoped alumina aerogel.

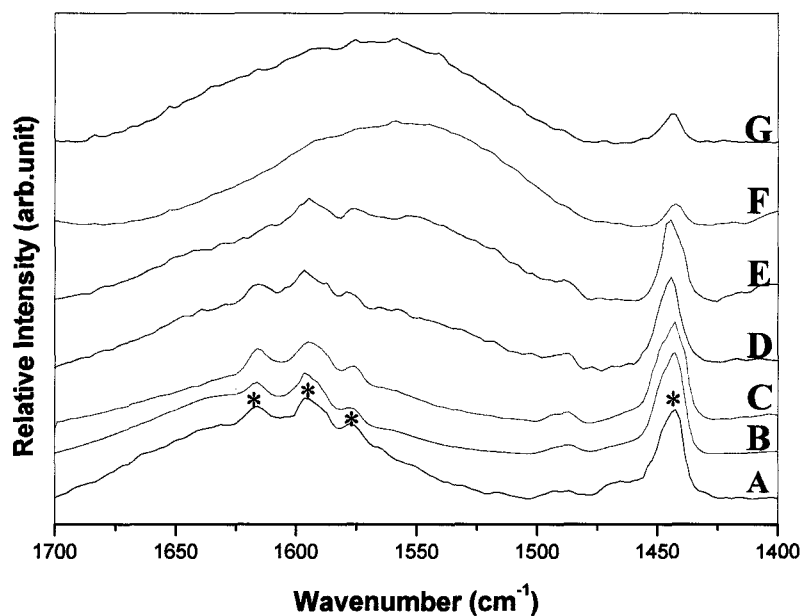


Fig.5.3: FTIR spectra of adsorbed pyridine on; a) conv.alumina, b) undoped alumina aerogel, c-e) yttria doped alumina aerogel with 5.0, 10.0 and 20.0 wt.% yttria, respectively, and f-g) 10.0 wt.% yttria impregnated alumina and alumina aerogel, respectively. (* Lewis sites)

Although the alumina aerogel, when compared to the conv.alumina, showed a higher dehydroxylation rate, and consequently a higher number of Lewis sites, it did not (surprisingly at first) experience a higher rate of hydrothermal sintering. The main reason behind the slightly lower rate of sintering of the undoped alumina aerogel can be ascribed to the sol-gel method, which strongly influenced the degree of crystallinity of the resulting material, and the structure and concentration of surface -OH groups. In fact, this aerogel was characterized by a low degree of crystallinity with small particle sizes compared to conv.alumina, as suggested by XRD and TEM measurements carried out in our previous communication concerning the thermal stability of alumina [14]. Therefore, it can be inferred from these results that the degree of crystallinity and particle size by minimizing the extent of hydrothermal sintering, played a larger role than expected. The observed significant improvements in the hydrothermal stability of alumina aerogel upon the incorporation of yttria are ascribed to the combined effect of sol-gel method and the presence of yttrium ions. The utilization of such procedures has resulted in minimizing the effect of several factors that are believed to favour the hydrothermal sintering. First, the number of -OH groups, which are well known to play the foremost role in the sintering, has been reduced upon the incorporation of yttrium ions into the lattice gel. The reduction can probably be ascribed to an exchange interaction mechanism (cross-condensation) between yttrium and hydroxyl groups of alumina aerogel [19]. Data of Table 3 showed that the dehydroxylation rate, and subsequently the number of Lewis sites was reduced as the amount of yttria loadings increased. Second, yttria doped alumina aerogel is expected to contain higher number of bridged -OH group with respect to terminal ones. This can be attributed to the sol-gel method, which allows in general the

formation of different types of -OH groups. These groups are the bridging groups between metal (M) centres (M-OH-M), and the terminal ones (M-OH). The structure of these groups depends to a large extent on the degree of hydrolysis reaction, which is in turn dependent on the ratio of water to alkoxide. In our current synthesis, the ratio of water to aluminium tri-sec butoxide (aluminium precursor) was 2.5, which is very close to the required stoichiometric ratio of 3.0 [14]. This has allowed an increase in the extent of hydrolysis reaction (close to completion), and consequently the formation of highly branched polymeric alumina aerogel instead of linear structure that would have been observed at a lower ratio (i.e. 1:1 water/alkoxide) [39]. The highly branched structure would certainly be characterized with higher number of bridged hydroxyl groups over terminal ones. The presence of bridged -OH groups play a major role in minimizing the extent of sintering. For instance, hydroxyl groups that are held by more than one bond (i.e. bridged such as $Al_o-OH-Al_o$, $Al_t-OH-Al_o$, $3Al_o-OH$ and Al_t-OH-Y where Al_o and Al_t are octahedral and tetrahedral alumina, respectively) are thus in fixed positions, and therefore their relative orientation of their O-H bonds and free orbitals is very unfavourable for H-bonding between two adjacent hydroxyl groups [31]. On the other hand, hydroxyl groups that are held by only one bond (i.e. terminal such as Al_o-OH and Al_t-OH) can provide more favourable orientation for H-bonding since they will have more degrees of freedom [31]. It is worth mentioning that 1H MAS NMR measurements were in complete agreement with above expectations. Ft-IR spectroscopy can be also used for that purpose, however poor resolution of the hydroxyl stretching bands in the region of $3200-4000\text{ cm}^{-1}$ often makes it quite difficult to determine whether any changes have actually occurred (i.e. appearance of new bands, or modification of existing bands)

[40,41]. The ^1H MAS NMR spectra of conv.alumina, undoped alumina aerogel and yttria doped alumina aerogel with different yttria loadings, all calcined at 750 °C are presented in Figure 5.4.

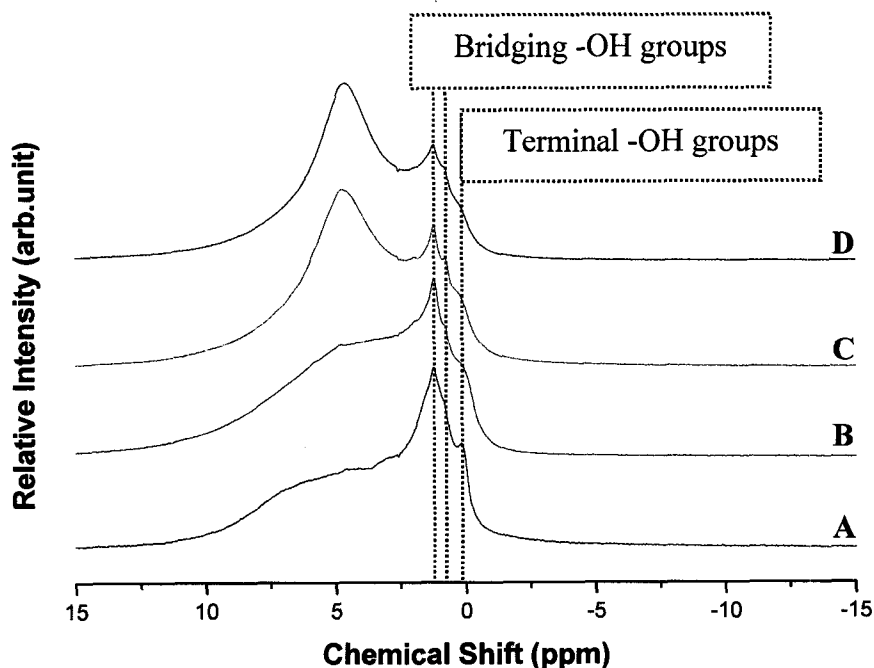


Fig.5.4: ^1H MAS NMR of samples calcined at 750 °C for 3 h. (A) conv.alumina, (B) undoped alumina aerogel, (C) 10.0 $\text{Y}_2\text{O}_3\text{-Al}_2\text{O}_3$, and (D) 20.0 $\text{Y}_2\text{O}_3\text{-Al}_2\text{O}_3$

The ^1H MAS NMR spectra of all samples clearly suggest a wide distribution of surface hydroxyl groups of variable basic and acidic strength of different structure (i.e. terminal and bridged -OH groups). ^1H MAS NMR spectrum of conv.alumina (Fig.5.4A) exhibits several resonance lines at ca. - 0.3 (shoulder), 0.2, 0.7, 1.3 and 1.9 (shoulder) ppm, which shows that there are five different OH groups present on the surface of alumina. This is in complete agreement with Knözinger and Ratnasamy model that was developed for alumina surface [31]. The peak at -0.3 ppm was previously attributed to the terminal basic OH groups attached to one aluminum atom in octahedral coordination

(Al_o-OH) [31,40-43]. The peak at 0.2 ppm can be also attributed to (Al_o-OH) but with an intermediate basic character [31]. The remaining peaks at 0.7, 1.3 and 1.9 ppm, with the peak at 1.3 ppm being the most intense line of these lines, are attributed to an overlap of more than one type of bridged -OH groups (i.e. Al_o-OH-Al_o, Al_t-OH-Al_o and 3Al_o-OH, where Al_o and Al_t are octahedral and tetrahedral coordination, respectively) [31, 40-43]. The low-field shift of these peaks indicates their acidic character. In addition, a very broad signal was found at 4.7 ppm and assigned to small amount of physisorbed and chemisorbed water on the alumina surface that probably occurred during transferring samples into the NMR holder (ZrO₂ rotor) [43]. Fig.5.4B also indicates that undoped alumina aerogel has the same types of hydroxyl groups as conv.alumina. However, Fig.4.4B showed that the peak that is normally assigned to terminal -OH groups (ca.-0.3 and 0.2 ppm) was less resolved and broader when compared to the one observed with conv.alumina. This could suggest that undoped alumina aerogel contained lower number of terminal -OH groups than conv.alumina. Yttria doped alumina aerogel with 10-20 wt.% Y₂O₃ loadings (Fig.5.4C-D), when compared to undoped alumina aerogel, showed that the intensity of the peak that is attributed to bridged -OH groups decreased with increasing the amount of yttria doped into the alumina aerogel. No significant changes were observed with respect to the terminal -OH peak. The reduction in the intensity, which may reflect that the population of alumina surface bridged -OH groups was decreased, can be attributed to an interaction mechanism between alumina aerogel hydroxyl groups and yttrium ions, as stated previously. It is very important to mention that the appearance of the very broad ca. 4.7 ppm peak (due to physisorbed water) could have serious implications on our ¹H MAS NMR results. For instance, it will be tricky to

distinguish between the real -OH groups and those formed as a result of H-bonding. Therefore, our observed results should be analyzed with extra caution. Detailed and thorough investigation of the chemistry of surface -OH groups on alumina aerogel and yttria doped alumina aerogel with various contents using ^1H MAS NMR, which should be taken into consideration the complete elimination of the ca. 5.5 ppm peak, will be carried out and the results will be the subject of future publication. Third, yttria doped alumina aerogel with various yttria loadings displayed a lower degree of crystallinity with smaller particle sizes, when compared to undoped alumina aerogel and conv.alumina, as suggested by XRD and TEM measurements [14]. Fourth, it is worthwhile mentioning that the improvements in the hydrothermal stability of alumina aerogel upon the incorporation of yttria into the alumina structure can be also attributed in part to the fact that yttria forms fairly stable $\text{Y}(\text{OH})_3$ on contact with water. This can be ascribed to the highly alkaline character of yttrium oxide. Fifth, the utilization of stable and strong binder (Bentonite (Table 5.1)) also played a small role in the improvements of the hydrothermal stability. This effect appeared to exist on all investigated supports.

5.3.3. Thermal and Hydrothermal Stability of yttria impregnated alumina

The thermal stability of both conv.alumina and alumina aerogel was improved upon the addition of yttria via impregnation method, as suggested by XRD, and BET specific surface area results. It was clearly observed that there was a delay or retardation of sintering and phase transformation of γ -phase into θ -phase or α -phase, upon addition of yttria via impregnation method. Furthermore, it was observed that the extent of stabilization was higher for alumina aerogel than conv.alumina. The X-ray diffraction patterns of yttria impregnated conv.alumina, which was calcined for 6h at 750, 1000,

1100, and 1200 °C, are shown in Fig.5.5. Their XRD patterns results are summarised in Table 5.4.

Table 5.4: X-ray diffraction pattern results of the conventional alumina, undoped alumina aerogel and yttria doped alumina with various yttria loadings^a

Sample	Calcination Temperature (°C)/6 h			
	750 °C	1000 °C	1100 °C	1200 °C
Conv.alumina [15]	γ -Al ₂ O ₃	θ -, and α -Al ₂ O ₃	α -Al ₂ O ₃ + traces of θ -phase	α -Al ₂ O ₃
5.0 wt.% Y ₂ O ₃ /conv.alumina	γ -Al ₂ O ₃	γ -Al ₂ O ₃	θ -Al ₂ O ₃ + YAlO ₃	α -Al ₂ O ₃ + traces of YAlO ₃
10.0 wt.% Y ₂ O ₃ /conv.alumina	γ -Al ₂ O ₃	γ -Al ₂ O ₃	θ -Al ₂ O ₃ + YAlO ₃	α -Al ₂ O ₃ + YAlO ₃
20.0 wt.% Y ₂ O ₃ /conv.alumina	Y ₂ O ₃	Y ₂ O ₃ + YAlO ₃	Y ₂ O ₃ + YAlO ₃ + traces of θ -Al ₂ O ₃	YAlO ₃ + Y ₂ O ₃ + traces of α -Al ₂ O ₃
Alumina aerogel [15]	γ -Al ₂ O ₃	γ -Al ₂ O ₃ + traces of θ -phase	θ -Al ₂ O ₃ + traces of α -phase	α -Al ₂ O ₃
5.0 wt.% Y ₂ O ₃ /alumina aerogel	γ -Al ₂ O ₃	γ -Al ₂ O ₃	θ -Al ₂ O ₃ + YAlO ₃	α -Al ₂ O ₃ + traces of YAlO ₃
10.0 wt.% Y ₂ O ₃ /alumina aerogel	γ -Al ₂ O ₃	γ -Al ₂ O ₃	θ -Al ₂ O ₃ + YAlO ₃	YAlO ₃ + traces of α -Al ₂ O ₃
20.0 wt.% Y ₂ O ₃ /alumina aerogel	Y ₂ O ₃	Y ₂ O ₃ + YAlO ₃	YAlO ₃	YAlO ₃ + traces of α -Al ₂ O ₃

^a γ -Al₂O₃ (JCPDS No. 10-425), θ -Al₂O₃ (JCPDS No. 35-0121), α -Al₂O₃ (JCPDS No. 10-173), YAlO₃ (JCPDS No. 16-219 or 38-222), and Y₂O₃ (JCPDS No. 25-1200)

Conv.alumina being metastable is transformed into several phases with increasing temperature. The observed phase transformation of conv.alumina in the present investigation was $\gamma \rightarrow \theta \rightarrow \alpha$, which was in complete agreement with previous investigations [14 and reference therein]. Conventional alumina that was calcined at 750 °C showed the presence of γ -phase and at 1000 °C this phase was transformed to both θ - and α -phase. Calcination at 1200 °C resulted solely in the formation of the α -phase (corundum). Y₂O₃/conv.alumina with different yttria loadings (5.0-20.0 wt.%), which

were calcined at 750 °C showed the presence of γ -phase in samples containing 5.0-10.0 wt.% Y_2O_3 . However, alumina impregnated with 20.0 wt.% Y_2O_3 showed clearly the presence of segregated bulk Y_2O_3 crystallites. Further calcination of yttria impregnated alumina with yttria loading of 5.0-10.0 wt.%, to 1000 °C did not result in any changes, when compared to the same samples calcined at 750 °C. In particular, the XRD pattern of sample containing 20.0 wt. % yttria showed the presence of bulk Y_2O_3 crystallites, along with traces of $YAlO_3$. The latter was probably formed as a result of solid state reaction between yttria and alumina. It is quite clear that yttria impregnated conv.alumina with yttria loading up to 10.0 wt.% did not show any diffraction peaks that could be attributed to either θ - or α -phase. This can be viewed as a clear indication of the improved thermal stability. However, further calcination of yttria impregnated alumina (with yttria loading up to 10.0 wt.%) to 1100 °C showed in addition to θ -phase, the presence of yttrium aluminate ($YAlO_3$) phase. The diffraction peaks of the latter were increased with increasing amount of yttria. It was also noted that yttria impregnated alumina samples that were calcined at 1200 °C displayed clearly the presence of α -phase, along with $YAlO_3$, whose peaks were more pronounced with higher yttria loadings (10.0 wt.%). The XRD pattern of 20.0 wt.% yttria impregnated alumina showed the presence of several reflections, which were attributed to bulk yttria and $YAlO_3$ crystallites, along with traces of α -phase.

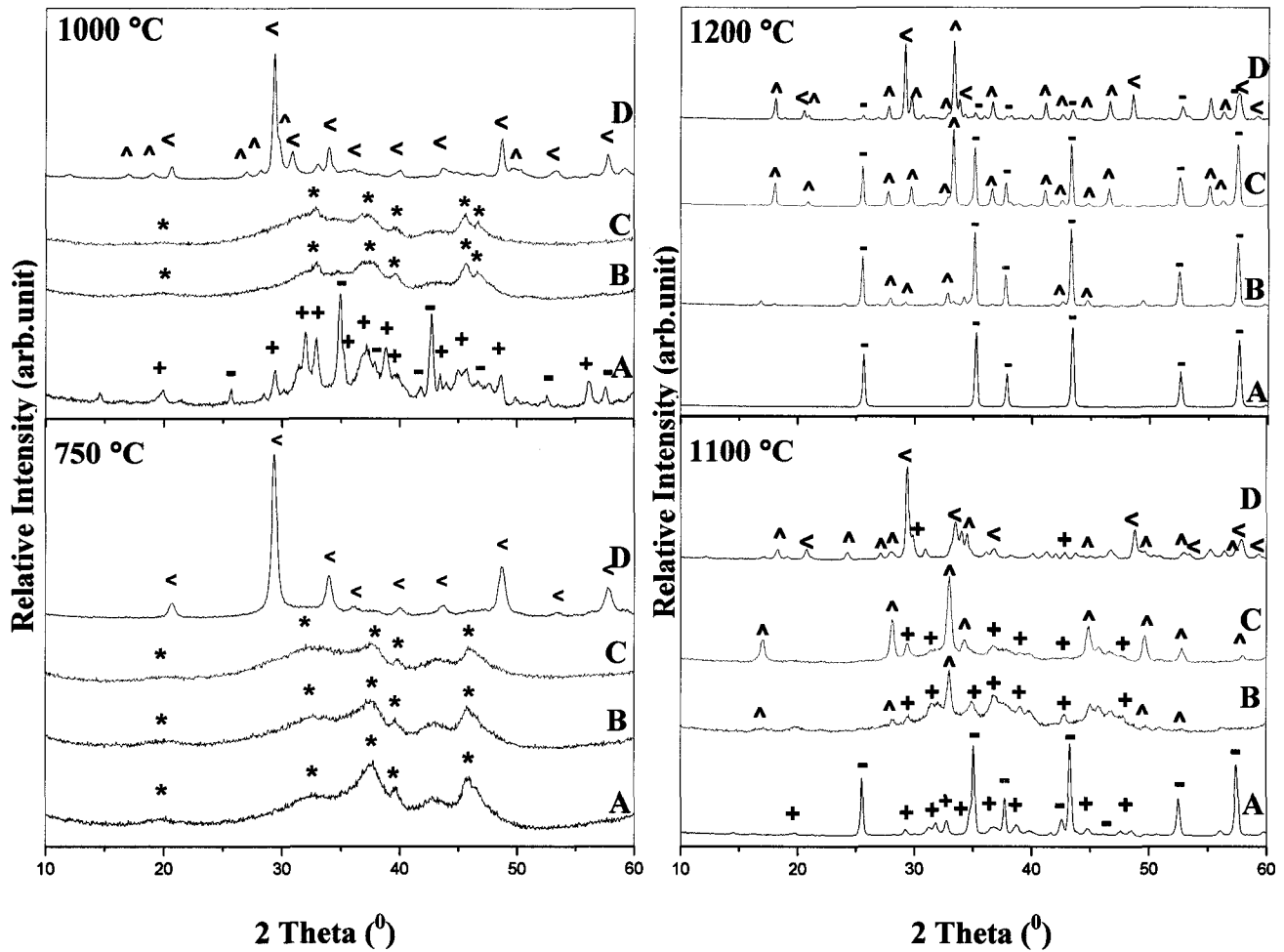


Fig.5.5: XRD patterns of calcined samples at different temperature; A- Conv.alumina, B- 5.0 Y₂O₃/Al₂O₃, C- 10.0 Y₂O₃/Al₂O₃, and D- 20.0 Y₂O₃/Al₂O₃. (*) γ-Al₂O₃, (+) θ-Al₂O₃, (-) α-Al₂O₃ (^) YAlO₃, and (<) Y₂O₃

The X-ray diffraction patterns of Y₂O₃/ alumina aerogel, which was calcined for 6 h at 750, 1000, 1100 and 1200 °C, are shown in Fig. 5.6 (also Table 5.4). Comparison between the XRD patterns of Y₂O₃/conv.alumina and Y₂O₃/alumina aerogel reveals that the thermal stability of alumina aerogel (which was already higher than that of conv.alumina [14] was further improved upon incorporating yttria via impregnation. This was evident from the retardation of sintering and phase transformation of γ-alumina into

θ -phase and α -phase. Furthermore, the formation of segregated yttria crystallites in yttria impregnated alumina aerogel with 20.0 wt.% yttria loading was significantly hindered, when compared to conv.alumina. This can be attributed to the large surface area [14] and high number of -OH groups observed with undoped alumina aerogel. It is quite important to mention that the stabilization of conv.alumina and alumina aerogel upon incorporating yttria (5-10.0 wt.%) via impregnation was noted to be no longer effective at temperature higher than 1000 °C. This is due to nucleation of $YAlO_3$ structure at 1100 °C, and due to the presence of $YAlO_3$ and α -phase at 1200 °C. Another important point to emphasize is that the addition of 20.0 wt.% yttria was not so effective in promoting thermal stabilization of alumina. This is due to the formation of segregated bulk yttria and yttrium aluminate crystallites.

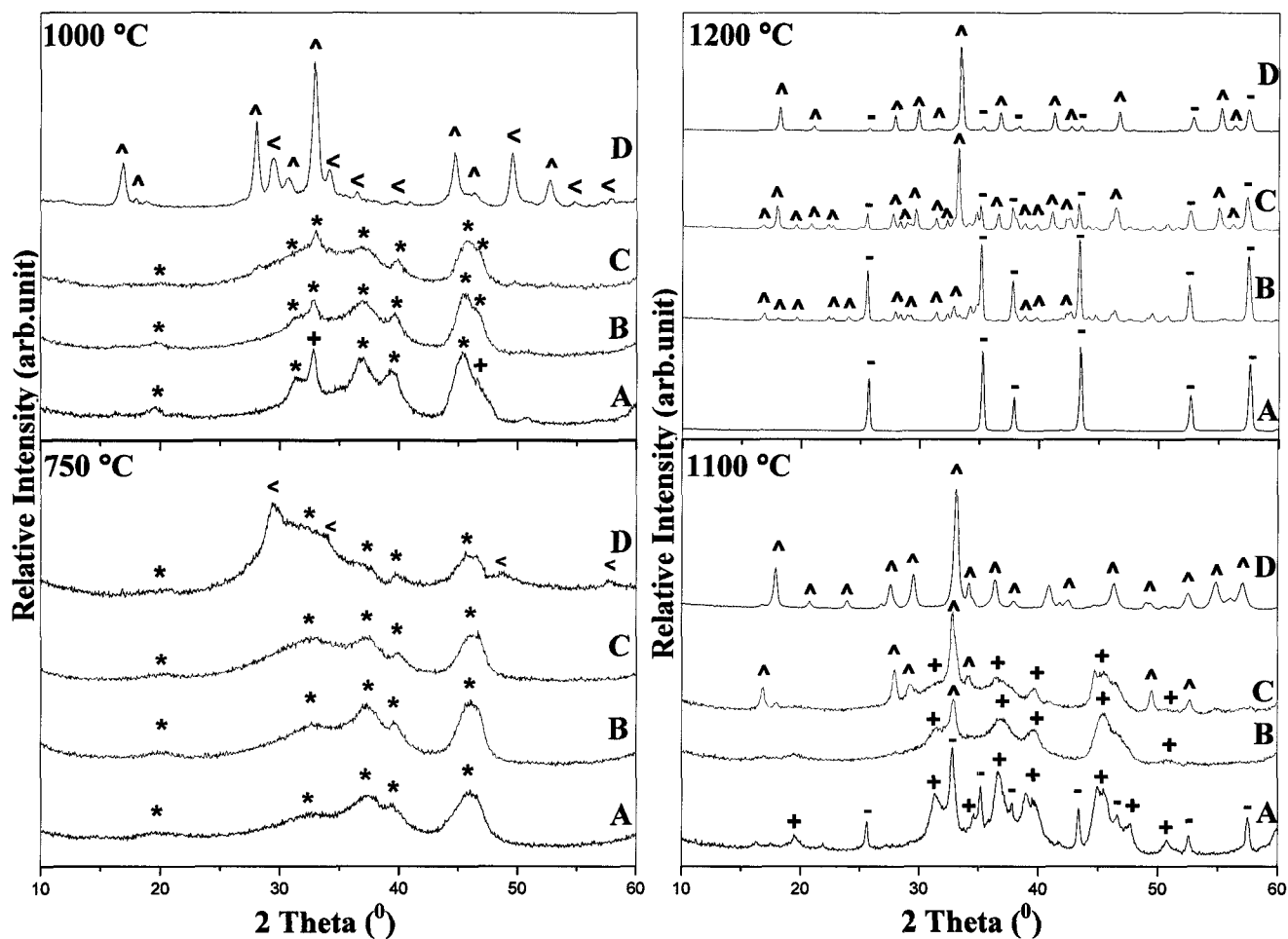


Fig.5.6: XRD patterns of calcined samples at at different temperature; A- alumina aerogel, B- 5.0 Y₂O₃/aerogel, C- 10.0 Y₂O₃/aerogel, and D- 20.0 Y₂O₃/aerogel. (Note: for symbols refer to Fig. 5.5)

Table 5.5 also reports the changes in the BET specific surface area and total pore volume of yttria impregnated conv.alumina and alumina aerogel with various yttria loadings (5.0-20.0 wt.% yttria), calcined at different temperature for 6h. It can be seen that yttria impregnated alumina and alumina aerogel showed higher specific surface area when compared to its conv.alumina counterpart, irrespective of the calcination temperature (750 or 1000 °C) and yttria loading (5.0-20.0 wt.%). This can be attributed the supercritical (or hypercritical) drying of liquids contained in the gel [14].

Table 5.5: Changes in the specific surface area (S_{BET}) and total pore volume of yttria-impregnated alumina (i.e. conv.alumina and alumina aerogel) as a function of calcination temperature for 6 h

Sample	Calcination Temperature (°C)							
	750°C		1000°C		1100°C		1200°C	
	S_{BET} (m ² /g)	PV ^a (cc/g)	S_{BET} (m ² /g)	PV (cc/g)	S_{BET} (m ² /g)	PV (cc/g)	S_{BET} (m ² /g)	PV (cc/g)
Conv.alumina [15]	116	0.253	51.0 (0.44) ^b	0.230	20.0 (0.17)	0.076	7.00 (0.06)	0.0
5.0 wt.% Y ₂ O ₃ /conv.alumina	105	0.210	70.0 (0.67)	0.192	32.0 (0.30)	0.126	8.0 (0.08)	0.021
10.0 wt.% Y ₂ O ₃ /conv.alumina	83.0	0.159	61.0 (0.73)	0.171	25.0 (0.30)	0.120	8.0 (0.08)	0.014
20.0 wt.% Y ₂ O ₃ /conv.alumina	63.0	0.123	31.0 (0.50)	0.105	17.0 (0.27)	0.066	7.0 (0.11)	0.011
Alumina aerogel [15]	277	1.15	126 (0.46)	0.599	62.0 (0.22)	0.281	11.0 (0.04)	0.003
5.0 wt.% Y ₂ O ₃ /alumina aerogel	192	0.503	137 (0.71)	0.465	102.0 (0.53)	0.351	11.0 (0.06)	0.062
10.0 wt.% Y ₂ O ₃ /alumina aerogel	158	0.369	110.0 (0.70)	0.349	65.0 (0.41)	0.240	6.0 (0.04)	0.014
20.0 wt.% Y ₂ O ₃ /alumina aerogel	110	0.279	57.0 (0.52)	0.204	31.0 (0.28)	0.140	5.0 (0.05)	0.011

^a PV is total pore volume. ^b ratio of S_{BET} of sample calcined at xT (°C) to S_{BET} of sample calcined at 750 °C, where x = 1000,1100 or 1200 °C

In addition, the N₂ adsorption results displayed in Table 5.5 are in complete agreement with the XRD measurements. First, the addition of yttria via impregnation onto either conv.alumina or alumina aerogel has resulted in significantly improved thermal stability, as suggested by the decrease in the sintering rate (smaller area loss). Second, the extent of decrease was observed to be higher for yttria doped alumina aerogel. It was also noted from Table 5.5 that 5.0 wt.% yttria impregnated conv.alumina or alumina aerogel that was calcined at 750-1100 °C displayed the higher S_{BET} area, when compared to the bare support or other yttria loaded samples.

The loss of specific surface area of yttria impregnated conv.alumina and alumina aerogel after 50 h of calcination at 750 and 1000 °C are presented in Fig.5.7. It is clearly shown that yttria impregnated conv.alumina and alumina aerogel displayed higher thermal stability compared to the bare supports. This was observed irrespective of yttria loadings. In addition to that, it was demonstrated that the extent of thermal stability improvement upon the addition of yttria via impregnation was higher for alumina aerogel than for conv.alumina. For instance, yttria impregnated conv.alumina with 5.0 wt.% Y₂O₃ that was calcined at 1000 °C for 50 h suffered a loss of ca. 35 % of its surface area, while alumina aerogel counterpart lost only ca. 18 % of its surface area. The observed loss for undoped alumina aerogel was ca. 44 %, whereas conv.alumina suffered ca. 69 % loss, upon calcination for 50h at 1000 °C.

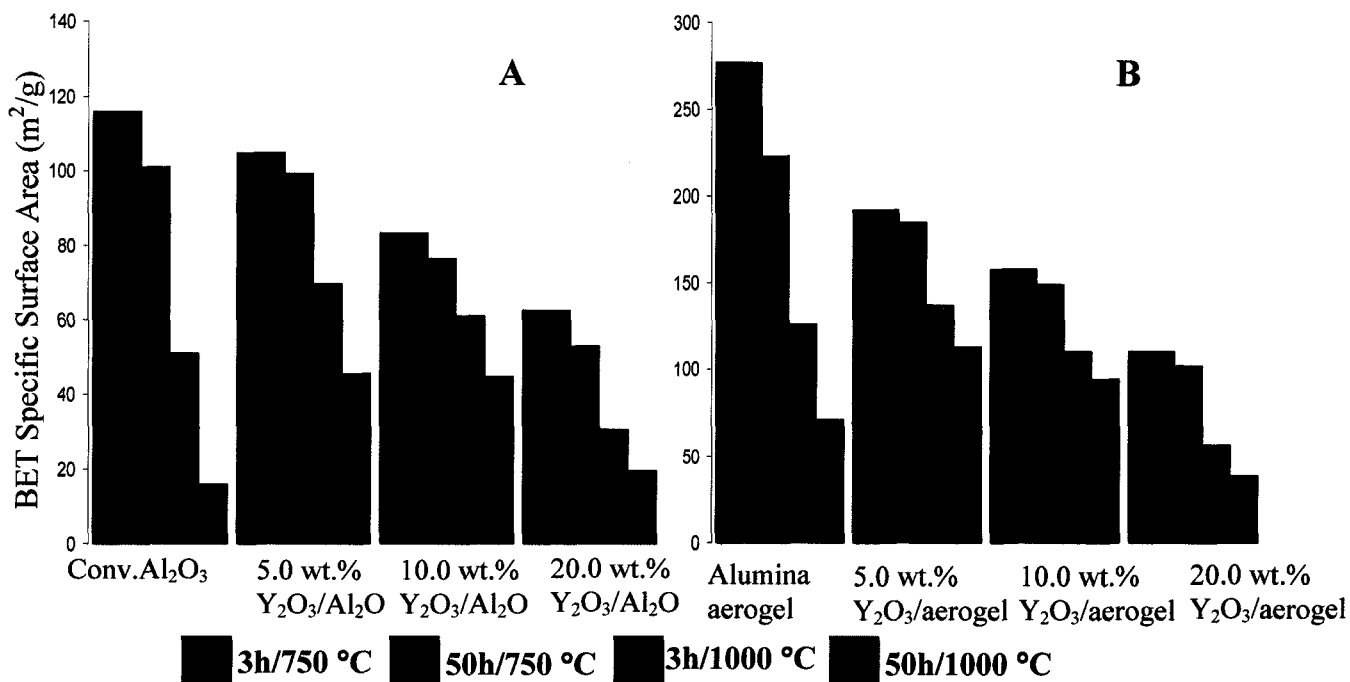


Fig.5.7: Loss of BET specific surface area (S_{BET}) as a function of different calcination temperature at different duration, of yttria impregnated conv.alumina (A) and alumina aerogel (B) with various yttria loadings, respectively

The change in BET specific surface area of 10.0 wt.% yttria impregnated conv.alumina or alumina aerogel, which were subjected to steaming at different temperatures with different exposure times are shown in Figure 5.8 (the correlation factor (R^2) was obtained in order to evaluate the linearity of the noted changes, which in turn may reflect the extent of surface area loss). It was noted that the hydrothermal stability of conv.alumina and alumina aerogel were also improved as a result of adding yttria via impregnation. This was suggested by the small loss in the surface area (Fig.5.8A) and the minimization of structural transformations (XRD patterns not shown here), when compared to the bare support. For instance, the area loss for 10.0 wt.% Y₂O₃/conv.alumina was ca. 6.5 % and 14 %, when exposed to steam at 750 °C for 1 h and 24 h, respectively (Fig.5.8 A), while

the corresponding area losses for conv.alumina were ca. 22 % and 35 %, respectively (Table 5.1).

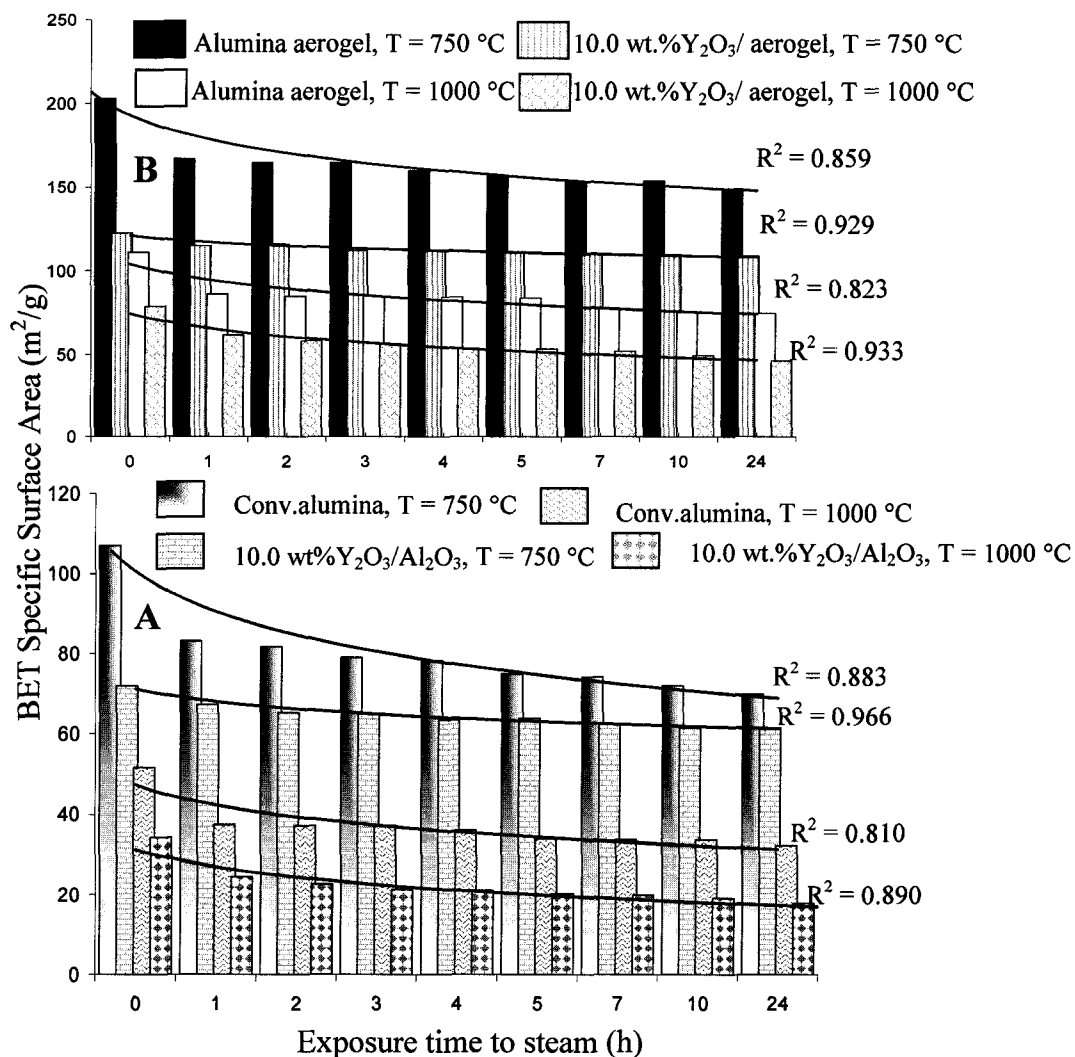


Fig.5.8: Loss of BET specific surface area (S_{BET}) as a function of different exposure time to steam at different temperature, of 10.0 wt.% yttria impregnated conventional alumina (A) and alumina aerogel (B), respectively

On the other hand, the area loss for 10.0 wt.% Y₂O₃/alumina aerogel was ca. 6.2 % and 11 %, when exposed to steam at 750 °C for 1 h and 24 h, respectively (Fig.5.8 B), while these numbers for alumina aerogel, were ca. 18 % and 26 %, respectively (Table 5.1).

These results also suggested that the extent of hydrothermal stability was slightly higher for alumina aerogel than for conv.alumina, upon yttria impregnation. It is worth mentioning that similar results were observed for 10.0 wt.% yttria impregnated conventional alumina or alumina aerogel, which were subjected to atmospheric steam at 1000 °C with different exposure time (Fig.5.8 B).

The improved thermal and hydrothermal stability of yttria impregnated conventional alumina and alumina aerogel with yttria loadings of 5-10.0 wt.% up to 1000 °C, when compared to the bare supports, can be attributed to the yttria. The loading of yttria via impregnation onto the surface of alumina has resulted in decreasing or neutralizing the effect of cationic and anionic surface defects, and more importantly in reducing the number of -OH groups. The TGA and FTIR spectra of adsorbed pyridine clearly showed that the number of removed -OH groups (Table 5.3) and subsequently the number of Lewis sites (cus) (Fig.5.3, Table 5.3) were drastically reduced. The noted effect of yttria occurred most probably through the formation of dispersed yttrium aluminate structure, which is more thermally stable than alumina and whose presence has been confirmed indirectly by XRD patterns (i.e. bulk $YAlO_3$ crystallites were clearly detectable at $T > 1000$ °C). The higher extent of thermal and hydrothermal stability of alumina aerogel compared to conv.alumina, upon yttria impregnation, can be mainly attributed to alumina aerogel itself and in turn to the sol-gel method.

5.3.4. Comparison between yttria doped alumina aerogel and yttria impregnated alumina (conventional alumina and alumina aerogel)

Careful comparison of the properties of yttria doped alumina aerogel, and that of yttria impregnated conv.alumina and alumina aerogel can lead to one definite conclusion. The textural properties (i.e. surface area, dispersion) [14,15], and thermal [14] and

hydrothermal stability of alumina aerogel (current work) were significantly improved, when yttria was incorporated via the sol-gel, rather than the impregnation method. First, the surface area was noted to be much higher for alumina aerogel, even after incorporating the yttria. For instance, the S_{BET} of 10.0 wt.% yttria doped alumina aerogel was 319 m^2/g [14], which is 161 m^2/g higher than its impregnated alumina aerogel counterpart (158 m^2/g) (Table 5.5). Second, yttria doped alumina aerogel was more thermally stable [14] compared to yttria impregnated alumina (conv.alumina and aerogel). This was suggested by the lower area loss and further delay in the phase transitions, upon calcination at high temperature (Figs. 5.5-6, Tables 5.4-5, and [14]). In addition, it was concluded that yttria doped alumina aerogel, impregnated aerogel, and impregnated conv.alumina are only thermally stable up to temperature below 1100 °C. The instability at higher temperature is due to nucleation of bulk YAlO_3 crystallites. Third, the influence of steam at high temperature was less pronounced in yttria doped alumina aerogel (Figs.5.1-2, and Tables 5.1-2), compared to yttria impregnated alumina (Fig. 5.8). Fourth, it was possible to incorporate a high loading of yttria (20.0 wt.%) into alumina aerogel without observing the oxide segregation phenomenon [14], which on the contrary occurred easily with the impregnated samples (Figs.5.5-6). Fifth, although the incorporation of yttria into alumina aerogel via sol-gel or impregnation has led to a reduction in the number of -OH groups, it was apparent that the extent of such reduction was smaller for yttria doped alumina aerogel (Table 5.3). All this has a practical consequence: the important properties of alumina such as the acid-base characteristics and the ability to disperse active species and promoters are significantly preserved. In fact, we have unambiguously found that the dispersion of mono-oxide MoO_3 and bi-

oxide $\text{MoO}_3\text{-CeO}_2$ were significantly improved when impregnated onto alumina aerogel [15]. We do anticipate that such dispersion will be enormously weakened if yttria impregnated alumina was used as a catalyst support. The main reason behind these outstanding properties of yttria doped alumina aerogel when compared to yttria impregnated alumina can be attributed to the fact that yttria was allowed to be efficiently inserted into the alumina aerogel lattice (or network). On the contrary, the solubility of yttria in alumina lattice was quite limited in the case of impregnation method. This was clearly supported by the ^{27}Al MAS NMR study. The ^{27}Al MAS NMR of conv.alumina [14], alumina aerogel [14], 10.0 and 20.0 wt.% yttria doped alumina aerogel [14], and yttria impregnated conv.alumina and alumina aerogel with various yttria loadings (current work) are shown in Fig.5.9 A-H. The ^{27}Al MAS NMR spectra of yttria impregnated conv.alumina or alumina aerogel with various yttria loadings (Fig.5.9 E-H) reveal the presence of two peaks, at ca. -3.0-7.0 ppm and another one at ca. 57-65 ppm. These peaks are assigned unambiguously to octahedral and tetrahedral coordinated aluminium, respectively [44,45]. No change can be observed when comparing these spectra to those of the bare supports, which were performed during our previous study (Fig.5.9 A-B) [14]. On the contrary, these spectra are noticeably different from those of yttria doped alumina aerogel, which were also carried out during our previous study (Fig.5.9 C-D) [14]. The peak at ca. 33.0 ppm, which was clearly observed in yttria doped alumina aerogel and assigned to surface distorted $\text{Al}_{\text{tetra}}\text{-O-Y}$ bond) [14 and references therein], was absent in yttria impregnated conv.alumina or alumina aerogel. Therefore, it can be inferred from these results that the incorporation of yttria via the sol-gel method provoked structural rearrangement of the aluminum coordination that played a major role

in preventing the formation of segregated bulk Y_2O_3 crystallites, and hence decreasing the tendency of forming large $YAlO_3$ crystallites.

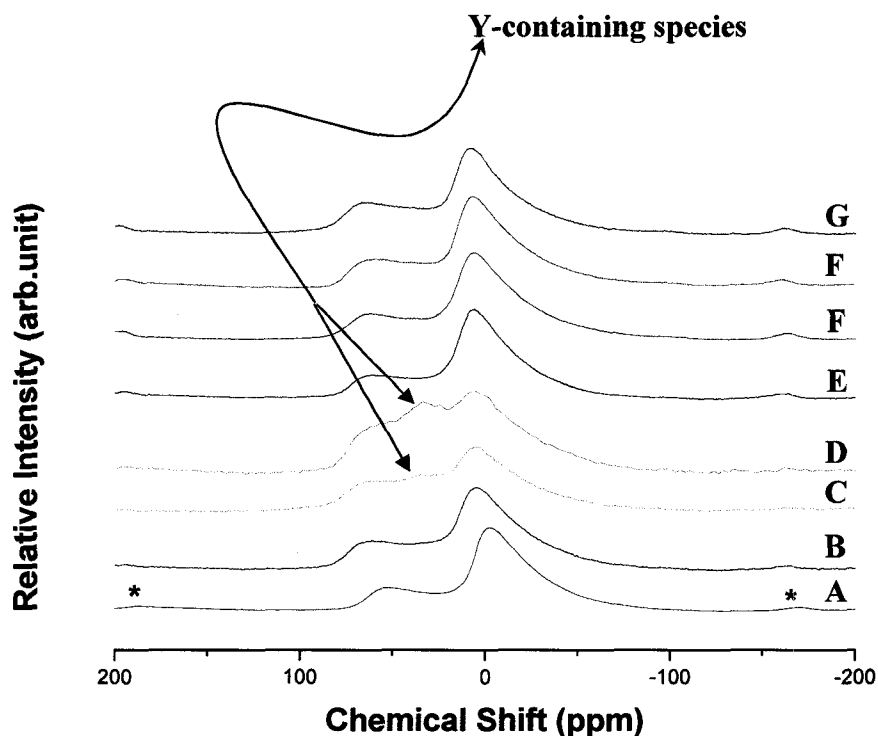


Fig.5.9: ^{27}Al MAS NMR of samples calcined at 750 °C for 6 h. (A) conv.alumina [15], (B) alumina aerogel [15], (C) and (D) 10.0 and 20.0 wt.% yttria doped alumina aerogel, respectively [15], (E) and (F) 10.0 and 20.0 wt.% yttria impregnated conv.alumina, respectively, and (G) and (H) 10.0 and 20.0 wt.% yttria impregnated alumina aerogel, respectively (* spinning side bands (SSB))

5.4. CONCLUSION

The results presented in this work reinforce our conclusion that yttria doped alumina aerogel is an effective support for TCC process. It was found that the incorporation of Y_2O_3 into alumina aerogel structure via the sol-gel method has another significant beneficial role, besides improving the thermal stability [14] and the ability to homogeneously disperse the active species and promoters at high calcination temperature (15). Yttria doped alumina aerogel with various yttria loadings (5.0-20.0 wt.%) was highly hydrothermally stable when compared to alumina aerogel and conv.alumina, as

suggested by N₂ adsorption measurements, XRD, TGA, FTIR of adsorbed pyridine. and ¹H MAS NMR. We have also observed that the thermal and hydrothermal stability of both yttria impregnated alumina aerogel and conv.alumina were improved but to a lower extent. These improved stabilities were attributed to the presence of yttria, and subsequently the formation of surface yttrium aluminate. Therefore, it can be concluded that in order to observe the most efficient stabilizing effect of yttria, it is quite essential to incorporate it into the alumina structure via the sol-gel preparation technique.

5.5. ACKNOWLEDGEMENTS

Financial support from NSERC (Natural Science and Engineering Research Council of Canada) and Valeo Management are acknowledged. The authors also thank Dr. Cedric Malveau (University of Montreal), and Dr. G. Denes (Concordia University) for technical assistance (¹H and ²⁷Al MAS NMR and XRD, respectively).

5.6. AUTHOR'S NOTES AND SIGNIFICANCE OF PAPER To THESIS

This work on the hydrothermal stability of yttria doped alumina aerogel was the first article published in the literature on the influence of atmospheric steam at 750 and 1000 °C, on the stability of yttria doped alumina aerogel. This study has shown that the hydrothermal stability of yttria doped alumina aerogel was greatly improved compared to alumina aerogel and conventional alumina. These significant improvements were attributed to the combined effect of sol-gel method and the presence of yttrium ions. In addition, this work showed for the first time that the thermal and hydrothermal stability of alumina (conventional or aerogel) could be improved by adding yttria onto the surface via impregnation method. However, the extent of these improvements was lower than those observed upon incorporating yttria into the alumina structure via sol-gel method.

This chapter is of great significance to the thesis, since it demonstrated that yttria doped alumina aerogel is hydrothermally stable. Thus, it can be used as a catalyst support in the TCC process, which requires the presence of steam.

The following chapter presents the influence of yttria used as a doping agent for catalyst support, on the dispersion and the resistance to sintering of MoO₃, CeO₂ and bi-oxide MoO₃-CeO₂ species. It is well known that the physico-chemical and consequently the catalytic properties of supported metal oxides catalysts are influenced by many factors, however the nature of the catalyst support is one of the most important. Therefore, it was imperative to investigate in great details the influence of yttria doped alumina aerogel on the physico-chemical properties of mono-oxide MoO₃, CeO₂ and bi-oxide MoO₃-CeO₂, and determine whether this support can show an additional and unique characteristic beside the high thermal and hydrothermal stability.

5.7. REFERENCES

- [1] P. Pujado, D. Greer, J. Andersen, T. Foley, V. Bhirud, pre-print Archive-American Institute of Chemical Engineering, [Spring National Meeting], New Orleans, LA, USA. March 11-14 (2002) 2471.
- [2] A. Corma, F. V. Melo, L. Sauvanaud, F. Ortega, *Catal.Today*. **107** (2005) 699.
- [3] J.S. Plotkin, *Catal.Today*. 106 (2005) 10.
- [4] A. Chauvel, G. Lefebvre, *Petrochemical Processes*, Vol. 1, Technip, Paris, 1989, p. 117.
- [5] S. Matar and L.F. Hatch, in: *Chemistry of Petrochemical Processes*, 2nd ed., Gulf Professional Publishing, Woburn, MA, (2001).
- [6] D.A. Hunt, in: *Handbook of Petroleum Refining Processes*, 2nd ed., ed. R.A. Meyers,

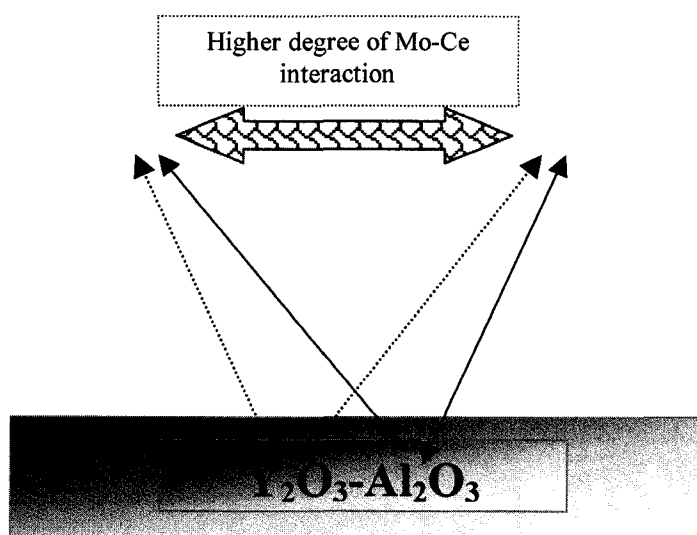
- McGraw Hill, Boston, (1997).
- [7] R. Le Van Mao, Concordia University, US Patent 4, 732, 881 (1988).
- [8] R. Le Van Mao, S. Melancon, C. Gauthier-Campbell, P. Kletnieks, *Catal. Lett.* **73** (2001) 181.
- [9] S. Melancon, R. Le Van Mao, P. Kletnieks, D. Ohayon, S. Intem, M.A. Saberi, D. McCann, *Catal. Lett.* **80** (2002) 103.
- [10] R. Le Van Mao, N. Al-Yassir, D. N., *Micropor. Mesopor. Mater.* **85** (2005) 176.
- [11] N. Al-Yassir, R. Le Van Mao, F. Heng, *Catal. Lett.* **100** (2005) 1.
- [12] N. Al-Yassir, R. Le Van Mao, *Appl. Catal. A: Gen.* **305** (2006) 130.
- [13] R. Le Van Mao, N-T. Vu, N. Al-Yassir, N. Francois, J. Monnier, *Top. Catal.* **37** (2006) 107.
- [14] N. Al-Yassir, R. Le Van Mao, *Appl. Catal. A: Gen.* **317** (2007) 275.
- [15] N. Al-Yassir, R. Le Van Mao, *Appl. Catal. A: Gen.* **332** (2007) 275.
- [16] H. Schaper, E.B.M. Doesburg, L.L. Van Reijen, *Appl. Catal.* **7** (1983) 211.
- [17] P. Burtin, J.P. Brunelle, M. Pijolat, M. Soustelle, *Appl. Catal.* **34** (1987) 239
- [18] F. Oudet, P. Courtine, A. Vejux, *J. Catal.* **114** (1988) 112.
- [19]. M.F.L. Johnson, *J.Catal.* **123** (1990) 245.
- [20]. M. Ozawa, M. Kimura, A. Isogai, *J. Less-common metals.* **162** (1990) 297
- [21]. B. Beguin, E. Garbowski, M. Primet, *J. Catal.* **127** (1991) 595.
- [22] H. Aria, M. Machida, *Appl. Catal. A: Gen.* **138** (1996) 161.
- [23] H. Topsoe, B.S. Clausen, F.E. Massoth, in: J.R. Anderson, M. Boudart (Eds.), *Catalysis Science and Technology*, vol. 11, Springer, New York, 1996.
- [24] M. Pijolat, M. Dauzat, M. Soustelle, *Solid State Ionics*, **50** (1992) 31.

- [25] J. Barbier Jr, D. Duprez, *Appl. Catal. B: Environ.* **4** (1994) 105.
- [26] E. Ponthieu, J. Grimblot, E. Elaloui, G. Pajonk. *J. Mater. Chem.* **3** (1993) 287.
- [27] E. Elaloui, R. Begag, B. Pommier, G.M. Pajonk, *Stud. Surf. Sci. Catal.* **143** (2002) 331.
- [28] R. Rostrup-Nielsen In: J.R. Anderson and M. Boudart, Editors, *Catalysis Science and Technology* vol. **5**, Springer-Verlag, New York (1984).
- [29] V. I. Vereshchagin, V. Yu. Zelinski, T.A. Khabas, N. N. Kolova, *Zhurnal Prikladnoi Khimii*, **55** (1982) 1046.
- [30] JCPDS, X-ray Powder Data File, International Center for Diffraction Data, Pennsylvania, 1989.
- [31] H. Knözinger, P. Ratnasamy, *Catal. Rev.-Sci. Eng.* **71** (1978) 31.
- [32] J.A. Wang, X. Bokhimi, O. Novaro, T. Lopez, F. Tzompantzi, R. Gomez, J. Navarrete, M. E. Llanos, E. Lopez-Salinas, *J. Mol. Cata. A: Chem.*, **137** (1999) 239.
- [33] D. J. Coster, J. J. Fripiat, M. Muscas, A. Auroux, *Langmuir*, **11** (1995) 2615.
- [34] M. Trueba, S. P. Trasatti, *Eur. J. Inorg. Chem.*, **17** (2005) 3393.
- [35] G. Busca, *Catal. Today*, **41** (1998) 191.
- [36] V. Baran, *Coord. Chem. Rev.*, **6** (1971) 65.
- [37] C. Morterra, G. Magnacca, *Catal. Today*, **27** (1996) 497.
- [38].S. Rajagopal, J.A. Marzari, and R. Miranda, *J. Catal.* **151** (1995) 192
- [39] R. D. Gonzalez, T. Lopez, R. Gomez, *Catal. Today*, **35** (1997) 293.
- [40] H. Kraus, R. Prines, *J. Catal.* **164** (1996) 260.
- [41] E.C. Decanio, J.C. Edwards, J.W. Bruno, *J. Catal.* **148** (1994) 76.
- [42] V.M. Mastikhin, V.V. Terskikh, O.B. Lapina, S.V. Filimonova, M. Seidl, H.

- Knozinger, *J.Catal.* **156** (1995) 1.
- [43] L. Qu, W. Zhang, P.J. Kooyman, R. Prins, *J.Catal.* **215** (2003) 7.
- [44] G.A. Pozarnsky, A.V. McCormicks, *J. Non-Cryst. Solid*, 190 (1995) 212.
- [45] T.E. Wood, A.R. Siedle, J.R. ill, R.P. Skarjune, C.J. Goodbrake, *J.Mater. Res. Soc. Symp. Proc.* **180** (1997) 97.

Chapter VI

Catalysts for the Thermo-Catalytic Cracking (TCC) Process: Interactions between the yttria in yttria doped alumina aerogel and the mono-oxide MoO_3 , CeO_2 , and bi-oxide $\text{MoO}_3\text{-CeO}_2$ species



Graphical Abstract: Schematic representation of the interaction between Mo, Ce, and Mo-Ce with the support (Al_2O_3 and $\text{Y}_2\text{O}_3\text{-Al}_2\text{O}_3$)

Published as:

N. Al-Yassir and R. Le Van Mao,

Applied Catalysis A: General **332** (2007) 273-288.

ABSTRACT

The influence of yttria used as a doping agent for catalyst support, on the dispersion and the resistance to sintering of MoO_3 , CeO_2 and bi-oxide $\text{MoO}_3\text{-CeO}_2$ species in the TCC catalysts has been investigated. Characterization techniques used included N_2 adsorption, X-ray diffraction, Raman, thermogravimetric analysis, and Isoelectric point (IEP). It was explicitly found that yttria doped alumina aerogel is far more capable of homogeneously dispersing the active molybdenum species and significantly retarding their sintering at quite high calcination temperature than conventional alumina and alumina aerogel. Characterization results of supported mono-oxide MoO_3 catalysts have clearly indicated that the fraction of (surface) tetrahedral monomolybdate species increases in the detriment of crystalline MoO_3 as we varied the support from conventional alumina to yttria doped alumina aerogel with increasing amounts of the yttria loading. This can be attributed to the incorporation of yttria into alumina aerogel network, which led to a change in the support surface charge (IEP) and subsequently the stability of surface molybdate species. The dispersion degree of ceria (substituted ceria) on supported mono-oxide CeO_2 was improved as well, upon using yttria doped alumina aerogel. Such improvement was attributed to the formation of stronger Ce-Y-O bonds, and/or the formation of $\text{CeO}_2\text{-Y}_2\text{O}_3$ solid solution. In the bi-oxide $\text{MoO}_3\text{-CeO}_2$, characterization results have indicated the presence of surface interaction between Mo and Ce, probably through the formation of surface “Mo-O-Ce” type phase between the dispersed ceria and the molybdate monolayer. This interaction, which was highly favourable over yttria doped alumina surface, contributed significantly to the overall surface stability of Mo-Ce catalysts.

6.1. INTRODUCTION

Light olefins and diolefins such as ethylene, propylene, butenes and butadienes are considered the backbone of the petrochemical industry [1,2]. They are the precursors of numerous plastic materials, synthetic fibers and rubbers. The most prevalent technology for producing these precursors from petroleum feedstocks is Steam Cracking (SC) [1-4]. However, this conventional technology cannot respond adequately to the rapidly growing demand for propylene, since the latter is only produced as a co-product [2]. In addition, the high-energy consumption and the increasingly stringent environmental regulations that require low green house gas emissions (i.e. CO₂) are also putting a stress on the SC process. Thermo-Catalytic Cracking (TCC) of petroleum feedstocks for the production of light olefins has been developed in an attempt to overcome some of these challenges [5-14]. The TCC process is considered more advantageous than SC since it produces higher yields of ethylene and propylene, it has low energy costs, and is a more environmentally friendly process. This process employs supported metal oxides (i.e. MoO₃-CeO₂) catalysts. Therefore, evaluating the influence of the catalyst support on the dispersion, structure and properties of active components and promoters is of paramount importance. In addition, any further knowledge that can contribute to a better understanding of the support effects on the physico-chemical properties of MoO₃ and CeO₂ based catalysts is tremendously significant. These supported catalysts have been proven to be effective in many industrial reactions. For instance, MoO₃ catalysts have been widely used in olefin metathesis [15], oxidation and ammoxidation reactions [16-17], as well as hydrotreating [18]. Whereas, CeO₂ catalysts

forms an integral part of three-way catalysts for automotive exhaust treatment [19], and serves as a promoter in the fluid catalytic cracking catalysts [20].

Support and active phase metal oxide interaction can influence the metal oxide morphology, dispersion and stability [21-25]. In addition, new active sites may develop at the interface between the support and the metal oxide [26]. Conventional alumina does not show high enough thermal stability or strong enough interaction with some oxides for the TCC process application. Our previous publication [13] has shown that alumina doped with Y and prepared via a sol-gel method using a supercritical drying technique has the desired properties of high thermal stability, porosity and surface area. In the present investigation, we would like to examine the suitability of using yttria doped alumina aerogel as a support for the TCC oxide catalysts. We will be examining whether yttria doped alumina aerogel is capable of inducing a homogenous distribution of impregnated metals (i.e. Mo, Ce, or Mo-Ce) and consequently improve their physico-chemical properties, at high calcination temperature. To the best of our knowledge, no work has been reported yet in the literature on $\text{MoO}_3\text{-CeO}_2$ supported on yttria doped alumina aerogel. Therefore, a systematic investigation of both mono- and bi-oxide supported on alumina aerogel and yttria doped alumina aerogel with various yttria loadings was undertaken. Conventional alumina was also used for comparison purposes. The various catalyst systems were characterized by diverse techniques such as Brunauer-Emmett-Teller (BET) surface area, X-ray diffraction (XRD), Laser Raman spectroscopy, differential and gravimetric thermal analysis (DTA/TGA), and Iso-electric point measurement (IEP).

6.2. EXPERIMENTAL

6.2.1. Catalyst Preparation

6.2.1.1. Catalyst support

There are three different catalyst supports used in this investigation; conventional alumina, undoped and yttria doped alumina aerogel. Conventional γ -alumina was available commercially from (Strem Chemicals) and noted in this text as conv.alumina. The yttria doped alumina aerogel was prepared by previously reported synthetic technique [13, 27,28]. Aluminum tri-sec-butoxide (Strem chemicals, 98 %) and yttrium (III) nitrate hexahydrate (Strem chemicals, 99.9 %) were used as precursors. They were dissolved in 2-butanol (Aldrich), and Methanol (Aldrich), respectively. The Yttrium concentration was varied in order to have 2.5, 10.0 and 20.0 wt.% of Y_2O_3 . $Y_2O_3-Al_2O_3$ with different Y_2O_3 contents is noted as $xY_2O_3-Al_2O_3$, where x is the Y_2O_3 content in wt.%. The preparation procedures for undoped alumina aerogel noted in this text as alumina aerogel were similar to that of yttria doped alumina aerogel, except no dopant was used. All catalyst supports were calcined in air at 750 °C for 6 h.

6.2.1.2. Supported mono- and bi-oxide based catalysts

Supported mono-oxide MoO_3 and CeO_2 based catalysts

Supported mono-oxide MoO_3 and CeO_2 catalyst preparation are discussed in details elsewhere [12]. A series of supported MoO_3 catalysts with MoO_3 loadings in the range of 2.0-20.0 wt.% MoO_3 were prepared by impregnating the three previously mentioned catalyst supports. After impregnation, samples were first left at 60 °C for 10 h. for slow evaporation of water, dried overnight at 120°C and finally calcined in air at 750 °C for 3 h. MoO_3 /support with different MoO_3 loadings is noted as $xMoO_3$ /support,

where x is the MoO_3 content in wt.%. Mono-oxide supported CeO_2 catalysts were prepared the same way as supported MoO_3 catalyst, with CeO_2 loadings in the range of 2.0-15.0 wt.% CeO_2 . CeO_2 /support with different CeO_2 loadings is noted as $x\text{CeO}_2$ /support.

Supported bi-oxide MoO_3 - CeO_2 based catalysts

The supported bi-oxide MoO_3 - CeO_2 catalyst preparation is discussed in detail elsewhere [12]. A series of supported MoO_3 - CeO_2 catalysts with three different $[\text{Ce}]/[\text{Mo}]$ molar ratios were prepared by co-impregnation method. The MoO_3 loadings were kept constant at 12.0 wt.%, while the CeO_2 loadings were varied from 2.0-15.0 wt.% (i.e. CeO_2 in wt.% was 2.0, 6.0 and 10.0 for samples with $[\text{Ce}]/[\text{Mo}] = 0.13, 0.41,$ and 0.88, respectively). After impregnation, samples were first left at 60°C for 10 h. for slow evaporation of water, dried overnight at 120°C and finally calcined in air at 750°C for 3 h. Supported bi-oxide catalysts prepared by co-impregnation are designated: $\text{MoCe}/\text{support}$.

6.2.2. Catalyst Characterization

6.2.2.1. The specific surface areas and pore size distributions of the samples were determined by the BET method using nitrogen physisorption at 77 K. The measurements were carried out using Micromeritics ASAP 2000 apparatus. Samples were outgassed in a vacuum for 4h at 220°C before N_2 physisorption. The S_{BET} surface area results were found to be accurate to within $3.1 \text{ m}^2/\text{g}$.

6.2.2.2. X-ray powder diffraction (XRD) was carried out on a Philips diffractometer equipped with a PW 1050/25 focusing goniometer, which has been automated with the VisX122D system from diffraction technologies. The Ni filtered $\text{K}\alpha$ radiation of Cu was

used ($\lambda_{K\alpha 1} = 1.54051 \text{ \AA}$) and diffractometer was operated at 40kV and 20mA. The powder patterns were recorded in the step scanning mode from 5-60°(2 θ) at a detector angular speed of 0.3 °/min with a step size of 0.05°. The XRD phases present in the samples were identified with the help of JCPDS (Joint Committee on Powder Diffraction Standards) powder data files [29]. The average CeO₂ crystallite size of all samples (i.e. mono- and bi-component catalysts) was determined from the X-ray line broadening of the most intense peak (2 θ = 28.6° using Scherrer equation (1)):

$$D = \frac{0.9 \lambda}{B_c (2\theta \cos (\theta))} \quad (1)$$

where $B_c (2\theta)$ represents the peak width at half height after correction of the experimental broadening by the use of Warren 's equation (2):

$$[B_c (2\theta)]^2 = [B_e (2\theta)]^2 - [B_r (2\theta)]^2 \quad (2)$$

where $B_e (2\theta)$ and $B_r (2\theta)$ represent the peak width at half height for the analyzed powder and for a standard material (silicon), respectively [30]. However, the average CeO₂ crystallite size in bi-component catalyst supported on conv.alumina and alumina aerogel was calculated based on the peak at 2 θ = 33.0° instead of 28.6°, since the latter peak overlap with another peak. The cell 'a' parameter values was calculated by standard cubic indexation using the 4 lines of CeO₂ [(111), (200), (220) and (311)].

6.2.2.3. Raman spectra were collected with Nexus FT-Raman spectrometer. The spectra were recorded at room temperature using the 1064 nm line of Nd-YAG laser for excitation. The laser was operated at 0.7 watt and data were recorded using OMNIC software. The wavenumber obtained from spectra are accurate to within 4 cm⁻¹.

6.2.2.4. Thermogravimetric and differential thermal analysis (TGA/DTA) were carried out using the automated Stanton Redcroft STA 1500 simultaneous thermal analyzer from PL Thermal Sciences. The samples were heated from ambient temperature to 1150 °C under dry air flow (20.0 ml min⁻¹). The sample weights were ca. 10.0 mg, and the heating rate was 10 °C min⁻¹. The average uncertainty in the results was determined to be ± 2.0 wt.% for the weight loss, and ± 8.0 °C for the temperature.

6.2.2.5. Iso-Electric Point Measurement (IEP) was carried out using the Zeta-Meter instrument (Model 3.0+ Zeta-Meter) from Zeta-Meter, INC, USA. About 25 mg of sample was dispersed in 200 ml of 10⁻³ molL⁻¹ KCl solution and the pH was varied using 0.1 N solutions of NaOH and HCl. Zeta potential measurements were determined at ambient temperature using a microelectrophoresis technique. A high-quality stereoscopic microscope was used to detect the colloidal particles inside an electrophoresis cell chamber. Mo and Pt electrodes were placed in each end of the chamber and connected to the 3.0+ zeta-meter and an electric field was generated across the chamber. Charged particles moved in the direction of the field and their velocity and directions were associated with their zeta potential (displayed by video display). Zeta potentials were calculated based on the measured electrophoretic mobility of the particles.

6.3. RESULTS AND DISCUSSION

6.3.1. Supported mono-oxide MoO₃

6.3.1.1. Textural properties

The surface area and porosity represent two physical characteristics that have significant impact on catalysis [31]. Table 6.1 reports the specific surface area (S_{BET}) and pore volume of mono-oxide MoO₃ catalysts with different loadings, which were

supported on different catalyst supports. It was observed that the decrease in total surface area at high metal oxide loadings appear to be significantly suppressed with yttria doped alumina aerogel that contain various yttria loadings as shown in Table 6.1. It is worth mentioning that the decrease in the specific surface area and pore volume as a function of MoO₃ content was moderate up to 12.0 wt.%, irrespective of the catalyst support. This can be attributed to the penetration of dispersed molybdena into the pores of support, as a result blocking some of the alumina pores. However, the drastic decrease in the surface area at higher loadings, which was only observed with conv.alumina and alumina aerogel can be attributed to the formation of large MoO₃ crystallites and the subsequent solid-state reaction between MoO₃ and the support (i.e. Al₂(MoO₄)₃).

Table 6.1: Textural properties of mono-oxide MoO₃ catalysts supported on different support

MoO ₃ (wt.%)	Catalyst Support									
	Conv.alumina		Alumina aerogel		Yttria doped alumina aerogel Y ₂ O ₃ -Al ₂ O ₃					
					2.5 wt.%Y ₂ O ₃ - Al ₂ O ₃		10.0 wt.%Y ₂ O ₃ - Al ₂ O ₃		20.0 wt.%Y ₂ O ₃ - Al ₂ O ₃	
	S _{BET} (m ² /g)	Pore volume (cm ³ /g) (a)	S _{BET} (m ² /g)	Pore volume (cm ³ /g) (a)	S _{BET} (m ² /g)	Pore volume (cm ³ /g) (a)	S _{BET} (m ² /g)	Pore volume (cm ³ /g) (a)	S _{BET} (m ² /g)	Pore volume (cm ³ /g) (a)
0.0	134.0	0.253	265.0	1.150	299.0	0.790	305.0	0.898	236.0	0.617
2.0	117.0	0.245	202.0	0.738	215.0	0.481	206.0	0.517	173.0	0.711
5.0	112.0	0.230	187.0	0.725	213.0	0.478	205.0	0.508	165.0	0.673
12.0	98.0	0.204	161.0	0.675	197.0	0.420	190.0	0.411	154.0	0.604
20.0	52.0	0.173	100.0	0.580	163.0	0.385	178.0	0.376	137.0	0.494

(^a) From BJH desorption of pores between 1.7 and 300 nm in diameter.

6.3.1.2. Surface configuration of Mo oxide species

XRD patterns of mono-oxide MoO₃ catalyst supported on yttria doped alumina aerogel with various yttria loadings are shown in Fig.6.1a-c. In agreement with previous

results [32-34], the different phases of MoO_3 on conv.alumina and alumina aerogel varied as a function of loadings (i.e. disperse at low loadings, bulk at high loadings and $\text{Al}_2(\text{MoO}_4)_3$ at even higher loadings). The phase change took place at higher Mo loadings for the aerogel compared to conv.alumina. The most striking results were observed with yttria doped alumina aerogel as a catalyst support (Fig.6.1a-c). Careful examination of these figures reveals that XRD reflections that are ascribed to bulk MoO_3 are significantly influenced by the amount of yttria doped into alumina aerogel. Alumina aerogel doped with 2.5 wt.% yttria showed that peaks start to appear as low as 12.0 wt.% MoO_3 loadings (Fig.6.1a), however the lines were less intense and broader when compared to samples supported on conv.alumina and alumina aerogel. In addition, samples containing MoO_3 loadings higher than 12.0 wt.% showed the presence of bulk crystallites that were not the same as the $(\text{Al}_2(\text{MoO}_4)_3)$, which was clearly observed with the conv.alumina and the alumina aerogel. This new phase was ascribed to $\text{Y}_2(\text{MoO}_3)_4$ phase, which resulted from a solid state reaction between MoO_3 and Y_2O_3 that is present in the support structure. The preferential formation of $\text{Y}_2(\text{MoO}_3)_4$ instead of $\text{Al}_2(\text{MoO}_4)_3$ is a very remarkable observation in this investigation. This could be explained by taking into consideration the following two points: the acidic-basic interactions, and the charge-to-radius ratio of the mixed oxides [35]. First, with respect to the acidic-basic interactions, MoO_3 is acidic and would selectively interact with Y_2O_3 , which is more basic than Al_2O_3 . The above explanation is supported by the IEP measurements performed in this study (see proceeding section), which are an accurate indicator of the acidity-basicity strength of metal oxides. The IEP of MoO_3 was reported to be 6.5 [36], whereas the IEP of Y_2O_3 was found in this study to be 9.15 verses 8.16 for alumina aerogel. Second, Roozeboom

et al [37] and Bond et al [38] have found that the formation of surface compounds on the oxide support can be related to the ratio of the charge of the support cation to the sum of the cation and oxide ions radii (q/r). It was found that lower (q/r) ratios favour the formation of surface compounds. The (q/r) ratio of the Mo-Y combination is lower than that of Y-Al combination, since the ionic radius of Y^{3+} (0.90 Å) is much higher than Al^{3+} (0.54 Å) [39]. Hence, MoO_3 should favourably interact with Y_2O_3 portion of the support. The XRD patterns of MoO_3 catalysts supported on alumina aerogel doped with 10.0-20.0 wt.% yttria (Fig.6.1b,c) revealed that the bulk crystallites only appeared in samples with MoO_3 loading of 15.0 wt.% and higher.

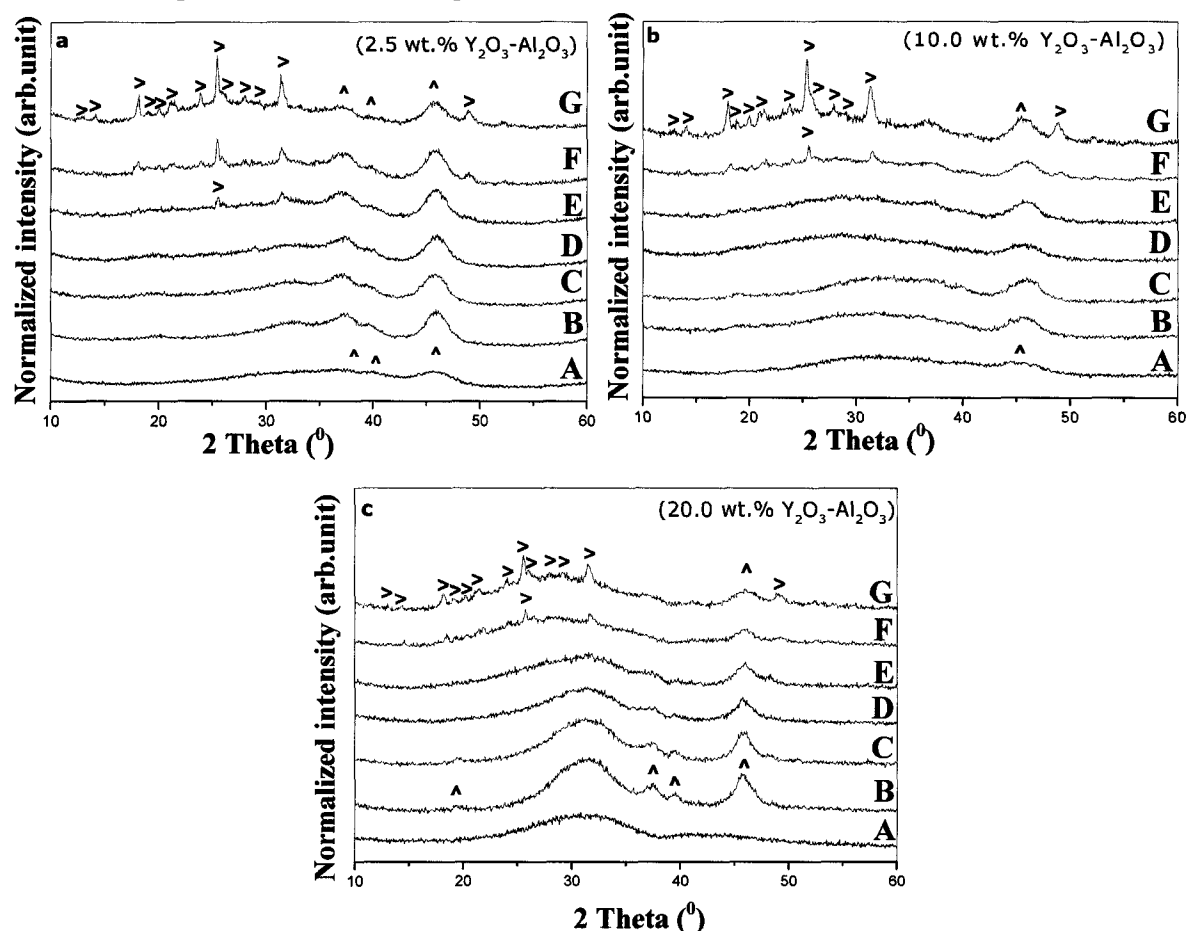


Fig.6.1 (a-c): X-ray diffraction patterns of supported mono-oxide MoO_3 catalysts, with different MoO_3 loadings (wt.%), (A) 0.0, (B) 2.0, (C) 5.0, (D) 8.0, (E) 12.0, (F) 15.0, and (G) 20.0. (^) Reflections due to $\gamma-Al_2O_3$ (JCPDS No. 29-0063), and (>) $Y_2(MoO_4)_3$ (JCPDS No.28-1451)

Overall, the XRD results clearly indicated that the population of bulk crystallites on the surface of yttria doped alumina aerogel was minimized in favour of the formation of highly dispersed surface bound molybdate species, when compared to conv.alumina and alumina aerogel. These findings were supported by Raman measurements.

Laser Raman spectroscopy has been widely considered as a very powerful tool to characterize the chemical states of metal oxide supported on various oxide supports [40]. Raman spectra of mono-oxide MoO_3 catalyst with different MoO_3 loadings that were supported on yttria doped alumina aerogel with various yttria loadings are shown in Fig.6.2a-c. In agreement with previous results [41-44], Raman spectra (not shown here) of Mo supported on the conv.alumina and the alumina aerogel showed the presence of several bands that were attributed to amorphous species (i.e. tetrahedral monomolybdate at low loadings and octahedral polymolybdate species at intermediate loadings). Raman spectra at high Mo loadings showed the presence of bulk MoO_3 and $\text{Al}_2(\text{MoO}_4)_3$ crystallites [45]. On the other hand, Raman spectra of MoO_3 samples supported on yttria doped alumina aerogel as a function of yttria loadings showed quite significant and interesting results. In addition, these results were found to corroborate very well with XRD patterns. It was noted that, irrespective of the amount of yttria doped into alumina aerogel, Raman spectra showed the presence of a broad band, which shifted upward in frequency from 916 to 960 cm^{-1} and increased in intensity, as the loading of MoO_3 increased from 2.0 to 20.0 wt.%. This band was attributed to the stretching mode of Mo=O bond. Another broad Raman band, which was attributed to the bending mode of Mo=O bond [40], was also shifted from 300 (very broad) to 340 cm^{-1} . These observed Raman bands are attributed to surface bound molybdate species. Raman bands observed

at ca. 916-924 cm^{-1} , and 300-315 cm^{-1} for samples with low MoO_3 loadings (≤ 4.0 wt.%) can be attributed to isolated tetrahedral monomolybdate species [41,42]. These monomolybdate species are expected to condense to form polymeric species at higher MoO_3 loadings, with characteristic lines at ca. 960 and 220 cm^{-1} [42-44]. However, it was quite apparent from Fig.6.2a-c that the degree of condensation (i.e. rate of formation of polymeric species) was significantly influenced by the amount of Y_2O_3 doped into the alumina aerogel. It was observed that the Raman bands that were attributed to surface bound molybdate species were shifted downward as we increased the amount of yttria doped into alumina aerogel. To elucidate this further, we compare the Raman spectra of samples with 20.0 wt.% MoO_3 that were supported on yttria doped alumina aerogel with various amounts of Y_2O_3 (i.e.2.5-20.0 wt.%) (Fig.6.2b-d). For instance, the position of the Raman band attributed to stretching mode of Mo=O bond of molybdate species was observed to be as follows; 956 cm^{-1} for 2.5 wt. % $\text{Y}_2\text{O}_3\text{-Al}_2\text{O}_3$, 948 cm^{-1} for 10.0 wt.% $\text{Y}_2\text{O}_3\text{-Al}_2\text{O}_3$, and 934 cm^{-1} for 20.0 wt.% $\text{Y}_2\text{O}_3\text{-Al}_2\text{O}_3$. Judging from the band positions and the MoO_3 loadings, the band observed at ca. 960 cm^{-1} can be assigned to octahedral polymeric species. The Raman band at ca. 934 cm^{-1} can be assigned to tetrahedral molybdate species [46]. In addition, surface bound octahedral polymeric molybdate species can contribute to this band as well. However, it is certain that these species exist in very small population based on the absence of Mo-O-Mo deformation band (220 cm^{-1}), and the very broad nature of Raman band in the 800-860 cm^{-1} region (asymmetric stretch mode of Mo-O-Mo) [40,46]. Moreover, since the XRD patterns showed the presence of bulk yttrium molybdate at high Mo loadings, one should expect to observe Raman bands that are characteristic of these crystallites. The Raman spectrum of yttrium molybdate

crystallites, which was prepared by solid-state reaction (the structure was confirmed by XRD), is depicted in the inset of Fig.6.2a. Based on this spectrum (Raman bands at ca. 946, 841, 820 and 338 cm^{-1}) and XRD patterns, the Raman band observed at ca. 934 cm^{-1} can be ascribed to $\text{Y}_2(\text{MoO}_4)_3$ crystallites as well. It is worthwhile mentioning that we have initially thought that the Raman band at 934 cm^{-1} could be attributed only to polymolybdate species that differ significantly from the highly polymeric octahedral molybdate species ($\text{Mo}_7\text{O}_{24}^{6-}$, $\text{Mo}_8\text{O}_{26}^{4-}$). These polymolybdate species were thought to be most likely dimeric ($\text{Mo}_2\text{O}_7^{2-}$) and/or trimeric ($\text{Mo}_3\text{O}_{10}^{2-}$) tetrahedral molybdate species [41,47,48]. However, this possibility has been eliminated since it has been shown that these species are not quite stable on the surface of oxide support, and due to the lack of band around 196 cm^{-1} . An estimate of the uncertainty of these frequency shifts was determined to be $\pm 4 \text{ cm}^{-1}$, thus the trends observed are well beyond experimental errors. Based on these observations, it must be therefore concluded that yttria doped into alumina aerogel played a major role in reducing the extent of molybdate polymerization. Subsequently, the surface of yttria doped alumina aerogel with high yttria loadings can be characterized as having tetrahedral molybdate species and bulk yttrium molybdate crystallites as predominate species, whereas polymolybdate species are only present in low concentration, upon loading with high Mo contents.

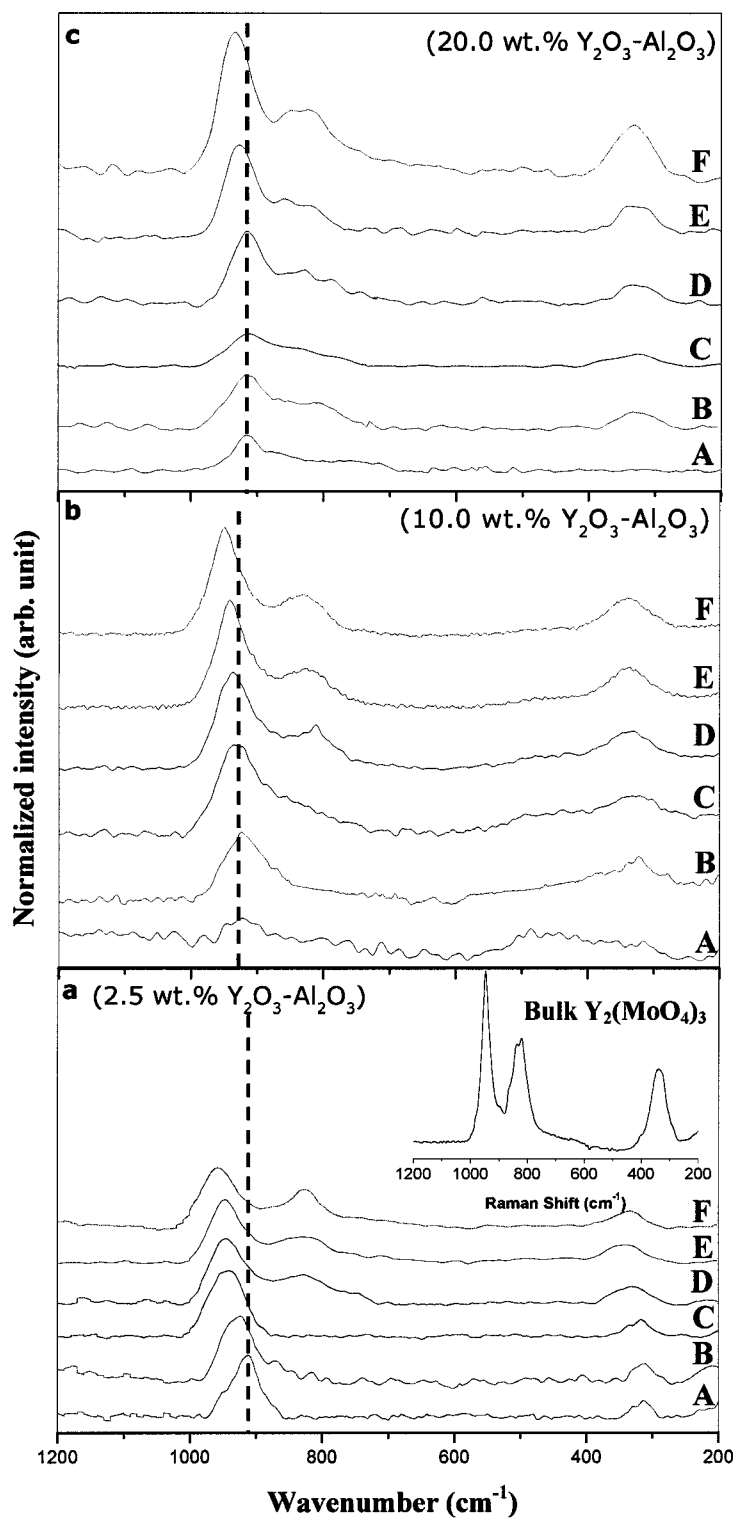


Fig.6.2 (a-c): Laser Raman spectra of mono-oxide MoO_3 catalysts, with different MoO_3 loadings (wt.%), (A) 2.0, (B) 5.0, (C) 8.0, (D) 12.0, (E) 15.0, and (F) 20.0

6.3.1.3. Retarding effect of doped yttria on the sublimation of MoO₃

In the present study, we employed the thermal analysis technique to further investigate the extent of support-metal interactions and to elucidate their effects on the thermal stability of MoO₃ in the mono-oxide MoO₃ and bi-oxide MoO₃-CeO₂ catalysts. MoO₃ is well known to begin subliming at ca. 750-800 °C [49,50], which is considered to be a major limitation for its use in high temperature reactions. The DTA/TGA curves of pure MoO₃ obtained by calcining the AHM for 5 h at 500 °C are shown in Fig.6.3A

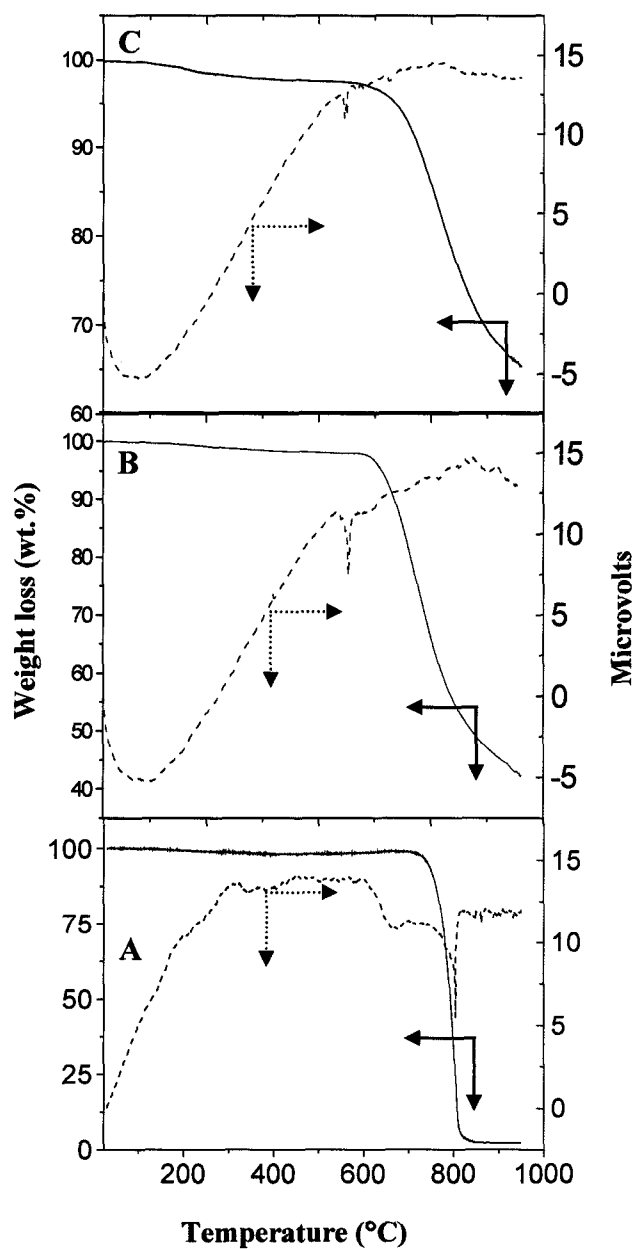


Fig.6.3: DTA/TGA curves of A) unsupported MoO₃, B) and C) unsupported bi-oxide MoO₃-CeO₂ with [Ce]/[Mo] of 0.13 and 0.44, respectively. (-----) DTA and (_____) TGA

As can be noted from Fig.6.3A, the pure MoO₃ displayed a complete weight loss (sublimation) that started as low as 743 °C with a major endothermic peak in that region. One would expect to observe a similar physical change, when loading the catalyst support with MoO₃. However, the sublimation temperature should be affected by the extent of support-metal interactions and the presence of other species (i.e. CeO₂ in the case of bi-oxide). The TGA curves of calcined supported mono-oxide MoO₃ catalysts with various loadings are shown in Fig.6.4 (A-C) (a-c), and the TGA results are summarized in Table 6.2.

Table 6.2: TGA of the region between 750 to 1100 °C of supported mono-oxide and bi-oxide catalysts

	Conv.alumina		Alumina aerogel		2.5 wt.% yttria doped alumina aerogel		10.0 wt.% yttria doped alumina aerogel	
Mono-oxide MoO₃								
Nominal MoO ₃ loading (wt.%)	12	20	12	20	12	20	12	20
Weight loss (wt.%)	8.80	16.21	8.3	15.6	3.60	9.7	0.0	0.0
T (°C) ^(a)	831	808	814	804	980	864	n.a.	n.a.
Bi-oxide MoO₃-CeO₂								
[Ce]/[Mo] molar ratio	0.13	0.44	0.13	0.44	0.13	0.44	0.13	0.44
Nominal CeO ₂ loading (wt.%) ^b	2.0	6.0	2.0	6.0	2.0	6.0	2.0	6.0
Weight loss (wt.%)	6.55	1.70	6.30	2.21	1.40	0.0	0.0	0.0
T (°C) ^(a)	858	940	873	932	1010	n.a.	n.a.	n.a.

^(a) Temperature at which the weight loss begins, ^(b) MoO₃ content was kept constant at 12.0 wt.%

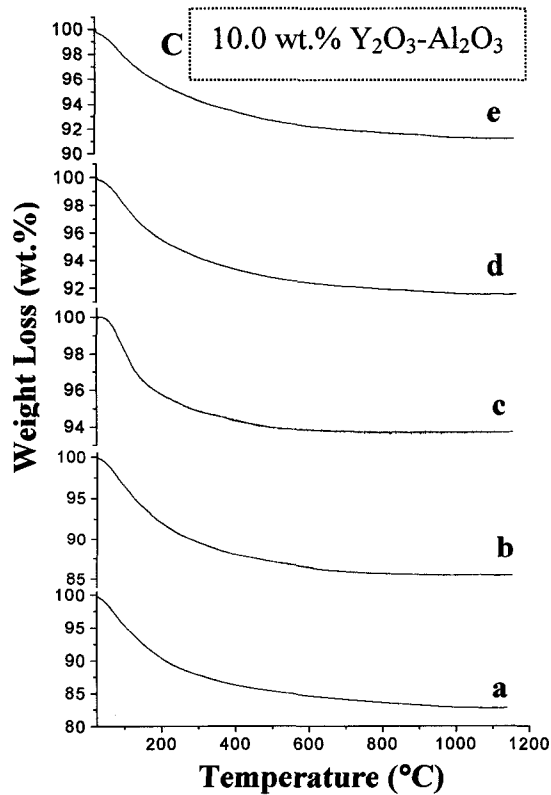
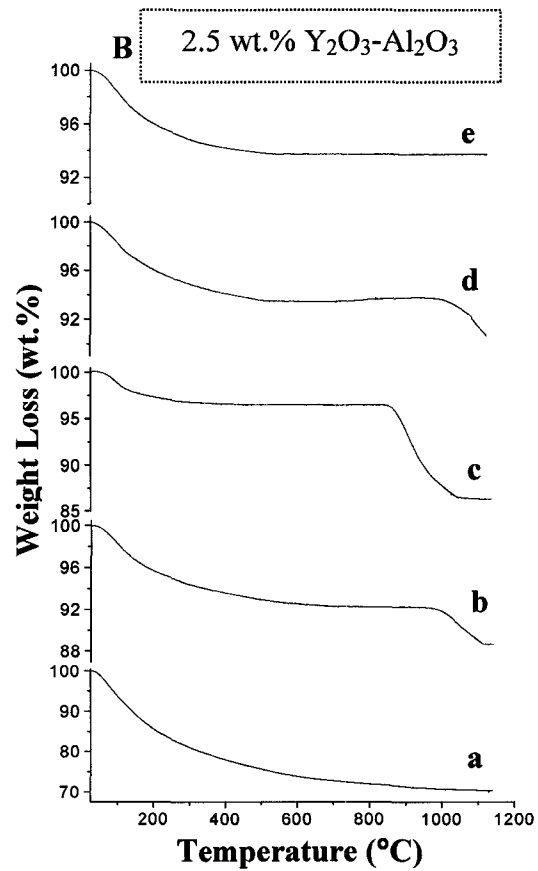
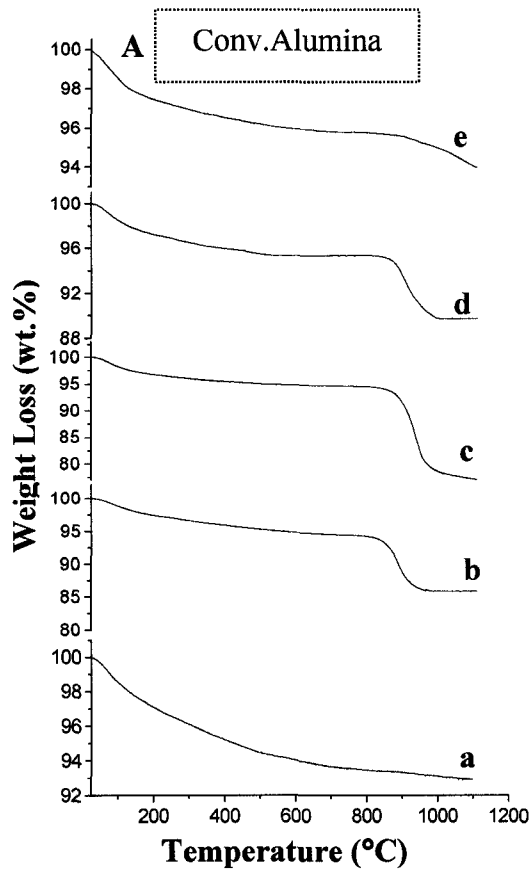


Fig.6.4 (A-C): TGA curves of calcined supported mono- and bi-oxide catalysts; a) support, b) and c) mono-oxide MoO₃ with 12.0 and 20.0 wt.% MoO₃ loadings, respectively, and d) and e) bi-oxide MoO₃-CeO₂ with [Ce]/[Mo] of 0.13 and 0.44, respectively

As can be observed from this figure, all samples exhibited several successive weight losses. The first weight loss in the range 25-250 °C is primarily due to the removal of physisorbed water held on the surface by hydrogen bonding. The second weight loss in the range of 300-700 °C corresponded to the loss of water due to dehydroxylation of the surface. However, the most important range for this investigation is in range of temperature ≥ 750 °C, where MoO₃ sublimation is expected to take place. It is apparent from Fig.6.4 (A-C) (b-c) and Table 6.2 that the sublimation temperature of MoO₃ was significantly influenced by the nature of support used. To elucidate this further, we discuss the TGA curves of mono-oxide catalyst with two different MoO₃ loadings (i.e. 12.0 and 20.0 wt.%) that were loaded onto different supports. Mono-oxide catalyst with 12.0 wt.% MoO₃ loaded onto conv.alumina, displayed a weight loss of about 8.80 wt.% that started at 831 °C. The shift in the sublimation temperature from 743°C observed for pure MoO₃ to 831 °C in the supported system is a clear case of support-metal interactions. Similar results were also observed with alumina aerogel. However, mono-oxide catalysts loaded onto yttria doped alumina aerogel showed a further shift in the sublimation temperature, as well as much lower weight loss. These changes were greatly influenced by the amount of yttria doped into alumina aerogel. Samples loaded onto 2.5 wt.% yttria doped alumina aerogel exhibited a weight loss of about 3.6 wt.%, which was observed to begin at 980 °C. No weight loss could be observed in the range between 750-1150 °C in catalysts utilizing 10.0 wt.% yttria doped alumina aerogel as a support (Fig 6.4C (b-c), Table 6.2). Therefore, it can be inferred from these results that most of the impregnated molybdenum on yttria doped alumina aerogel was in the surface dispersed form, which is in complete agreement with the Raman measurements. The TGA curves

of 20.0 wt.% MoO₃ mono-oxide catalyst loaded onto different supports are presented in Fig.6.4 (A-C) (c), Table 6.2). Analysis of these TGA results revealed that they displayed similar patterns to those of 12.0 wt.% MoO₃ catalyst (Fig.6.4 (A-C) (b), with the same conclusion that the formation of bulk crystallites was minimized by using yttria doped alumina aerogel as a support. Furthermore, these interesting observations were noted: First, we have observed a different sublimation temperature between these two different MoO₃ loadings, irrespective of the catalyst support used. For instance, the weight loss associated with 20.0 wt.% MoO₃ loaded onto conv.alumina started at ca. 808 °C, which is 23 °C lower than the one observed for the 12.0 wt.% MoO₃ catalyst. The difference in MoO₃ sublimation temperature was expected and could be mainly attributed to the presence of monolayer or multiple layers of MoO₃ on the support surface. In both cases, the presence of bulk MoO₃ crystallites, which is responsible for the observed weight loss, has been detected by XRD and Raman measurements (Fig.6.2-3). However, the MoO₃ crystallites that were formed at a coverage that is slightly above one monolayer are believed to have stronger interactions with the support than those found at higher coverage [45,51]. Second, the weight loss observed for the 20.0 wt.% MoO₃ supported samples is certainly due to the sublimation of MoO₃ crystallites. However, that loss is not entirely due to the MoO₃ crystallites that were present on the surface, but also due to those formed as result of the thermal decomposition of Al₂(MoO₄)₃ crystallites to Al₂O₃ and MoO₃ at temperature ≥ 800 °C [49], as in the case of conv.alumina and alumina aerogel. Third, it appeared that the Y₂(MoO₄)₃ is more thermally stable than Al₂(MoO₄)₃ when heated to 1150 °C. This was supported by the lack of weight loss observed for samples supported on 10.0 wt.% yttria doped alumina aerogel.

6.3.1.4. More on the effect of doped yttria on the MoO₃ dispersion

The dispersion degree of MoO₃ on yttria doped alumina aerogel was greatly improved compared to con.alumina and undoped alumina aerogel. The BET surface area and pore volume (Table 6.1), XRD patterns (Fig.6.1a-c), Raman measurements (Fig.6.2a-c), and thermal analysis (Fig.6.4a-e), and Table 6.2) of MoO₃ supported on yttria doped alumina aerogel have unambiguously revealed the presence of higher population of dispersed surface molybdate species (i.e. tetrahedral monomolybdate) compared to bulk crystallites. In addition, the observed bulk crystallites on the surface of yttria doped alumina aerogel were characterized by weak, less intense and broader XRD reflections compared to those observed with conv.alumina and alumina aerogel. Furthermore, it was clearly apparent that the dispersion degree of MoO₃ was continuously improved as the amount of yttria incorporated into alumina aerogel increased. Therefore, it can be concluded that the incorporation of yttrium ions into the alumina aerogel structure is well related to these improvements. The observed positive effects of doping alumina aerogel with yttria should be closely linked to the factors that influence the adsorption mechanism of molybdate ions, which is sequentially related to the adopted preparation method. The mechanism of aqueous impregnation (method used to prepare MoO₃ catalysts) can be summarized as two consecutive steps: formation of solution ions followed by adsorption of these ions onto the surface hydroxyl groups of the oxide support. Accordingly, some of the most important factors to be considered for aqueous impregnation would be the pH of the impregnating solution and the type of catalyst support. The chemistry of surface hydroxyl groups (i.e. concentration, types (i.e. acidic and basic), and respective strength), and the iso-electric point constitute one of the most

important characteristics of the support. All these factors have been reported to significantly influence the structure of solution ions as well as the nature of surface adsorbed species [40]. Prior to presenting our proposed explanation, it was felt that a short review of the pertinent information to the effect of pH on the formation of solution ions, as well as the surface charge (i.e. IEP) was necessary. The pH of the impregnating solution plays a major role in influencing the structure of solution ions. This effect can be seen quite well in mono-oxide MoO₃ catalysts that are normally prepared by impregnation from aqueous AHM solution. It has been shown that upon dissolving AMH in an aqueous solution, different ions (i.e. tetrahedral monomolybdate or octahedral polymolybdates) will be formed depending on the pH of the solution [40]. The effect of the pH can be described by the following equilibrium equation between monomolybdates and polymolybdates,

$$7\text{MoO}_4^{2-} + 8\text{H}^+ \rightarrow \text{Mo}_7\text{O}_{24}^{6-} + \text{H}_2\text{O} \quad (3)$$

These monomolybdate ions are stable in solution with pH of 8 or higher, while at lower pH polymolybdates are found. The adsorption process of these ions onto the hydroxyl groups is believed to occur through electrostatic interactions that are governed by the surface pH value (surface pH at IEP), as well as the buffering capacity of the support. The observed improvements in the dispersion degree of Mo upon its impregnation onto yttria doped alumina aerogel can be ascribed to the incorporation of yttria into the alumina aerogel network. This incorporation has affected the acidity-basicity of the support, and subsequently its surface charge (IEP), as suggested by the IEP measurements. The results of zeta-potential measurements for the determination of the IEP of all oxide supports investigated in this present work are presented in Fig.6.5. The IEP determined for conv.alumina and alumina aerogel were 7.70 and 8.16, respectively.

These results are in complete agreement with the reported IEP of alumina in the literature, which was found to be in the range of 7-9 [52-55]. This range of values was attributed to several factors such as the preparation method, nature of alumina precursor, structure defects, impurities and extent of sample hydration [56]. The IEP of pure Y_2O_3 obtained from zeta-potential measurements (Fig.6.5) was found to be 9.15, which implies a high basic character. This value was similar to that obtained by Sprycha et al for Y_2O_3 [57]. Based on the IEP of Y_2O_3 , it was expected that incorporation of Y_2O_3 into the alumina aerogel would result in shifting the IEP to higher value. We have observed that as the amount of Y_2O_3 increases, the IEP of the undoped alumina aerogel increased accordingly. The IEP of the alumina aerogel was shifted from 8.16 to 8.60 upon doping it with 10.0 wt.% Y_2O_3 whereas, the IEP of 20.0 wt.% yttria doped alumina aerogel was found to be 8.95 (Fig.6.5). The change in the IEP of the surface plays a major role in determining the nature of surface molybdate species. As the surface becomes more basic (higher IEP), the tetrahedral monomolybdate species are stabilized [46] and would exist at much higher concentration, when compared to the octahedral polymolybdate species. Thus, reducing the extent of bulk crystallites formation since the highly polymeric molybdate species have been considered to be the possible precursor of these crystallites [58]. For example, 20.0 wt.% yttria doped alumina aerogel (IEP = 8.95) was explicitly found to contain high concentration of monomolybdate species along with small amount of polymeric species and poorly crystallized bulk species, upon impregnating it with high loading of Mo.

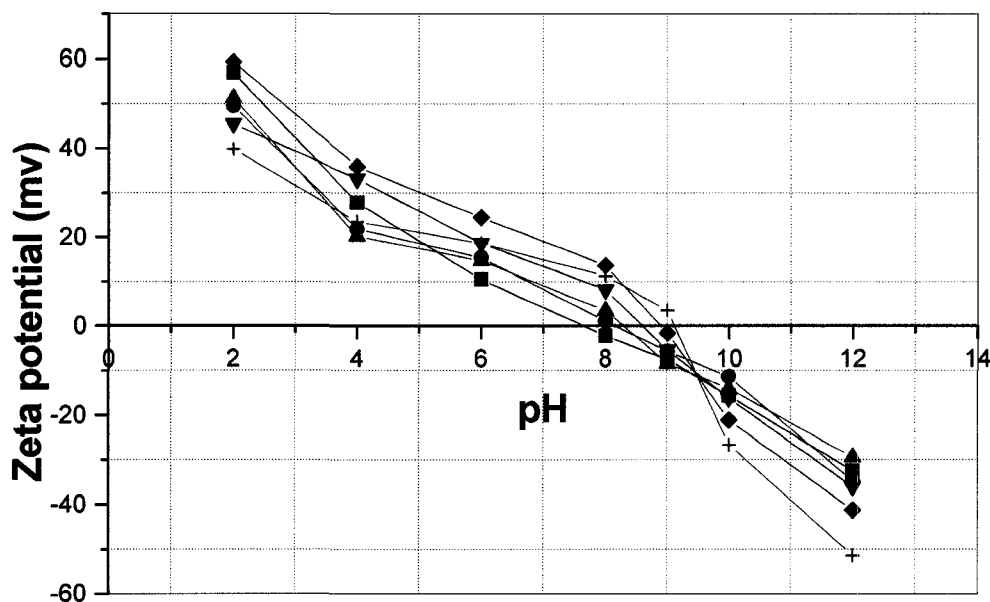


Fig.6.5: Zeta potential curves of dispersed particles versus pH of aqueous solutions for pure Y₂O₃ (+), conv.alumina (■), alumina aerogel (●), 2.5 wt.% (▲), 10.0 wt.% (▼) and 20.0 wt.% (◆) yttria doped alumina aerogel (Y₂O₃-Al₂O₃)

6.3.2.Supported mono-oxide CeO₂

6.3.2.1.Textural Properties

As with the mono-oxide MoO₃ catalysts, the decrease in the S_{BET} was also observed for mono-oxide CeO₂ catalysts loaded on different supports at various CeO₂ loadings (Table 6.3). Careful assessment of the decrease in the S_{BET} and pore volume reveals the following points: First, it was observed that the decrease was less dramatic even at very high ceria loadings for catalysts supported on the conv.alumina and the alumina aerogel than that of supported MoO₃ catalysts using the same type of support. This can be attributed mainly to the formation of small CeO₂ crystallites, which are deposited on the walls and/or in the mouth of the pores of the support. Furthermore, to

the fact that no solid state reaction between the CeO₂ and the support (i.e. formation of bulk CeAlO₃ crystallites) was observed. Second, comparison between CeO₂ catalysts supported on different supports, in terms of % decrease in the S_{BET}, reveals that the influence of the catalyst support appears to be less pronounced, when compared to supported MoO₃ catalysts.

Table 6.3: Textural properties of mono-oxide CeO₂ catalysts supported on different support

CeO ₂ (wt.%)	Catalyst Support									
	Conv. alumina		Alumina aerogel		Yttria doped alumina aerogel Y ₂ O ₃ -Al ₂ O ₃					
					2.5 wt.% Y ₂ O ₃ -Al ₂ O ₃		10.0wt.% Y ₂ O ₃ -Al ₂ O ₃		20.0 wt.% Y ₂ O ₃ - Al ₂ O ₃	
	S _{BET} (m ² /g)	Pore volume (cm ³ /g)	S _{BET} (m ² /g)	Pore volume (cm ³ /g)	S _{BET} (m ² /g)	Pore volume (cm ³ /g)	S _{BET} (m ² /g)	Pore volume (cm ³ /g)	S _{BET} (m ² /g)	Pore volume (cm ³ /g)
2.0	100.0	0.230	203.0	0.734	213.0	0.502	198.0	0.447	187.0	0.619
6.0	96.0	0.211	184.0	0.648	186.0	0.385	195.0	0.359	168.0	0.410
10.0	90.0	0.196	160.0	0.552	172.0	0.339	179.0	0.327	141.0	0.307
15.0	82.0	0.167	149.0	0.494	154.0	0.288	173.0	0.320	129.0	0.291

6.3.2.2. Surface configuration of Ce oxide species

XRD patterns of various mono-oxide CeO₂ catalysts supported on yttria doped alumina aerogel with various yttria loadings, are shown in Fig.6.6 (a-c). The XRD patterns of CeO₂ supported on conv.alumina and alumina aerogel (not shown here) were also obtained and were in complete agreement with previous reports [59,60]. The XRD patterns revealed the presence of only two crystalline phases: γ -Al₂O₃ and bulk CeO₂ crystallites, regardless of the support used. Furthermore, we have observed that CeO₂ does form a non-stoichiometric solid solution with Y₂O₃ portion of the support. This was evident by the gradual and noticeable shift in the ceria XRD peaks position, as we varied the ceria support from conv.alumina to yttria doped alumina aerogel with various

contents of yttria (subsequent section). However, XRD did not detect the presence of any compounds or solid solution between the support (con.alumina and alumina aerogel) and CeO_2 [60,61]. It is also worthwhile mentioning that the results clearly showed the presence of two different ceria phases irrespective of the type of support used; the disperse and bulk ceria phase. The former phase is characterized by the presence of surface dispersed ceria that are not detectable by XRD. These dispersed species are most probably Ce^{3+} -like species, and/or to smaller extent bulk CeO_2 [59].

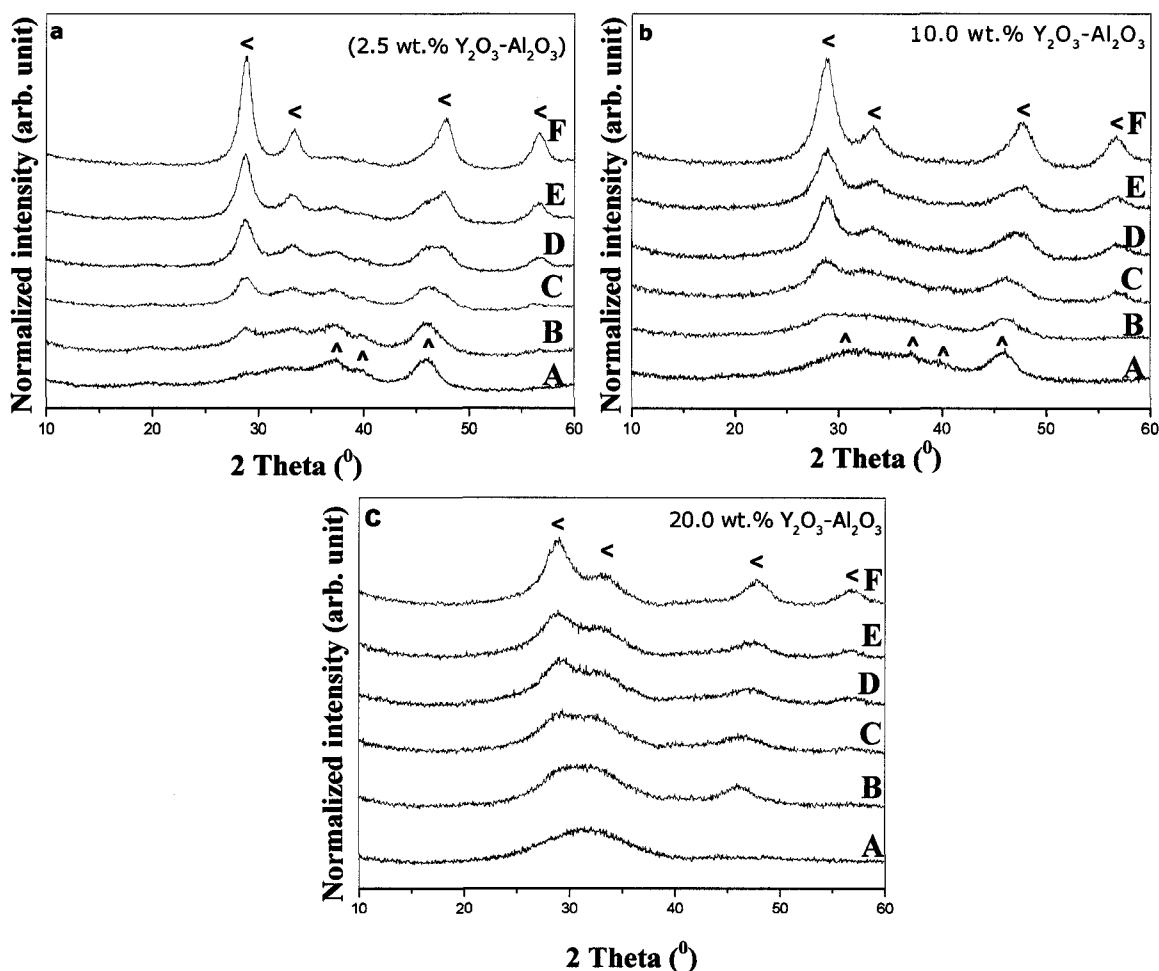


Fig.6.6 (a-c): X-ray diffraction patterns of supported mono-oxide CeO_2 catalysts, with different CeO_2 loadings (wt.%), (A) 2.0, (B) 4.0, (C) 6.0, (D) 8.0, (E) 10.0 and (F) 15.0. (^) Reflections due to $\gamma\text{-Al}_2\text{O}_3$, and (<) CeO_2 (JCPDS No.34-0394)

Careful examination of the XRD patterns of CeO₂ supported on different supports reveals that the type of support used significantly influenced the formation and the dispersion (i.e. crystallite size) of CeO₂. Such influence on the crystallite size of CeO₂ in different samples, as determined from X-ray line broadening of the most intense peak ($2\theta = 28.6^\circ$) using Scherer equation, is shown in Table 6.4.

Table 6.4: The crystallite size (nm) of substituted CeO₂ solid solution in the supported mono-oxide CeO₂, and CeO₂ crystallites in the bi-oxide MoO₃-CeO₂

CeO ₂ (wt.%)	Catalyst Support				
	Conv.alumina	Alumina aerogel	Yttria doped alumina aerogel		
			X ^(b) = 2.5	10.0	20.0
<i>Pure unsupported CeO₂</i> (The crystallite size = 58.1nm)					
<i>Mono-oxide supported CeO₂</i>					
2.0	n.a.	n.a.	n.a.	n.a.	n.a.
4.0	9.85	9.51	n.a.	n.a.	n.a.
6.0	12.6	12.8	8.13	5.66	n.a.
8.0	13.7	14.5	9.51	7.58	4.04
10.0	14.9	15.6	11.5	8.15	5.15
15.0	17.3	18.1	13.6	9.56	6.30
<i>Bi-oxide supported MoO₃-CeO₂</i>					
2.0 (0.13) ^a	15.9	18.0	9.15	6.89	5.74
6.0 (0.44) ^a	34.2	35.7	17.1	11.6	6.89
10.0 (0.88) ^a	40.8	42.2	24.3	17.8	7.67

(^a) Number in parentheses represents the [Ce]/[Mo] molar ratio, and (^b) X represents the amount of Y₂O₃ doped into alumina aerogel

First, the transition between the dispersed and the bulk ceria phases occurred at different ceria loadings, depending on the type of support used. Conv.alumina and alumina aerogel showed that the transition occurred in the loading range between 2.0 and 4.0 wt.% of CeO₂. However, the transition was shifted to higher loadings (i.e. 4.0-6.0 wt.% CeO₂) upon using alumina aerogel doped with 10.0 wt.% yttria as a support. The dispersion of ceria was further improved by using alumina aerogel doped with 20.0 wt.% yttria, since

the transition was observed to occur in the loading range between 6.0-8.0 wt.% CeO₂. Second, the size of CeO₂ crystallites formed on the surface was continuously decreasing as a function of the amount of yttria incorporated into the alumina aerogel lattice. The average crystallite sizes of CeO₂ in supported mono-oxide samples, which are expected to increase as the CeO₂ loadings increased, were all below 58.1 nm. The latter was the value obtained for the crystallite size of unsupported CeO₂. For instance, the CeO₂ average crystallite size in the supported CeO₂ samples with 20.0 wt.% CeO₂ loading decreased from 17.3 to 6.30 nm when the support was changed from conv.alumina to 20.0 wt.% yttria doped alumina aerogel, respectively. These results were in complete agreement with Raman measurements (not shown here). The following observations were noted from Raman. First, Raman spectra showed the presence of only one prominent band at ca. 464 cm⁻¹. The 464 cm⁻¹ Raman band, which is characteristics of bulk CeO₂, corresponds to the triply degenerate F_{2g} mode and can be viewed as a symmetric breathing mode of oxygen atoms around cerium ions [61]. The mere appearance of this band supports the findings by XRD that impregnated CeO₂ and the support (i.e. conv.alumina and alumina aerogel) do not form any compounds or mixed phases. Second, the intensity and shape of the 464 cm⁻¹ Raman band were influenced by the type of support used. That influence was quite apparent on the appearance of this band, since the band appeared broader as we varied the support from conv.alumina to the yttria doped alumina aerogel. The above observation is indicative of the decrease in the size of CeO₂ crystallites as we go toward using yttria doped alumina aerogel as a support (complete agreement with XRD). Third, the Raman results showed an interesting feature, which is the presence of bulk CeO₂ crystallites in the ceria dispersed phase. These crystallites were

not detectable by XRD since their sizes were below 4.0 nm. This particular observation is in complete agreement with Shyu et al. [59] findings that bulk CeO₂ crystallites exist in the ceria dispersed phase.

6.3.2.3. More about CeO₂ dispersion

CeO₂ catalysts have shown improved physical properties with respect to ceria (substituted ceria) dispersion, when loaded onto yttria doped alumina aerogel. It is well established in the literature that CeO₂ unlike other lanthanides has showed a low affinity or interaction with various metal oxide supports [11,59,60,62-64]. In fact, CeO₂ loaded onto the surface of these metal oxide supports was observed to be in the dispersed phase only at low CeO₂ loadings, ca.3-5 wt.%. The key factor which is known to significantly determine the degree of ceria dispersion is its redox ability, besides other expected factors such as loadings, preparation methods and calcination temperature [63,64]. Cerium easily shifts from its (3+) oxidation state to (4+) under the typical preparation conditions of supported mono-oxide CeO₂ catalysts (i.e. calcination in air (oxidation)). That shift has been regarded as the main reason behind the low interactions between the cerium and the support, which consequently resulted in low dispersion [64]. The high ceria dispersion on alumina at low loadings for instance has been attributed to the formation of mainly Ce³⁺-like species (i.e. CeAlO₃ precursor) that were stabilized in the surface vacancies of the support [59,62,65]. Damyanova et al [63] have also ascribed the high ceria dispersion to the formation of Ce³⁺-like species. This was attributed to the electron deficient interaction of the alumina with the cerium that resulted in the formation of Ce-O-Al bond. The latter is believed to stabilize cerium in its lower oxidation state. Their explanation was supported by the XPS measurements, which showed that samples with low CeO₂

loadings exhibited Ce^{3+} -like XPS spectrum. Our results concerning the dispersion of ceria on the surface of conv.alumina support were in good agreement with the previous investigations [59-64], which is that CeO_2 can be dispersed on the surface of conv.alumina only at low ceria loadings (below 4.0 wt.%). The dispersion of ceria on the surface of alumina aerogel was observed to be the same as conv.alumina. However, the results indicated unambiguously that by using yttria doped alumina aerogel as a support, it was possible to further improve the dispersion degree. In fact, as the amount of yttria incorporated into alumina aerogel network increases, there is a continuous positive shift in the transition between the dispersed ceria (substituted ceria) and the bulk phase, and also a continuous decrease in the size of dispersed and bulk CeO_2 crystallites. Therefore, yttria played a significant role in improving the dispersion of ceria on both levels; the dispersed and the bulk phases. This could be possibly attributed to one of the following proposed mechanisms involving the cerium-support interaction and the CeO_2 - Y_2O_3 solid solution. It is also highly possible that these improvements are the result of co-operative effect between these two mechanisms. In the case of the ceria dispersed phase, the dominating factors are the strong interactions between the cerium and the support that contains both aluminum and yttrium (Y_2O_3 - Al_2O_3). It is highly probable that these interactions have ultimately resulted in the formation of strong Ce-O-Al and Ce-O-Y bonds. The Ce-O-Al bond has been extensively shown to stabilize the cerium in lower oxidation state (Ce^{3+}) [59,62,63]. By analogy, it is expected that Ce-O-Y bond will have the same effect. In fact, the extent of Ce^{3+} stabilization in the Ce-O-Y bond, and consequently the prevention of the CeO_2 segregation is expected to be much higher than that in the Ce-O-Al bond under the typical preparation conditions of supported CeO_2

catalysts. This is due to the lower polarization effect induced by Y^{3+} (Charge density = $102 \text{ C}\cdot\text{mm}^{-3}$) on the oxygen anion, when compared to that induced by Al^{3+} (Charge density = $364 \text{ C}\cdot\text{mm}^{-3}$). The difference in polarization effect is due to the large difference in the ionic radii between Al^{3+} and Y^{3+} (0.54 \AA and 0.90 \AA , respectively) [66]. The validity of the above mechanism could be only established by the presence of mainly Ce^{3+} -like species and some small CeO_2 crystallites in the ceria dispersed phase [59,62,63]. The small-sized and well-dispersed CeO_2 crystallites can be supported by the lack of XRD peaks (Fig.6a-c), and by the appearance of Raman band at ca. 461 cm^{-1} . However, the presence of Ce^{3+} (or Ce^{3+} -like species), and whether their structure is similar to those in the case of alumina [59] cannot be confirmed in this present investigation. Tentatively, we believe that these species exist on the surface of the yttria doped alumina aerogel. No comments can be made with respect to their exact structure. This is due to the fact that the techniques that were employed (XRD and Raman) cannot easily distinguish between different oxidation states, particularly if the species are in the dispersed phase. XPS experiments are being planned as future work, and the results will be the subject of a future publication. The small CeO_2 crystallites observed in the ceria dispersed phase are expected to grow with ceria loadings to bulk species that can be easily detected by XRD. The formation of these bulk species will only take place once the surface of the yttria doped alumina aerogel reaches the saturation degree. Undoubtedly, these species will be growing at slower rate than those on conv.alumina and alumina aerogel, due to their smaller size in the dispersed phase. Therefore, the bulk CeO_2 associated with yttria doped alumina aerogel will be smaller than those associated with other supports (Table 6.4). Nevertheless, there is another mechanism that could

elucidate the superiority of yttria doped alumina aerogel over conv.alumina and alumina aerogel. This involves the formation of a solid solution between CeO_2 and Y_2O_3 . This mechanism was proposed on the basis of the observation that there was a gradual and noticeable shift in the CeO_2 XRD peaks position, as we varied the ceria support from conv.alumina to yttria doped alumina aerogel with various contents of yttria (Fig.6.7A).

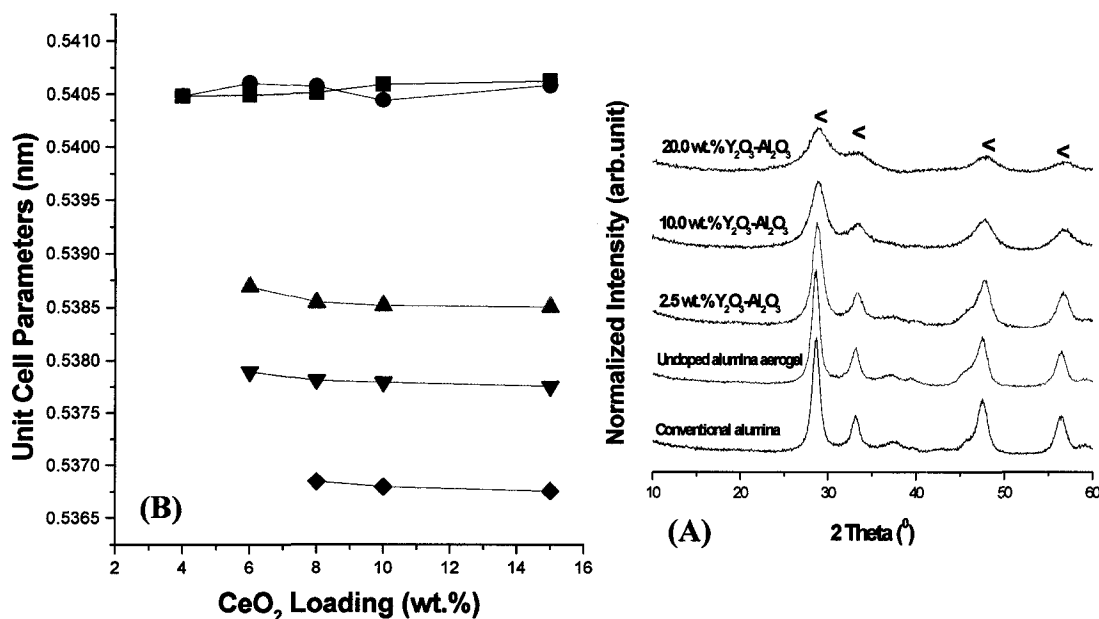


Fig.6.7: A) X-ray diffraction patterns of 15.0 wt.% CeO_2 catalysts loaded onto different supports (re-plot of Fig.6 (a-c). B) Unit cell parameters (nm) of unsubstituted CeO_2 or substituted CeO_2 solid solution ($\text{Ce}_{1-x}\text{Y}_x\text{O}_{2-x/2}$) as a function of various catalyst supports; (■) conv.alumina, (●) alumina aerogel, (▲) 2.5 wt.%, (▼) 10.0 wt.% and (◆) 20.0 wt.% yttria doped alumina aerogel

The observed shifts are normally considered as a sign of formation of a solid solution. In order to confirm that, unit cell lattice parameters (i.e. cubic; $a = b = c$) of all supported CeO_2 samples were calculated. The change in the 'a' unit cell parameter as a function of support is shown in Figure 3a. The 'a' cell parameter of pure CeO_2 was calculated to be = 0.54057 nm, which is in agreement with other reports [67]. In the case of $\text{CeO}_2/\text{Al}_2\text{O}_3$

system (both conv.alumina and alumina aerogel), the 'a' unit cell parameter remains almost the same as pure CeO₂. This was expected since the formation of a solid solution between CeO₂ and Al₂O₃ is not favourable, due to the large difference in the ionic radii between Al³⁺ and Ce⁴⁺ (Al³⁺ = 0.54 Å and Ce⁴⁺ = 0.97 Å) [66]. In the case of CeO₂/Al₂O₃-Y₂O₃, the calculated 'a' unit cell parameter was observed to be lower than that for CeO₂/Al₂O₃, irrespective of the amount of ceria loadings. In fact, a steady decrease in the lattice parameter values with increasing amount of yttria doped into alumina aerogel can be observed (Fig.6.7B). The 'a' cell parameter was reduced from 0.54057 nm for pure unsupported CeO₂ to 0.53714 nm for 15.0 wt.% CeO₂ loaded onto alumina aerogel doped with 10.0 wt.% yttria. Whereas, the 'a' cell parameter was 0.53642 nm for 15.0 wt.% CeO₂ loaded onto alumina aerogel doped with 20.0 wt.% yttria. The observed decrease in the lattice parameter is attributed to substitution (i.e. aliovalent substitution) of Ce⁴⁺ (0.97 Å) by Y³⁺ (0.90 Å) [66]. Since this type of substitution involves a substitution by different and lower valance cation (Y³⁺), changes will be needed to preserve electroneutrality in the host structure (Ce⁴⁺). These changes can be achieved either by creating anion (oxygen) vacancies (i.e. Ce_{1-x}Y_xO_{2-x/2}) or interstitial cations (i.e. Ce_{1-x}Y_{4x/3}O₂) [68,69]. In our case, it is quite clear that the solid solution mechanism did involve the creation of anionic vacancies, as evident from the lattice shrinkage (lower unit cell parameter). The formation of CeO₂-Y₂O₃ solid solution appeared to retard the crystallite growth, as evident by the decrease in the average crystallite size. Reddy et al. [70] have also observed that the formation of CeO₂-ZrO₂ solid solution retards the crystallite growth, thus paving the way for the formation of thermodynamically more stable phases. It is quite significant to emphasize that since Ce and Y have been proven to mix with

each other (solid-solution), it is not accurate to refer to the dispersion of CeO₂ supported on yttria doped alumina aerogel as the dispersion of ceria. This would imply that ceria phase remains a pure phase. Therefore, it would be more proper to refer to the dispersion of ceria as the dispersion of substituted ceria.

6.3. Supported bi-oxide MoO₃-CeO₂

6.3.3.1. Textural properties

The results presented in Table 6.5 also suggested that yttria doped alumina aerogel is more efficient support than conv.alumina and alumina aerogel. In fact, as the [Ce]/[Mo] ratio increases, there was a reduction in the S_{BET}, presumably to the effect of pore blocking by bulk CeO₂ crystallites as supported by XRD and Raman.

Table 6.5: Textural properties of bi-oxide MoO₃-CeO₂ catalysts supported on different support; all samples were activated at 750 ° C in air for 3 h

[Ce]/[Mo]] molar ratio	Catalyst Support									
	Conv.alumina		Alumina aerogel		Yttria doped alumina aerogel XY ₂ O ₃ -Al ₂ O ₃					
					2.5 wt.% Y ₂ O ₃ -Al ₂ O ₃		10.0 wt.% Y ₂ O ₃ -Al ₂ O ₃		20.0 wt.% Y ₂ O ₃ -Al ₂ O ₃	
	S _{BET} (m ² /g)	Pore volume (cm ³ /g)	S _{BET} (m ² /g)	Pore volume (cm ³ /g)	S _{BET} (m ² /g)	Pore volume (cm ³ /g)	S _{BET} (m ² /g)	Pore volume (cm ³ /g)	S _{BET} (m ² /g)	Pore volume (cm ³ /g)
0.13 (2.0) ^a	60.0	0.200	140.0	0.773	197.0	0.440	202.0	0.477	168.0	0.608
0.44 (6.0) ^a	53.0	0.185	105.1	0.664	175.0	0.422	169.0	0.363	140.0	0.334
0.88 (10.0) ^a	45.0	0.152	80.8	0.509	139.0	0.334	130.0	0.264	100.0	0.242

(^a) Number in parenthesis represents the amount of CeO₂ in wt.%, the MoO₃ content was kept constant at 12.0 wt.%

Although this was observed irrespective of the catalyst support, it was apparent that the degree of this reduction is influenced by the nature of the support used. For example, the

10.0 wt.% yttria doped alumina aerogel support when loaded with bi-oxide catalyst ($[Ce]/[Mo] = 0.13$) displayed a loss of ca. 34 %, while conv.alumina when loaded with the same catalyst showed a ca. 55 % loss (Table 6.5). Furthermore, it can be noted that the S_{BET} and pore volume of bi-oxide catalyst when supported onto the yttria doped alumina aerogel, was slightly different from that of its corresponding mono-oxide ones. This was contrary to what was observed with conv.alumina and alumina aerogel bi-oxide catalyst.

6.3.3.2. Surface configuration of bi-oxide Mo-Ce species

XRD patterns of bi-oxide MoO_3-CeO_2 catalyst loaded on different supports, with various $[Ce]/[Mo]$ molar ratio are shown in Fig.6.8 (a-d). It can be noted from Fig.6.8 that there are several phases formed on the support surface, $\gamma-Al_2O_3$, CeO_2 and MoO_3 crystallites. Although XRD measurements did not detect any peaks that may reflect the presence of MoO_3-CeO_2 mixed phase, Raman measurements and thermal analyses have clearly indicated the presence of distinctive interactions between the co-impregnated Mo and Ce metals. More importantly, the influence of the support on the phases formed was noticeably detected. To elucidate this further, we compare the XRD pattern of bi-oxide MoO_3-CeO_2 (i.e. $[Ce]/[Mo] = 0.13$) that was loaded onto different support. The XRD pattern of bi-oxide catalyst supported on conv.alumina showed the presence of $\gamma-Al_2O_3$, MoO_3 and traces of CeO_2 crystallites. The XRD pattern of catalyst supported on alumina aerogel showed also the presence of $\gamma-Al_2O_3$ and MoO_3 , however the CeO_2 reflections were clearly observed. The XRD patterns of bi-oxide catalyst supported on yttria doped alumina aerogel showed the presence of only $\gamma-Al_2O_3$ and CeO_2 crystallites, without the presence of any bulk MoO_3 crystallites peaks. Another interesting feature was the

influence of the support on the average CeO_2 crystallite size in the bi-oxide catalysts (Fig.6.8 (a-d) and Table 6.4). For example, the average CeO_2 crystallite size in the supported bi-oxide catalyst with $[\text{Ce}]/[\text{Mo}] = 0.44$ decreased from 34.2 to 6.89 nm when the support was changed from conv.alumina to 20.0 wt.% yttria doped alumina aerogel, respectively. The observed pattern of decreasing CeO_2 crystallite size was in accordance with that observed for mono-oxide CeO_2 . It is also worth mentioning that the average CeO_2 crystallite size determined for the CeO_2 catalysts was lower than that of the MoO_3 - CeO_2 catalysts, although similar loading of CeO_2 was used.

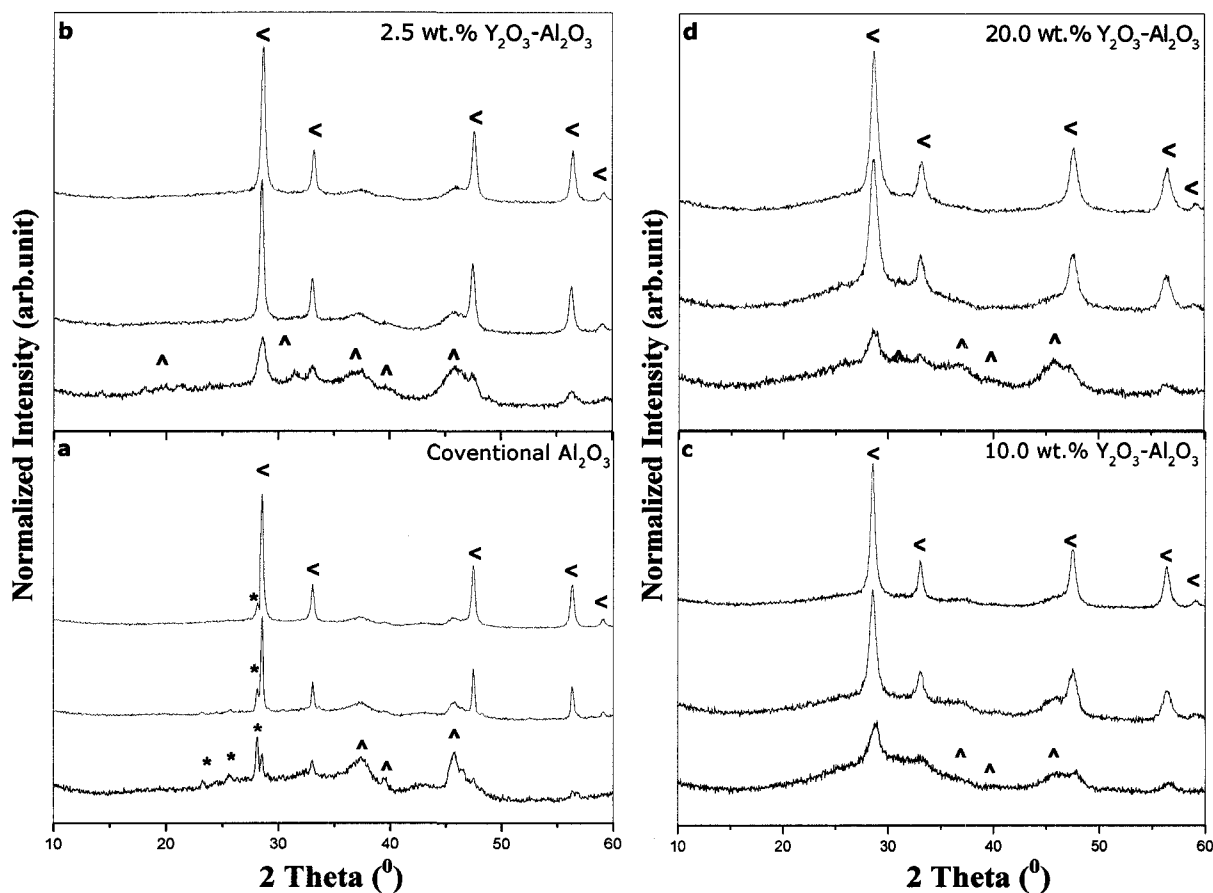


Fig.6.8 (a-d): X-ray diffraction patterns of supported bi-oxide MoO_3 - CeO_2 catalysts, with different $[\text{Ce}]/[\text{Mo}]$ molar ratio; (A) 0.13, (B) 0.44, and (C) 0.88. (^) Reflections due to γ - Al_2O_3 , (<) CeO_2 , (*) MoO_3 (JCPDS No. 35-0609)

Raman Spectra of bi-oxide $\text{MoO}_3\text{-CeO}_2$ catalyst loaded on different supports, with various $[\text{Ce}]/[\text{Mo}]$ ratio were also performed. Fig.6.9 (a-d), which shows the Raman spectra of supported bi-oxide catalysts displayed the appearance of several Raman bands: 287-320, 464, 667, 819-835, 920-971 and 996 cm^{-1} . These bands were ascribed to different crystalline and amorphous phases in corroboration with the XRD patterns (Fig.6.8).

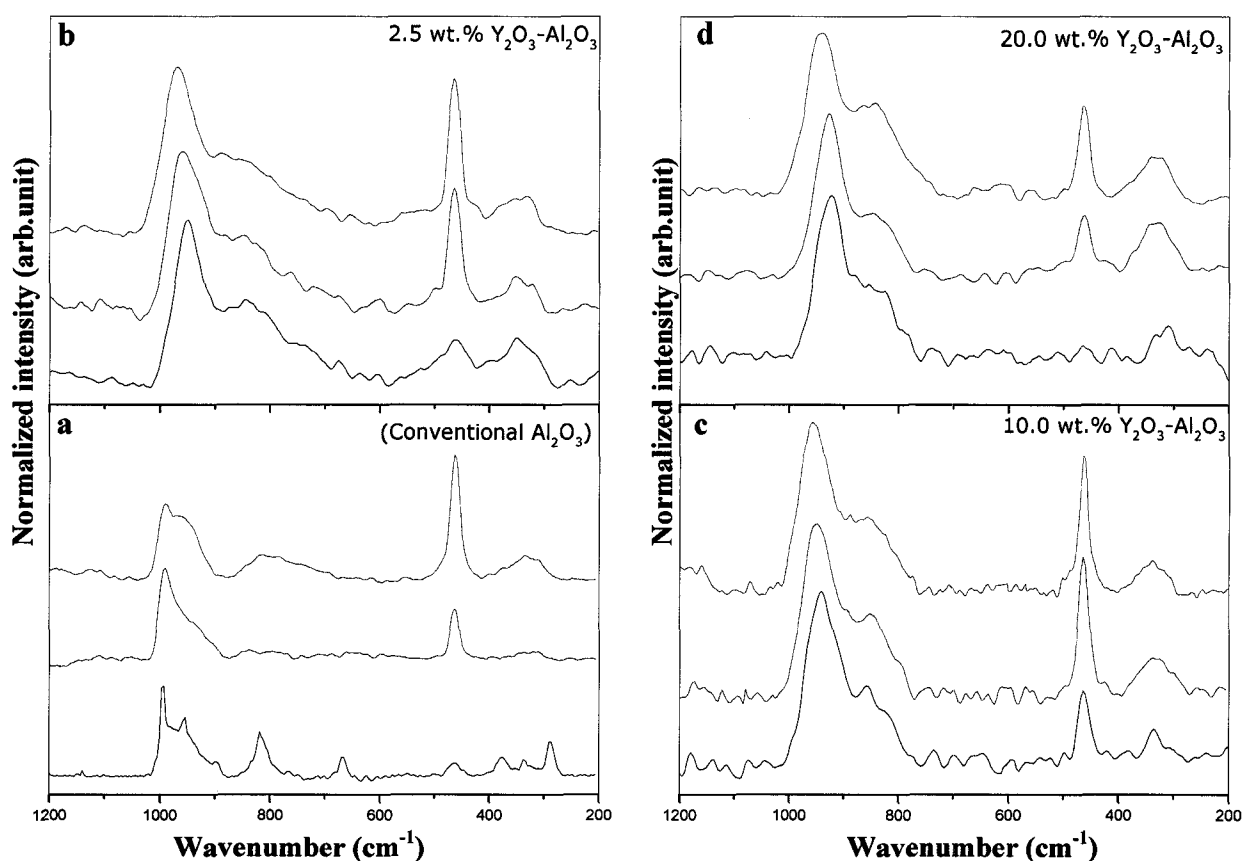


Fig.6.9 (a-d): laser Raman spectra of supported bi-oxide $\text{MoO}_3\text{-CeO}_2$ catalysts with different $[\text{Ce}]/[\text{Mo}]$ molar ratio; (A) 0.13, (B) 0.44, and (C) 0.88

The Raman band observed at 464 cm^{-1} is assigned to bulk CeO_2 crystallites [62], while the simultaneous presence of Raman bands 288, 668, 819 and 996 cm^{-1} are clearly

indicative of bulk MoO_3 crystallites [71]. Analysis of the Raman spectra of bi-oxide catalysts (Fig.6.9) and comparison with those of their mono-oxide counterparts (Fig.6.2) revealed the following points: First, it was noted that the presence, the shape and intensity of the observed Raman bands that are ascribed to bulk MoO_3 and CeO_2 crystallites, were significantly influenced by the nature of the support used. For instance, the 464 cm^{-1} bulk CeO_2 Raman band was apparent in all catalysts and its intensity increased as we increased the $[\text{Ce}]/[\text{Mo}]$ ratios, irrespective of the catalyst support used. However, the peak appeared less intense and very broad as we varied the support from conv.alumina to yttria doped alumina aerogel with various yttria loadings. The decrease in the intensity is indicative of a decrease in the average crystallite size of CeO_2 , and is in accordance with the trend that was observed with mono-oxide CeO_2 catalysts. Furthermore, bulk MoO_3 crystallites were only observed with samples supported on conv.alumina and alumina aerogel. Nevertheless, we could not detect their presence with samples supported on yttria doped alumina aerogel. Second, Raman spectroscopy, which is more sensitive to the vibration of Mo-O bonds, led to an interesting observation: the presence of interaction between Mo and Ce that appeared to be strongly enhanced over yttria doped alumina aerogel surface. This particular observation is very significant, since XRD has failed to detect the presence of Mo-Ce interaction. This can be attributed to the fact that the crystallite formation, as a result of this type of interaction, is well below the detection limit of the XRD ($< 40\text{Å}$). To elucidate the role of Raman in revealing the existence of Mo-Ce interaction, we compare the Raman spectra of 20.0 yttria doped alumina aerogel supported bi-oxide samples having various $[\text{Ce}]/[\text{Mo}]$ ratios, with those of their respective mono-oxide MoO_3 . The main Raman band, which was ascribed to surface

tetrahedral monomolybdate species, was observed at ca. 915 cm^{-1} in the supported monoxide MoO_3 catalyst (12.0 wt.% MoO_3). However, this band was shifted to higher frequency upon incorporation of CeO_2 (Fig.6.9d (A-C)). Its position was observed to be as follows: 921, 927, and 938 cm^{-1} for the supported bi-oxides with $[\text{Ce}]/[\text{Mo}]$ ratio of 0.13 (2.0 wt.% CeO_2), 0.44 (6.0 wt.% CeO_2), and 0.88 (10.0 wt.% CeO_2), respectively. Therefore, it can be concluded that the upward shift is indicative of an interaction between MoO_3 and CeO_2 , and the shifted band can be possibly assigned to cerium molybdate species. Bi-oxide that was supported on the conv.alumina and the alumina aerogel also indicated the presence of Mo-Ce interaction. On the contrary, the extent of this interaction was significantly lower than that observed with yttria doped alumina aerogel, as is evident from the appearance of large bulk MoO_3 crystallites.

6.3.3.3. Thermal Analysis Results

The effect of the CeO_2 presence on the sublimation temperature of MoO_3 in the bi-oxide catalyst was investigated. Prior to presenting the TGA curves of supported bi-oxide $\text{MoO}_3\text{-CeO}_3$ with various $[\text{Ce}]/[\text{Mo}]$ ratio, it is imperative to discuss the DTA/TGA of the corresponding unsupported bi-oxide (Fig.6.3 (B,C)). The XRD patterns and Raman measurements of unsupported $\text{MoO}_3\text{-CeO}_2$ catalysts presented in our previous investigation have shown the presence of MoO_3 and Mo-Ce mixed oxide, irrespective of $[\text{Ce}]/[\text{Mo}]$ ratios [11]. The TGA curves of the unsupported sample with $[\text{Ce}]/[\text{Mo}] = 0.13$ displayed a weight loss of ca. 54.0 wt.% that started at $740\text{ }^\circ\text{C}$ (similar temperature observed for pure MoO_3), with broad endothermic peak as shown by DTA. The TGA curves of unsupported samples with higher CeO_2 content ($[\text{Ce}]/[\text{Mo}] = 0.44$) have shown a weight loss of ca. 30.1 wt.% that begun at $755\text{ }^\circ\text{C}$. Furthermore, correlating the

observed weight losses that are attributed to the sublimation of MoO_3 in these samples, to the calculated amount of MoO_3 , clearly indicate the presence of Mo-Ce mixed oxide. For instance, unsupported bi-oxide samples with $[\text{Ce}]/[\text{Mo}]$ of 0.13 showed a weight loss of 54.0 wt.%, where the total MoO_3 content was 86.0 wt.%. Therefore, the observed retardation of the sublimation temperature of MoO_3 is attributed to the formation of $\text{MoO}_3\text{-CeO}_2$ compounds that are thermally stable up to 1150 °C (maximum temperature examined in this investigation). The TGA curves of supported bi-oxide catalysts with various $[\text{Ce}]/[\text{Mo}]$ ratios are shown in Fig.6.4 (d-f), and Table 6.2. The following observations can be noted. First, the MoO_3 sublimation temperature increased progressively as a function of the amount of CeO_2 added, irrespective of the catalyst support used. For instance, bi-oxide catalyst with $[\text{Ce}]/[\text{Mo}]$ ratio of 0.13 loaded onto 2.5 wt.% yttria doped alumina aerogel, displayed a weight loss of about 1.40 wt.% that started at 1010 °C. Whereas, catalysts with a $[\text{Ce}]/[\text{Mo}]$ ratio of 0.44 showed no weight loss up to 1150 °C (Table 6.2). Accordingly, the retardation of the MoO_3 sublimation for the supported bi-oxide catalysts can be attributed to the presence of CeO_2 . Second, the thermal analysis results do not only support the existence of Mo-Ce interaction, but also suggest another interesting phenomenon. It was observed that the extent of Mo-Ce interaction is more enhanced over yttria doped alumina aerogel, compared to conv.alumina and alumina aerogel. For instance, the addition of 2.0 wt.% CeO_2 onto 2.5 wt.% yttria doped alumina aerogel that contains ca. 12.0 wt.% MoO_3 has resulted in the shift of the temperature where the weight loss started to occur by 30 °C. Moreover, the addition of 6.0 wt.% CeO_2 has caused the temperature to shift by 170 °C. On the other hand, the influence of CeO_2 was less prominent for catalysts supported on the

conv.alumina and the alumina aerogel. These observations are in complete agreement with XRD (Fig.6.8) and Raman (Fig.6.8), which have indicated the presence of more enhanced interaction between Mo and Ce on the surface of yttria doped aerogel compared to other supports.

6.3.3.4. More on the dispersion of supported bi-oxide $\text{MoO}_3\text{-CeO}_2$ catalysts

The significance of supported bi-oxide catalysts stems from the beneficial effect of the synergistic interaction between the two metal oxides. This interaction plays a considerable role in influencing the physico-chemical properties and subsequently the catalytic performance of supported bi-oxide catalysts [72,73]. The existence and the extent of synergetic interaction, as well as their subsequent influences depend on several factors including the nature and concentration of active species and promoters, and more significantly the catalyst support. The textural, structural and thermal measurements have explicitly shown the existence of synergetic interaction between Mo and Ce in supported bi-oxide $\text{MoO}_3\text{-CeO}_2$ catalyst, irrespective of the type of support used. However, they demonstrated that the extent of this interaction was much higher on the surface of the yttria doped alumina aerogels with various yttria loadings, compared to conv.alumina and alumina aerogel. Although XRD could not unequivocally detect Mo-Ce mixed oxides, Raman and TGA measurements suggested that Mo-Ce interaction does exist in the supported bi-oxide catalysts. Thus, this interaction can be ascribed to surface “Mo-O-Ce” type interaction phase, which is the precursor of a Mo-Ce mixed oxide. It is probable that this surface phase is formed as a result of an interaction between the dispersed ceria and the molybdate monolayer, where it is likely that Ce would be located within that monolayer or exists as a bilayer structure. On the basis of that, it can be inferred that in

either case the nature of Mo and Ce phases on the surface, is quite important for such interaction to occur effectively. Therefore, it is reasonable to expect that the extent of Mo-Ce synergistic interaction would be more enhanced with bi-oxide catalysts supported on yttria doped alumina aerogel compared to those on conv.alumina and alumina aerogel. To characterize this further, we discuss supported bi-oxide $\text{MoO}_3\text{-CeO}_2$ ($[\text{Mo}]/[\text{Ce}] = 0.13$), and its respective supported mono-oxide MoO_3 (12.0 wt.%) and CeO_2 (2.0 wt.%) catalysts. In the supported mono-oxide MoO_3 catalyst, the population of bulk crystallites was significantly reduced by using yttria doped alumina aerogel as a support, thus affording a large population of surface molybdate species (tetrahedral monomolybdates). Similarly, the population of ceria (substituted ceria) dispersed phase was increased upon supporting CeO_2 catalyst onto yttria doped alumina aerogel. Hence, the co-impregnation of Mo and Ce onto the yttria doped alumina aerogel resulted in the formation of large population of the surface “Mo-O-Ce” interaction phase, together with small bulk CeO_2 crystallites (9.15 nm). On the contrary, conv.alumina and alumina aerogel failed to achieve a high degree of MoO_3 and CeO_2 dispersion, as evident from the presence of large population of bulk crystallites on the expense of surface dispersed species.

6.4. CONCLUSION

The results presented in this work reinforce our conclusion that yttria doped alumina aerogel is an effective support for TCC catalysts than conv.alumina and alumina aerogel. It was found that the incorporation of Y_2O_3 into alumina aerogel structure has another significant beneficial role, besides improving the thermal and hydrothermal stability [13,14]. Yttria doped alumina aerogel was highly effective in homogenously dispersing the active species, thus minimizing the formation of bulk crystallites.

- 1- Textural, structural, and thermal measurements of supported mono-oxide MoO_3 catalysts explicitly suggested that yttria doped alumina is more capable of reducing the formation of bulk crystallites, thus affording a larger population of surface dispersed molybdate species (tetrahedral monomolybdate), when compared to the other investigated supports. This was attributed to the incorporation of Y_2O_3 into alumina aerogel network, which led to a change in the IEP of the surface and subsequently its affinity strength to molybdate species.
- 2- Two significant improvements were noted with mono-oxide CeO_2 catalysts upon using yttria doped alumina aerogel. First, a noticeable delay in the transition from the ceria (substituted ceria) dispersed phase to the bulk phase. Second, the decrease in the average crystallite size of bulk ceria. These improvements could be possibly attributed to the cerium-support interaction mechanism, and/or the formation of $\text{CeO}_2\text{-Y}_2\text{O}_3$ solid solution mechanism.
- 3- More significantly, it was found that surface interaction between the dispersed ceria and the molybdate monolayer does exist, most probably through the formation of “Mo-Ce-O” type interaction phase. This interaction was highly favourable over yttria doped alumina aerogel compared to the other supports.

6.5. ACKNOWLEDGEMENTS

Financial support from NSERC (Natural Science and Engineering Research Council of Canada) and Valeo Management are acknowledged. The authors thank Prof. G. Denes (Concordia University) for useful discussion about $\text{CeO}_2\text{-Y}_2\text{O}_3$ solid solution. Also, we thank Suiling Wang (Concordia University, Department of Building, Civil, and Environmental Engineering) for technical assistance with the IEP measurements.

6.6. AUTHOR'S NOTES AND SIGNIFICANCE OF PAPER TO THESIS

This work on the interactions between yttria and MoO₃, CeO₂ and MoO₃-CeO₂ species was the first article to be published in the literature on yttria doped alumina aerogel supported mono-and bi-oxide MoO₃-CeO₂. This study has shown that this particular support is more capable of homogenously dispersing impregnated metals at high calcination temperature than the undoped alumina aerogel and conventional alumina. That behaviour was mainly attributed the incorporation of yttria into the alumina aerogel network.

The following chapter presents the most important part of the thesis, since it correlates the Thermo-Catalytic Cracking activities and kinetic study of the supported mono- and bi-oxide MoO₃-CeO₂, with the previously investigated physico-chemical properties (Chapter IV, V, and VI). The Thermo-Catalytic Cracking Performance and kinetic study of n-hexane over supported mono- and bi-oxide MoO₃-CeO₂ has been investigated in order to determine the catalytic roles of surface acidity and other physico-chemical properties.

6.7. REFERENCES

- [1] P. Pujado, D. Greer, J. Andersen, T. Foley, V. Bhirud, *pre-print Archive-American Institute of Chemical Engineering*, [Spring National Meeting], New Orleans, LA, USA. March 11-14 (2002) 2471.
- [2] J.S. Plotkin, *Catal.Today*. **106** (2005) 10
- [3] A. Chauvel, G. Lefebvre, *Petrochemical Processes*, Vol. 1, Technip, Paris, 1989, p. 117.
- [4] S. Matar, L.F. Hatch, *Chemistry of Petrochemical Processes*, 2nd ed., Gulf

- Professional Publishing, Woburn, MA, 2001, p. 117.
- [5] R. Le Van Mao, Concordia University, US Patent 4, 732, 881 (1988).
- [6] R. Le Van Mao, S. Melancon, C. Gauthier-Campbell, P. Kletnieks, *Catal. Lett.* **73** (2001) 181.
- [7] S. Melancon, R. Le Van Mao, P. Kletnieks, D. Ohayon, S. Intem, M.A. Saberi, D. McCann, *Catal. Lett.* **80** (2002) 103.
- [8] R. Le Van Mao, N. Al-Yassir, D. N., *Micropor. Mesopor. Mater.* **85** (2005) 176.
- [9] N. Al-Yassir, R. Le Van Mao, F. Heng, *Catal. Lett.* **100** (2005) 1.
- [10] R. Le Van Mao, Concordia University, PCT Patent (2005).
- [11] Nabil Al-Yassir, R. Le Van Mao, *Appl. Catal. A: Gen.* **305** (2006) 130.
- [12] R. Le Van Mao, N-T. Vu, N. Al-Yassir, N. Francois, J. Monnier, *Top. Catal.* **37** (2006) 107.
- [13] N. Al-Yassir, R. Le Van Mao, *Appl. Catal. A: Gen.* **317** (2007) 275.
- [14] N. Al-Yassir, R. Le Van Mao, submitted to Canadian Journal of Chemistry (August 2007).
- [15] J. Handzlik, J. Stoch, J. Ogonowski, M. Mikolajczyk, *J. Mol. Catal. A: Chem.* **157** (2000) 237.
- [16] C. Louis, J.M. Tatibouet, and M. Che, *J. Catal.* **109** (1988) 354
- [17] M. de Boer, A.J. van Dillen, D.C. Koningsberger, J.W. Geus, M.A. Vuurman, I.E. Wachs, *Catal. Lett.* **11** (1991) 227.
- [18] C. Song and X. Ma, *Appl. Catal. B: Environ.* **41**(2003) 207.
- [19] A.Trovarelli, *Catal. Rev.-Sci.Eng.* **38** (1996) 439.
- [20] J. Scherzer, *Catal. Rev.-Sci. Eng.* **31** (1989) 215.

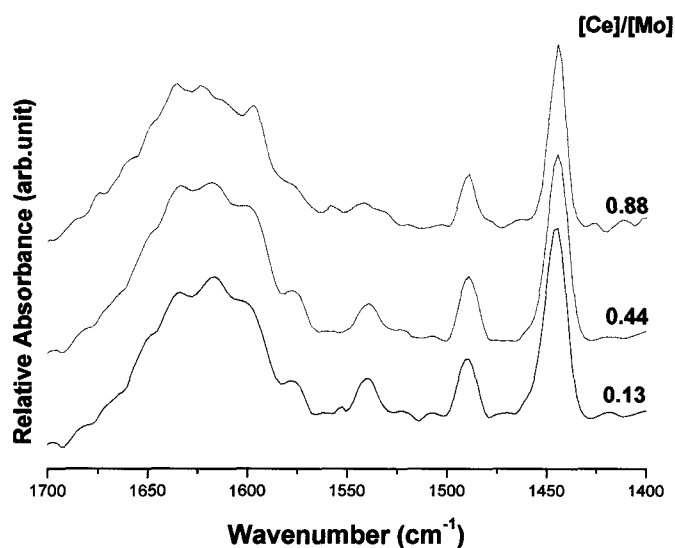
- [21] Z. Qu, W. Huang, S. Zhou, H. Zheng, X. Liu, M. Cheng, X. Bao, *J.Catal.* **234** (2005) 33.
- [22] M.A.Banares, *Catal.Today.* **51** (1999) 319.
- [23] J.T. Miller, B.L. Mojet, D.E. Ramaker, D.C. Koningsberger, *Catal.Today.* **62** (2000) 101.
- [24] M. Breysse, P. Afanasiev, C. Geantet, M. Vrinat, *Catal.Today.* **86** (2003) 5.
- [25] Y. Okamoto, M. Breysse, G.M. Dhar, C.Song, *Catal.Today.* **86** (2003) 1.
- [26] K. Hayek, R. Kramer, Z. Paal, *Appl. Catal. A: Gen.* **162** (1997) 1.
- [27] E.Elaloui, R. Begag, B. Pommier, G.M. Pajonk, *Stud. Surf. Sci. Catal.***143** (2002) 331.
- [28] E.Ponthieu, J. Grimblot, E. Elaloui, G. Pajonk. *J. Mater.Chem.* **3** (1993) 287.
- [29] JCPDS, X-ray Powder Data File, International Center for Diffraction Data, Pennsylvania, 1989.
- [30] J.-Y. Tilquin, R. Cote, G. Veilleux, D. Guay, J.P. Dodelet, G. Denes, *Carbon* **33** (1995) 1265.
- [31] K.R. Reddy, T. Bhaskar, K. V.R. Chary, *Langmuir* **19** (2003) 10795.
- [32] Y. Okamoto, T. Imanaka, *J. Phys. Chem.*, **92** (1988) 7102.
- [33] Y.C. Xie, Y.Q. Tang, *Adv. Catal.* **37** (1990) 1.
- [34] A. L. Diaz, M. F. Bussell, *J. Phys. Chem.*, **97** (1993) 470.
- [35] B. M. Reddy, P. Lakshmanan, A. Khan, *J. Phys. Chem. B.* **108** (2004) 16855.
- [36] R. Lopez Cordero, F. J. Gil Llambias, A. Lopez Agudo, *Appl. Catal.* **74** (1991) 125.
- [37] F. Roozeboom, T. Fransen, P. Mars, P. J. Gellings, *Anorg. Allg. Chem.*, **449** (1979) 25.

- [38] G. C. Bond, S. F. Tahir, *Appl.Catal.* **71** (1991) 1.
- [39] R. D. Shannon, C. T. Prewitt *Acta. Crystallogr.B* **25** (1969) 925.
- [40] G.Mestl, T.K.K.Srinivasan, *Catal.Rev. - Sci.Eng.* **40** (1998) 451.
- [41] H. Jeziorowski, H. Knozinger, *J.Phys.Chem.*, **83** (1979) 1166.
- [42] H.Hu, I.E.Wachs and S.R.Bare, *J.Phys.Chem.* **99** (1995) 10897.
- [43] A.N.Desikan, L.Huang, and S.T.Oyama, *J.Phys.Chem.* **95** (1991) 10050.
- [44] P. Dufresne, E. Payen, J.P. Grimblot, and J.P. Bonnelle, *J. Phys.Chem.* **85** (1981) 2344.
- [45] I.E. Wachs, *Catal. Today* **27** (1996) 437.
- [46] C. C. Williams, J. G. Ekerdt, J-M. Jehng, F. D. Hardcastle, I. E. Wachs, *J. Phys.Chem.* **95** (1991) 8791.
- [47] J. Medema, C. Van Stam, V. H. J. de Beer, A. J. A. Konings, D. C. Koningsberger, *Catal.*, **53** (1978) 386.
- [48] F. D. Hardcastle, I. E. Wachs, *J. Mol. Catal.*, **46** (1988) 173.
- [49] H.G. El-Shobaky, M. Mokhtar, A.S. Ahmed, *Thermochim.Acta.* **327** (1999) 39.
- [50] V. Behrani, Oxidation behavior and chlorination treatment to improve oxidation resistance of Nb-Mo-Si-B alloys, Masters thesis, Iowa State University, 2004.
- [51] K. Chen, S. Xie, A. T. Bell, E. Iglesia, *J.Catal.* **198** (2001) 232.
- [52] G. A. Parks, *Chem. Rev.* **65** (1965) 177.
- [53] H. H. Kung, *Transition Metal Oxides: Surface Chemistry and Catalysis*. Elsevier, Amsterdam 1989.
- [54] M. Kosmulski, *J. Colloid Interface Sci.* **275** (2004) 214.
- [55] F. Pinna, *Catal.Today*, **41** (1998) 129.

- [56] M. Trueba, S. P. Trasatti, *Eur. J. Inorg. Chem.* (2005) 3393.
- [57] R. Sprycha, J. Jablonski, E. Matijevec, *J. Colloid Interface Sci.* **149** (1992) 561.
- [58] N. Giordano, J. C. J. Bart, A. Vaghi, A. Castellan, G. Martinotti, *J. Catal.*, **36** (1975) 81.
- [59] J. Z. Shyu, W.H. Weber, H.S. Gandhi, *J.Phys.Chem.* **92** (1988) 4964.
- [60] M.M. Mohamed, *Appl. Catal. A: Gen.* **267** (2004) 135.
- [61] A. Piras, S. Colussi, A. Trovaerlli, V. Sergio, J. Llorca, R. Psaro, L. Sordelli, *J.Phys.Chem. B* **109** (2005) 11110.
- [62] S. Damyanova, C. A. Perez, M. Schmal, J. M. C. Bueno, *Appl. Catal. A Gen.*, **234** (2002) 271.
- [63] T. Yamamoto, T. Matsuyama, T. Tanaka, T. Funabiki, and S. Yoshida, *Phys. Chem. Chem. Phys.*, **1** (1999) 2841.
- [64] S. Humbert, A. Colin, L. Monceaux, F. Oudet, P. Courtine, *Stud. Surf. Sci. Catal.* **96** (1995) 829.
- [65] B. M. Reddy, A. Khan, *Catal. Surv. Asia* **9** (2005) 155.
- [66] A. R. West, *Basic Solid State Chemistry*, 2nd edition, John-Wiley & Sons Ltd., England, 1999, p.230-233.
- [67] J. G. Li, T. Ikegami, Y. Wang, T. Mori, *J. Solid State Chem.* **168** (2002) 52.
- [68] B. M. Reddy, A. Khan, P. Lakshmanan, M. Aouine, S. Loridant, J.-C. Volta, *J. Phys. Chem. B* **109** (2005) 3355.
- [69] V. Ponc, *Appl. Catal. A.*, **222** (2001) 31.
- [70] K. Persson, A. Ersson, K. Jansson, N. Iverlund, S. Jaras, *J. Catal.* **213** (2005) 139.

Chapter VII

Supported $\text{MoO}_3\text{-CeO}_2$ catalysts used in the Thermo-Catalytic Cracking (TCC) Process for the Production of Light Olefins. Effects of Surface Acidity and other Physico-Chemical Properties on performance and kinetic behavior



Graphical Abstract: FTIR spectra of 10.0 wt.% yttria doped alumina aerogel supported bi-oxide $\text{MoO}_3\text{-CeO}_2$, after pyridine adsorption and desorption at 100 °C

To be submitted to:

N. Al-Yassir and R. Le Van Mao,

Catalysis Letters, November 2007.

ABSTRACT

Performance and kinetic behavior of catalysts based on MoO₃-CeO₂ supported on yttria doped alumina aerogels have been investigated in the Thermo-Catalytic Cracking (TCC) of n-hexane, in order to determine the effects of surface acidity and other physico-chemical properties. Infrared spectroscopy of chemisorbed pyridine, combined with ion-selective electrode NH₃-TPD measurements, were used to study the acidic properties of supported mono- and bi-oxide catalysts. It was found that the surface acidity was significantly influenced by the nature of the catalyst support, the loading level and nature of the metal oxides. Supported mono-oxide CeO₂ catalysts displayed only Lewis type-sites, which were attributed to the coordinatively unsaturated sites (cus) of Al³⁺_{cus} and Ce⁴⁺_{cus}. The surface acidity of supported mono-oxide MoO₃ catalysts showed both Brönsted and Lewis sites, which were attributed to the monodentate alumina-molybdate species, and the Al³⁺_{cus}, respectively. The Brönsted sites of Mo supported on yttria doped alumina aerogel catalysts were found to exist in lower concentration and lower strength, when compared to those supported on conventional alumina or undoped alumina aerogel. This was mainly attributed to the incorporation of yttrium ions into the alumina aerogel structure, which significantly altered the chemistry of surface -OH groups and thus those of the Mo catalysts. Addition of CeO₂ to the supported MoO₃ catalysts led to a decrease in the density of Brönsted acid sites most likely due to neutralization effects, whereas Lewis acid sites appeared to be only slightly altered.

The study of the TCC activity, which was strongly dependent on the surface Brönsted-Lewis acidity, showed that supported mono-oxide MoO₃ and bi-oxide MoO₃-CeO₂ catalysts are much more catalytically active than supported CeO₂. It was also noted

that the total conversion, which increased as the MoO₃ loadings increased up to 12.0 wt.% (irrespective of the catalyst support), was mainly attributed to the presence of Brönsted acid sites. The selectivity to aromatics also increased at the expense of light olefins. The extent of that increase was much higher upon using yttria doped alumina aerogel instead of undoped alumina aerogel as a support. This was mainly attributed to the presence of Brönsted sites in lower density compared to the large population of Lewis sites, which favour the hydrogen transfer and aromatization reactions. Addition of CeO₂ to the MoO₃ supported on yttria doped alumina aerogel resulted in the decrease of the total conversion and the selectivity to aromatics. This was mainly related to the decrease in the total acid density, thus resulting in reduced activity of hydrogen transfer and aromatisation. Our preliminary kinetic results clearly showed that the apparent activation energy of 10.0 wt.% yttria doped alumina aerogel supported mono- (MoO₃) and bi-oxide (MoO₃-CeO₂) based catalysts is much lower than that in steam cracking.

7.1. INTRODUCTION

7.1.1. Production of Light Olefins

Commercially proven light olefins production technologies such as Steam Cracking (SC), Fluid Catalytic Cracking (FCC), ZSM-5 modified FCC, and Deep Catalytic Cracking (DCC) are expected to face great challenges in the near future [1-6]. The market demand for ethylene and propylene, which is driven largely by the escalating demand for the production of polyethylene and polypropylene, is projected to be about 140 and 90 million tons by year 2010, respectively [1-3]. This is an annual growth of about 4.5-5.5 %, and 5.5-6.0 % for ethylene, and propylene, respectively [1-3]. On the other hand, these current technologies cannot respond sufficiently to the rapidly growing demand for propylene, since propylene is only produced as a co-product of ethylene production (for mechanistic reasons) [3,5]. In addition, the high-energy consumption and the high green house gas emissions are major setbacks for SC, which is regarded as the main light olefin technology [3].

Thermo-Catalytic Cracking (TCC) of petroleum feedstocks for the production of light olefins has been developed in an attempt to overcome some of these challenges [7-17]. This emerging process is considered more advantageous than other light olefin technologies since it produces higher combined yields of ethylene and propylene, requires low energy costs and is more environmentally friendly process. One of the TCC catalyst versions is the supported mixed metal oxides based catalysts (i.e. supported $\text{MoO}_3\text{-CeO}_2$) [10-16]. These catalysts operate under mild reaction temperature (720 °C) and in the presence of steam (steam is co-fed along with liquid hydrocarbons). Therefore, evaluating the stability, the physico-chemical properties, and subsequently the catalytic

activities of supported bi-oxide catalysts, are of paramount importance for the TCC process. In our previous work [14-16], we have found explicitly that the structural and the thermal-hydrothermal stability, as well as the physico-chemical properties were significantly improved upon incorporating CeO₂ into the MoO₃ catalyst and using yttria doped alumina aerogel as a catalyst support. The surface acidity, the TCC performance (product selectivity and catalyst stability), and the deactivation behaviour of these metal oxide based catalysts, remained crucial properties to investigate.

7.1.2. Thermal cracking and catalytic cracking

The conversion of paraffin (i.e. n-hexane) in the TCC process is expected to proceed through the chain reaction of the free radicals (steam cracking/ homolytic bond cleavage), and the longer lived-more selective carbocations (catalytic cracking/heterolytic bond cleavage) [7,8,12 and references therein]. The latter are formed on the active acidic sites (i.e. Brønsted and Lewis) of the catalyst. The main products of steam cracking are olefins (C₂-C₅⁺) along with H₂ [4-6]. The formed olefins and the remaining unconverted paraffin will undergo catalytic reactions as well. The presences of olefins in such high concentration will certainly be the main initiator of several catalytic reactions through the formation of carbenium ions (i.e. protonation of olefinic species by Brønsted acid sites) [18-21]. Lewis acid sites are also expected to participate but to a lesser extent in the initiation step via the H-abstraction from available paraffins [22,23]. It is possible that the catalytic reactions will also start via the formation of carbonium ions (i.e. protonation of a C-C bond by the Brønsted sites, (non-classical monomolecular cracking, also referred to as Haag-Dessau cracking)) [24,25]. Once the carbocation (i.e. carbenium or carbonium ions) are adsorbed on the active sites of the catalysts, they may undergo several types of

reaction [5, 19, 26 and reference there in]. First, they can desorb as an olefin and restore the acidic sites. Secondly, they can undergo a monomolecular reaction. For instance, they can crack by β -Scission (C-C bond cleavage), leading to the formation of a smaller olefin and a smaller carbenium ion. It is also possible that they may undergo an isomerization reaction (skeletal or charge) in order to generate a more stable carbenium ion. The branched carbenium ion can either desorb giving a branched olefin, or may crack by β -scission giving in an olefin and surface carbenium ions. Thirdly and more significantly, they may undergo a bimolecular reaction. In this reaction, surface carbenium ions can react with neutral paraffin molecule via intermolecular hydride transfer (HT) forming a new carbenium ion, which in turn undergoes a β -scission cracking. In addition, other unfavourable secondary reactions (i.e. cyclization, aromatisation via (HT: olefin + naphthene \rightarrow paraffin + aromatic) and/or (dehydrocyclization of paraffin)), condensation, polymerization, etc.) are also expected to take place. One of the primary objectives of the TCC process is to maximize the yield of light olefins with a long lasting on-stream stability. The latter is quite important, because the TCC process utilizes a fixed bed reactor technology, which in turn requires a separate production-regeneration cycle. Thus, the long on-stream stability of the catalysts is a vital requirement. The hydrogen transfer and aromatization reactions play a key role in reducing the concentration of olefins in the product stream, and contributing to coke formation [27-38]. Therefore, it is highly beneficial for the TCC process that the HT reactions should be suppressed. The extent of the bimolecular HT reactions has been shown to depend significantly on several factors such as the density and strength of surface acid sites [27-38]. For instance, Scherzer and Ritter [30] stated that the lower density of acid sites in USY when

compared to HY zeolite is responsible for the reduced rate of conversion of olefins into paraffin, and aromatics into condensed polycycles (coke). The presence of both Brønsted and Lewis acidic sites has been also reported to enhance the HT reactions [31,35-37]. In addition to that, diffusion limitation (steric constraint) plays a significant role in hindering such reactions. For example, zeolites such as MFI limit the significance of the bimolecular HT reactions, which requires bulkier intermediates and transition states, due to their narrow pores [38].

7.1.3. Objectives of the present study

This study addresses the effect of the physico-chemical properties (i.e. dispersion, metal crystallite size, etc.), and the surface acidity, which were influenced by the utilization of yttria doped alumina aerogel as a catalysts support and the presence of cerium in the bi-oxide based catalyst, on the catalytic performance and in particular the secondary reactions (HT and aromatization). Therefore, in order to fulfill our objectives, the important features of surface acidity of yttria doped alumina aerogel supported mono- and bi-oxide catalysts were investigated via the Fourier transform infrared spectroscopy of adsorbed pyridine, and the Ion-selective electrode and back-titration NH_3 -TPD. The catalytic activities of these catalysts were evaluated in the TCC of n-hexane (used as a model molecule for petroleum naphtha). A detailed analysis of the the kinetics of both steam cracking and TCC reactions were also carried out in order to determine the rate constant and the activation energy of both reactions. The deactivation behaviour of these catalysts and the combustive properties (amount and combustion temperature) of carbonaceous deposits were also examined using gravimetric and differential thermal

analysis. Conventional alumina based catalysts were investigated only for comparison purposes.

7.2. EXPERIMENTAL

7.2.1. Catalyst Preparation

Supported Catalysts

The catalyst supports were prepared by previously reported synthetic technique [14 and reference therein]. Conventional alumina, undoped alumina aerogel, and yttria doped alumina aerogel are noted in this text as; conv.alumina, alumina aerogel, and $x\text{Y}_2\text{O}_3\text{-Al}_2\text{O}_3$, where x is the Y_2O_3 content in wt.%. The details of the preparation method for supported mono-oxide MoO_3 , CeO_2 and bi-oxide $\text{MoO}_3\text{-CeO}_2$, with various metal loadings, are given elsewhere [10-12,15]. All samples were calcined in air at 750 °C for 3 h. Bulk MoO_3 , and CeO_2 crystallites were obtained via calcination (at 700 °C for 10 h) of ammonium heptamolybdate (Aldrich) and Cerium (III) nitrate (Aldrich), respectively.

Extrudates

The extrudates of all catalysts were obtained by extrusion with bentonite clay (Aldrich, 20.0 wt.%). They were dried overnight at 120 °C and then calcined in air at 700 °C for 3 h.

7.2.2. Catalyst Characterization

7.2.2.1. The specific surface areas and pore volume of samples were determined by the BET method using nitrogen physisorption at 77 K. The measurements were carried out using Micromeritics ASAP 2000 apparatus. Samples were outgassed in a vacuum for 4 h at 220 °C before N_2 physisorption.

7.2.2.2. Acid sites properties:

Total acidity and strength profile of acidic sites

The NH₃-TPD of various samples was recorded using a fixed-bed reactor equipped with a programmable temperature controller and NH₄⁺ ion selective electrode (NH₄⁺-ISE). Data were collected and processed by a computer. In addition, the total surface acidity was measured by a back-titration method when necessary. The detailed procedure has been described before [34].

Nature of acidic sites and strength profile (Infrared Spectroscopy)

Fourier transform infrared spectra of adsorbed pyridine were recorded in order to evaluate the nature of acidic sites (i.e. Brønsted and Lewis sites). The transmission spectra were recorded in Nicolet FTIR spectrometer (Magna 500 model) in the region of 1400-1700 cm⁻¹, with resolution of 4 cm⁻¹. The detailed measurements have been described before [10,12,16]. The identification and the assignment of bands formed upon pyridine adsorption is well documented in the literature [35-37], and thus only reference will be made to these assignments without any further explanation.

7.2.2.3. The amount and combustive properties of coke deposited onto the spent non-regenerated catalyst surface were determined using the thermal analysis technique. Thermogravimetric analysis (TGA) and differential thermal analysis (DTA) were carried out using the automated Stanton Redcroft STA 1500 simultaneous thermal analyzer from PL Thermal Sciences. The catalysts were heated from ambient temperature to 800 °C under dry air (oxidative atmosphere) (Flow: 20.0 ml min⁻¹). Prior to that, the spent catalysts were heated from 25 to 900 °C under Argon (20 ml min⁻¹) (inert atmosphere) in order to remove any surface bound species. The sample weights were ca. 10.0 mg, and the heating rate was 10 °C min⁻¹.

7.2.3. Thermo-Catalytic Cracking Activities

Experimental set-up for catalytic testing

Experiments were performed using a Lindberg one zone tubular furnace. The reactor vessel consisted of a quartz tube 55 cm in length and 1.5 cm in diameter.

Testing procedures and data reporting

n-hexane was used as a model molecule for the conversion of petroleum light naphthas. Liquids, n-hexane and water, were injected into a vaporizer using two infusion pumps. In the vaporizer, nitrogen used as a carrier gas was mixed with n-hexane vapors and steam. The gaseous stream was then sent into the tubular reactor. The testing conditions were as follows: weight of catalyst = 2.2 g, weight hourly space velocity (WHSV) = 1.52 h⁻¹, water/hydrocarbon molar ratio = 0.5 (0.11 g/g), reaction temperature = 680 °C, nitrogen flow rate = 5.0 ml/min, and duration of the run = 10h. All catalytic activities were carried out at atmospheric pressure. Gaseous and liquid products were collected separately using a system of condensers. The gas-phase components were analyzed using a Hewlett-Packard 5890 Flame Ionization Detector (FID) gas chromatograph (GC) equipped with Agilent J&W GS-alumina column (30 m x 0.53 mm x 30 µm), while the liquid phase analysis was carried out using a Hewlett-Packard 5890 GC-FID equipped with Alltech Heliflex ATTM-5 column (30 m x 0.32 mm x 0.25 µm). The catalytic activities results were reproducible within ± 2.0 wt.%.

The total n-paraffin conversion (mol% or wt.%) is expressed as follows:

$$C_t = \frac{\text{moles of converted n-paraffin}}{\text{moles n-paraffin fed}} \times 100$$

The selectivity (to product i) is expressed as follows:

$$S_i = \frac{\text{number of carbon atoms of product } i}{\text{number of carbon atoms of converted products}} \times 100$$

7.2.4. Kinetic study of steam cracking and TCC reactions

The thermo-catalytic cracking actually involves both thermal cracking and catalytic cracking. However, the rate of conversion of the feed (n-hexane) is not merely an addition of these two rates. In fact, some reaction products of thermal cracking may adsorb on the catalyst and then undergo a catalytic conversion. Conversely, products of catalytic cracking may be further thermally cracked. However, it is always useful to have kinetic behaviours related to the overall TCC reaction and thermal (steam) cracking, respectively.

7.2.4.1. Thermal (steam) cracking (SC)

The SC study consists of sending n-hexane (along with steam) into the empty reactor and then recording the conversion. At constant reaction temperature, the key factor that affects the conversion is the residence time (t_r), i.e. the time spent by the feed molecules in the reaction zone. t_r can be expressed as the volume of the reaction zone (V_R) divided by the flow-rate of the (gas phase) hydrocarbon feed (F_v), the latter being expressed as the volume per second. Thus, t_r has the dimension of second (s). Since the volume of the reaction zone in the TCC process is reduced by the mass of the catalyst (reduced void with respect to the empty tube), to reflect the level of SC conversion in the presence of a TCC catalyst, a solid substance – catalytically inert and non porous (such as quartz) – is used.

The rate of SC reaction at constant temperature T is the first derivative of the conversion (C_t) with respect to the residence time (t_r). To have the value of the initial rate, the curve C_t as a function of t_r is set up, and its derivative is determined at $t_r = 0$.

$$C_t = f(t_r); \text{ rate} = (dC_t / dt_r); \text{ initial rate} = (dC_t / dt_r)_0 \text{ when } t_r = 0.$$

If a polynomial of degree 2 is used for the function f , $C_t = a_0 + a t_r + b t_r^2$. However, since $C_t = 0$ when $t_r = 0$, $a_0 = 0$ and then, $C_t = a t_r + b t_r^2$. Thus, the initial rate is equal to $(dC_t / dt_r)_0 = a$.

The classical Arrhenius equation is used for the determination of the apparent activation energy (E_a) and the pre-exponential factor (A):

$$k = A e^{-E_a/RT}$$

$$\ln k = \ln A - E_a/RT$$

Assuming that the rate constant k is first order with respect of the molar concentration of n-hexane in the feed (or partial pressure), we have: $(dC_t / dt_r)_0 = k [\text{n-hexane}]$.

By varying the temperature T and keeping $[\text{n-hexane}]$ constant, we can calculate k for each temperature T. Therefore, E_a and A are calculated by using the Arrhenius equation.

In our series of steam cracking (SC) tests, the residence time (t_r) and the temperature were varied in the range from 0.1-1.3 s, and 640-720 °C, respectively.

7.2.4.2. Thermo-Catalytic Cracking (TCC)

The TCC study consists of sending n-hexane (along with steam) into the catalyst bed and then recording the conversion. If the TCC were only a catalytic reaction, the contact time t_c (weight of the catalyst W divided by weight flow rate of the feed FW) would be the key factor that affects the conversion due to the catalyst. However, as mentioned earlier, thermal cracking is also present in the process. Therefore, if we use the

same procedure as for the SC to determine the rate of the TCC reactions, it will be impossible to separate the effect of SC from that of catalytic cracking (CC). Fortunately, if we want to vary t_c (by varying the flow rate of the feed or eventually, the catalyst weight), t_r varies in the same direction. For example, if FW decreases, F_v decreases, and both t_r and t_c increase (same values for W and VR).

Therefore, the values obtained for the apparent activation energy and the pre-exponential factor in the case of the TCC study when the function $C_t = \varphi(t_c)$ is used, reflect the kinetic behaviour of the TCC reactions quite well.

It is also worth noting that, t_c being the reciprocal of the weight hourly space velocity (W.H.S.V.), is expressed in h. In our TCC kinetic study, the W.H.S.V. was varied in the range of 0.75-1.52 h⁻¹ (t_c : from 1.33 – 0.66 h), whereas the temperature range was similar as the steam cracking (640-720 °C). The reaction time in both SC and TCC studies was 5h, which corresponds to the unsteady state kinetic.

7.3. RESULTS AND DISCUSSION

7.3.1. Detailed acidity investigation

The acid-types, Brönsted and Lewis-types, are a fundamental property of solid acids as well as the strength and density of acid sites [43-45]. This surface acidity is determining for the catalytic activity [46,47]. The FTIR spectra of pyridine chemisorbed on the supported mono-and bi-oxide catalysts, which allow a clear distinction between Brönsted and Lewis acid sites, are shown in Fig.7.1-3. Data of acid sites density is reported in Table 7.1.

It has been shown in our previous work that the FTIR spectra of chemisorbed pyridine on different catalyst support, displayed the presence of different peaks

(1444,1575, 1595,1615, and 1625 cm^{-1}) [16]. These peaks are ascribed to Lewis acid sites, which corresponds to oxygen vacancies or more accurately coordinatively unsaturated sites (cus) of Al. The bands, which appeared in region higher than 1550 cm^{-1} are considered to be more sensitive to aluminum coordination and structural vacancies [16 and references therein]. It was also apparent that the density of Lewis acid sites (assessed from the integrated area under each band, all extinction coefficients being assumed to be equal) depends on the nature of the support. Undoped alumina aerogel showed higher concentration of Lewis sites compared to conv.alumina. The concentration of these sites decreased with increasing the amount of yttria doped into the alumina aerogel lattice. The higher density of Lewis acid sites in the undoped alumina aerogel was mainly attributed to the sol-gel preparation method, which has resulted in the presence of higher concentration of intrinsic anionic surface defects (oxygen vacancies) and surface hydroxyl groups. The latter results in the formation of oxygen vacancies upon calcination at high temperature (i.e through dehydroxylation) [16]. The observed decrease in the density of Lewis acid sites with increasing amount of doped yttria was attributed to the presence of yttrium ions in alumina aerogel lattice, which has resulted in decreasing the number of anionic surface defects and surface -OH groups [14,16]. Furthermore, the conv.alumina, the undoped alumina aerogel, and the yttria doped alumina aerogel with various yttria loadings did not show any Brönsted acid sites. Since the presence of Brönsted surface acid sites on alumina has been suggested in other reports [48]. It was very clear that these sites are very weak and thus are not capable of protonating pyridine at the given adsorption temperature (100 °C). These results were also supported by the total acid density measurements (Table 7.1). As expected, the total acid density of

conv.alumina (0.22 mmol NH₃ g⁻¹ catalyst) was lower than that of alumina aerogel (0.35 mmol g⁻¹). The total acid density of the latter decreased with increasing concentration of yttria; however they remained higher than that of conv.alumina.

Table 7.1: Total acid sites density (mmol g⁻¹) by NH₃-TPD of supported mono-oxide and bi-oxide based catalysts

Different Catalyst Supports	Conv. alumina	Alumina Aerogel	10.0 wt.% Y ₂ O ₃ -Al ₂ O ₃	20.0 wt.% Y ₂ O ₃ -Al ₂ O ₃
Free support	0.22	0.35	0.27	0.23
<i>Supported mono-oxide CeO₂ catalyst with various CeO₂ loading (wt.%)</i>				
2.0	0.21	0.35	0.25	0.25
6.0	0.16	0.22	0.19	0.22
15.0	0.13	0.16	0.16	0.12
<i>Supported mono-oxide MoO₃ catalyst with various MoO₃ loading (wt.%)</i>				
4.0	0.28	0.41	0.33	0.27
8.0	0.31	0.47	0.44	0.31
12.0	0.36	0.60	0.52	0.51
20.0	0.23	0.41	0.69	0.61
<i>Supported bi-oxide MoO₃-CeO₂ catalyst with various [Ce]/[Mo] ratios</i>				
0.13	0.21	0.54	0.47	0.40
0.44	0.25	0.33	0.31	0.32
0.88	0.24	0.29	0.20	0.15

The surface acidity of supported mono-oxide CeO₂ based catalysts has been also examined. It was noted that only bands that are normally assigned to Lewis acid sites are apparent (1442, 1575, 1596, 1615 cm⁻¹). Fig.7.1. shows the variation of the area of the foremost band (1442 cm⁻¹) as a function of the catalyst support with various ceria loadings. Careful comparison between the surface acidity of supported mono-oxide CeO₂, Fig.4 and the preceding paragraph reveals the following points, which were in complete agreement with previous well-documented studies [42,49]. First, it was very clear that the impregnated ceria did not impart any surface Brönsted acidity, which if present could be readily revealed by the appearance of adsorption band at ca.1540-1550 cm⁻¹. Secondly and more notably, only surface Lewis acidity was observed (1442, 1575, 1596, 1615 cm⁻¹

¹), which increased moderately upon the impregnation of ceria. That increase depended on the ceria loadings and more significantly the nature of the catalyst support. In the case of conv.alumina and the undoped alumina aerogel, we have noted that the Lewis acidity increased upon the addition of ceria with loadings above 2.0 wt.%. Whereas, only slight increases in Lewis acidity was observed to occur upon the impregnation of high loadings of ceria (> 6.0 wt.%) onto yttria doped alumina aerogel (i.e. 20.0 wt.% Y₂O₃-Al₂O₃). It is worth mentioning that such increase was coincident with the presence of segregated ceria crystallites on the surface. The FTIR spectrum of chemisorbed pyridine on pure ceria crystallites (not shown here) showed the appearance of Lewis acid sites. These sites can be ascribed to the coordinative unsaturated cationic Ce⁴⁺ sites (Ce⁴⁺_{cus}), which most probably are intrinsic and/or formed as a result of the formation of oxygen vacancies upon calcination at high temperature (i.e. through probable reduction of Ce⁴⁺ to Ce³⁺) [41]. Therefore, it is plausible to state that the noted increase in the Lewis acidity upon the impregnation of ceria onto the support is due to the formation of Ce⁴⁺_{cus} sites, which are associated with segregated bulk ceria crystallites. The reason behind observing the increase in Lewis acidity at low ceria loading when using conv.alumina or undoped aerogel compared to yttria doped alumina aerogel, can be mainly attributed to the incorporation of yttria into the alumina aerogel lattice. The presence of yttria has succeeded in minimizing the ceria segregation [15] and thus prevented the increase in Lewis acidity, as confirmed in this current study. In another note, it appears that there is no difference in terms of strength and type between Al³⁺_{cus} and Ce⁴⁺_{cus} sites, since both were detected at the same absorption band (ca. 1444 cm⁻¹). However, it is possible that there was a difference, but could not be easily detected due to the broad nature of Lewis

sites band. Although, the pyridine-FTIR results indicated that there was an increase in the surface acidity, the total acid sites measurements by NH_3 -TPD did not yield the same conclusion. As a matter of fact, the results (Table 7.1) indicated that supported CeO_2 catalysts (with high ceria contents, ≥ 6.0 wt.%) contained lower numbers of acid sites compared to the bare support, irrespective of the catalysts support.

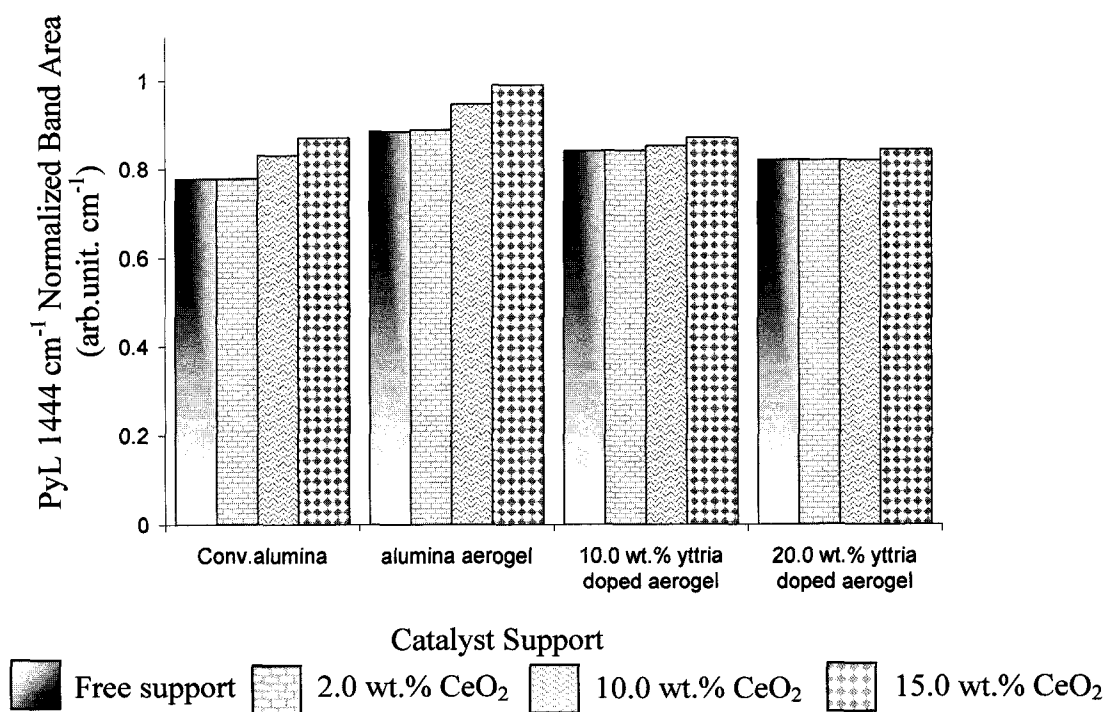


Fig.7.1: Variation of the 1444 cm^{-1} Lewis sites band area as a function of different catalyst support with various ceria loadings

Fig.7.2a-b, which shows the FTIR spectra of chemisorbed pyridine on supported mono-oxide MoO_3 catalyst with various Mo loadings, display the presence of different peaks (1444, 1490, 1540, 1575, 1595, 1616, and 1635 cm^{-1}). The Brønsted/Lewis sites ratio as a function of MoO_3 loadings for different supports is presented in Fig.7.2c.

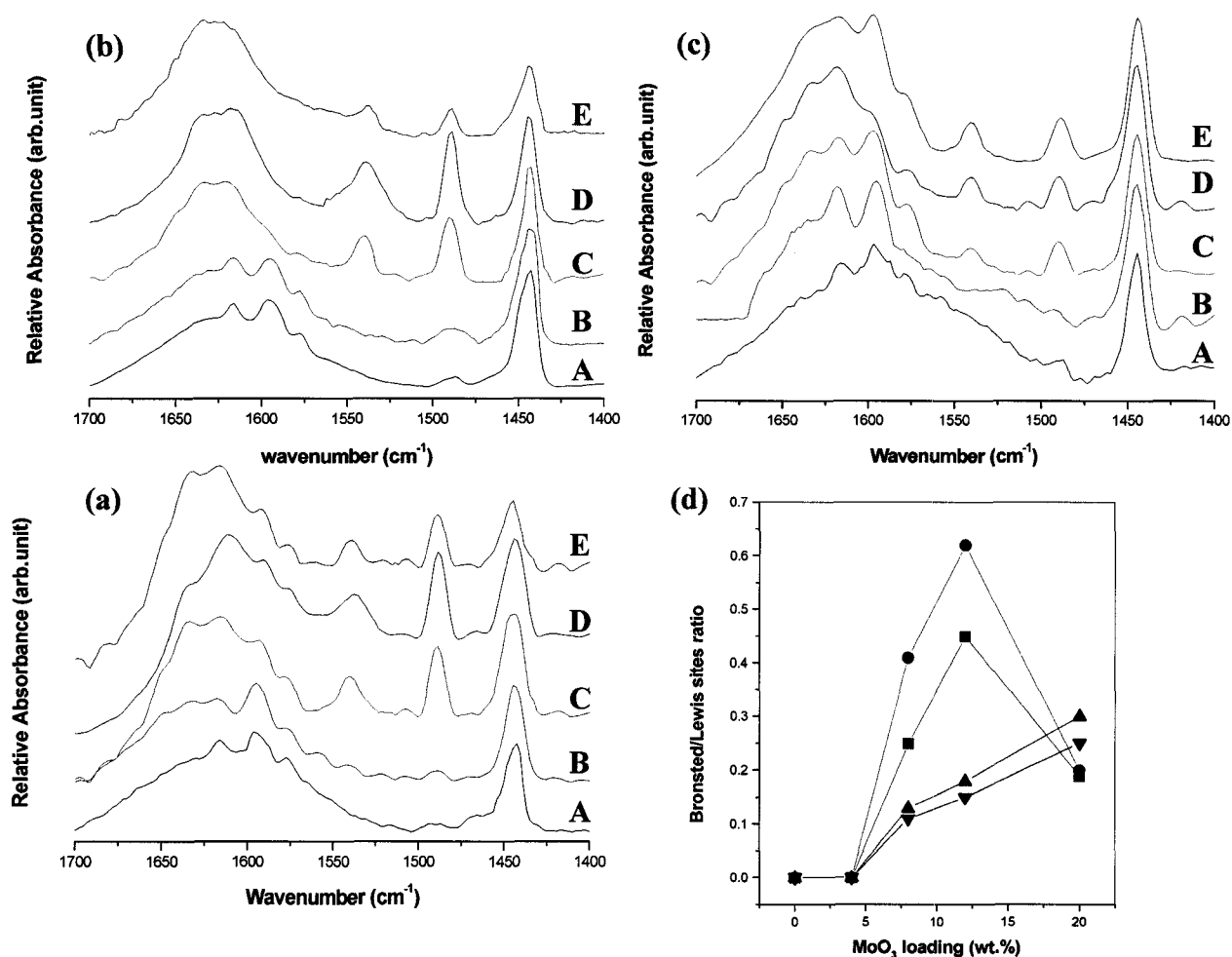


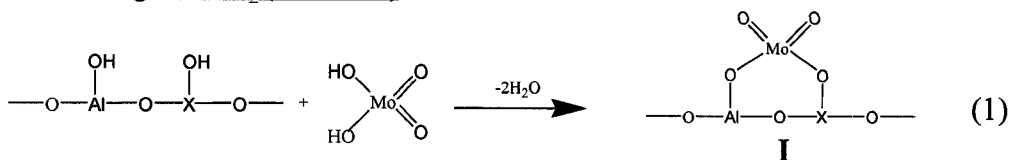
Fig.7.2: FTIR spectra of supported mono-oxide MoO_3 with various MoO_3 loadings (wt.%); A) 0.0, B) 4.0, C) 8.0, D) 12.0, and E) 20.0 after pyridine adsorption at 100 °C for two different catalyst support (a) conv.alumina, (b) undoped alumina aerogel, and (c) 10.0 wt.% yttria doped alumina aerogel. (d) represents Brønsted/Lewis sites ratio versus different MoO_3 loadings on different supports; (■) conv.alumina, (◆) undoped aerogel, (▲) and (▼) are 10.0 and 20.0 yttria doped alumina aerogel

Careful examination of Fig.7.2 reveals the following. First, it was noted that supported Mo catalysts showed the presence of both Brønsted and Lewis acid sites, irrespective of the catalyst support used. Secondly, it was observed that the density of these sites depends strongly on two factors: the Mo loadings (quite logical) and ii) the nature of the catalyst support. In agreement with previous results concerning Mo catalysts supported on conv.alumina [50], Brønsted acid sites only appeared at loadings higher than 4.0 wt.% MoO₃. The density of these sites increased with increasing Mo loading up to 12.0 wt.%, and then decreased (Fig.7.2c). Lewis acid sites were not affected by the addition of Mo up to 4.0 wt.% MoO₃. However, the Lewis acidity decreased at higher Mo contents (Fig.7.1c). Similar results were obtained with Mo supported on undoped alumina aerogel, with only one difference that the density of acid sites was much higher. The acidity changes that took place upon the deposition of Mo onto the support can be attributed to the monolayer structure of Mo oxide [50]. At very low loadings, Mo exists as highly dispersed surface tetrahedral monomolybdate species (MoO₄²⁻). These species are expected to interact through electrostatic interactions with basic alumina surface -OH groups, forming a bidentate species (reaction 1, species I, (Scheme 7.1)). At higher Mo loadings, octahedral polymeric molybdate species (Mo₇O₂₄⁶⁻) become the predominate species. The adsorption of these polymeric species has been suggested by many to occur through interaction with the remaining surface -OH groups of different type (i.e. acidic) (reaction 3, species III, (Scheme 7.1)) [51]. However, other reports have suggested that other adsorption mechanisms might be involved. Van Veen et al [52] suggested that the adsorption of heptamolybdate, in the second branch of their isotherm, occurs on coordinatively unsaturated sites (Al³⁺_{cus}) (reaction 4, species IV, (Scheme 7.1)).

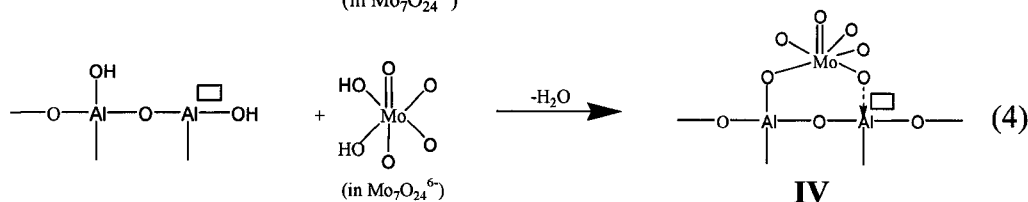
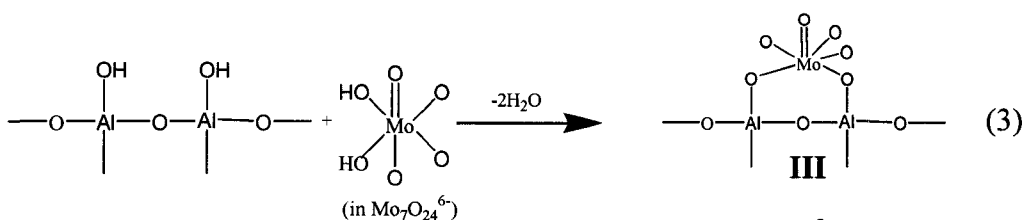
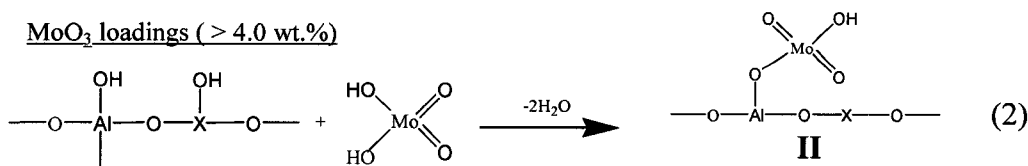
Therefore, the noted reduction observed in this study with regard to the Lewis acid sites upon the deposition of high Mo loadings (> 4.0 wt.%) can be attributed in part to the anchoring of polymeric molybdate anions on the Al^{3+}_{cus} sites. The generation of Brønsted acidity upon the addition of MoO_3 onto alumina has been observed by many. For instance, Suarez et al. [53] have observed and attributed the formation of Brønsted sites in molybdenum-alumina to the presence of molybdena clusters. They stated that it was possible that the acidity of surface alumina -OH groups was increased due to the inductive effects induced by the more electronegative molybdenum (average Sanderson electronegativity of MoO_3 is 3.89 versus 3.72 for Al_2O_3 [54]). Rajagopal et al [50] attributed the presence of Brønsted sites to the absence of dense population of basic hydroxyls. Therefore, during the impregnation of high Mo loadings (> 4.0 wt.%), MoO_4^{2-} anions will interact with -OH groups forming mainly the monodentate species. These species are very acidic, since they are the product of reaction of strong acids with weakly basic hydroxyls. Furthermore, they noted that the Brønsted sites could be also due to the presence of monodentate species on top of multilayers of amorphous Mo oxide. By the same analogy, the observed Brønsted sites that are associated with Mo supported on either conv.alumina or undoped alumina aerogel in this current study can be also related to the acidic monodentate alumina-molybdate species (reaction 2, Species II, (Scheme 7.1). The deposition of Mo onto 10.0 wt.% yttria doped alumina aerogel also caused a change in the acidity of alumina aerogel (Fig.7.2b). However, the following remarkable observations were noted. First, we couldn't detect any change in the Lewis acidity upon the addition of MoO_3 up to 12.0 wt.%, which is in stark contrast to Mo supported on conv.alumina or undoped alumina aerogel. This observation can mainly be ascribed to the

presence of yttrium ions in the alumina aerogel structure. We have found explicitly via several characterization techniques (i.e. Raman) that the fraction of surface tetrahedral monomolybdate species increases in the detriment of octahedral polymolybdate and crystalline MoO_3 species as we varied the support from conv.alumina to yttria doped alumina aerogel with increasing amounts of the yttria loadings [15]. The main reason behind that was attributed to the increase in the iso-electric point (IEP) of the surface, which was induced by the presence of yttria. As the surface becomes more basic (higher IEP), the tetrahedral monomolybdate species are stabilized and hence would exist at much higher concentration at high Mo loadings, when compared to the octahedral polymolybdate species. Therefore and as a logical consequence, the concentration of Lewis acid sites (potential adsorption sites for polymolybdate species) in the Mo-yttria doped alumina aerogel system should not be significantly affected. This implies that the reactions 3 and 4 (Scheme 7.1) will be prevented or significantly slowed down when using yttria doped alumina aerogel as a support for MoO_3 . Secondly, although, the Brönsted acid sites only appeared at Mo loadings higher than 4.0 wt.%, it was very clear that their concentration is much smaller compared to their counterparts for conv.alumina and undoped alumina aerogel. The low concentration of Brönsted sites can be attributed as well to the presence of yttria in the alumina aerogel structure. This is due to the low concentration of the monodentate species (species II, scheme 7.1), which was caused as a result of the strong stabilization of the bidentate tetrahedral monomolybdate species (species I, scheme 7.1).

Low loadings of MoO₃ (< 4.0 wt.%)



MoO₃ loadings (> 4.0 wt.%)



X = Al (conv.alumina), = Al or Y (yttria doped alumina aerogel), □ Al³⁺ coordinative unsaturated sites

Scheme 7.1: Tetrahedral and octahedral surface molybdate species on the surface of yttria doped alumina aerogel [50]

Thirdly, it was also observed that Brönsted-Lewis acid sites were weaker than those observed with the corresponding MoO₃ catalysts supported on either conv.alumina or undoped alumina aerogel. Fig.7.3 shows the variation of (a) the 1540 cm⁻¹ Brönsted sites band area and (b) the 1444 cm⁻¹ Lewis sites band area of 12.0 wt.% MoO₃ catalysts supported on different supports, as a function of pyridine desorption temperature (i.e.100-500 °C). For instance, the number of Lewis acid sites of MoO₃ supported on conv.alumina or undoped alumina aerogel remained almost unchanged as the pyridine desorption temperature increased from 100 to 300 °C. The number of Brönsted acid sites

also remained unchanged as the pyridine desorption temperature increased from 100 to 300 °C. However, at higher desorption temperature these sites decreased drastically. As a matter of fact, they completely disappeared at 500 °C. The number of Lewis sites of MoO₃ supported on 10.0 wt.% yttria doped alumina aerogel decreased moderately up to pyridine desorption temperature of 400 °C and then suffered a drastic decrease at 500 °C (ca. 70 % loss). In addition, the number of Brönsted sites suffered a moderate decrease up to 300 °C, and drastic ones at higher desorption temperature (complete elimination at 500 °C). The low strength of both Brönsted and Lewis sites can be ascribed to the formation of low acidic monodentate species. In the case of yttria doped alumina aerogel, these species were formed as a result of the reaction between MoO₄²⁻ anions species and strongly or moderately basic alumina -OH groups (suggested by the high IEP). It is worth mentioning that similar pattern of acidity changes was also observed upon using 20.0 wt.% yttria doped alumina aerogel as a support (Fig.7.3c). It is also worth mentioning that although both surface Brönsted and Lewis sites were observed at very high MoO₃ loading (20.0 wt.%), their concentrations were clearly reduced with respect to other lower Mo loadings. These acidic sites can be attributed in part to the portion of the surface (i.e. molybdate monolayer species, and alumina), which was not fully covered (or blocked) by the bulk large crystallites (i.e. MoO₃, Al₂(MoO₄)₃ and Y₂(MoO₄)₃) that are readily formed at such high loading and calcination temperature [15]. Contribution from the bulk crystallites to the observed acidity should also be taken into consideration, since our results suggested that bulk MoO₃ crystallite for instance contains both Brönsted and Lewis acidity. The FTIR spectrum of chemisorbed pyridine on bulk MoO₃ crystallite (not shown here) is in complete agreement with Kataoka et al [55] and Belokopytov et al [56]

findings. The total density measurements (Table 7.1) clearly showed that the total concentration of acid sites increases with increasing Mo loadings up to 12.0 wt.%. Such increase in density was more pronounced and higher for the undoped and the yttria doped alumina aerogel based catalysts compared to conv.alumina.

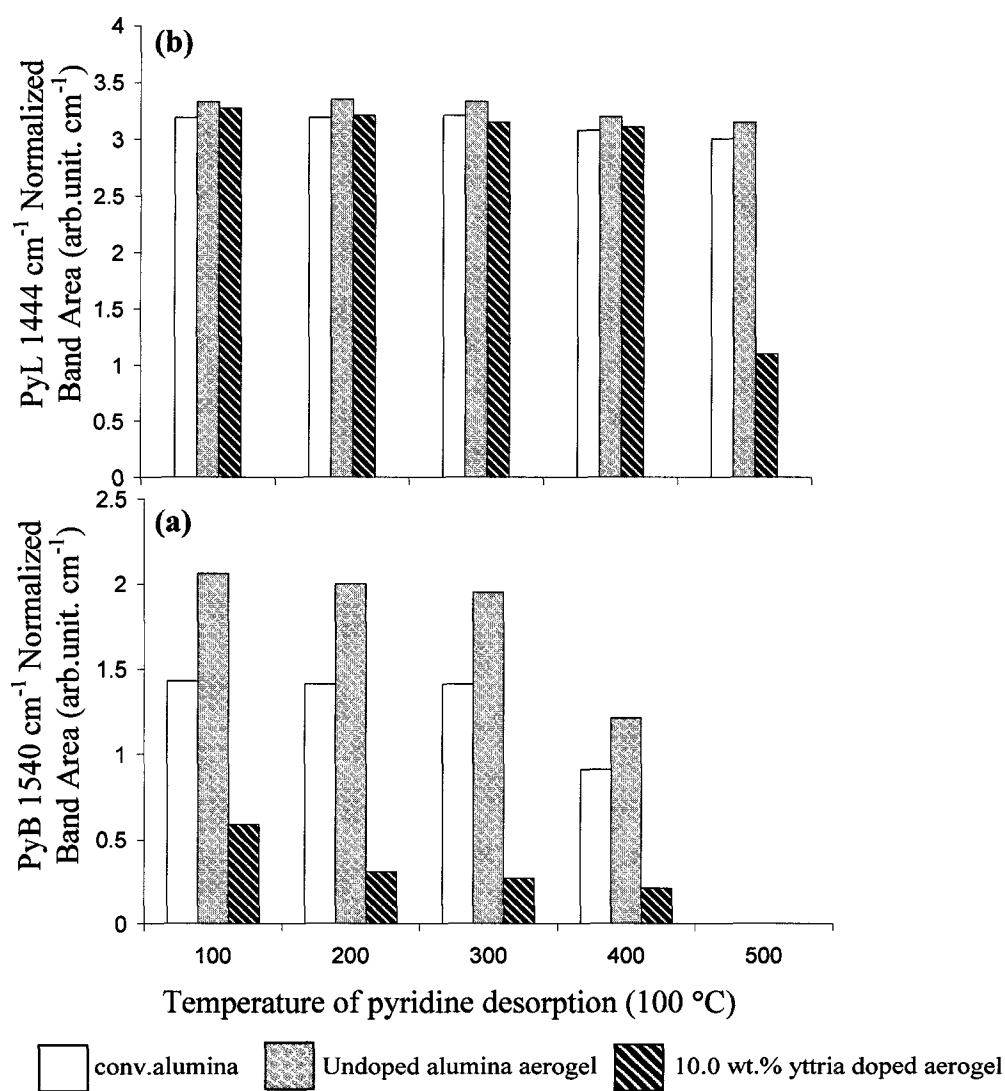


Fig.7.3: Variation of (a) the 1540 cm⁻¹ Brønsted sites band area and (b) the 1444 cm⁻¹ Lewis sites band area of Mo supported catalysts as a function of pyridine desorption temperature

It is well known that the acid properties of a metal oxide can be significantly changed by chemical mixing with another oxide. Thus, the addition of cerium ions to the supported MoO_3 based catalysts is expected to change the acidic properties of these catalysts. Such change can be predicted to be in the forming a new acid type, and/or altering the concentration and the strength of existing acidity. Figs.7.4a-b show the FTIR spectra of chemisorbed pyridine on supported bi-oxide $\text{MoO}_3\text{-CeO}_2$ catalyst with various $[\text{Ce}]/[\text{Mo}]$ ratios (constant MoO_3 loading (12.0 wt.%)). Fig.7.4c shows the variation in the Brönsted/Lewis sites ratio as a function of $[\text{Ce}]/[\text{Mo}]$ ratios for different supports. Careful assessment and comparison of Fig.7.4 with the Fig.7.1 and 7.2 reveals the following major and interesting points. First, the addition of cerium to supported Mo catalysts did not result in the formation of any new Brönsted–Lewis acid types that are different from those observed with the respective supported mono-oxides catalysts. Secondly, it was apparent that the existing surface Brönsted-Lewis acidity was altered, as indicated by the change in the relative intensities of various pyridine adsorption bands (Figs.7.4a-c). The extent of the change depended considerably on the structure of the catalyst support, and should be carefully evaluated in conjunction with the surface structural properties of supported bi-oxide catalysts. In the case of conv.alumina and undoped alumina aerogel, in our previous communication [15], we showed that the surface was mainly populated with segregated bulk MoO_3 and CeO_2 crystallites along with small population of dispersed cerium molybdate phase, upon the co-impregnation of Mo and Ce. The observed Lewis acidity can be mainly attributed to the segregated large MoO_3 and CeO_2 crystallites, whereas the Brönsted acidity to bulk MoO_3 . In addition, the dispersed cerium molybdate phase can also contribute but in smaller extent to the noted

Brönsted-Lewis acidity. The surface acidity of supported bi-oxide (i.e. $[\text{Ce}]/[\text{Mo}] = 0.13$) appeared to be reduced when compared to the respective mono-oxides. It is highly possible that the reduction is not related to the existing acidity, but rather to the formation of layer of segregated bulk crystallites that blocked the dispersed species acidity. As the $[\text{Ce}]/[\text{Mo}]$ ratio increases, the Lewis acidity increases, while the Brönsted acidity decreases. The observed change in the Lewis acidity can be mainly attributed to the formation of segregated bulk CeO_2 crystallites (formation of $\text{Ce}^{4+}_{\text{cus}}$ sites). The change in the Brönsted acidity though can be attributed to a possible neutralizing effect induced by cerium ions on the molybdate monolayer species (i.e. Species II) or possibly on the Bulk MoO_3 . Therefore, it can be inferred from above that it is very hard to determine the real effect of cerium ions on the surface acidity of dispersed cerium molybdate phase due to the presence of segregated bulk crystallites. In the case of yttria doped alumina aerogel (10.0-20.0 wt.% Y_2O_3), XRD, Raman and TGA techniques showed that the surface are mainly populated with dispersed cerium-molybdate species, along with small population of small CeO_2 crystallites [15]. As a result, the surface Brönsted-Lewis acidity can be ascribed mainly to the dispersed cerium-molybdate phase, whereas CeO_2 crystallites can slightly contribute to the Lewis acidity. The role of cerium ions on the surface acidity of yttria doped alumina aerogel supported MoO_3 can be seen much better than the case of conv.alumina and undoped alumina aerogel. This can be primarily ascribed to the presence of a low population of small segregated CeO_2 crystallites. At low $[\text{Ce}]/[\text{Mo}]$ ratio (0.13), we have observed a very minor increase in the Lewis acidity coupled with a decrease in the Brönsted acidity, when compared to the respective mono-oxide based catalysts. The same pattern of changes occurred at higher ratios as well. The continuous

slight increase in the Lewis acidity as a function of $[Ce]/[Mo]$ ratio can be attributed to the formation of Ce^{4+}_{cus} sites. While, the decrease in the Brønsted acidity can be attributed to the neutralization effect induced by cerium ions. The pyridine-FTIR results are in full agreement with the acid sites density measurements (Table 7.1). The latter clearly showed a decrease in the acid site density of supported MoO_3 catalysts as the amount of ceria increases.

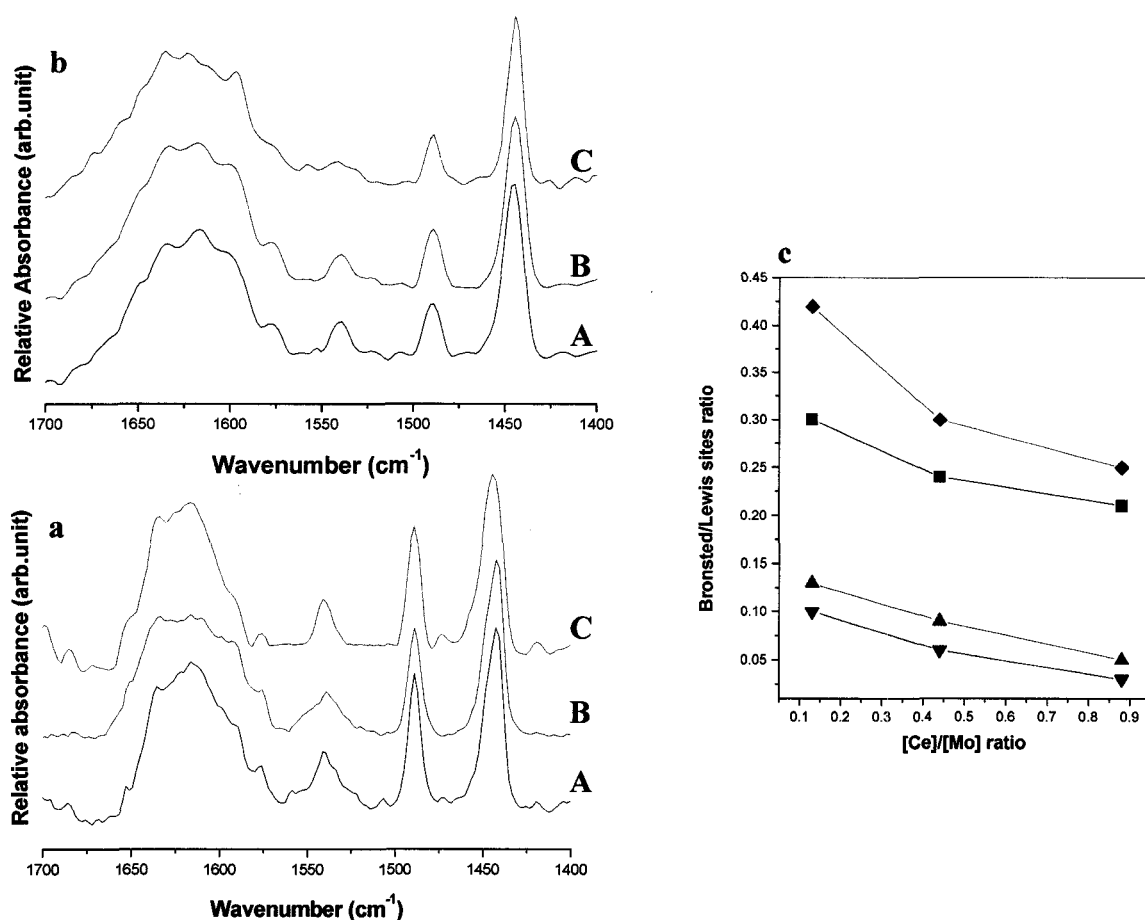


Fig.7.4: FTIR spectra of supported bi-oxide MoO_3-CeO_2 with different $[Ce]/[Mo]$ ratios; A) 0.13, B) 0.44, and C) 0.88, after pyridine adsorption at 100 °C for two different catalyst support (a) conv.alumina and (b) 10.0 wt.% yttria doped alumina aerogel. (c) represents Brønsted/Lewis sites ratio vs. various $[Ce]/[Mo]$ ratios on different supports; (■) conv.alumina, (◆) undoped aerogel, (▲) and (▼) are 10.0 and 20.0 yttria doped alumina aerogel

We have also carried out another key test in order to determine if ceria incorporation influenced the strength of supported MoO₃ acidity. Fig.7.5a-b shows the FTIR spectra of 10.0 wt.% yttria doped alumina aerogel supported MoO₃ (a) and bi-oxide (b) catalysts after pyridine adsorption (100 °C) followed by desorption at different temperature (i.e.100-500 °C). Fig.7.5c displays the concentration of Brönsted and Lewis acid sites (integrated band area) as a function of desorption temperature. Fig.7.5a-c shows that the number of both Brönsted and Lewis acid sites of supported mono- and bi-oxide samples decreased moderately and as expected with increasing desorption temperature. For instance, the number of Brönsted acid sites of supported mono-oxide MoO₃ samples (12.0 wt.% MoO₃) at 400 °C was ca.64 % lower than those observed at 100 °C. Whereas, the number of Brönsted sites at 400 °C was ca. 60 % lower than those at 100 °C for supported bi-oxide MoO₃-CeO₂ samples (12.0 wt.% MoO₃, 6.0 wt.% CeO₂). Hence, it can be suggested that there was no change in the strength of the supported MoO₃ Brönsted and Lewis acidic sites upon the incorporation of ceria. It is worth mentioning that several studies have suggested that the presence of cerium ions tend to increase the strength of existing Brönsted acidic sites. For instance, Lemos et al. [57] have found that Brönsted acidic sites of CeHY zeolite are stronger than those of HY. They attributed the increase in the strength to the polarizing effects of Ce³⁺ cations. In addition, Kalita et al. [58] have recently found the strength of Al-MCM-41 acidic sites increased as a result of cerium incorporation. This was mainly attributed to the polarizing effects of cerium ions on the bridging O-H bond, thereby increasing the eases of deprotonation. It is possible that the cerium addition to the supported MoO₃ has led to an increase in the acidity strength, but the changes were too small to be detected. This can be attributed to the

utilization of strong base (i.e. pyridine), which has been shown to be not very suitable for detecting small variations in the acidity strength [59].

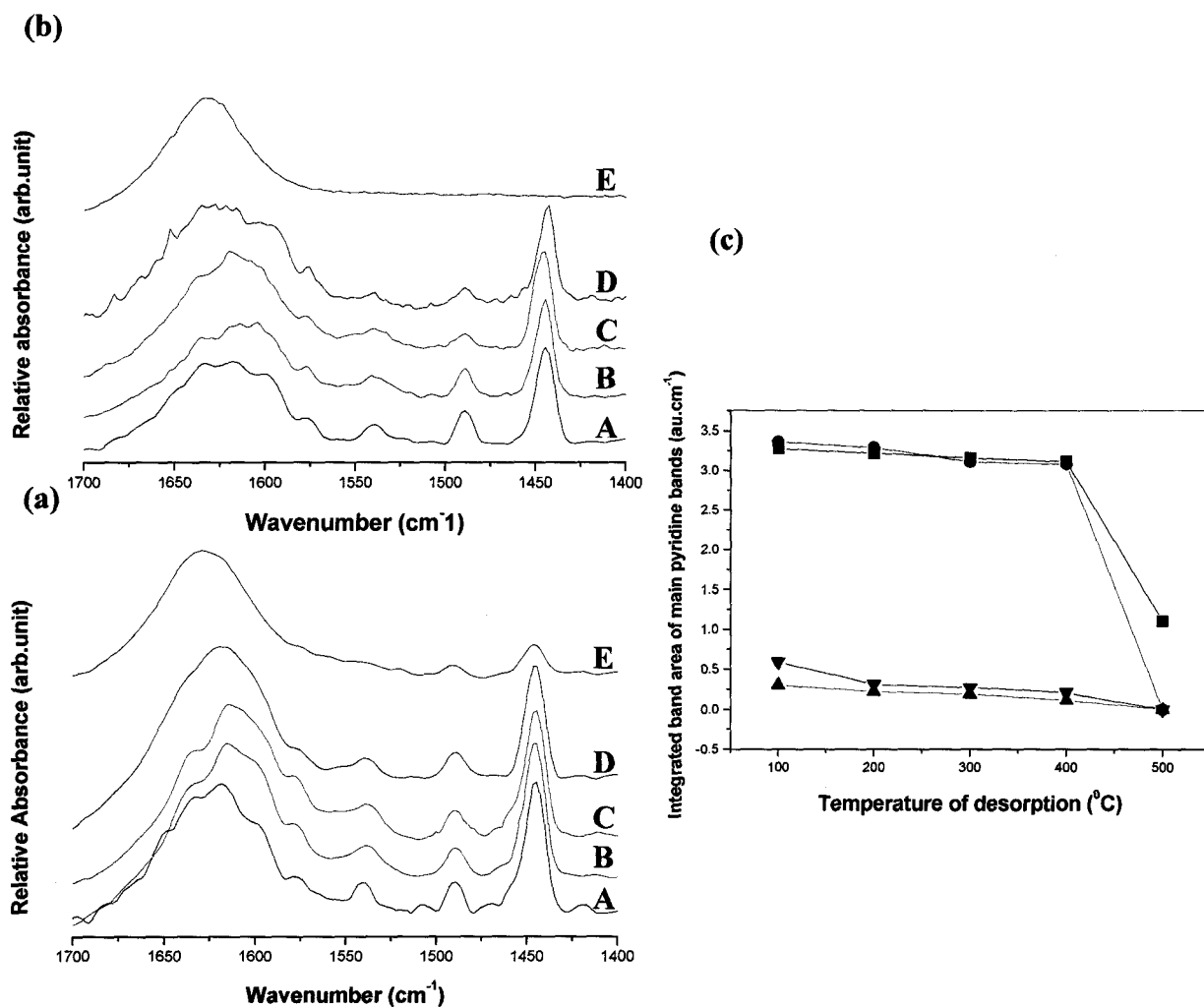


Fig.7.5: FTIR spectra of yttria doped alumina aerogel supported (a) 12.0 wt.% MoO₃, and (b) 0.44 MoO₃-CeO₂, after pyridine adsorption at 100 °C and outgassing at different temperature; (A) 100, (B) 200, (C) 300, (D) 400, and (E) 500 °C. (c) represents the Brønsted (B) and Lewis (L) acid sites band area of supported MoO₃ and MoO₃-CeO₂ ((■) and (▼) are L and B of supported MoO₃, respectively). ((◆) and (▲) are L and B of supported MoO₃-CeO₂, respectively)

7.3.2. Thermo-Catalytic Cracking (TCC) activities of supported mono- and bi-oxide based catalysts

Catalytic activity in terms of total conversion, product selectivity and catalyst stability is considered a very crucial factor for evaluating the catalytic performance of any catalyst. Prior to discussing the TCC activities of supported mono- and bi-oxide based catalysts, it is imperative to emphasize on the following points. First, the TCC activities are a combination of steam cracking and catalytic cracking. Thus, it is important to always evaluate the catalytic activities parallel to those of steam cracking (non-catalytic). Secondly, as stated in the introduction section, there are several reactions that are expected to take place in the TCC process. However, we are going to limit the discussion to β -scission cracking and secondary reactions (hydrogen transfer (HT) reactions and subsequent aromatization). As a result, we will focus on the process selectivity to light olefins ($C_2^=$ - $C_4^=$) and BTX (Benzene-Toluene-Xylene) aromatics, since their formation is a clear indication of the extent of these reactions, respectively. The TCC of n-hexane over all investigated catalyst supports are shown in Table 7.2. In addition, the steam cracking results are included in the same table. As expected, the steam cracking (SC) of n-hexane produced mainly light olefins ($C_2^=$ - $C_4^=$). Minor amounts of BTX aromatics were detected. The TCC activities over different alumina supports were slightly different from those of SC. We have noted a minor increase in the total conversion and selectivity to BTX. These trivial changes can be mainly attributed to alumina structure, which showed a very low concentration of acid sites (Lewis type) (Table 7.1).

Table 7.2: Thermo-Catalytic Cracking (TCC) of n-hexane over different alumina oxide based catalysts ^a

	Steam Cracking	conv.alumina	Alumina Aerogel	10.0 wt.% Y ₂ O ₃ -Al ₂ O ₃
<i>Conversion, C_i (wt.%)</i>	50.3	51.3	52.1	50.7
<i>Product Selectivity, S_i (wt.%)</i>				
CH ₄	6.21	4.57	5.17	5.03
C ₂ -C ₄ alkane	4.25	6.52	7.95	7.32
C ₅ ⁺	6.02	7.78	7.60	8.37
C ₂ ⁼ -C ₄ ⁼ olefins and diolefins	81.6	78.0	75.9	76.0
BTX aromatics	1.95	3.11	3.34	3.32

^a; (C₁-C₄): Methane, Ethane, Propane, Butane, (C₂⁼-C₄⁼): Ethylene, Propylene, Butenes, Butadiene; (BTX): Benzene + Toluene + Xylene

Incorporation of CeO₂ by the impregnation method onto different alumina supports appeared to have a minor influence on the TCC activities. The extent of that influence depended on the nature of catalyst support and ceria loadings. Figure 7.6 shows the TCC activities, in terms of total conversion and selectivity to light olefins and BTX aromatics, of supported mono-oxide CeO₂ with various ceria loadings. In the case of conv.alumina and undoped aerogel, the total conversion of n-hexane decreased slightly as the ceria loadings increased up to 15.0 wt.%. Whereas, the selectivity to BTX aromatics increased, the selectivity to light olefins decreased (Fig.7.6A-B). On the contrary, it was noted that the total conversion remained unchanged and only trivial changes in the product selectivities occurred, when using yttria doped alumina aerogel (10.0 wt.% yttria) as a catalyst support (Fig.7.6C). The noted minor influence of CeO₂ on the TCC activities of alumina support can be attributed to several factors. First, the incorporation of CeO₂ did not impart any Brönsted acid sites, as confirmed by our FTIR pyridine acidity measurements (Fig.7.1). The presence of these acid sites is crucial for promoting higher extent of β-scission cracking, and thus higher catalytic activities (higher concentration of olefins). Secondly, the slight decrease in the total conversion at higher ceria loadings,

which coincided with the appearance of segregated bulk ceria crystallites on the surface [15], can be attributed to covering the acid sites or blocking the accessibility of reactant molecules to the active acid sites by large ceria crystallites. In fact, the total acid sites density measurements clearly showed a decrease in the number of acid sites upon the addition of high contents of ceria (Table 7.1). Therefore, it can be inferred that the Lewis acid sites of ceria ($\text{Ce}^{4+}_{\text{cus}}$) (Fig.7.1) are not as catalytically active as those of alumina ($\text{Al}^{3+}_{\text{cus}}$).

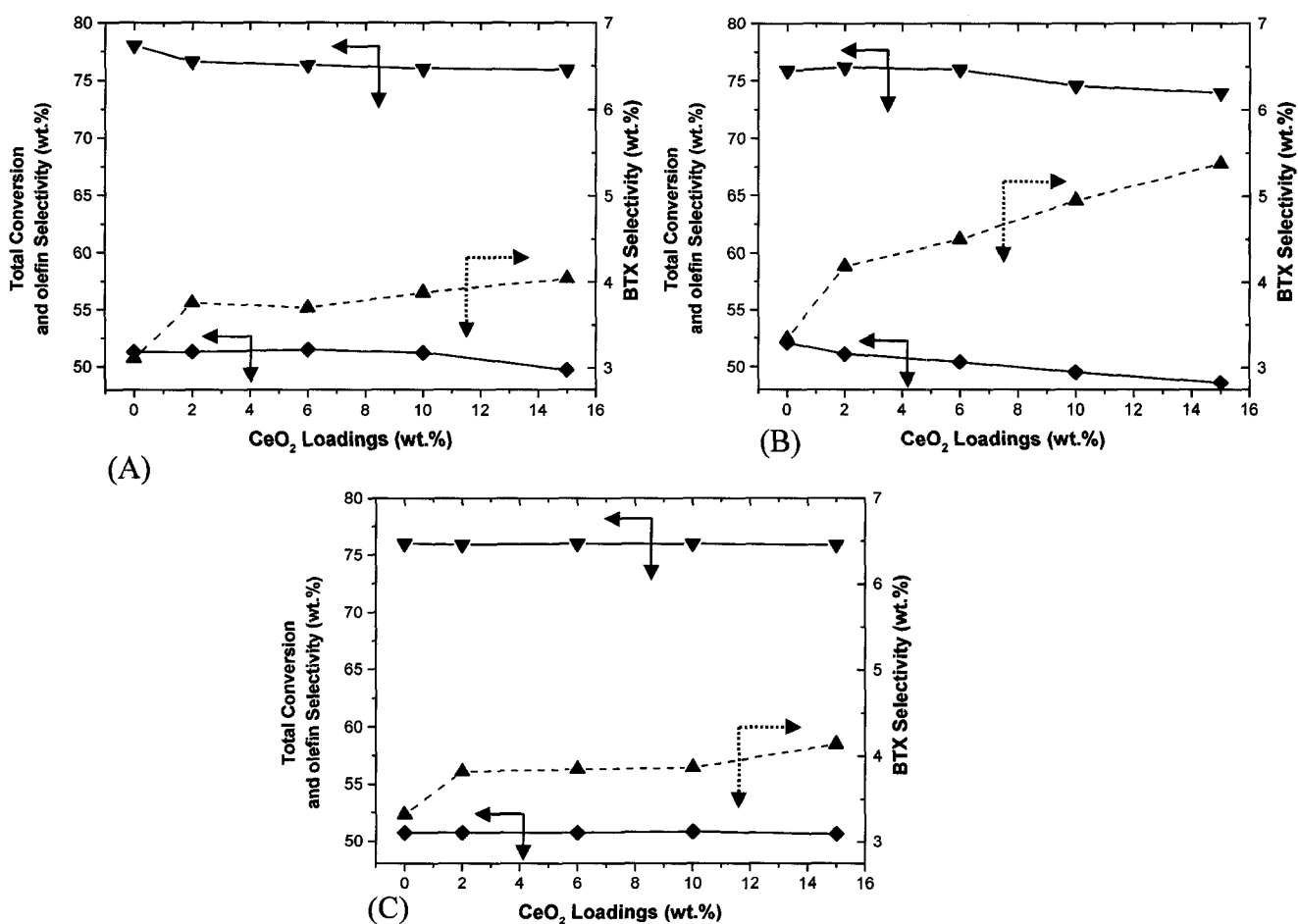


Fig.7.6: TCC activities of mono-oxide CeO₂ with various ceria loadings supported on A) conv.alumina, B) undoped alumina aerogel, C) 10.0 yttria doped alumina aerogel. (▼) total conversion (C_t); (◆) selectivity to light olefins; (▲) selectivity to BTX.

The unchanged TCC activities upon the utilization of the yttria doped alumina aerogel can be related to the significant minimization of ceria segregation [15]. Thus, alumina Lewis acid sites were easily accessible to the reactant molecules. Thirdly, the slight increase in the selectivity to BTX aromatics at high ceria loadings, which was observed irrespective of the catalyst support, can be probably attributed to hydrogen transfer (HT) and aromatization reactions. Although, the extent of these reactions was observed to be very low, it is clear that they were enhanced by the presence of bulk ceria crystallites. The exact role of bulk ceria crystallites in the secondary reactions is not very clear at this moment, since it has always been suggested that HT reactions (for instance) are mainly influenced by Brønsted-Lewis acid sites (primarily Brønsted sites) [31,35-37] in the catalytic cracking of hydrocarbons. Nevertheless, since in this current investigation supported mono-oxide CeO_2 catalysts showed the presence of only Lewis acid sites, it is then reasonable to accept that Lewis acid sites and/or redox properties are probably the determining factors for these secondary reactions in the TCC activities of supported mono-oxide CeO_2 [60].

The impregnation of MoO_3 onto the alumina support has drastically influenced its TCC activity; both at the total conversion and the product selectivity levels. The TCC activities of alumina supported mono-oxide MoO_3 with various MoO_3 loadings are shown in Table 7.3. It was quite noticeable that the influence of MoO_3 depended significantly on the nature of catalyst support, which subsequently influenced the nature of active surface species and their acidity.

Table 7.3: Thermo-Catalytic Cracking (TCC) of n-hexane over supported mono-oxide MoO₃ based Catalysts ^a

MoO₃ Loading (wt.%)	4.0	8.0	12.0	15.0	20.0
conv.alumina					
<i>Conversion, C_t (wt.%)</i>	52.6	56.0	60.7	53.3	51.9
<i>Product Selectivity, S_i (wt.%)</i>					
CH ₄	6.18	6.29	6.15	6.03	6.12
C ₂ -C ₄ alkane	5.43	6.93	6.60	6.60	6.45
C ₅ ⁺ naphthenes	6.50	7.17	7.38	7.19	6.84
C ₂ ⁻ -C ₄ ⁻ olefins and diolefins	76.0	72.2	71.1	78.2	78.7
BTX aromatics	5.86	7.44	8.75	1.96	1.86
undoped alumina aerogel					
<i>Conversion, C_t (wt.%)</i>	57.0	63.3	64.9	57.5	55.9
<i>Product Selectivity, S_i (wt.%)</i>					
CH ₄	6.18	5.78	5.54	5.96	5.91
C ₂ -C ₄ alkane	7.18	7.72	7.27	6.77	6.68
C ₅ ⁺ naphthenes	7.94	8.19	7.81	7.26	7.10
C ₂ ⁻ -C ₄ ⁻ olefins and diolefins	71.6	68.3	67.1	72.4	43.9
BTX aromatics	7.13	10.0	12.2	7.57	6.37
10.0 wt.% Y₂O₃-Al₂O₃					
<i>Conversion, C_t (wt.%)</i>	54.6	60.5	61.8	60.2	59.3
<i>Product Selectivity, S_i (wt.%)</i>					
CH ₄	5.17	5.22	5.22	5.42	5.91
C ₂ -C ₄ alkane	7.22	6.95	6.89	6.76	5.86
C ₅ ⁺ naphthenes	8.34	7.73	7.43	7.42	7.11
C ₂ ⁻ -C ₄ ⁻ olefins and diolefins	69.4	67.6	67.1	68.0	72.8
BTX aromatics	9.87	12.5	13.4	12.3	8.33

For symbols, refer to Table 7.2

It was observed that the total conversion (C_t) of n-hexane increased as the MoO₃ loadings increased up to 12.0 wt.%. That was the case with conv.alumina and undoped alumina aerogel, while the increase in C_t was observed up to 20.0 wt.% MoO₃ when yttria doped alumina aerogel was used as a support. The notable increase in the C_t can be mainly attributed to the formation of Brönsted acid sites (surface acidic monodentate tetrahedral molybdate species (species II, Scheme 7.1)). However, at MoO₃ loadings of 20.0 wt.% (for instance), the decrease in the C_t can be related to the formation of bulk MoO₃ and Al₂(MoO₄)₃ crystallites. The presence of these crystallites most probably covered a large portion of the active acid sites associated with dispersed molybdate

species (Brönsted sites) and alumina structure (Lewis sites) (Fig.7.2aE), and thus prevented the accessibility to reactant molecules. In addition, the noted Brönsted-Lewis acidity of these crystallites are considered catalytic inactive in the TCC of n-hexane (Table 7.3). It was also evident from the catalytic activities that alumina aerogel-Mo based catalysts was the most active (highest C_1) followed closely by 10.0 wt.% yttria doped alumina aerogel, and then conv.alumina. The total acid density measurements (Table 7.1) displayed the same pattern in terms of concentration of acid sites. Table 7.3 also suggests that there was an increase in the selectivity to BTX aromatics at the expense of light olefins, as the MoO_3 loadings increased. More importantly, it was quite apparent that the degree of that increase, which may reflect the extent of cracking reaction verses secondary reactions (i.e. hydrogen transfer, aromatization, etc.), is enhanced upon using yttria doped alumina aerogel as a support for mono-oxide MoO_3 . Therefore, it is reasonable to suggest that the secondary reactions, which are extremely unfavourable for the TCC process, are promoted by the yttria doped aerogel support. Hydrogen transfer reactions are influenced by several factors that encompass the catalyst structure and its surface acidity [27-38]. These reactions are bimolecular in type, and require bulkier intermediates and transition states. Therefore, they are more favourable with mesoporous over microporous materials, due to steric constraints (diffusion limitations). All supported MoO_3 catalysts, which have been investigated in this current work, were found to be mesoporous. Figure 7.7a-b shows the pore size distribution (PSD) of mono- and bi-oxide catalyst, supported on a) conv.alumina, and b) 10.0 wt.% yttria doped alumina aerogel, respectively. It is clear from that figure that there is no significant change in the mesoporosity of MoO_3 catalysts upon changing the catalyst support from conv.alumina

(or even undoped alumina aerogel) to yttria doped alumina aerogel. Thus, the porosity cannot be considered a determining or influencing factor in our case.

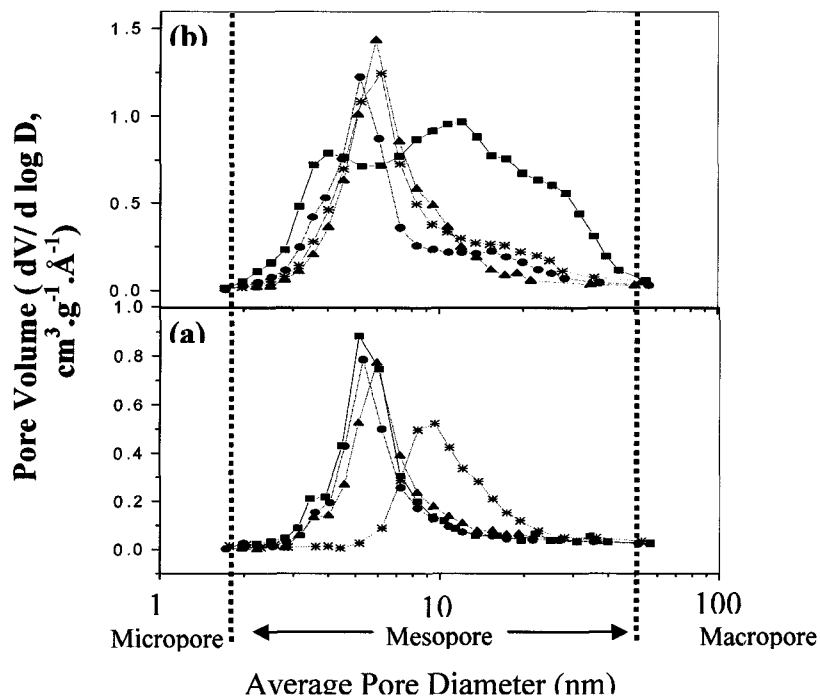
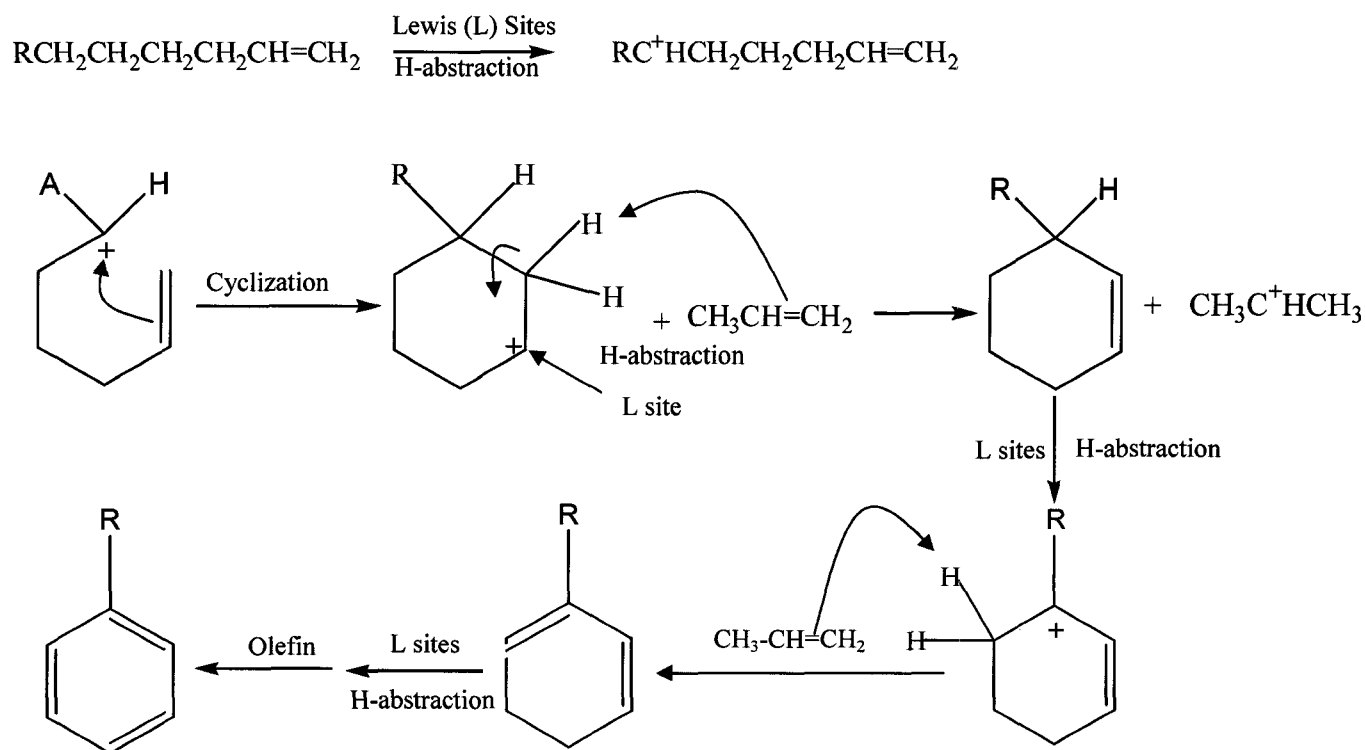


Fig.7.7: Pore size distribution curves ($dv/d \log D$) of MoO_3 (\bullet), CeO_2 (\blacktriangle) and MoO_3 - CeO_2 ($*$) catalysts supported on (a) conv.alumina (\blacksquare) and (b) 10.0 wt.% Y_2O_3 - Al_2O_3 (\blacksquare). The contents of MoO_3 and CeO_2 were 12.0 wt.% and 2.0 wt.%, respectively for mono-oxide catalyst, and $[\text{Ce}]/[\text{Mo}]$ ratio = 0.13 for bi-oxide catalyst

Another important factor that influences the HT reactions is the concentration and strength of surface acidity. First, these reactions are favourable with catalysts containing high acid site density, since they occur between molecules coadsorbed on adjacent acid sites (recall that they are bimolecular reactions) [27-37]. The total surface acid density measurements (Table 7.1) showed that the total acid site concentration of Mo catalysts supported on the yttria doped alumina aerogel is slightly lower than those supported on the alumina aerogel. Then, the HT reactions associated with the supported Mo based catalyst should be reduced upon using yttria doped alumina aerogel as a support

according to our total density measurements and the HT character (Table 7.1). On the contrary, the TCC activity data did not support this (Table 7.3). It is probable that the total acid density factor did not play a determining role, since yttria doped alumina aerogel and undoped alumina aerogel Mo based catalysts differ slightly in the total acid density. Secondly, the strength of Brønsted and Lewis sites were weaker in yttria doped alumina aerogel-Mo based catalysts compared to those supported on undoped alumina aerogel, as can be seen from the pyridine FTIR adsorption-desorption measurements (Fig.7.3a-c). This should have an important influence on the cracking reactions, which are promoted by strong acid sites [61], while HT reactions are more favourable over moderate strength acidic sites [61]. Lemos et al. [57] showed that the hydrogen transfer / cracking rate ratio in the catalytic cracking of n-heptane was smaller in CeHY zeolite than in HY. The former was characterized by stronger Brønsted acidity compared to HY. Similar findings were also obtained by the same group [62] using LaHY zeolite. Another significant point to mention is the ratio of Brønsted/Lewis sites (B/L). It was apparent from Fig.7.2c that the B/L is much higher for undoped alumina aerogel-Mo based catalysts (i.e. B/L = 0.62, MoO₃ = 12.0 wt.%) when compared to the corresponding yttria doped alumina aerogel-Mo based catalysts (i.e. B/L = 0.18, MoO₃ = 12.0 wt.%). Although, Brønsted sites are the most active acidic sites in catalytic reactions, the presence of Lewis sites in high concentration can also exert an influential role in these cracking reactions. It has been suggested by de Jong [31] that if Lewis sites are present, they can adsorb hydrocarbons in a polarized form (HR⁺), thus rendering them reactive. In addition, the presence of high concentration of Lewis sites will certainly play a role in promoting the dehydrocyclization reaction of paraffin (aromatization). Scheme 7.2 shows

the reaction pathway of the dehydrocyclization reaction of paraffin molecule over Brönsted-Lewis acidic sites. In that scheme, it is shown that such reaction cannot proceed without the Lewis acid sites that participate in the hydride abstraction in order to form the starting carbenium ion and eventually the allylic carbenium ion. Epron et al. [63] also showed that the yield of toluene from the conversion of n-heptane (used as a model reaction of paraffin dehydrocyclization) increased as the number of Lewis sites increased.



Scheme 7.2: Reaction pathway of the dehydrocyclization reaction of paraffin molecule (olefins are formed by β -scission cracking of starting carbenium ion, R = -H or -CH₃) [5]

The TCC activities of supported MoO₃ catalysts were altered upon the incorporation of CeO₂, irrespective of the nature of the catalyst support. Table 7.4 reports the TCC of n-hexane over supported bi-oxide catalysts (MoO₃-CeO₂) with various [Ce]/[Mo] ratio. It was noted that as the [Ce]/[Mo] ratio increased in bi-oxide catalyst supported on either conv.alumina or undoped alumina aerogel, the total conversion of n-

hexane decreased. The decrease in the C_t can be mainly attributed to the decrease in the total acid density (Table 7.1). As suggested in the previous section, the decrease in the total density was primarily caused by the formation of large segregated bulk CeO_2 and MoO_3 crystallites. These segregated crystallites, whose acidic sites are catalytically inactive, blocked most of the active acid sites associated with surface dispersed molybdate species. In addition, it is possible but to a lower extent that the decrease can be partially attributed to the neutralization effect induced by cerium ions. The selectivity to BTX aromatics of supported MoO_3 catalysts decreased upon the incorporation of 2.0 wt.% CeO_2 ($[Ce]/[Mo] = 0.13$), however as the ratio increased the selectivity increased as well. The increase in the BTX selectivity can be attributed to the presence of large population of bulk CeO_2 crystallites, which is believed to promote the HT and aromatization reactions, as it was seen in the case of supported mono-oxide CeO_2 catalysts. Addition of CeO_2 to 10.0 wt.% yttria doped alumina aerogel supported MoO_3 also led to a decrease in the C_t . That decrease can be closely related to the decrease in the total acid density (Table 7.1), which was found to be mainly caused by the neutralization effect of cerium ions, and slightly by the presence of small segregated ceria crystallites. The selectivity to BTX decreased as the $[Ce]/[Mo]$ ratio increased, which is in stark contrast to the observed product distributions of the corresponding conv.alumina or alumina aerogel supported bi-oxide catalyst. The decrease in the BTX selectivity, in our opinion (based on the changes in the total acid density (Table 7.1)), can be ascribed to the reduction in the density of acid sites. This has significantly reduced the extent of HT and aromatization reactions that are responsible for enriching the product spectrum with BTX aromatics. It is also possible that the decrease in the BTX selectivity was caused by an

increase in the protonic (Brönsted) site strength, due to the strong polarization effect of cerium ions. However, this cannot be certainly confirmed in our current study, since the acidity strength measurements failed to show any changes in the acidity strength of supported MoO₃ upon the addition of cerium (Fig.7.5a-c).

Table 7.4: Thermo-Catalytic Cracking (TCC) of n-hexane over supported bi-oxide MoO₃-CeO₂ based Catalysts

[Ce]/[Mo]	0.13	0.44	0.88
conv.alumina			
<i>Conversion, C_i (wt.%)</i>	55.3	54.6	52.4
<i>Product Selectivity, S_i (wt.%)</i>			
CH ₄	6.32	5.70	5.85
C ₂ -C ₄ alkane	5.50	5.65	5.07
C ₅ ⁺ naphthenes	7.70	8.00	8.11
C ₂ ⁼ -C ₄ ⁼ olefins and diolefins	75.9	74.6	73.0
BTX aromatics	4.56	6.10	7.91
undoped alumina aerogel			
<i>Conversion, C_i (wt.%)</i>	62.0	61.9	61.1
<i>Product Selectivity, S_i (wt.%)</i>			
CH ₄	6.82	6.22	5.80
C ₂ -C ₄ alkane	7.34	7.70	7.65
C ₅ ⁺ naphthenes	7.85	7.13	8.12
C ₂ ⁼ -C ₄ ⁼ olefins and diolefins	68.4	67.8	65.8
BTX aromatics	9.63	11.2	12.7
10.0 wt.% Y₂O₃-Al₂O₃			
<i>Conversion, C_i (wt.%)</i>	62.6	58.3	57.4
<i>Product Selectivity, S_i (wt.%)</i>			
CH ₄	5.18	5.25	5.24
C ₂ -C ₄ alkane	6.71	6.02	5.98
C ₅ ⁺ naphthenes	7.27	8.00	7.80
C ₂ ⁼ -C ₄ ⁼ olefins and diolefins	71.0	72.4	72.0
BTX aromatics	9.78	8.29	8.93

These catalytic activities were further supported by the catalyst deactivation studies (i.e. amount and combustive properties of carbonaceous deposits (coke)). Fig. 7.8a-b, which display the amount and combustion temperature of coke deposits, clearly showed that the amount of coke and its combustion temperature decreased as the [Ce]/[Mo] ratio increased. For instance, the amount of coke deposited on the surface

supported mono-oxide MoO_3 was estimated to be ca. 12.2 wt.%, whereas the amount of coke on the supported $\text{MoO}_3\text{-CeO}_2$ with $[\text{Ce}]/[\text{Mo}]$ ratio of 0.13, 0.44, and 0.88 was ca. 11.3, 10.9, and 9.75 wt.%, respectively. Similarly, the combustion temperature decreased from 548 °C (supported 12.0 wt.% MoO_3) to 507 °C ($[\text{Ce}]/[\text{Mo}] = 0.88$).

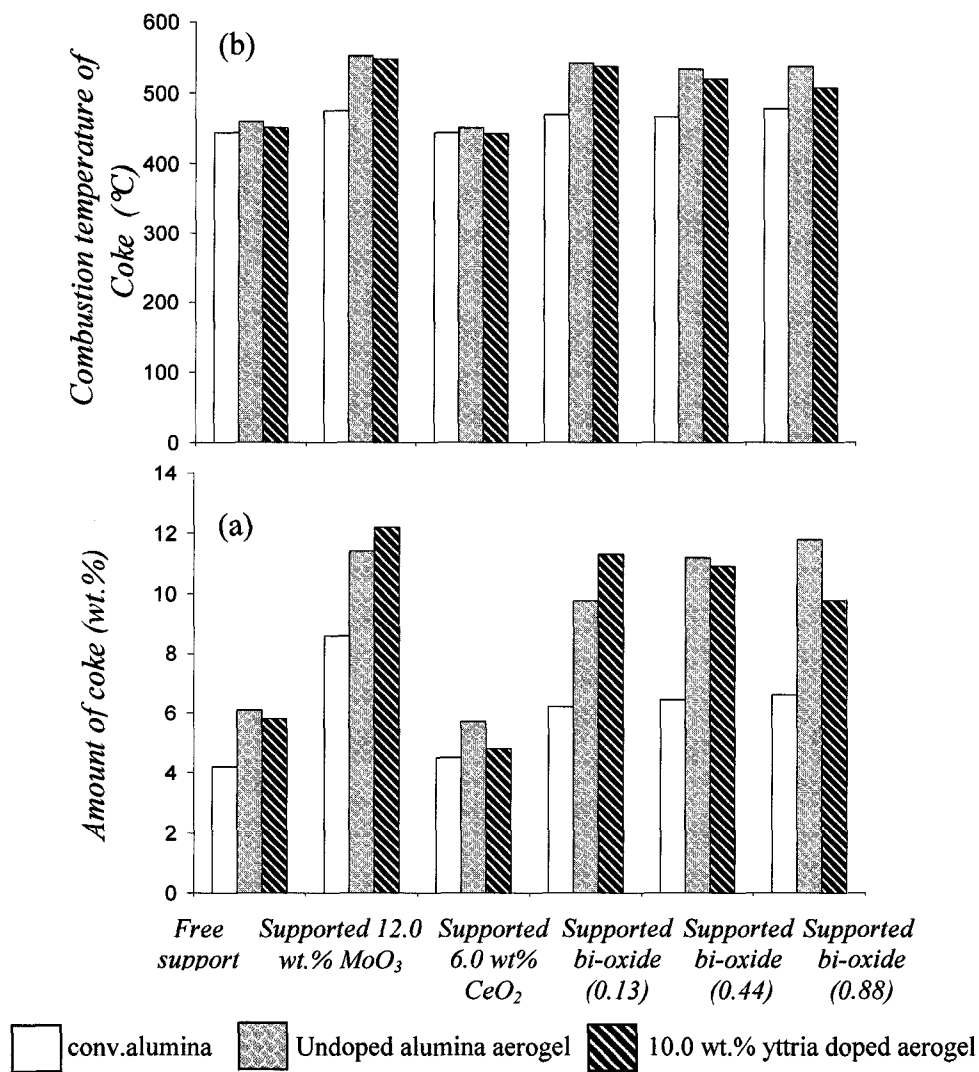


Fig.7.8: Amount (a) and combustion temperature (b) of carbonaceous deposits (coke) on different supported catalyst system. The number between parenthesis represents the $[\text{Ce}]/[\text{Mo}]$ ratio

7.3.3. Kinetic study

The kinetic data obtained for the n-hexane steam cracking reported in Table 7.5 and Fig.7.9 are in quite good agreement with those reported by Volkan and April [64] for the thermal decomposition of propane as follows:

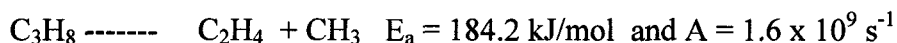
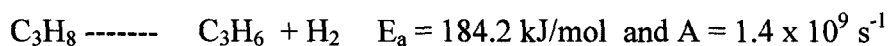


Table 7.5: The activation energy (E_a) and the pre-exponential factor (A) in the steam cracking and Thermo-Catalytic Cracking (TCC) of n-hexane

	E_a (kJmol ⁻¹)	A (pre-exponential or frequency factor) (s ⁻¹)
Steam Cracking (no catalyst)	170.0	4.03×10^9
Thermo-Catalytic Cracking (TCC)		
12.0 wt.% MoO ₃ /10.0 wt.% yttria doped alumina aerogel	47.2	0.35
12.0 wt.% MoO ₃ -6.0 wt.% CeO ₂ /10.0 wt.% yttria doped alumina aerogel [Ce]/[Mo] = 0.44	57.8	1.30

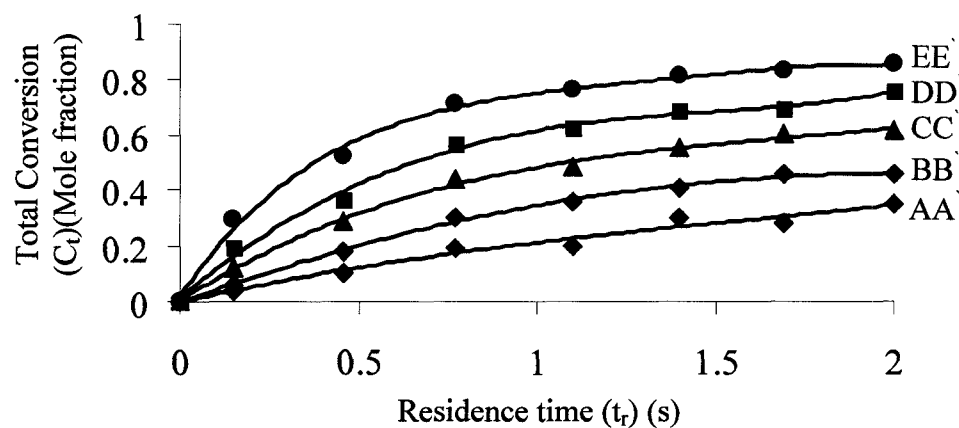


Fig.7.9: Total conversion (C_t in Mole fraction) versus residence time (t_r in s) in the steam cracking of n-hexane; A,A = 913.15 K, B,B = 933.15 K, C,C = 953.15 K, D,D = 973.15 K, E, E = 993.15 K

It is worth noting that since thermal cracking goes by a chain reaction mechanism, it is “energetically more advantageous” than the molecular mechanism [65], i.e. that the overall activation energy may be slightly lower than the (thermal) dissociation energy in the initiation step.

The kinetic results for the Thermo-Catalytic Cracking are reported in Table 7.5 and Fig.7.10a-b.

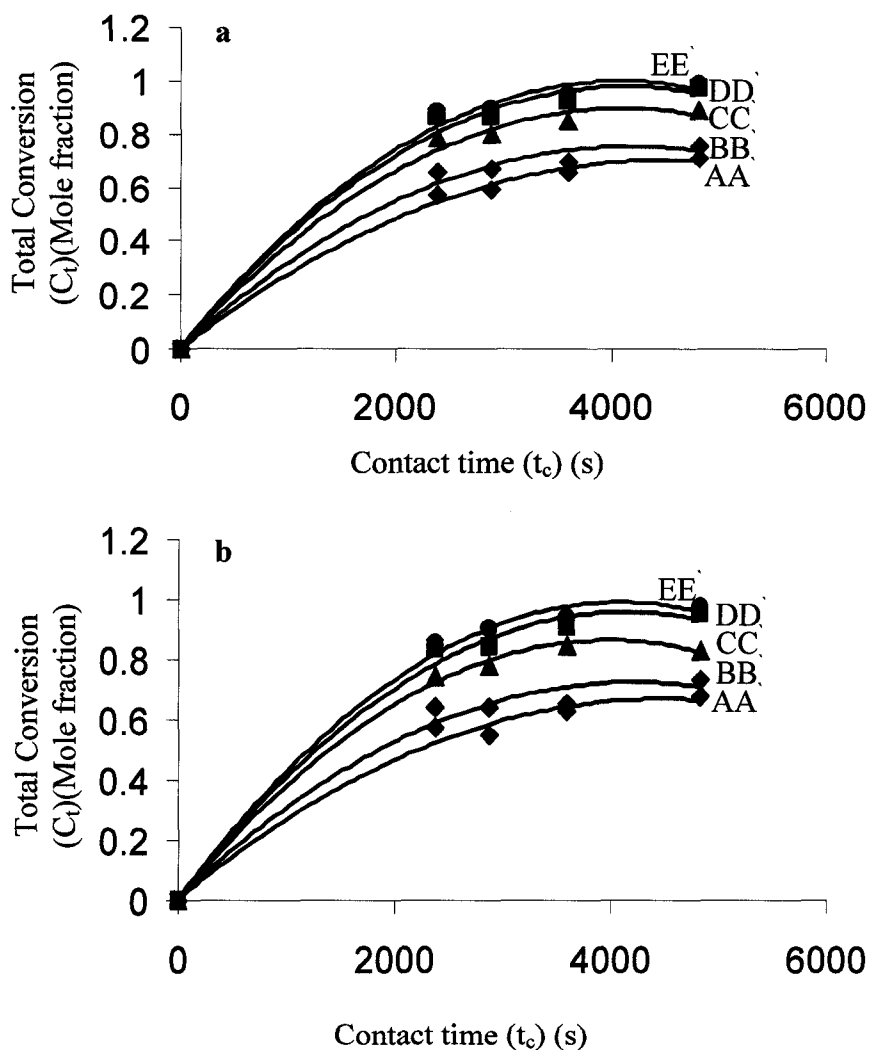


Fig.7.10: Total conversion (C_t in Mole fraction) versus contact time (t in s) in the TCC of n-hexane; A,A = 913.15 K, B,B = 933.15 K, C,C = 953.15 K, D,D = 973.15 K, E, E = 993.15 K,(a) 12.0 wt.% MoO_3 / 10.0 wt.% yttria doped alumina aerogel, and (b) 12.0 wt.% MoO_3 -6.0 wt.% CeO_2 / 10.0 wt.% yttria doped alumina aerogel

These kinetic results are very unusual. Since the TCC is a combination of thermal cracking and catalytic cracking, these data although very preliminary, deserve some special comments.

It is known that the apparent activation energy for catalytic cracking of n-hexane is 36.6 kcal/mole (153.2 kJ/mol) [66], the TCC data reported herein do not reflect those of either thermal cracking or catalytic cracking. It is natural to admit that there are very strong interactions between reaction intermediates, so that the final reaction products result from numerous and subsequent reactions in the reactor and on the catalyst surface. Since enhanced product yields are observed in the TCC process, it was technically difficult to obtain low values of conversion at low contact times, so that the calculated values of initial rates were not accurate.

Nevertheless, the unusual kinetic data of TCC suggest the following interpretation:

- a) In our most recent report [17], it was pointed that the surface of the TCC catalyst on-stream was covered in permanence with a layer of polyalkyl-aromatics.
- b) In recent years, numerous studies have shown that in the reaction of methanol-to-hydrocarbons (MTH), polyalkyl-aromatics appear to be the key reaction intermediates, with the heptamethylbenzene (heptaMB⁺) ion assuming the leading role in the gaseous product formation and also for coke formation [67].

More recently, an all-dominating indirect route for the MTH conversion known as the “hydrocarbon pool mechanism” has been proposed and is gaining favour among researchers [68]. This suggestion has defined the context in which our more detailed mechanistic and kinetic investigations will be carried out in the near future.

7.4. CONCLUSION

Surface acidity of yttria doped alumina aerogel supported mono-and bi-oxide catalysts was investigated by the Infrared spectroscopy of chemisorbed pyridine, combined with ion-selective electrode NH_3 -TPD. Supported mono-oxide CeO_2 catalysts displayed only Lewis type-sites ($\text{Al}^{3+}_{\text{cus}}$ and $\text{Ce}^{4+}_{\text{cus}}$). Supported mono-oxide MoO_3 catalysts showed the presence of mainly Lewis sites with a small number of Brönsted acid sites. This was mainly attributed to the incorporation of yttrium ions into the alumina aerogel structure, which significantly altered the chemistry of surface -OH groups and thus those of the Mo catalysts. Comparison between the surface acidity of supported bi-oxide and that of supported mono-oxide MoO_3 showed that the density of Brönsted acid sites were decreased most likely due to neutralization effects, whereas Lewis acid sites appeared to be only slightly increased. In addition, the TCC activity of yttria doped alumina aerogel supported bi-oxide MoO_3 - CeO_2 catalysts depended strongly on the density, strength and nature of surface acidity. The latter was influenced by nature of the catalyst support, and the loading and the type of metal oxide. It was found that supported mono-oxide MoO_3 and bi-oxide MoO_3 - CeO_2 are more catalytically active than supported CeO_2 catalysts. The total conversion and the selectivity for BTX aromatics (at the expense of light olefins) increased as the MoO_3 loadings increased. The increase in the selectivity to aromatics was much higher for catalyst supported on the yttria doped alumina aerogel than those supported on undoped alumina aerogel. This was due to the presence of Brönsted acid sites compared to a much larger population of Lewis sites, which favour the hydrogen transfer (HT) and aromatization reactions. Addition of CeO_2 to supported MoO_3 resulted in the decrease of the total conversion and the selectivity to

aromatics. This was mainly related to the decrease in the total acid density, thus reducing the extent of HT and aromatization reactions.

7.5. ACKNOWLEDGEMENTS

Financial support from NSERC (Natural Science and Engineering Research Council of Canada) and Valeo Management are acknowledged.

7.6. AUTHOR'S NOTES AND SIGNIFICANCE OF PAPER TO THESIS

This chapter presents the most important part of the thesis, since it correlates the Thermo-Catalytic Cracking activities and kinetic of the supported mono- and bi-oxide $\text{MoO}_3\text{-CeO}_2$, with the previously investigated physico-chemical properties (Chapter IV, V, and VI). It was found in this study that the catalytic activities depend strongly on the surface acidity and other physico-chemical properties.

The work presented in this chapter clearly showed that the supported bi-oxide catalyst configuration is not the best for use in the TCC of heavy petroleum feedstocks. This is due to the high HT and aromatisation character of these catalysts. Therefore, it is imperative at this stage to develop another catalyst configuration that can be more effective in the cracking of heavier petroleum fractions.

7.7. REFERENCES

- [1] P. Pujado, D. Greer, J. Andersen, T. Foley, V. Bhirud, pre-print Archive-American Institute of Chemical Engineering, [Spring National Meeting], New Orleans, LA, USA. March 11-14 (2002) 2471.
- [2] A. Corma, F. V. Melo, L. Sauvanaud, F. Ortega, *Catal.Today.* **107** (2005) 699.
- [3] J.S. Plotkin, *Catal.Today.* 106 (2005) 10.

- [4] A. Chauvel, G. Lefebvre, *Petrochemical Processes*, Vol. 1, Technip, Paris, 1989, p. 117.
- [5] S. Matar and L.F. Hatch, in: *Chemistry of Petrochemical Processes*, 2nd ed., Gulf Professional Publishing, Woburn, MA, (2001).
- [6] D.A. Hunt, in: *Handbook of Petroleum Refining Processes*, 2nd ed., ed. R.A. Meyers, McGraw Hill, Boston, (1997).
- [7] R. Le Van Mao, S. Melancon, C. Gauthier-Campbell, P. Kletnieks, *Catal. Lett.* **73** (2001) 181.
- [8] S. Melancon, R. Le Van Mao, P. Kletnieks, D. Ohayon, S. Intem, M.A. Saberi, D. McCann, *Catal. Lett.* **80** (2002) 103.
- [9] R. Le Van Mao, Concordia University, PCT Patent (2005).
- [10] N. Al-Yassir, R. Le Van Mao, F. Heng, *Catal. Lett.* **100** (2005) 1.
- [11] R. Le Van Mao, N. Al-Yassir and D. Nguyen, *Micropor. Mesopor. Mater.* **85** (2005) 176.
- [12] N. Al-Yassir, R. Le Van Mao, *Appl. Catal. A: Gen.* **305** (2006) 130.
- [13] R. Le Van Mao, N.T. Vu, N. Al-Yassir, N. Francois, J. Monnier, *Top. Catal.* **37** (2006) 107.
- [14] N. Al-Yassir, R. Le Van Mao, *Appl. Catal. A: Gen.* **317** (2007) 275.
- [15] N. Al-Yassir, R. Le Van Mao, *Appl. Catal. A: Gen.* **332** (2007) 273.
- [16] N. Al-Yassir, R. Le Van Mao, *Can. J. Chem.* (in press, Ms. No. CJC 07316).
- [17] R. Le Van Mao, N.T. Vu, N. Al-Yassir, H.T. Yan, *Ind. Eng. Chem. Res.* (Submitted, Ms. No. tie071629).
- [18] B. S. Greensfelders, H. H. Voge, G. M. Good, *Ind. Eng. Chem. Res.* **41** (1949) 2573.

- [19] J. Scherzer, *Catal. Rev.-Sci. Eng.* **31** (1989) 215.
- [20] B. A. Williams, S. M. Babitz, J. T. Miller, R. Q. Snurr, H. H. Kung, *Appl. Catal. A: Gen.* **177** (1999) 161.
- [21] A. Corma, A. V. Orchilles, *Micropor. Mesopor. Mater.* **35-36** (2000) 21.
- [22] S. E. Tung, E. McNinch, *J. Catal.* **10** (1968) 166.
- [23] D. M. Nace, *Ind. Eng. Chem. Prod. Res. Dev.*, **8** (1969) 31.
- [24] W. O. Haag, R. M. Dessau, Proc. 8th Int. Congr. Catal.(Berlin, 1984, Vol. II) 305.
- [25] S. Kortel, H. Knozinger, B. C. Gates, *Micropor. Mesopor. Mater.* **35-36** (2000) 11.
- [26] A. Corma, A. Martnez, in: M. Guisnet, J-P. Gilson (Eds.), *The Chemistry of Catalytic Processes*, Imperial College Press, London, 2001, Vol. III, pp. 29-55.
- [27] V. W. Weekman, Jr. *Ind. Eng. Chem. Prod. Res. Dev.*, **3** (1969) 385.
- [28] X. Zhao, R.H. Harding, *Ind. Eng. Chem. Res.* **38** (1999) 3854.
- [29] P. B. Venuto, P. S. Landis, *Adv. Catal.* **18** (1968) 303.
- [30] J. Scherzer, and R. E. Ritter, *Ind. Eng. Chem. Prod. Res. Dev.* **17** (1978) 219.
- [31] J. I. de Jong, Ketjen Catalyst Symposium 1986, Scheveningen, The Netherlands, Paper F-2.
- [32] A. Corma, M. Faraldos, A. Martinez, A. Mifsud, *J. Catal.* **122** (1990) 230.
- [33] B. Mercier Des Rochettes, C. Marcilly, G. Gueguen, J. Bousquet, *Appl. Catal.* **58** (1990) 35.
- [34] M. Guisnet, N. S. Gnep, *Appl. Catal. A.* **58** (1990) 35.
- [35] A. F. H. Wielers, M. Vaarkamp, M. F. M. Post, *J. Catal.* **127** (1991) 51.
- [36] D. B. Lukyanov, *J. Catal.* **147** (1994) 494.
- [37] G. de la Puente, E.F. Souza-Aguiar, F. M. Z. Zotin, V. L. D. Camorim, U. Sedran,

- Appl. Catal. A.*, **197** (2000) 41.
- [38] S. Altwasser, C. Welker, Y. Traa, J. Weitkamp, *Micropor. Mesopor. Mater.* **83** (2005) 345.
- [39] R. Le Van Mao, N. Al-Yassir, L. Lu, N.T. Vu, A. Fortier, *Catal. Lett.* **112** (2006) 13.
- [40] E. P. Parry, *J. Catal.* **2** (1963) 371.
- [41] M. I. Zaki, G. A. M. Hussein, S. a. A. Mansour, H. A. El-Ammawy, *J. Mol. Catal.* **51** (1989) 209.
- [42] C. Morterra, G. Magnacca, *J. Chem. Soc., Faraday Trans.*, **92** (1996) 5111.
- [43] K. Tanabe, "Solid Acids and Bases", Academic Press, New York, N.Y., 1970.
- [44] J. A. Rabo, G. J. Gajda, *Catal. Rev. Sci. Eng.*, **31** (1989/1990) 385.
- [45] W. F. Farneth, R. J. Gorte, *Chem. Rev.* **95** (1995) 615.
- [46] H. Sato, *Catal. Rev. Sci. Eng.*, **39** (1997) 395.
- [47] A. Corma, *Chem. Rev.* **95** (1995) 559.
- [48] J. B. Peri, *J. Phys. Chem.* **69** (1965) 231.
- [49] C. Morterra, V. Bolis, G. Magnacca, *J. Chem. Soc., Faraday Trans.*, **92** (1991) 1996.
- [50] S. Rajagopal, J. A. Marzari, R. Miranda, *J. Catal.*, **151** (1995) 192.
- [51] H. Kraus, R. Prins, *J. Catal.* **164** (1996) 260.
- [52] J. A. R. Van Veen, P. A. J. M. Hendriks, E. J. G. M. Romers, R. R. Andrea., *J. Phys. Chem.* **94** 1990 (5275).
- [53] W. Suarez, J.A. Dumesic, C.G. Hill, Jr. *J. Catal.* **94** (1985) 408.
- [54] R. T. Sanderson, "Inorganic Chemistry." Reinhold, New York, 1967.
- [55] T. Kataoka, J. A. Dumesic, *J. Catal.*, **112** (1988) 66.
- [56] Yu. V. Belokopytov, K. M. Kholyavenko, S. V. Gerei, *J. Catal.*, **60** (1979) 1.

- [57] F. Lemos, F. Ramoa Ribeiro, M. Kern, G. Giannetto, M. Guisnet, *App. Catal.* **29** (1987) 43.
- [58] P. Kalita, N. M. Gupta, R. kumar, *J.Catal.* **245** (2007) 338.
- [59] R. Le Van Mao, M. A. Saberi, *Appl. Catal. A: Gen.* **199** (2000) 99.
- [60] P. Fornasiero, R. Di Monte, G. Ranga Rao, J. Kaspar, S. Meriani, A. Trovarelli, M. Graziani, *J. Catal.* **151** (1995) 168.
- [61] D. A. Keyworth, J. Nieman, P. O'Connor, C. W. Stanger, Jr., NPRA Annual Meeting, March 1987, San Antonio, TX, AM-87-62.
- [62] F. Lemos, F. Ramoa Ribeiro, M. Kern, G. Giannetto, M. Guisnet, *Appl. Catal.* **39** (1988) 227.
- [63] F. Epron, C. Carnevillier, P. Marecot, *Appl. Catal. A.*, **295** (2005) 157.
- [64] A. G. Volkan, G. C. April, *Ind. Eng. Chem. process Des. Dev.* **16** (1977) 429.
- [65] S. Raseev, in *Thermal Catalytic Processes in Petroleum Refining*, Marcel Dekker, New York, (2003) 54.
- [66] J. E. Germain, in *Catalytic Conversion of Hydrocarbons*, Academic Press, New York, (1969) 208 (and ref. therein).
- [67] M. Bjorgen, U. Olsbye, S. Kolboe, *J. Catal.* **215** (2003) 30.
- [68] M. Bjorgen, S. Svell, F. Joensne, J. Nerlov, S. Kolboe, F. Bonino, L. Palumbo, S. Bordiga, U. Olsbye, *J. Catal.* **249** (2007) 195.

CHAPTER VIII

CONCLUSIONS, ONGOING and FUTURE WORK, AND SIGNIFICANCE

8.1. GENERAL CONCLUSION

The results obtained in this thesis reinforce our conclusion that Thermo-Catalytic Cracking of petroleum feedstocks for the production of light olefins can be considered as a strong and viable alternative to the current key technologies for olefins production. We have studied thoroughly several catalyst configurations for their potential use in the TCC process. These configurations include the hybrid, and the supported metal oxide configurations.

The hybrid catalyst investigated in this thesis consisted of an acidified silica-rich ZSM-5 zeolite, the microporous H-silicalite, and a mesoporous cocatalyst, being an amorphous silica-alumina doped with molybdenum and cerium oxides. When compared to a mechanical mixture of extrudates made of H-silicalite and silica-alumina based cocatalyst, respectively, the hybrid catalyst gave faster adsorption of nitrogen and desorption of preadsorbed nitrogen. On the other hand, a much higher conversion of n-hexane (cracking) was obtained with the hybrid catalyst while the product selectivities were identical in all. Such behavior is ascribed to the kinetic effect of the “pore continuum” being formed in the hybrid catalyst pore system, which has as a consequence to speed up the diffusion of reactant molecules and that of reaction products from the zeolite micropores.

The other catalyst configuration was based on the supported metal oxide ($\text{MoO}_3\text{-CeO}_2$). The effect of metal loadings, preparation methods, calcination temperature, and the nature of the support on the physico-chemical properties and subsequently the Thermo-Catalytic Cracking (TCC) activities of this configuration were methodically

investigated. It was found that the impregnated molybdenum species were the active species in the TCC, while cerium species acted as the promoter. In addition, it was noted that the co-impregnation of MoO_3 and CeO_2 , corresponded to the formation of (surface) cerium molybdate to the highest extent. On the other hand, the catalysts prepared by the two-step impregnation methods (sequential and reverse sequential impregnation) showed much lower catalytic performance due to low Mo-Ce interactions as implied by the segregation of the active phases, mostly MoO_3 . Furthermore, the catalyst support was found to play a crucial role on the performance of the mono-and bi-oxide based catalysts. Amorphous silica-alumina ($\text{SiO}_2 = 86.0 \text{ wt.}\%$, $\text{Al}_2\text{O}_3 = 14.0 \text{ wt.}\%$) was the first support to be investigated. It was found that silica-alumina showed a weak metal-support interaction that led to the segregation of the active MoO_3 phase and consequently low TCC activities. The low ability of the support to promote a high surface dispersion of impregnated Mo metals was attributed to the low concentration of basic surface hydroxyl groups and low isoelectric point (IEP). Conventional transition alumina, which is mainly obtained by the thermal dehydration of boehmite, was also examined. However, it was evident that this particular support could not be used as it is in the TCC process, which operates at mild temperature in the presence of steam. This is mainly attributed to the presence of significant drawbacks of alumina that include poor thermal-hydrothermal stability, and weak ability to homogeneously disperse metal particles at high calcination temperature. Therefore, our yttria doped alumina aerogel was prepared via sol-gel method using a supercritical drying technique. It was observed that the yttria doped alumina aerogel was more thermally stable than alumina aerogel and conventional alumina. The probable explanation for the improvements in the thermal stability of yttria

doped alumina aerogel is believed to be due to the combined effect of the sol-gel method and the formation of stable Y-containing alumina species (i.e. contain lower number of cationic and anionic defects). The hydrothermal stability of yttria doped alumina aerogel was also found to be greatly improved compared to undoped alumina aerogel and conventional alumina. This was evident from the decrease in the loss of surface area and pore volume, and the minimization of structural transformations. The significant improvements were attributed to the combined effect of the sol-gel method and the presence of yttrium ions, which resulted in minimizing the effect of several factors that are believed to favour the hydrothermal sintering. Yttria doped alumina aerogel with various yttria loadings exhibited a lower concentration of surface -OH groups, a higher number of bridged -OH groups that are less susceptible to sintering versus terminal groups, and lower degree of crystallinity with smaller particle sizes, as compared to undoped alumina aerogel. It was also noted that the addition of yttria via impregnation onto the alumina aerogel or conventional alumina resulted in improving the thermal and hydrothermal stability. However, the extent of these improvements was found to be much lower than in the case of doping yttria into the alumina structure (or network). Therefore, it was concluded that in order to observe the most effective roles of yttria, it is quite essential to incorporate it into the alumina structure via the sol-gel, rather than the impregnation method. Another interesting finding was the superior ability of yttria doped alumina aerogel to homogeneously disperse metal particles at high calcination temperature, compared to undoped alumina aerogel and conventional alumina. Explicitly, it was found that yttria doped alumina aerogel is by far more capable of homogeneously dispersing the active molybdenum species and significantly retarding their sintering at

very high calcination temperature than conventional alumina and the alumina aerogel. This was attributed to the incorporation of yttria into alumina aerogel network, which led to a change in the support surface charge (IEP) and subsequently the stability of surface molybdate species. The dispersion degree of ceria (substituted ceria) on supported mono-oxide CeO_2 was improved as well, upon using yttria doped alumina aerogel. In the bi-oxide $\text{MoO}_3\text{-CeO}_2$, characterization results indicated the presence of surface interaction between Mo and Ce, probably through the formation of surface “Mo-O-Ce” type phase between the dispersed ceria and the molybdate monolayer. This interaction, which was highly favoured on the yttria doped alumina surface, contributed significantly to the overall surface stability of Mo-Ce catalysts. The Thermo-Catalytic Cracking performance and kinetic study of n-hexane over yttria doped alumina aerogel supported bi-oxide has been also thoroughly investigated in order to determine the catalytic roles of surface acidity and other physico-chemical properties. It was found that the surface acidity was significantly influenced by the nature of the catalyst support, and the nature and loading of metal oxides. Supported mono-oxide CeO_2 catalysts displayed only Lewis type-sites, which were attributed to the coordinatively unsaturated sites (cus) of $\text{Al}^{3+}_{\text{cus}}$ and $\text{Ce}^{4+}_{\text{cus}}$. The surface acidity of supported mono-oxide MoO_3 catalysts was characterized by the presence of Brönsted and largely Lewis sites, which were attributed to the monodentate alumina-molybdate species, and the $\text{Al}^{3+}_{\text{cus}}$, respectively. The Brönsted sites of yttria doped alumina aerogel supported Mo catalysts were found to exist in lower concentration and were less acidic, when compared to those supported on conventional alumina or undoped alumina aerogel. This was mainly attributed to the incorporation of yttrium ions into the alumina aerogel structure, which significantly altered the chemistry of surface -

OH groups and thus those of the Mo catalysts. Addition of CeO_2 to the supported MoO_3 catalysts led to a decrease in the density of Brønsted acid sites most likely due to neutralization effects, whereas Lewis acid sites appeared to be only slightly altered. The Thermo-Catalytic Cracking activities, which were noted to depend strongly on the catalyst structure (metal loadings and nature of the support) and the surface Brønsted-Lewis acidity, suggested that supported mono-oxide MoO_3 and bi-oxide $\text{MoO}_3\text{-CeO}_2$ catalysts are more catalytically active than supported CeO_2 . It was noted that the total conversion, which increased as the MoO_3 loadings increased up to 12.0 wt.%, was mainly attributed to the presence of Brønsted acid sites. The selectivity to aromatics also increased at the expense of light olefins. The extent of that increase was much higher upon using yttria doped alumina aerogel instead of undoped alumina aerogel as a support. This was mainly attributed to the presence of few acidic Brønsted sites compared to a large population of Lewis sites, which favour the hydrogen transfer (HT) and aromatization reactions. Addition of CeO_2 to the yttria doped alumina aerogel supported MoO_3 resulted in the decrease of the total conversion and the selectivity to aromatics. This was mainly related to the decrease in the total acid density, thus reducing the extent of HT and aromatization reactions. The preliminary kinetic results clearly showed that the apparent activation energy (E_a) of 10.0 wt.% yttria doped alumina aerogel supported mono- (MoO_3) and bi-oxide ($\text{MoO}_3\text{-CeO}_2$) based catalysts are much lower than that of steam cracking.

The final assessment of the results obtained in this thesis, in particular the TCC activities of n-hexane (a model molecule for petroleum light naphtha), revealed that the supported bi-oxide $\text{MoO}_3\text{-CeO}_2$ is not the best configuration to be used in the TCC

process of heavy petroleum feedstocks (i.e. atmospheric and vacuum gas oil, heavy distillates, etc.). This can be ascribed to the weak ability of the supported bi-oxide to convert the naphthenic and aromatic compounds, which exist in large concentration in heavy petroleum fractions, into commercially valuable products.

8.2. ONGOING and FUTURE WORK

8.2.1. Short Term Objectives

The results described in this thesis, in particular the yttria doped alumina aerogel supported bi-oxide catalysts are very interesting from a fundamental and applied point of view. However, we have come across certain points that remain unclear and require more advanced work. First, the existence and the catalytic role of the redox property of supported bi-oxide $\text{MoO}_3\text{-CeO}_2$ should be investigated thoroughly by H_2 -Temperature Programmed Reduction (TPR). Since, cerium species are well known for their unique redox behavior (i.e. shift easily between the oxidized and reduced states ($\text{Ce}^{3+} \rightleftharpoons \text{Ce}^{4+}$)). For example, we have reported in Chapter VII, which that the selectivity to aromatics increased with the formation of segregated ceria crystallites. That increase was attributed to a possible enhancement in the hydrogen transfer and aromatization reactions. However, we have not, as of yet, excluded other more complex mechanisms, which takes into account the redox properties of ceria. Second, the dispersion of ceria (substituted ceria) was observed to be drastically improved upon using yttria doped alumina aerogel as a support instead of undoped alumina aerogel and conventional alumina (chapter VI). The improvement was mainly attributed to the support-cerium interaction. Based on our XRD and Raman measurements, we have stated tentatively that ceria dispersed phase is most probably Ce^{3+} -like species, and/or to smaller extent bulk CeO_2 crystallites whose crystallite size is less than 4.0 nm. However, it is very clear that without X-ray Photo Electron Spectroscopy (XPS), we will not be able to definitely confirm neither the presence nor (particularly) the structure of Ce^{3+} like species (i.e. if they are the same as those proposed by Shyu et al (reference 59, Chapter VI). Therefore, XPS measurements

must be carried out in order to provide a better explanation. Third, we have thoroughly investigated the physico-chemical properties of the supported mixed oxide based catalysts before the TCC reaction. It would be essential to examine these properties during, and after the reaction and the reaction-regeneration cycle. This would allow us to be able to evaluate the influence of reaction conditions and in particular the presence of carbon deposits on the properties of these catalysts. For instance, surface acidity measurements can provide information about the influence of carbon deposit on the structure of Brønsted-Lewis acid site and the degree of coverage by coke. Fourth, hydrogen is produced in-situ (via steam cracking) during the TCC reaction. The presence of hydrogen will certainly affect the physical-chemical and catalytic properties of supported mono-and bi-oxide based catalysts, which are composed of transition metal with multiple oxidation states (i.e. Mo). For instance, hydrogen can generate the coordinative unsaturated sites (cus). Thus, affecting not only the surface acidity, but also the adsorption capacity. Therefore, it is quite critical to examine the influence of hydrogen on the structure of the supported mono- and bi-oxide based catalysts. This can be performed using the H₂-TPR. Fifth, yttria stabilized alumina aerogel displayed outstanding properties (i.e. high surface area, high thermal-hydrothermal-structural stability, and strong support-metal interactions). However, it was clear that the surface acidity was negatively influenced. Most of the generated surface Brønsted sites were less acidic, due to the incorporation of yttria into the alumina aerogel lattice. Therefore, other less basic dopants but effective enough to stabilize the structure of alumina, should be explored. Possible candidate is lanthanum oxide.

8.2.2. Long Term Objectives

With the continuous decline of conventional oil reserves, the utilization of heavy petroleum feedstocks (vacuum gas oil, bitumen derived crude oil, etc.) is becoming an essential alternative. Therefore, one of the strategic objectives of the Thermal-Catalytic Cracking process is to use these heavy feedstocks for the production of light olefins. Our preliminary results of the catalytic activities of supported bi-oxide $\text{MoO}_3\text{-CeO}_2$ catalysts in the TCC of heavy feedstocks have indicated unfavourable catalytic activities and stabilities (Table 8.1) [1].

Table 8.1: TCC activities of heavy feedstocks using the hybrid catalyst containing the co-catalyst ^a

Product Yield (wt.%)	Hybrid catalyst (80.0 wt.% supported $\text{MoO}_3\text{-CeO}_2$ (MCC) + 20.0 wt.% Ni-containing catalyst (cocatalyst /HSO promoter))			
	Amount of Ni in the cocatalyst (wt.%)			
	0.0	1.7	2.8	3.4
C ₁ -C ₄ alkanes	13.8	13.2	12.5	14.2
C ₂ -C ₄ olefins and diolefin	49.0	51.2	51.7	54.7
BTX	14.1	13.4	13.3	11.1
(C ₅ -200 °C, non BTX)	12.2	13.3	13.7	12.2
200-400 °C	9.4	7.4	7.3	6.2

^a: T = 725 °C, total W.H.S.V. = 1.7 h⁻¹, catalyst weight = 7 g, feed = AGO-2 (heavy atmospheric gas oil), steam/feed wt. ratio = 1.0, and reaction time is 10 h.

It was noted that these catalysts displayed poor on-stream-long-term stability (fast decay), and higher selectivity to aromatics. As a result, a catalyst regeneration cycle was required frequently, which was not an ideal situation for the TCC process that operates with a fixed bed reactor configuration. These observations were mainly attributed to the weak ability of supported bi-oxide catalyst to convert the naphthenic and aromatics compounds, which exist in high concentration in heavy fractions (Table 8.2), into more

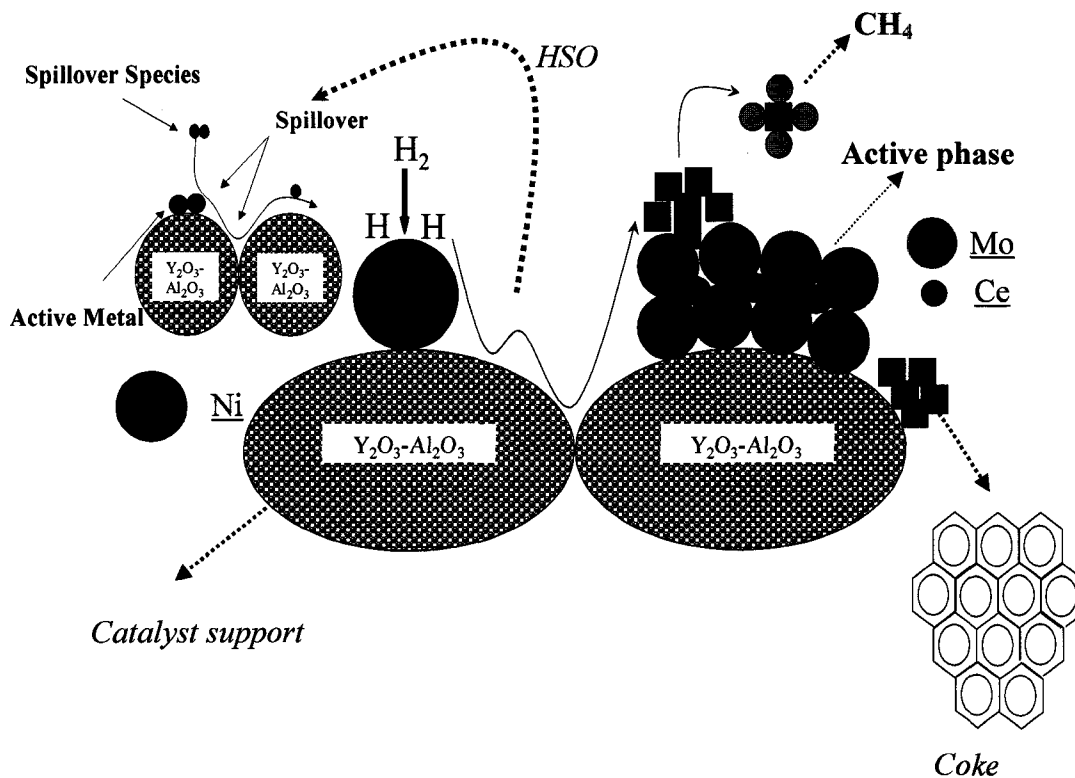
valuable products such as light olefins. Due to the hydrogen transfer (HT) and aromatization character of the supported bi-oxide catalysts, which are expected to be greatly enhanced in the presence of these compounds (i.e. HT: olefins + naphthene → aromatic + paraffin).

Table 8.2: Typical analysis of different petroleum feedstocks

Petroleum Feedstocks	Boiling Point (°C)	Paraffins	Naphthenes	Aromatics
Light naphtha [2] Vacuum Gas Oil	58-170	62.7	29.1	8.2
(Conventional crude oil sources) [3] Vacuum Gas Oil	343-525	22.8	38.2	39.0
Bitumen derived) [3]	343 °C +	4.1	42.7	53.2

8.2.2.1. Hydrogen Spillover (HSO) Phenomenon

Therefore, the best approach to address these challenges would be to design and develop an advanced catalyst with proper structure, which has the ability to effectively promote certain phenomenon that might be useful in resolving the problems of catalyst longevity as well as stability of activity and selectivity. For instance, hydrogen spillover (HSO) phenomenon, which is associated with the transport of the active species adsorbed on one surface onto another that does not adsorb these species under the same conditions (scheme 8.1), is well recognized for its outstanding role in stabilizing the catalytic activities and selectivity of solid catalysts [4-10]. Such roles include maintaining the catalytic stabilities via controlling and removing harmful by-products (carbonaceous deposits). For instance, spillover species can react with surface carbon (coke) and remove it as methane and carbon dioxide [4,6-10].



Scheme 8.1: schematic representation of spillover phenomenon; from an active metal adsorbing surface onto a catalyst support, and then onto another surface that is in contact with the support

This role is schematically represented in scheme 8.1. Other beneficial roles include the creation of new adsorption or selective active sites [4], and prompting the ring opening reaction of naphthenic compounds [10]. The HSO phenomenon requires the presence of certain important elements in order to occur effectively. These elements include the presence of active metal (Ni, or noble metals), which has the capability to adsorb hydrogen dissociatively. It is worth mentioning that some of these elements are already available in the TCC reaction stream, while others can be easily implemented. The active metal can be incorporated with a proper loading and method onto the supported bi-oxide catalyst. Hydrogen, which is the source of spillover species, will be available in-situ in the TCC via the thermal (steam) cracking reactions [11] and the steam reforming properties of Ni [12]. Our preliminary results (Table 8.1) [1] showed that the supported Ni-cocatalyst of the TCC hybrid catalyst produces very active hydrogen species. Such species once transferred (spilt-over) onto the surface of the main catalyst component (cracking sites), interact with the adsorbed reaction intermediates, resulting in a decreased formation of coke precursors (poly-nuclear aromatics) and de-aromatization/ring-opening of some heavy compounds of the feed. Simultaneously, there is a significant increase of the product yields of light olefins.

8.2.2.2. Pore Continuum Configuration

In addition, it was also evident the influence of the HSO promoter was much enhanced upon using the pore continuum configuration (Ni-cocatalyst //zeolite). Our recent work (Table 8.3) [1] showed that the pore continuum configuration (Ni-cocatalyst //zeolite) is more active than the previous investigated (MoO₃-CeO₂ cocatalyst //zeolite) (Chapter II) and (Ni-cocatalyst // MoO₃-CeO₂) (Table 8.1).

Table 8.3: Performance of the hybrid catalyst containing HZSM-5 (Si/Al = 25) as the microporous zeolite component, and Ni-cocatalyst as the mesoporous component ^a

Petroleum Feedstocks	Light naphtha	Medium Naphtha	Atmospheric Gas Oil (AGO)	Vacuum Gas Oil (VGO)
R (steam/feed) (wt/wt)	0.5	0.6	0.8	1.0
Product yield (wt.%)				
C ₁ -C ₄ alkanes	15.8	16.6	15.7	15.8
C ₂ =C ₄ olefins and diolefin	62.6	56.6	51.4	54.3
(C ₅ -200 °C, non BTX)	11.3	8.0	6.4	6.7
BTX	8.1	14.9	11.5	8.5
200-400 °C	0.6	2.3	13.5	13.1

^a : temperature = 725 °C; W.H.S.V. = 2.0 h⁻¹, W (catalyst) = 5g and reaction time is 10 h.

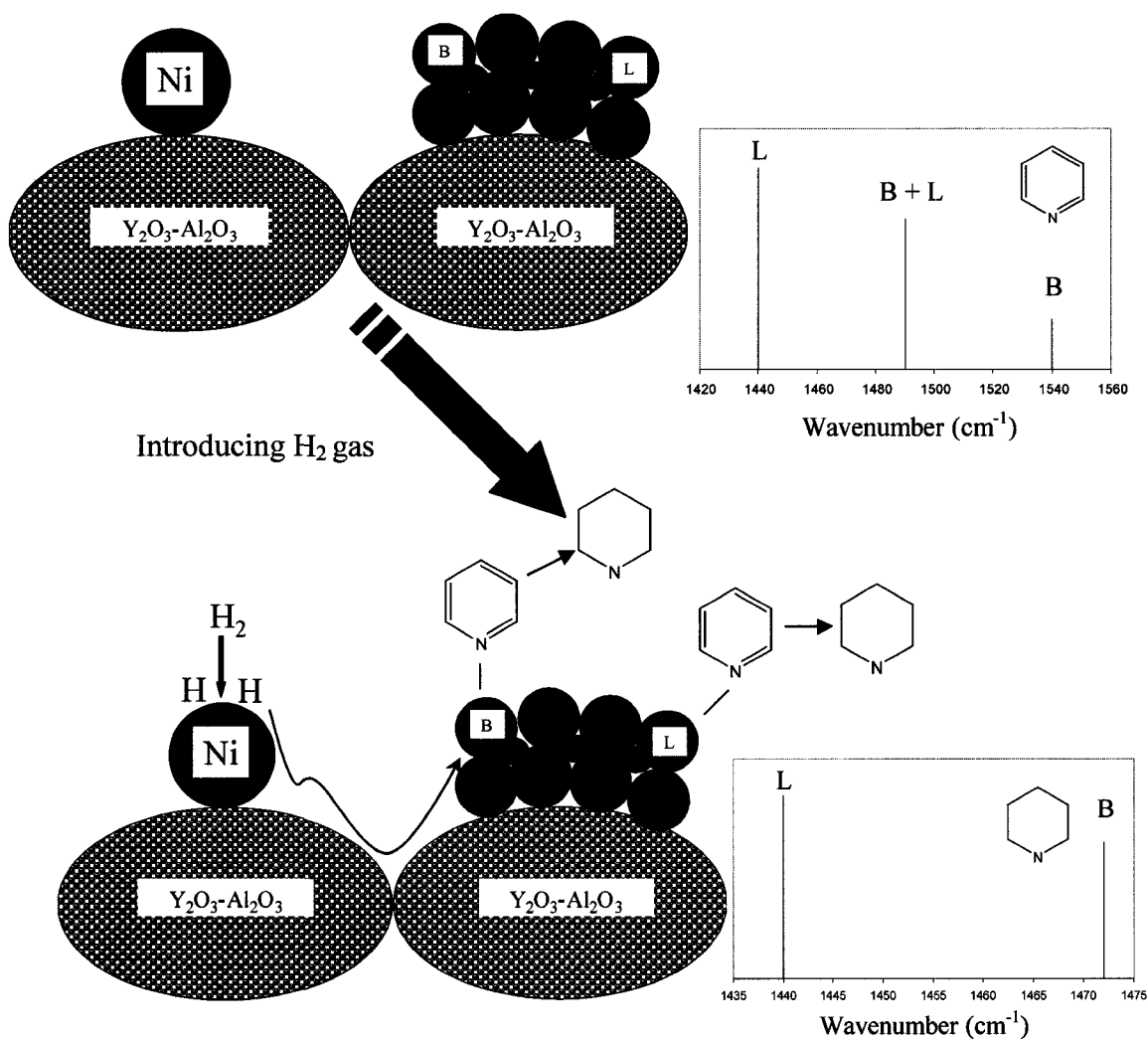
These recent results (Ni-cocatalyst // zeolite (pore continuum configuration)) are very interesting and encouraging, however more work is need for further development. Any further work should mainly aim at answering several key questions in relation to the HSO phenomenon and pore continuum catalyst configuration. These questions are,

- a) Does the HSO phenomenon exist in the TCC of heavy petroleum feedstocks, using Ni-cocatalyst // zeolite pore continuum configuration?
- b) What is the beneficial role of the HSO on the TCC process?

8.2.2.3. Evaluation of the existence of hydrogen spillover phenomenon (HSO) with Ni-cocatalyst // zeolite pore continuum configuration in the TCC process

The occurrence of the HSO phenomenon can be determined from the Thermal Catalytic-Cracking activities of Ni-promoted // zeolite catalysts. However, any observed catalytic results cannot be certainly attributed to one particular reason. For instance, any changes with regard to total conversion, and product selectivity upon using pore continuum configuration catalyst, cannot be simply ascribed to the HSO actions. This is

because of the complexity and numerous number of TCC reactions. Therefore, in order for us to unambiguously confirm the occurrence of HSO, it would be essential to utilize a more direct and convincing method that has minimum number of interfering factors. We will be employing the FT-IR of adsorbed pyridine technique, which was developed by Fujimoto group [7,8], for studying the HSO phenomenon (scheme 8.2).



Scheme 8.2: schematic representation of hydrogenation of chemisorbed pyridine to piperidine on Ni promoted supported bi-oxide hybrid catalysts, after exposure to H₂ (the effect of HSO phenomenon)

In this method, we will monitor the changes in the IR spectrum of chemisorbed pyridine on the Ni-cocatalyst // zeolite catalyst upon introducing H₂ gas (i.e. appearance of new peaks, and/or modification of existing peaks (intensity or position)). There should be two different scenarios, according to this established method. First, if there is a HSO, we should expect changes that indicate a hydrogenation reaction (i.e. pyridine to piperidine). Second, if the IR spectrum remains unchanged after exposing the catalyst to H₂ gas, this would indicate that no hydrogenation reaction took place, and hence no HSO phenomenon can be accounted for. These two scenarios are represented in scheme 8.2.

8.2.2.4. Identification of the beneficial role of HSO on the TCC catalyst

As previously mentioned that there are many important roles of HSO phenomenon on the catalytic activities. However, we will limit our investigation to its role on the catalyst deactivation (coking) rate. In order to identify that role, we will need to thoroughly study the catalytic activities and stability, as well as characterize the carbonaceous deposits on the surface. The catalyst performance and stability in the TCC should be investigated at different reaction-regeneration cycles that represent the on-stream and long-term stability..

8.2.2.4.1. The TCC activities and stabilities of model molecules

The Thermal-Catalytic Cracking (TCC) activities over Ni-cocatalyst // zeolite configuration should be performed using other model molecules such as unsaturated naphthenes (i.e. cyclohexene) and poly nuclear aromatics (PNA) (i.e. naphthalene) (Table 8.4). The catalytic activities in terms of total conversion and product selectivity (toward the BTX and PNA compounds, should be monitored closely.

Table 8.4: The chemical structure and boiling point range of different class of PNA hydrocarbons

Poly nuclear aromatic (PNA) Class	Boiling Point Range (° C)	Reference Compound
Condensed biaromatics	200-300	Naphthalene
Condensed triaromatics	300-400	Phenanthrene
Condensed polyaromatics	> 400	Benzo (a) pyrene

8.2.2.4.2. Analysis of Carbonaceous deposits (coke)

The carbonaceous deposits (catalyst poison) on the surface of spent and regenerated catalysts should be methodically characterized by different techniques in order to determine the structure and chemical nature, as well as the concentration of these deposits. These techniques include the differential and gravimetric thermal analysis (DTA/TGA) techniques for determining the amount and combustive properties of these deposits. In addition, carbon-hydrogen analyzer, ¹³ C Magic Angle Spinning (MAS) NMR, and Deep UV-Raman should be used for evaluating the structure and chemical nature. Temperature-programmed oxidation combined with Gas chromatography (TPO-GC) should be also used for determining the concentration of carbon oxides (CO_x).

8.3. THE SIGNIFICANCE OF THIS THESIS

This Doctoral thesis is of great significance to many areas including the Thermal-Catalytic Cracking process, research and development in the field of catalysis, and the Canadian petroleum industry and the environment.

8.3.1 Thermal-Catalytic Cracking process

The results obtained from this dissertation allowed us to acquire a deep understanding of the Thermal-Catalytic Cracking activities of supported bi-oxide $\text{MoO}_3\text{-CeO}_2$ from a mechanistic and kinetic point of view. As a matter of fact, the thesis work has paved the way for developing a more active and stable catalyst, which is the hybrid catalyst containing Ni species (hydrogen spill over (HSO) promoter), for dealing with heavy petroleum fractions.

8.3.2. Research and development in the field of catalysis

This dissertation also provided significant contributions in the area of advance material design of supported metal oxides catalysts. An area of great interest because of the numerous applications of these catalysts in various fields (i.e. hydrotreatment (hydrodesulfurization), and three-way catalyst (TWC)). Other significant contributions to the field of catalysis were the concepts of pore continuum and hydrogen spill over phenomenon (HSO). These concepts have found applications in several important industrial reactions such as aromatization, and selective hydrocarbon ring opening, respectively. The thesis work has been published or is soon to be appeared in top periodical international journals in the field of catalysis and porous materials such as *Applied Catalysis A: General*, *Catalysis Letters*, *Topics in Catalysis*, *Industrial and Engineering Chemistry Research*, and *Microporous and mesoporous Materials*. It was

brought to our attention recently that our published work (R. Le Van Mao, N. Al-Yassir and D. N., *Micropor. Mesopor. Mater.* **85** (2005) 176), which presented the concept of pore continuum, has been cited three times in top journals (Q. Tan, X. Bao, T. Song, Y. Fan, G. Shi, B. Shen, C. Liu, X. Gao, *J. Catal.* **251** (2007) 69; Y. Ding, J. Liang, Y. Fan, Y. Wang, X. Bao, *Catal. Today*, **125** (2007) 178; and V. M. Akhmedov, S. H. Al-Khowaiter, *Cat. Rev. - Sci. Eng.*, **49** (2007) 33).

8.3.3. The Canadian petroleum industry and the environment

Thermal-Catalytic Cracking (TCC) process for the production of light olefins from heavy petroleum feedstocks is strongly regarded as a promising and alternative route for light olefins production over the current conventional ones. This process when fully developed and commercialized will help to produce both ethylene and propylene as the primary products from heavy feedstocks, while at the same time minimizing the energy costs and the emissions of greenhouse gas, a problem with great interest to the petroleum industry. Thus, both the Canadian petrochemical industry and environment may benefit from this research. More significantly, this process aims at exploiting synthetic crude oil (SCO) derived from bitumen (oil sand) as potential petroleum feedstocks. Canada is considered to be one of the largest hydrocarbon deposits in the world with an estimation of 1.7-2.5 trillion barrels of bitumen in place putting Canada on par with Saudi Arabia's conventional oil reserves [58,66]. Although, the Canadian oil sands (bitumen) resources has been increasingly recognized as a strategic source of world energy supply, they suffer from major disadvantages largely related to high contents of aromatic and naphthanic compounds. The TCC advanced Ni promoted supported bi-oxide hybrid catalysts will allow the utilization of the SCO as a feedstock in the TCC

process. Thus, upgrading the lower-value materials (SCO) to more valuable products such as ethylene and propylene. This unquestionably will have a major impact on the Canadian petroleum industry, particularly the oil sand industry.

8.4. REFERENCES

- [1] R. Le Van Mao, N.T. Vu, N. Al-Yassir, H.T. Yan, *Ind. Eng. Chem. Res.* (Submitted, Ms. No. tie071629).
- [2] S. Matar and L.F. Hatch, in: *Chemistry of Petrochemical Processes*, 2nd ed., Gulf Professional Publishing, Woburn, MA, (2001).
- [3] S. H. Ng, J. Wang, C. Fairbridge, Y. Zhu, L. Yang, F. Ding, S. Yui, *Energy and Fuel*, **18** (2004) 160.
- [4] W. C. Conner, Jr., J. L. Falconer, *Chem. Rev.* **95** (1995) 759.
- [5] U. Roland, T. Braunschweig, F. Roessner, *J. Mol. Catal. A: Chem.*, **127** (1997) 61.
- [6] B. Delmon, *Solid State Ionics*, **101-103** (1997) 655.
- [7] A. Zhang, I. Nakamura, K. Fujimoto, *J. Catal.*, **168** (1997) 328.
- [8] R. Ueda, T. Kusakri, K. Tomishige, K. Fujimoto, *J. Catal.*, **194** (2000) 14.
- [9] G. M. Pajonk, *Appl. Catal. A: Gen.*, **202** (2000) 157.
- [10] H. Du, C. Fairbridge, H. Yang, Z. Ring, *Appl. Catal. A: Gen.*, **294** (2005) 1.
- [11] A. Chauvel, G. Lefebvre, in: *Petrochemical Processes*, Vol. 1, Technip, Paris, (1989), pp.117-165.
- [12] J. R. H. Ross, M. C. F. Steel, A. Zeini-Isfahani, *J. Catal.*, **52** (1978) 280.